PhD Thesis

Localized generation of the catalytic metallic nanostructures and pH mapping with scanning electrochemical microscopy

Magdalena Michalak

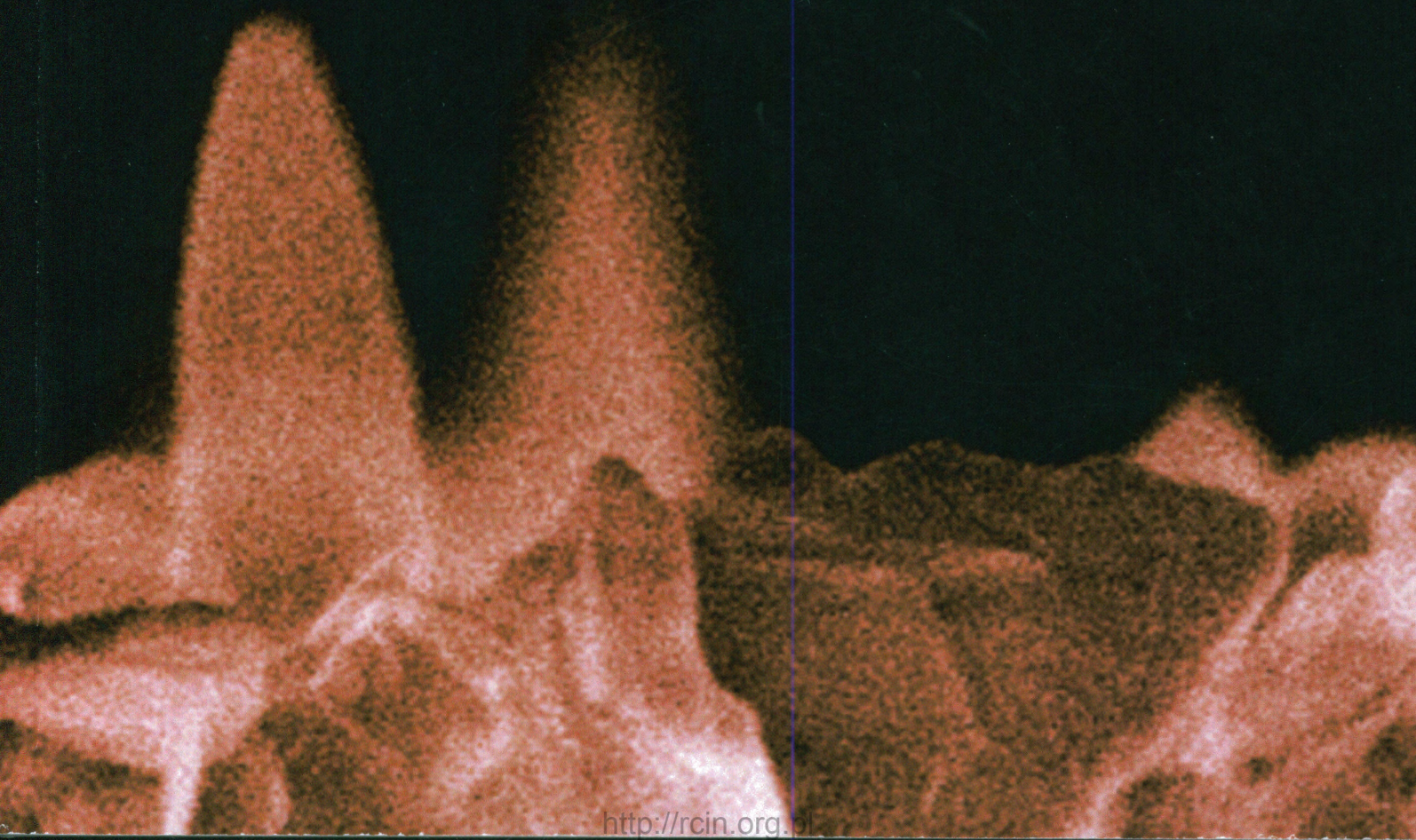

http://rcin.org.pl

Institute of Physical Chemistry
Polish Academy of Sciences
Kasprzaka 44/52
01-224 Warsaw, Poland

Localized generation of the catalytic metallic nanostructures and pH mapping with scanning electrochemical microscopy

Magdalena Michalak

PhD thesis

This dissertation was prepared within the International Ph.D. Studies
at Institute of Physical Chemistry, Polish Academy of Sciences

K-9-175, K-9-161, A-21-7

Supervisor: prof. dr hab. Marcin Opałło

Auxiliary supervisor: dr inż. Wojciech Nogala

Biblioteka Instytutu Chemii Fizycznej PAN
F-B.519/20
10000000107072

Warsaw, December 2019

http://rcin.org.pl

Acknowledgements

I would like to thank:

Prof. dr. hab. Marcin Opałło and **Dr. Wojciech Nogala**, my Supervisors, for they support, understanding, patience, kindness and motivation during my PhD studies.

Prof. dr. Gunther Wittstock for the opportunity of research work in his laboratory at Carl von Ossietzky University of Oldenburg in Germany.

Dr. Agata Roguska and **Dr. hab. Martin Jönsson-Niedziółka** for EDX experiments, **Dr. Adam Leśniewski** for AFM experiment; and for their constructive scientific comments and friendliness.

I would like to thank all my colleagues from the Department of Electrode Processes, especially **Dr. Justyna Kalisz, Justyna Matyjewicz-Walczyk, Magdalena Kundys-Siedlecka, Dr. Dorota Buczyńska** and **Joanna Dolińska**.

I would like to thank **my parents** for their love, help and support for my school career.

Also I would like to thank **my parents-in-law** for their faith and help, and **my friends,** especially **Daria and Basia**, for their emotional support.

Finally I would like to thank **my husband Jarosław** for his love and invaluable care.

Instytut Chemii Fizycznej PAN
BIBLIOTEKA
B. 519/20

http://rcin.org.pl

I would like to acknowledge financial support from:

Institute of Physical Chemistry Polish Academy of Sciences

Polish National Science Centre, NCN Poland

Grants: UMO-2012/05/D/ST4/01956 and UMO-2016/21/N/ST4/03559

Polish Ministry of Science and Higher Education

Grant: IP2012 048872

http://rcin.org.pl

Abstract

In the first part of the thesis, the development of a method of preparation of ligand-free copper (CuNS), gold (AuNS), and bimetallic nanostructures (NS) was described. NS were obtained by localized electrorefining of polycrystalline metal wires from the microelectrodes on indium tin oxide (ITO) and glassy carbon (GC) supports, using scanning electrochemical microscopy (SECM). The morphology of the obtained NS and thus their catalytic properties were adjusted by the electrorefining parameters, *e.g.* the potential of electrodeposition, translation rate of the microelectrode and composition of the electrolyte. A number of various NS prepared on a single support were studied for their catalytic activity toward oxygen reduction reaction (ORR) in alkaline media and carbon dioxide reduction reaction (CO_2RR) by SECM feedback mode. Their electrocatalytic activity toward the afore-mentioned reactions depends on electrorefining conditions.

In the second part preparation of syringaldazine (Syr) modified carbon nanoelectrode for local pH imaging was described. pH was determined from the mid-peak potential of a cyclic voltammogram of an adsorbed Syr. Voltammetric pH nanosensor exhibited a stable quasi-reversible voltammetric response within the pH range of 2 – 12 with fast response and high spatial resolution. It was successfully applied for mapping of local alkalization of buffered electrolyte in the vicinity of a Pt microelectrode during ORR.

http://rcin.org.pl

Streszczenie

W pierwszej części pracy przedstawiona została metoda otrzymywania czystych (nie pokrytych grupami funkcyjnymi), miedzianych, złotych oraz mieszanych nanostruktur metalicznych (NS). NS otrzymano za pomocą miejscowej elektrorafinacji poprzez kontrolowane roztwarzanie polikrystalicznych drutów odpowiednich mikroelektrod. Nanostruktury osadzane były miejscowo na elektrodzie ITO (tlenku indu domieszkowanego tlenkiem cyny) lub na elektrodzie z węgla szklistego (GC), przy użyciu skaningowej mikroskopii elektrochemicznej (SECM). Morfologię otrzymanych NS (kształt i wielkość), a tym samym ich właściwości katalityczne, dostosowywano zmieniając parametry elektrorafinacji, np. potencjał elektroosadzania, szybkość przesuwu mikroelektrody lub skład elektrolitu. Właściwości katalityczne NS osadzonych na tym samym podłożu, podczas różnych warunków elektroosadzania, badano względem reakcji redukcji tlenu (ORR) w środowisku alkalicznym i reakcji redukcji dwutlenku węgla (CO_2RR), używając trybu sprzężenia zwrotnego SECM. Aktywność NS względem wymienionych reakcji katalitycznych zależała od warunków w jakich prowadzone było ich elektroosadzanie.

W drugiej części opisano otrzymanie nanoczujnika do lokalnego obrazowania zmian pH. Czujnik ten uzyskano przy użyciu nanoelektrod węglowych zmodyfikowanych syryngaldazyną (Syr). Wartość lokalnego pH została wyznaczona poprzez pomiar potencjału redoks zaadsorbowanej Syr. Sensor wykazywał stabilną kwazi-odwracalną odpowiedź w zakresie pH od 2 do 12. Cechował się szybkim czasem odpowiedzi i wysoką rozdzielczością przestrzenną. Zastosowano go do wykonania mapy lokalnych zmian pH w roztworze buforowym, przy powierzchni mikroelektrody platynowej, podczas prowadzenia na niej reakcji redukcji tlenu.

http://rcin.org.pl

Abbreviations

Abbreviation	Meaning
[Bmim][NTf_2]	1-butyl-3-methylimidazolium bis (trifluoromethylsulfonyl) imide
3D	three-dimensional
AC	alternating current
AC-SECM	alternating current SECM mode
AFC	alkaline fuel cell
AFM	atomic force microscopy
AuNS	gold nanostructures
AuUME	gold microelectrode
CHE	computational hydrogen electrode
CNE	carbon nanoelectrode
CNTs	carbon nanotubes
CO_2RR	carbon dioxide reduction reaction
CuNS	copper nanostructures
CuUME	copper microelectrode
CV	cyclic voltammetry
DC	direct current
DCE	direct current electrodeposition
DCE	1,2-dichloroethane
DFT	density functional theory
DPA	9,10-diphenylanthracene
EC-AFM	electrochemical atomic force microscopy
ECL	electrochemiluminescence
EC-SPMs	electrochemical scanning probe microscopies
EC-STM	electrochemical scanning tunneling microscopy
EDX	energy dispersive X-ray spectroscopy
EMF (ΔV)	electric potential difference (formerly called electromotive force)
E_{mp}	midpeak potential
E_p	peak potential
FB	feedback SECM mode
FDM	ferrocendimethanol
GC	glassy carbon plate electrode
HER	hydrogen evolution reaction
i.d.	inner diameter
ICEs	internal combustion engines
ISME	ion selective microelectrode
IT/ET	Ion transfer/electron transfer SECM mode
ITO	indium tin oxide electrode
IUPAC	International Union of Pure and Applied Chemistry
LIA	lock-in amplifier
MOFs	metal organic frameworks
NCNTs	nitrogen-doped carbon nanotubes

http://rcin.org.pl

non-PGM	non-platinum group metal
NPs	nanoparticles
NS	nanostructures
o.d.	outer diameter
OC	open circuit
OCP	open circuit potential
ORR	oxygen reduction reaction
PANI	polyaniline
PAQ	9,10-phenanthraquinone
PBS	phosphate buffered saline
PCE	pulse current electrodeposition
PEMFC	proton exchange membrane fuel cells
PtUME	platinum microelectrode
QRCE	quasi-reference counter electrode
RC	redox competition SECM mode
SCE	saturated calomel electrode
SECCM	scanning electrochemical cell microscopy
SECM	scanning electrochemical microscopy
SECPM	scanning electrochemical potential microscopy
SEM	scanning electron microscope
SF-SECM	shearforce SECM mode
SG/TC	substrate generation/tip collection SECM mode
SHE	standard hydrogen electrode
SICM	scanning ion conductance microscopy
SI-SECM	Surface-interrogation SECM mode
SPM	scanning probe microscopies
SPR	surface plasmon resonance
STM	scanning tunneling microscopy
Syr	4-Hydroxy-3,5-dimethoxybenzaldehyde azine (syringaldazine)
TG/SC	tip generation/substrate collection SECM mode
UME	ultramicroelectrode (microelectrode)
UPD	underpotential deposition
VA-NCNTs	vertically aligned nitrogen-containing carbon nanotubes

http://rcin.org.pl

Table of content

http://rcin.org.pl

http://rcin.org.pl

http://rcin.org.pl

1. Introduction and research goals

Electricity (electrical power) is generated by the conversion of primary energy sources like fossil fuels, nuclear, wind or solar. It is an essential element of everyday life and economic vitality. In some places, *e.g.* in European Union, fossil fuels are still the major power source.[1] Reaching the carbon balance in the environment is currently one of the most extensively investigated topics. Electricity generated from low efficient internal combustion engines (ICEs) is gradually replaced by the one obtained in proton exchange membrane fuel cells (PEMFC) or alkaline fuel cells (AFCs), where direct conversion of chemical energy into electricity occurs.[2,3]

Many researches are focused on innovations in electricity generation, energy storage, and exploitation of renewable energy sources. Oxygen reduction reaction (ORR) in alkaline media is a well-known reaction which is important in the conversion of the chemical energy to electricity. ORR is well-catalyzed by an expensive Pt catalyst.[4] Finding an inexpensive and efficient catalyst for ORR is challenging. Researches are also focused on carbon dioxide reduction reaction (CO_2RR) which suggests a new approach to the topic of energy storage and reduction of this greenhouse gas in the atmosphere. However, the mechanism of CO_2RR is very complicated, and still not well understood.[5]

Crucial parameter influencing the product selectivity and thus the reaction pathway during catalytic reactions is the pH of the solution.[6] pH determination in micro- and nanoscale, and its control, are indispensable for maintaining desired process conditions. It is a challenge to develop a fast, sensitive and reliable sensor to detect small pH changes. Carbon-based voltammetric sensors seem to be the best candidates for these applications since they are biocompatible, conductive, appropriate for surface modification and suitable for experiments in nanoscale.[7–9]

The main goal of the presented thesis is to develop a procedure of obtaining a new nanomaterials with high electrocatalytic activity toward ORR in alkaline media and CO_2RR. This methodology should allow to obtain nanomaterials in an environment-friendly and efficient way. Their morphology and catalytic properties should be easily adjusted. It is important to understand the mechanisms of how the procedure conditions influences the structure of obtained nanomaterials. The second goal is to develop a tool allowing to indicate which features of nanomaterials are responsible for their catalytic properties. Many electrocatalytic processes driven on the nanomaterials in aqueous solutions cause local changes in the acidity of the solution, near the surface of the catalyst. There is a current interest to investigate how much local pH can change even in buffered electrolytes. This requires development of a sensor able to detect low pH variations at nanometric spatial resolution.

http://rcin.org.pl

Literature review

2. Oxygen reduction reaction

2.1. Introduction

Internal combustion engines (ICEs) have harmful impact on the environment, as they have low efficiency (15%) and emit dangerous pollutants like CO_2. Essential innovations in electricity generation and alternative methods for fueling transportation, as well as exploitation of renewable energy sources such as solar, wind, and hydroelectric power are necessary. Proton exchange membrane fuel cells (PEMFC) involve electrochemical oxidation of fuel (*e.g.* hydrogen) and show off much higher energy efficiencies (50–60%) than ICEs, with low operating temperature, quick starting, and a compact construction.[2,10–12]

Despite the problems with the hydrogen production, fuel station infrastructure and their high cost, PEMFC are already commercialized.[13] One of the most expensive component of the PEMFC production cost is the price of the catalyst – platinum, which catalyzes both anodic and cathodic reactions. On the anode, platinum catalyzes oxidation of H_2 into protons. This process needs relatively low overpotential and low loadings of platinum.[14] However, on the cathode, a much larger amount of catalyst is required, since platinum catalyzes the slow process of oxygen reduction reaction (ORR). Also, platinum natural resources are not rich enough to maintain the global mass production of fuel cell cars without its cost-effective recycling methods.[10] A lot of researches toward finding an alternative catalyst were performed, but the cost of PEMFC still remains a main barrier in exploitation for transport and powering of stationary or portable devices.[2,15]

Recent advances in polymer anion exchange membranes have led to increasing studies of alkaline fuel cells (AFCs).[3] AFCs have a lot of advantages in comparison to traditional PEMFCs. They requires lower overpotentials to ORR in the alkaline media and, instead of Pt, they use transition metals that are cheaper and more easily accessible,[16] *e.g.* palladium as an anode catalyst[17] and silver as the cathode catalyst.[18] Silver is also a promising replacement for platinum because it has similar mechanisms and kinetics for ORR catalysis.[19] Even though low anodic overpotentials facilitate alcohol oxidation in alkaline media, the slow kinetics of the ORR remains a significant challenge.

http://rcin.org.pl

2.2. ORR mechanism

In the ORR, molecular oxygen can be electrochemically reduced to stable products by two or four electrons pathways. Products depend on the catalyst, electrode potential, temperature, electrolyte composition and other physiochemical parameters. The mechanism of ORR strongly depends on the pH of the solution.

In acidic media, [E^0 *vs.* standard hydrogen electrode (SHE)]:

$$O_2 + 4(H^+ + e^-) \rightleftarrows 2H_2O \qquad E^0 = 1.229\ V \qquad \text{(Eq.2.1)}$$

$$O_2 + 2(H^+ + e^-) \rightleftarrows H_2O_2 \qquad E^0 = 0.695\ V \qquad \text{(Eq.2.2)}$$

$$H_2O_2 + 2(H^+ + e^-) \rightleftarrows 2H_2O \qquad E^0 = 1.763\ V \qquad \text{(Eq.2.3)}$$

In alkaline and neutral media, (E^0 *vs.* SHE):

$$O_2 + 2H_2O + 4e^- \rightleftarrows 4OH^- \qquad E^0 = 0.401\ V \qquad \text{(Eq.2.4)}$$

$$O_2 + H_2O + 2e^- \rightleftarrows HO_2^- + OH^- \qquad E^0 = -0.065\ V \qquad \text{(Eq.2.5)}$$

$$HO_2^- + H_2O + 2e^- \rightleftarrows 3OH^- \qquad E^0 = 0.867\ V \qquad \text{(Eq.2.6)}$$

In acid solutions, ORR occurs by direct four electron-proton reaction or by consecutive two-electron-proton steps. In the first case O_2 yields directly to H_2O formation, in the second one - to H_2O_2 and then H_2O. In alkaline media, the four-electron direct reduction results in the formation of four equivalents of hydroxide, while the two-electron reduced product is one equivalent of hydroxide and one hydroperoxyl anion. The hydroperoxyl anion can then be further reduced by two electrons to three hydroxide ions.[4,10,11,20,21]

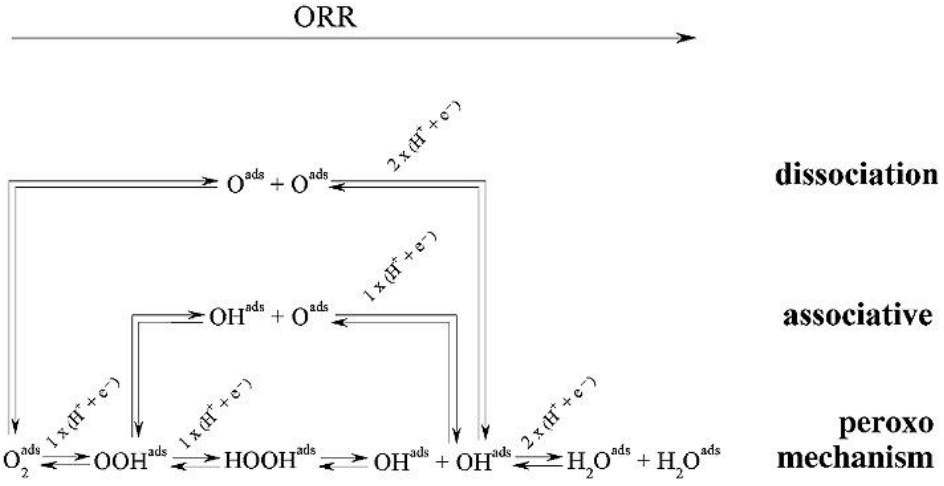

Fig. 2.1. Proposed ORR mechnisms.[22]

http://rcin.org.pl

The proposed ORR mechanisms can be unified in a single scheme (Figure 2.1). The ORR proceeds through a dissociation mechanism when the O-O bond of oxygen breaks directly upon adsorption and the formed O_{ads} is reduced successively to OH_{ads} and to H_2O_{ads}. The associative mechanism of the ORR involves the formation of OOH_{ads}, which breaks into O_{ads} and OH_{ads}. Moreover, the ORR can proceed through the peroxo mechanism when two electron-transfer steps lead successively to OOH_{ads} and to $HOOH_{ads}$, and then breaks into OH_{ads}.[22]

Density functional theory (DFT) was used to calculate the adsorption energies on metallic surfaces and indicated that the binding energy between oxygen intermediates and the catalyst surface is correlated with the catalytic efficiency for ORR. In accordance to the Sabatier principle, a reactant must bind to the catalyst surface in an appropriate manner: strong enough, to make the reaction happen and weak enough to dissociate and therefore to protect the catalyst from poisoning by the intermediates or the reactants.[23] To find the optimal oxygen binding energy (ΔE_O) for an ORR catalyst one can compare catalytic activity to ΔE_O, and based on theoretical calculations and experimental data create a "volcano plot" graph showing these correlations (Figure 2.2).[4,20,24,25]

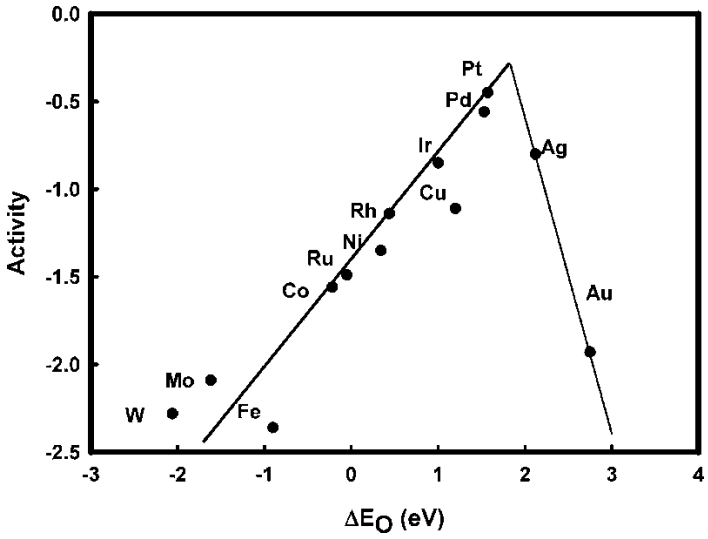

Fig. 2.2. Volcano plot showing relationship between oxygen binding energy and catalytic activity toward ORR calculated using Sabatier Analysis.[4]

As it is seen in the Figure 2.2, Pt catalysts lies in the most optimal position, closest to the potential activity maximum. However, it is not occupying the most optimal position (peak of the volcano plot), so there is still a room for the improvement in design more efficient ORR catalysts.[10,11]

http://rcin.org.pl

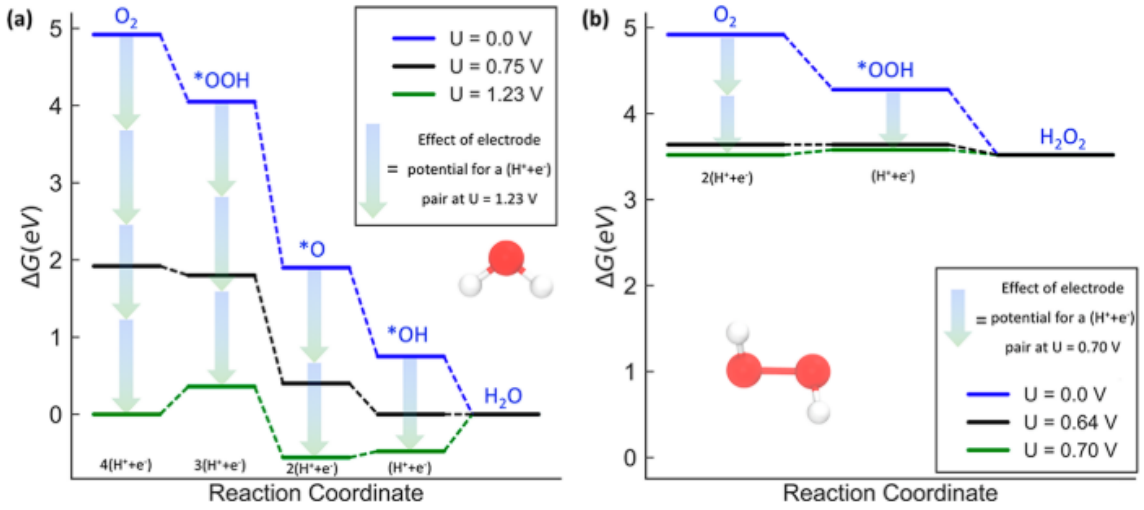

Fig. 2.3. (a) Free enthalpy diagram for the four-electron associative ORR on Pt(111)[26] *and (b) two-electron ORR on* $PtHg_4$.[27] *The free energy diagram is shown at three different potentials: 0 V (blue lines), the corresponding equilibrium potential (green lines), and the limiting potential (black lines). The blue-green arrows indicate the effect of the potential based on the CHE model.*[4,11]

Pt(111) is the best example of catalytic surface to understand ORR mechanism in comparison to the theoretical work, because of large volume of available experimental data.[28] Figure 2.3 shows DFT calculated diagram for the a) four- and b) two-electron ORR mechanism, using computational hydrogen electrode (CHE) model.[4] In CHE model, the free energy of a single proton-electron pair is defined as $-eU$ relative to H_2 in the gas phase at standard conditions, where U is the electrode potential with respect to the reversible hydrogen electrode (RHE). When the energies of adsorbate solvation (ΔE_w),[29] electric field effect (ΔE_{field}),[30] zero-point energy (ΔZPE),[4] and entropic correlations ($-T\Delta S$)[4] are added to a DFT calculated binding energy (ΔE_{ele}), one can calculate the adsorption free energies of a reaction intermediate (with n proton-electron pairs) as a function of the potential, by the equation 2.7:[11]

$$\Delta G = \Delta E_{ele} + \Delta E_w + \Delta E_{field} + \Delta ZPE - T\Delta S - neU \qquad \text{(Eq. 2.7)}$$

The dissociative process of ORR is not important for the Pt(111) surface,[4] therefore figure 2.3-a describes only the associative pathway of the studied reaction.

As it is shown in figure 2.3-a, at the potential U = 0.0 V, the reaction is facile, because all the reaction steps are downhill. At the equilibrium potential (U = 1.23 V), in accordance with the equation 2.7, the adsorption energies are shifted by $-neU$, by the number of $H^+ + e^-$ pairs corresponding to each intermediate. Consequently the reduction step of *OH to H_2O is uphill in energy, which means that the surface of the catalyst is covered by these species blocking further O_2 adsorption. U = 0.8 V is the maximum potential, where all of the reaction steps are downhill

http://rcin.org.pl

in free energy (it is called limiting potential, U_L), what is in agreement with observed maximum potential for large ORR current densities.[31] One can calculate the theoretical overpotential (η_{theo}) for Pt(111), which is a difference between the equilibrium potential U = 1.23 V and the limiting potential U_L = 0.8V. It is equal $\eta_{theo} \approx 1.2-0.8$ V ≈ 0.4 V. Figure 2.3-b shows two-electron ORR, which leads to undesirable product in fuel cells – H_2O_2. In this reaction only one intermediate occurs (*OOH). Similar CHE analysis can be used to see the thermodynamic behavior of this reaction. Again, at the U = 0.0 V the reaction is facile, but at the equilibrium potential, U = 0.7 V, formation of the intermediate is slightly uphill. In this case the $\eta_{theo} \approx 0.70-0.63$ V = 0.07 V.[11]

Two- and four electron ORR processes were widely studied in details. However, SECM experiments show desorption of a very active reductive intermediate, *OH radicals, when O_2 is reduced at a Pt electrode in aqueous solution. These observations demonstrated that ORR cannot be longer described as a simple competition between two reaction pathways: 2-electron from O_2 to H_2O_2, and 4-electron, from O_2 to H_2O. These studies show that ORR at Pt surface leads to another, 3-electron pathway, from O_2 to *OH radical, besides the formation of water. *OH radical can be produced in two ways: by 3-electron reduction reaction of molecular oxygen (equation 2.8)

$$O_2 + 2H^+ + 3e^- \rightarrow HO^* + OH^- \qquad \text{(Eq. 2.8)}$$

or by 1-electron reduction of H_2O_2 (equation 2.9):[32]

$$H_2O_2 + e^- \rightarrow HO^* + OH^- \qquad \text{(Eq. 2.9)}$$

2.3. Platinum and non-platinum ORR catalysts.

The weakening of the binding energy of the intermediates in ORR (*OH, *O, and *OOH) can move Pt(111) catalyst closer to the top of the thermodynamic volcano. The major difficulty in this area of research is that the newly designed catalysts have to fulfill the Sabatier principle. Various investigations are focused on changing the structure of Pt, *e.g.* alloying it with another metals, or on replacing it with non-platinum group metal (non-PGM) materials with similar catalytic activity.[10,11] Within platinum-based materials the highest catalytic activity can be obtained by using nanoscale Pt catalysts with high surface-to-volume ratio, with controlled size, morphology, composition and architecture, or by alloying Pt with other metals. The origin of catalytic activity toward ORR of non-PGM catalysts is still not well understood, however, non-PGM catalysts based on carbon (graphene, carbon nanotubes (CNTs)), and metal organic frameworks (MOFs), are widely studied because of their promising properties.[33] In bi- or multimetallic platinum alloys with transition metals, the interactions between two metals change

http://rcin.org.pl

the electronic properties of the material, results in higher catalytic activity. Furthermore, alloying of Pt with other metals reduces the quantity of this expensive material.[34,35]

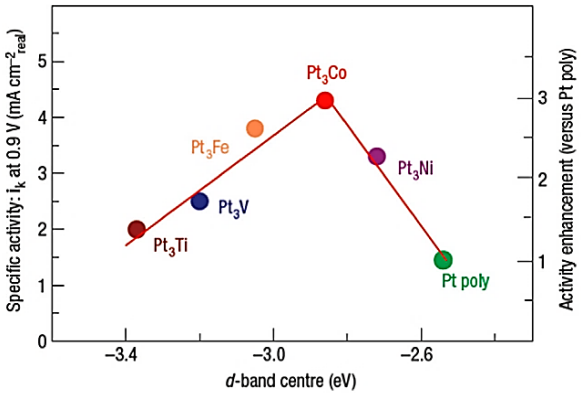

Fig. 2.4. Relationships between experimentally measured specific activity for the ORR on Pt_3M surfaces in 0.1 M $HClO_4$ at 333 K vs. the d-band center position.[36]

In 1995 Mukerjee *et al*. observed[37] the relationship between electronic (d-band vacancies per atom) and geometric (Pt–Pt bond distances) factors in Pt alloys and their effect on the chemisorption of OH species from the electrolyte, that enhance the catalytic activity of these catalysts. Figure 2.4 shows a series of different Pt alloys and a volcano-type correlation between their specific activity towards ORR and the d-band center position *vs*. metallic Fermi level.[36] The adsorption energies of the intermediates, the surface coverage by other oxygenated species and the specifically adsorbed anions on the surface of the catalyst should stay in balance to achieve the maximum catalytic activity toward ORR. It is clearly visible that the best catalyst should bind oxygen weaker than Pt_{poly} and stronger than Pt_3V and Pt_3Ti. In the case of Pt_{poly}, the activity of ORR is restricted by the rate of removing surface oxides and anions from the surface. On the Pt_3V and Pt_3Ti catalysts, the oxygen binds too weakly, thus the activity is slowed down by the rate of transferring electron and proton to adsorbed O_2. Clearly, alloying Pt with Ni, Co, and Fe is the most effective. Furthermore, alloying Pt in the form of nanoparticles (NPs) with these three 3d transition metals improved ORR activity even more than any other approaches.[34]

Platinum can be also alloyed with other noble metals, as they are known to be resistant to oxidation and robust in acidic environments. They also improve stability of Pt in PEMFC because they prevent the Ostwald ripening of platinum.[38] A number of researches show the enhancement of activity of Pt-noble metal alloys in comparison to pure Pt catalyst, e.g. Pt/Au nanodendrites,[39] Pt/Au nanoparticles,[40] IrRe nanoparticles covered by Pt monolayer,[41] or IrNi alloy core coated at first by a monolayer of iridium and then by a monolayer of platinum.[10,42]

Apart from lowering platinum loading in PEMFC, researchers are also focused on the substitution of Pt with other metal catalysts. Palladium,[43] iridium,[44] ruthenium,[45] silver,[46] and

Instytut Chemii Fizycznej PAN BIBLIOTEKA

copper[47] based ORR catalysts have been widely investigated, however, the mechanism of ORR at these materials is not precisely established. Theoretical calculations and experimental results have shown that Pd exhibits relatively high ORR activity in comparison to other catalysts, stability and availability, with a low cost of the material.[34,48] It was demonstrated[49] that Pd nanoparticles exhibit lover catalytic activity toward ORR as compared to Pt. Modification of the atomic structure of Pd-based catalysts, *e.g.* by addition of foreign metals, improves its efficiency.[48,50] A very promising results show studies of catalysts based on Fe and Co, however, their exact nature and their actual active structure remains unknown.[51,52] Cu-based catalysts were studied in acidic and alkaline media.[21,47,53] Pyrolyzed MOFs materials can also act as efficient catalysts for ORR, because of the large number of their active centers. It was reported that the Co/Zn Methyl-Imidazolate Frameworks exhibit better catalytic activity in O_2 saturated 0.1 M $HClO_4$ solution, at 25^0C, than a commercially available Pt/C catalyst.[54]

There is also a wide range of metal-free catalysts for ORR, mainly dominated by carbon-based materials. Vertically aligned nitrogen-containing carbon nanotubes (VA-NCNTs) can act as an example of an efficient, metal-free catalyst that is free from CO poisoning.[55] Doping graphene with nitrogen also results in enhanced catalytic properties toward ORR for large overpotentials (Figure 2.5). It was reported that at 0.6 V *vs.* RHE, in air saturated 0.1 M KOH, N-doped-graphene shows improved electrocatalytic activity versus commercial catalyst – Pt/C.[10,56] Higher activity of nitrogen-doped carbon nanotubes (NCNTs), with inner diameters of 20–50 nm and outer diameters of 70–200 nm, heated at 800^0C, in O_2 saturated 1 M NaOH in comparison to commercially available Pt/C catalysts was also reported.[57]

a) b)

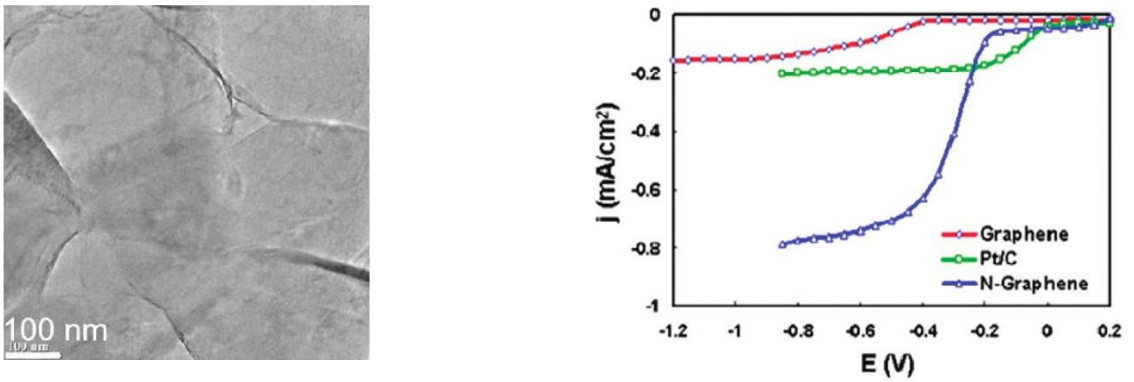

Fig. 2.5. a) Low-magnification TEM image showing a few layers of the CVD-grown N-graphene film on a grid.[56] *b) Linear sweep voltammogram comparing Pt/C and N-Graphene.*[56]

http://rcin.org.pl

2.4 Summary

Finding an inexpensive and active catalyst for ORR is still challenging. Researchers need to find a balance between the amount of platinum loading and activity: catalysts containing Pt are the most active but also the most expensive, whereas Pt-free catalyst are much cheaper, however they show lower activity. There are four main research paths that should be developed by ORR catalysts researchers. The first one involves studies about activity optimization of pure Pt catalysts, second focuses on alloying Pt with other metals to increase the catalytic activity with decreased Pt content. Third one involves research on nonprecious metallic catalysts and fourth is development of metal-free catalysts. A numerous theoretical studies have to be done to suggest an efficient, low-cost ORR catalyst. Researchers have to consider the thermodynamic description of ORR, investigate the mechanism on Pt-based and Pt-free catalysts in alkaline and acidic media and focus on discovering new materials via computational strategies.[10,11]

http://rcin.org.pl

3. Carbon dioxide reduction reaction

3.1. Introduction

There are two main sources of carbon dioxide (CO_2) in the atmosphere: natural and anthropogenic. The majority of CO_2 is released into the atmosphere by its natural sources: oceans, animals and plants respiration, decomposition of organic matter, forest fires, emissions from volcanic eruptions and naturally occurring CO_2 deposits found in rock layers in the Earth's crust. To anthropogenic CO_2 sources (Figure 3.1) one can count transportation, industry, chemical and petroleum production and agricultural practices. Many of these source types burn fossil fuels (coal, oil and natural gas) which are the leading cause of CO_2 emissions.[58]

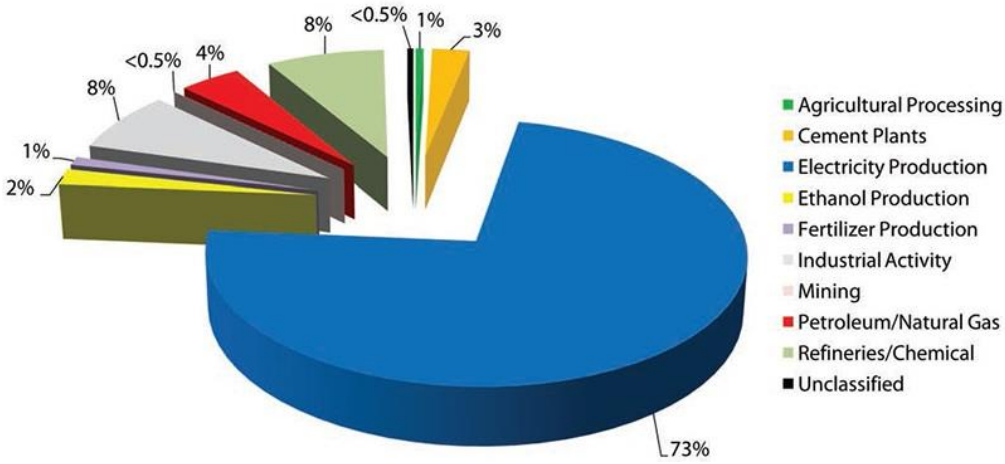

Fig. 3.1. CO_2 stationary source emissions by category.[58]

During the last 400 000 years, the level of the concentration of CO_2 in the atmosphere correlates with glacial/interglacial cycles (Figure 3.2).

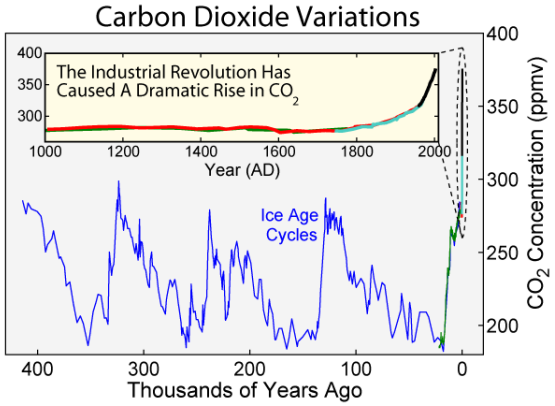

Fig. 3.2. CO_2 concentrations over the last 400,000 years.[59]

Since the Industrial Revolution in 1900 the amount of CO_2 in the atmosphere increased from approximately 250 ppm to almost 400 ppm (Figure 3.2).[59] This rise of atmospheric CO_2

http://rcin.org.pl

concentration (approximately 2.1 ppm per year) over the past decade is caused by anthropogenic emissions arising from fossil fuel burning, deforestation and cement production.[60–62] Fossil fuels are still a major power sources in European Union (Figure 3.3). However, they are gradually replaced by renewable power sources such as solar and wind. Between 2000 and 2018 the amount of electricity generated by coal dropped in all member states except the Netherlands, and renewable energy sources increased their share everywhere except in Latvia.[1]

Reaching a carbon balance in the environment is currently one of the extensively investigated topics. A lot of research is focused on the production of synthetic fuels and on the generation of renewable carbon feed stock to temporary storage of electricity produced by renewable energy sources. The electrochemical carbon dioxide reduction reaction (CO_2RR) to hydrocarbons has become a crucial method in utilizing CO_2.

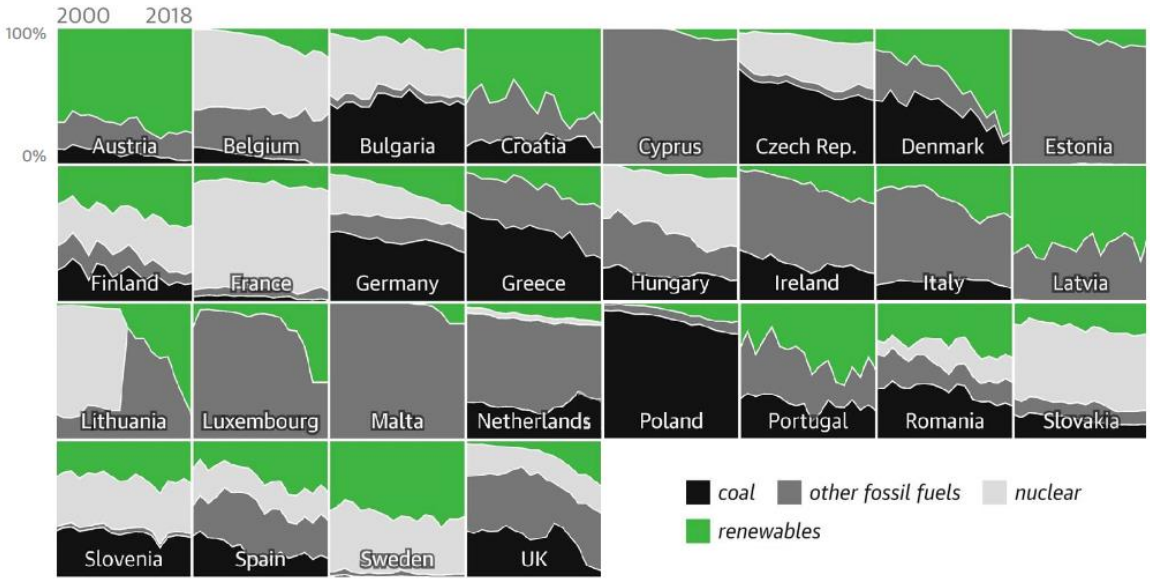

Fig. 3.3. Power generation by source (2000-2018).[1]

3.2. CO_2RR mechanism

The main difficulties with CO_2RR process are high overpotential, poor product selectivity and poor Faradaic efficiency. The first two phenomena occur because of an inappropriate adsorption energies of a key reaction intermediates. Low Faradaic efficiency is the result of a competitive hydrogen evolution reaction (HER) which occurs in the same range of potentials as CO_2 reduction. Because of these impacts a selective, cheap and stable catalyst is essential to reduce CO_2 at low overpotential and with improved efficiency.[5,6,63,64]

The electrochemical CO_2RR is a multiple proton−electron transfer reaction (Equation 3.1), which leads to a wide variety of other products. Because of the different numbers

http://rcin.org.pl

of electrons transferred during the process, one can obtain products ranging from CO and HCOOH (2e$^-$ transferred) to $CH_3CH_2CH_2OH$ (18 e$^-$ transferred). The most typical products in aqueous media, the stochiometric coefficients *k*, *n*, and *m* and the equilibrium potentials are shown in Table 3.1.[5,65]

$$k\mathrm{CO_2} + n(\mathrm{H^+} + \mathrm{e^-}) \rightleftarrows \text{ products} + m\,\mathrm{H_2O} \qquad \text{(Eq. 3.1)}$$

Table 3.1. Main Products of the Electrochemical Reduction of CO_2 in aqueous media.[5]

Product name and formula	***k***	***n***	***m***	**E^0 (V *versus* RHE)**
carbon monoxide, CO	1	2	1	-0.10
formic acid, HCOOH	1	2	0	-0.20 (for pH <4); -0.20 + 0.059[pH-4] (for pH >4)
formaldehyde, HCHO	1	4	1	-0.07
methanol, CH_3OH	1	6	1	0.02
methane, CH_4	1	8	2	0.17
ethanol, CH_3CH_2OH	2	12	3	0.09
ethylene, C_2H_4	2	12	4	0.08

Suggesting an exact mechanism for the CO_2RR is challenging. The empirical Butler–Volmer theory and the molecular–level Marcus theory are focused on the role of the electrode potential and the solvent during electrochemical reaction, not on the role of the metal catalyst. Understanding the interaction between catalyst and reaction intermediates is crucial for finding the mechanisms of the CO_2RR. The Sabatier principle[66] says that the best catalyst binds the key reaction intermediates in an optimal fashion – neither too weakly nor too strongly. When the binding of the intermediate is too strong, the catalyst will become poisoned. In an opposite case, when the bond is too weak, the catalyst is unable to activate the reactant and the commencement of the reaction is prohibited.[5,67]

According to the thermodynamic theory of multiple proton−electron transfer, when only two electrons (n = 2 in equation 3.1) are transferred during reaction, the catalysis is called "reversible" because the catalyst accelerate the corresponding reactions in both directions (reduction and oxidation), with negligible overpotentials. In agreement with the Marcus theory simultaneous transfer of two electrons requires an activation energy which is four times larger

http://rcin.org.pl

than that of a single electron-transfer. Thus, energetically more favorable is to store charge in intermediate species. For such reactions usually only a single intermediate occurs, so the detection and identification of it is simpler and the mechanism of the reaction is easier to discover. When more than two electrons and protons are involved in the redox reactions, more than one catalytic intermediate exists, what causes the irreversibility.[5,68]

3.3. The role of the catalysts

The electrochemical conversion of CO_2 into useful products is one of the most sustainable ways of utilizing CO_2. It occurs under ambient conditions, neutral pH and is catalyzed by non-noble metals, *e.g.* by copper.

Figure 3.4-a shows volcano-shaped activity trend for CO_2RR *vs.* CO binding strength, in the case of methane and methanol production. It indicates, that Au has the highest current density for CO_2RR thus represents the peak of the plot with activity decreasing for metals on either side. DFT suggests that metals such as Ag and Zn exhibit lower CO binding energy and lower activity because of the slower activation of CO_2, which is the first step in the CO_2RR sequence. Contrary, metals such as Cu, Ni, Pt, and Fe bind CO more tightly and activation of CO_2 is limited by the slow CO desorption or further reaction of CO to other products, because of the strong surface−CO bond. Thus, Au has a CO binding energy closer to the ideal value than any of the other investigated metals. However, the major product of CO_2RR on Au is CO. Figure 3.4-b shows that Cu, which is located on the strong-binding side of Au, exhibits greater selectivity toward methane/methanol – more reduced products. It means that to obtain products with greater than two electrons transferred, the surface of the catalyst have to bind CO stronger than Au.[69]

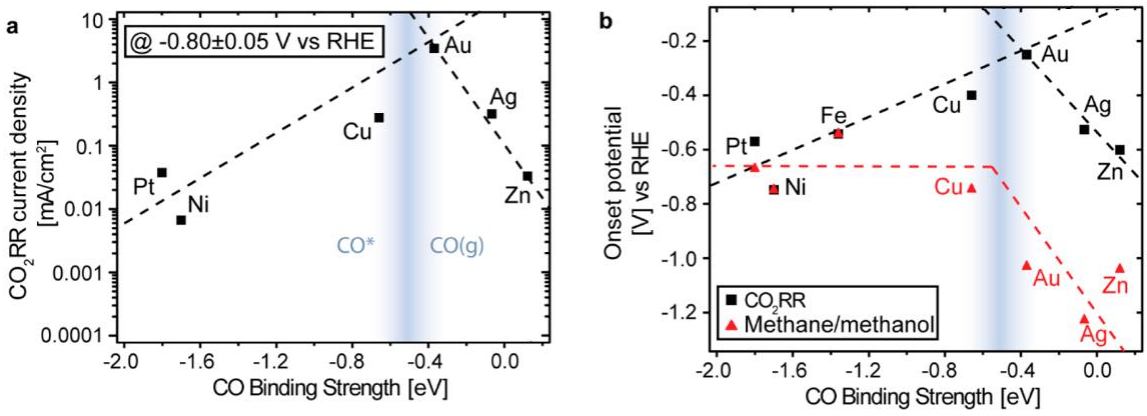

Fig. 3.4. a) Volcano plot of current density for CO_2RR at −0.8 V vs. CO binding strength. b) Three distinct onset potentials plotted vs. CO binding energy: the overall CO_2RR, and methane or methanol. Dashed lines are to guide the eye. A vertical line labeled CO|CO(g) is included to indicate the thermodynamics of chemical CO adsorption/desorption. Metal surfaces that favor CO in an adsorbed state, CO*, are located to the left of the line while those that favor CO desorption, CO(g), are located to the right.*[69]

http://rcin.org.pl

Figure 3.5-a shows DFT calculated volcano-shaped activity trend for CO_2RR *vs.* *COOH binding energy, in the case of CO production. Figure 3.5-b shows DFT calculated volcano-shaped activity trend for CO_2RR *vs.* *OCHO binding energy, in the case of $HCOO^-$ production.

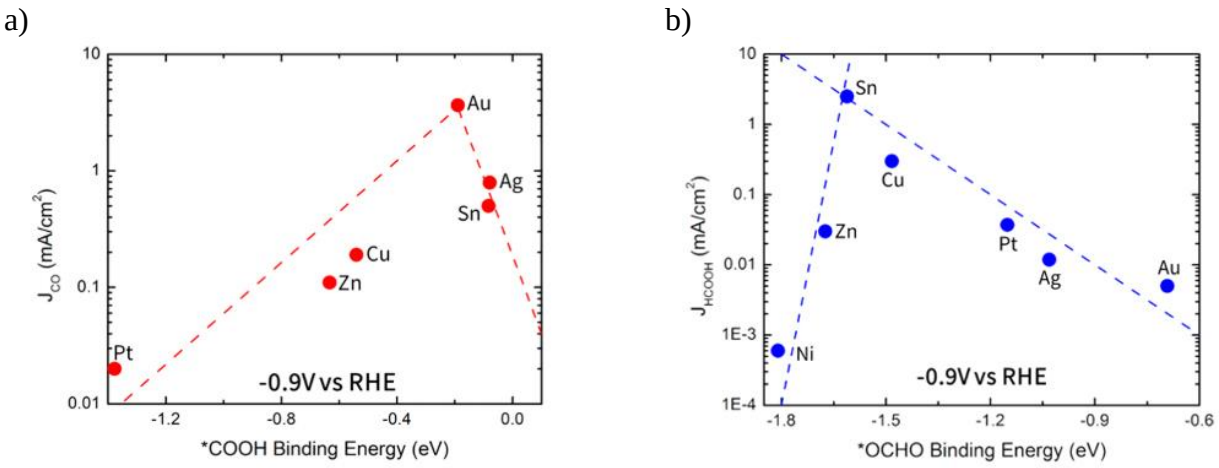

*Fig. 3.5. a) Volcano plot using *COOH binding energy as a descriptor for CO partial current density at −0.9 V vs. RHE. b) Volcano plot using *OCHO binding energy as a descriptor for $HCOO^-$ partial current density at −0.9 V vs. RHE.*[70]

Volcano plot in figure 3.5-a suggests that Au has a near-optimal binding energy of the key intermediate *COOH to produce CO. Sn and Ag appear on the weak-binding leg of the volcano due to its weak interaction with *COOH. Pt, Zn, and Cu are placed on the strong-binding side what means that *COOH binds too strongly to their surface. Figure 3.5-b shows that Sn is near the top of this volcano and has a near-optimal binding energy of the key intermediate *OCHO to produce $HCOO^-$. Au, Ag, Pt, and Cu are on the weak-binding side of the volcano, so *OCHO may not interact strongly enough with their surface. Ni and Zn are on the strong-binding leg of the volcano indicating that *OCHO binds too strongly to the surface for further reduction to formate. For the metals with activity far from maximum the peaks in figures 3.4 and 3.5 (*e.g.* Pt, Ni) the major product obtained at −0.9 V *vs.* RHE is H_2. Both Pt and Ni have a very strong binding behavior for *COOH and *CO what means that CO may poison the metal surface and limits the amount of CO produced on these electrodes. For Au and Ag (metals that are not near the peak of the *OCHO volcano but near the peak of the *COOH, Figure 3.5) the major product obtained at −0.9 V *vs.* RHE is CO, with only a small amount of $HCOO^-$ detected. This suggests that, although the *COOH binding energies for most of the metals in this study are weaker in comparison to *OCHO, kinetic limitations that are not captured in the electronic energy calculations might play a nontrivial role in determining selectivity for these metals.[70]

In 1985 Hori *et al.* demonstrated that copper has the unique ability to electrochemically reduce CO_2 with good Faradaic efficiencies in comparison to other metals.[71] Nowadays copper

http://rcin.org.pl

is well known catalyst[6,72–74] for selective production of formate, CO, and hydrocarbons at relatively low overpotentials and with improved efficiencies.[75] Unfortunately, an unambiguous mechanism and all factors that influence the catalytic activity and selectivity of Cu electrodes for CO_2RR are not fully understood.[76] Recently Garza *et al.* verified a hypothesis of crucial role of subsurface oxygen for adsorption and electrochemical reduction of CO_2 on copper. Using DFT, they found that surface oxygen is unnecessary for CO_2 adsorption on Cu.[77] As it is shown in figure 3.6, proposing a mechanism for the CO_2RR on copper is challenging because of variety of major, intermediate, and minor products that are formed. Not only methane and ethylene are obtained but also a broad mixture of aldehydes, ketones, carboxylic acids, and alcohols. The origin of these products stays largely unclear, however, they occur in traces detectable with NMR spectroscopy.[5,78]

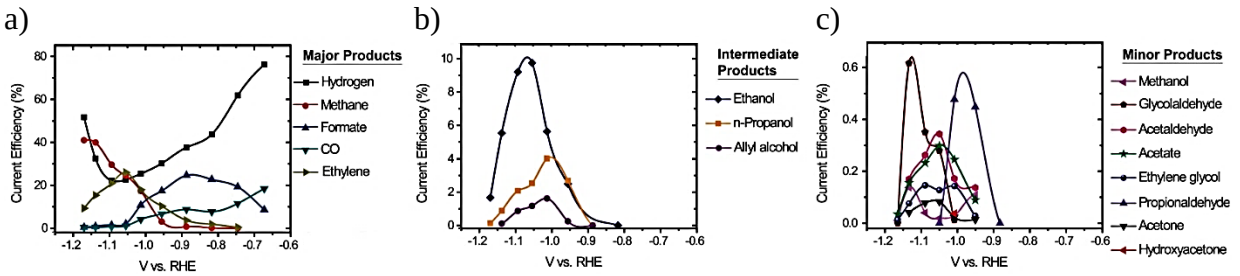

Fig. 3.6. Current efficiencies of the products of CO_2 reduction on Cu electrodes in 0.1 M $KHCO_3$ (pH = 6.8) as a function of potential for: a)major, b) intermediate, c) minor products.[78]

Figure 3.7 shows possible pathways for the electrochemical production of methane from CO_2 on Cu electrodes based on a thermodynamic analysis (Figure 3.7-a) and combined thermodynamic and kinetic analysis (Figure 3.7-b). After the initial formation of *CO there is subsequent hydrogenation to *HCO, *H_2CO, and *H_3CO (methoxy), and this methoxy intermediate is reduced to CH_4 and *O, which is finally reduced to H_2O. These two mechanisms are identical up to the second proton−electron transfer, that is, until *CO is formed, after which they form *CHO (Figure 3.7-a) or *COH (Figure 3.7-b).[5]

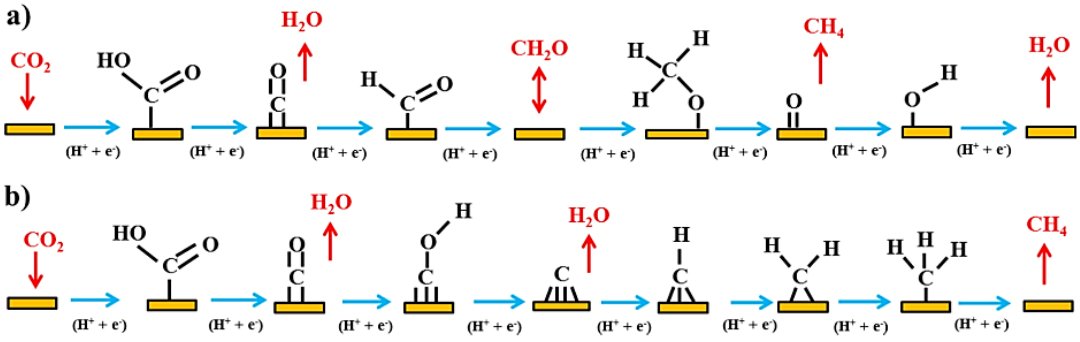

Fig. 3.7. Pathways for the electrochemical production of methane from CO_2 on Cu electrodes from a) a thermodynamic analysis and b) a combined thermodynamic and kinetic analysis [5]

http://rcin.org.pl

On transition metals not only carbon monoxide is produced but also formate, methane, and methanol, however in small amounts.[69,79] Proposed reaction pathways for CO_2RR on transition metals and molecular catalysts are shown in figure 3.8.[5]

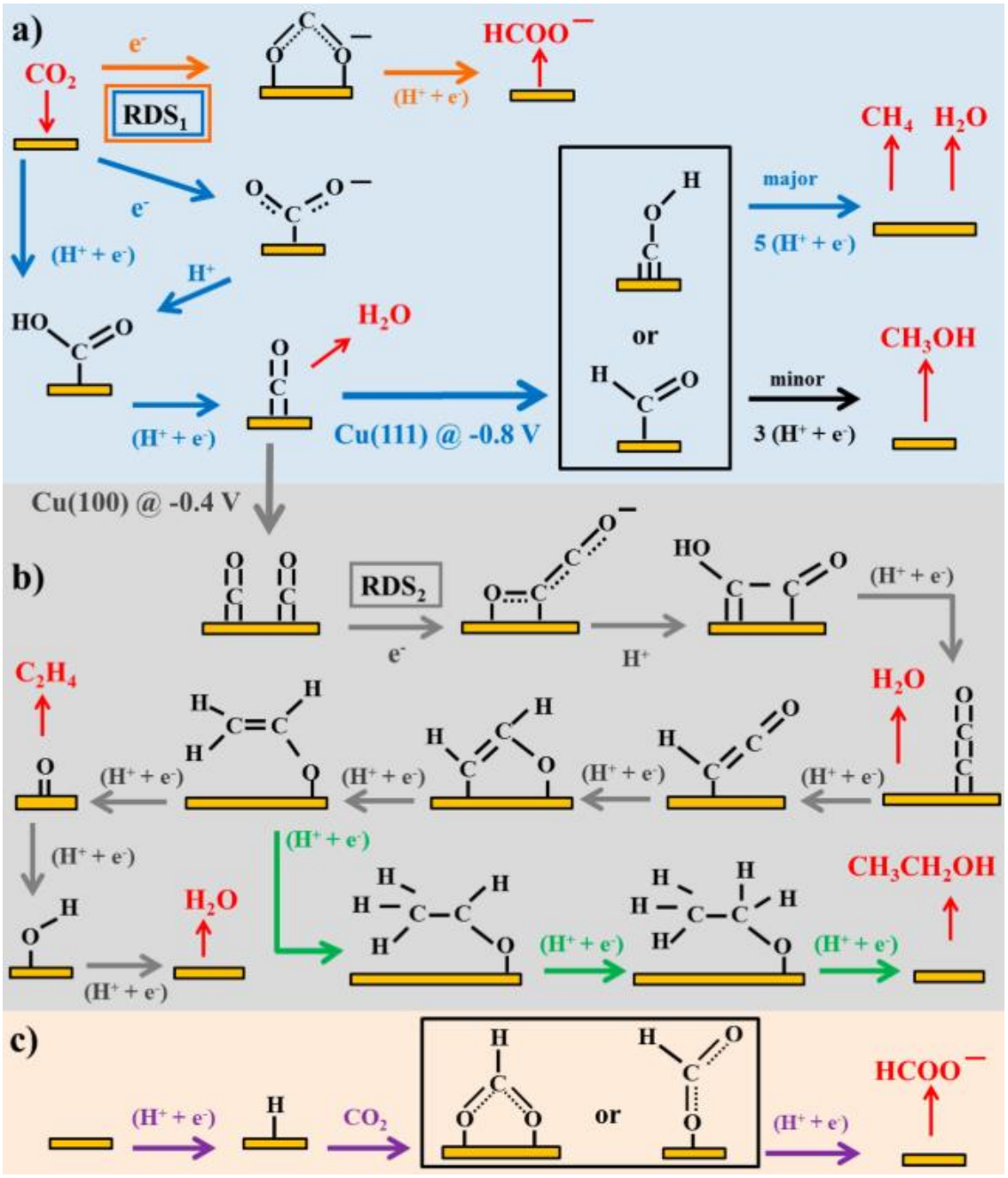

Fig. 3.8. Possible reaction pathways for the electrocatalytic reduction of CO_2 to products on transition metals and molecular catalysts: (a) pathways from CO_2 to CO, CH_4, CH_3OH, and $HCOO^-$; (b) pathways from CO_2 to ethylene and ethanol); (c) pathway of CO_2 insertion into a metal−H bond yielding formate. Potentials are reported versus RHE, while RDS indicates rate-determining steps and ($H^+ + e^-$) indicates steps in which either concerted or separated proton−electron transfer takes place.[5]

CO_2RR also occurs on p-block metals like Sn, In, and Pb. The main products are formic acid and formate.[70,80] They are obtained with high selectivity because these metals acts as a poor catalysts for the competing HER.[5]

http://rcin.org.pl

Not only bulk metals can act as catalysts for CO_2RR but also other structures are obtained and studied, *e.g.* nanoparticulate copper electrodes,[81] copper mesocrystals covered electrodes,[82] Ag nanoparticles supported on carbon,[83] and carbon-supported Pd nanoparticles.[84] For such electrodes the onset potential of formic acid and CO evolution is reduced and the selectivity toward hydrocarbons is increased. The catalytic activity and the selectivity are also determined by the size, geometry and morphology of the metal structure.[5] It is important to find an optimal size of the catalyst because Cu nanoparticles of 2 nm and smaller exhibit enhanced catalytic selectivity towards H_2 and CO formation, while the evolution of hydrocarbons is lower than for polycrystalline Cu catalyst (Figure 3.9).[5,75]

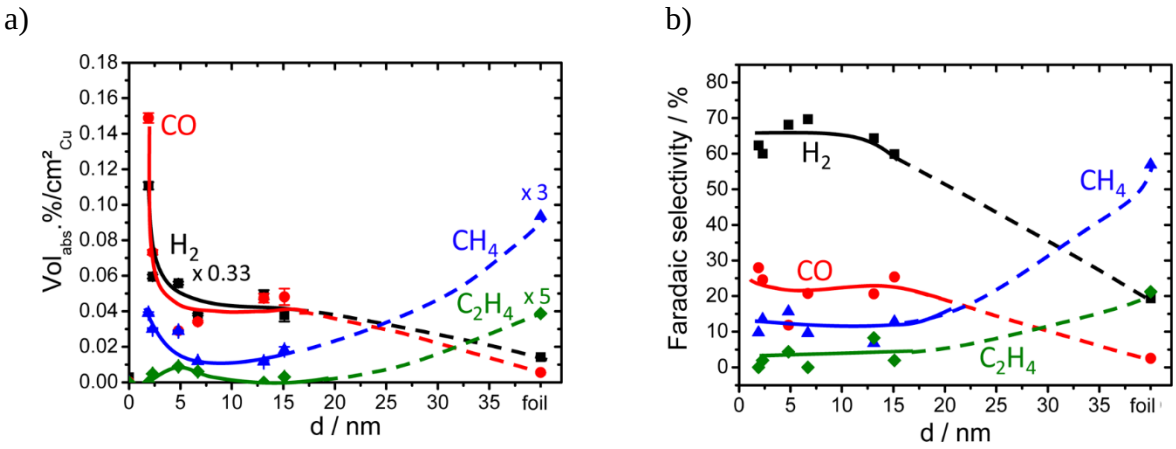

Fig. 3.9. Particle size dependence of a) the composition of gaseous reaction products (balance is CO_2) during catalytic CO_2 electroreduction over Cu NPs, b) the faradic selectivities of reaction products during the CO_2 electroreduction on Cu NPs. Lines are guides to the eye. Conditions: 0.1 M $KHCO_3$, E = −1.1 V/RHE, 25°C. For a), volume concentrations were normalized using the Cu surface areas. Values for H_2, CH_4, and C_2H_4 are scaled by factors of 0.33, 3, and 5, respectively.[75]

There is also a wide range of bimetallic catalysts for the reduction of CO_2. Alloying can be beneficial because some products can only be obtained using alloyed metals as a catalyst.[5] In the early works the effect of alloying of Cu with Ni, Sn, Pb, Zn, Cd, and Ag was studied.[85] It was shown that the selectivity towards CO can be changed by the underpotential deposition of adatom on the electrode surface.[86] Nowadays, researchers are still developing new, efficient and stable alloyed catalysts for CO_2RR. They alloyed copper with gold,[87] indium,[88] tin,[89] and palladium[90] to enhance CO production.[91] Improved selectivity towards production of formate was achieved with Sn-Pb,[92] Sn-Ag,[93] Pd-Pt,[94] and Au-Pd[95] alloys. Catalytic activity and selectivity depends on the composition of the catalyst, therefore the number of Cu layers that covered Au core in bimetallic core-shell cubic nanoparticles determined reaction products. 7 – 8 layers of Cu favor hydrogen and ethylene and formic acid production, while more than 14 atomic Cu layers – hydrogen and methane.[76] Figure 3.10 illustrates examples of monometallic and bimetallic

http://rcin.org.pl

catalysts divided into four groups on the basis of which products are favored during CO_2RR, respectively: CO, HCOOH, hydrocarbons and H_2.[91]

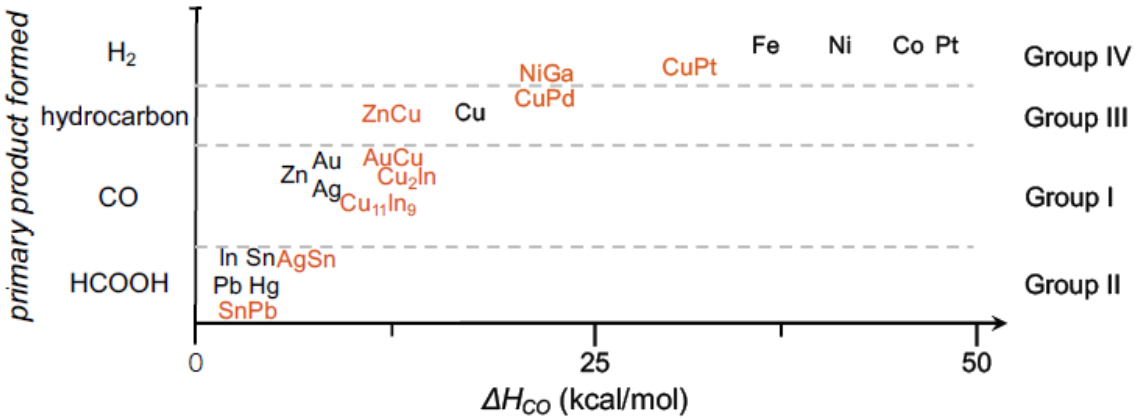

Fig. 3.10. General relationship between the primary product formed and ΔH_{CO} for metal (black) and mixed-metal (orange) CO_2 electrocatalyst films. (ΔH_{CO} for In, Sn, Pb, Hg are assumed to fall between 0 – 7 kcal mol $^{-1}$.) The metal catalysts for CO_2 reduction can be divided into four groups according to their binding energy with CO. Group I metals are characterized by a weak CO binding energy and favor the production of CO. Group II metals do not form M-C bonding, and HCOOH is the main product. The binding energy of group III metals is most optimized for CO_2 reduction to hydrocarbons. Group IV metals have a strong CO binding energy, that poison the catalyst and favors hydrogen evolution.[91]

Molecular complexes with metal centers were also used as catalysts of electrochemical CO_2RR. In the first studies, nickel and cobalt phthalocyanines deposited on a graphite electrode were used.[96] Later different kinds of metal complexes were employed, such as metal porphyrins,[97] cyclams[98] and phthalocyanines anchored on carbon nanotubes.[99] These complexes catalyze mainly two electron transfer CO_2RR leading to CO and HCOOH.[5]

Finding efficient, cheap and stable electrocatalyst is still challenging, therefore scientists are also investigating metal-free materials that reduce CO_2 to appropriate products. For example, one of the new approaches was to employ organic catalysts - conductive polymer - polydopamine on sponge-type carbon felt, that produces C_1 species: CO and formate.[63]

3.4. Influence of the electrolyte

CO_2RR mechanism is strongly dependent on the nature of the electrolyte which plays an important role during the catalysis. The solvent, pH and the presence of some cations and anions influence the range of products of the reaction by changing its pathway. The afore-mentioned factors affect the concentration of the reactants (CO_2 and H^+), stabilize reaction intermediates or inhibit their formation. Therefore not only suitable catalyst but also an appropriate electrolyte, importantly with optimized pH value, is significant in CO_2RR.[5]

http://rcin.org.pl

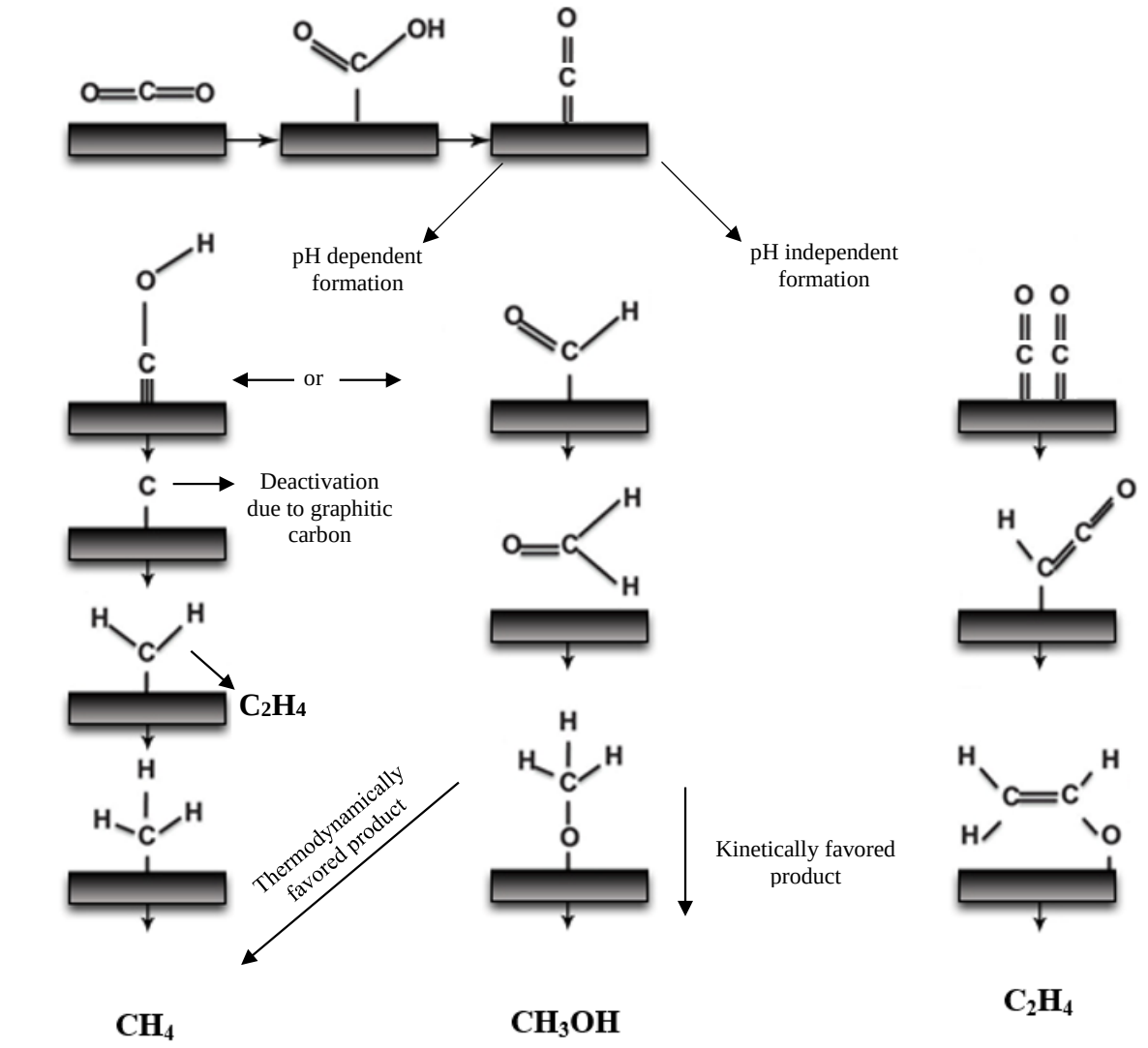

Fig. 3.11. Reaction scheme showing influence of pH on CO_2RR mechanism from ref [6] *with corrections.*

CO_2RR is usually carried out at the pH close to neutral (slightly acidic solution). CO_2 forms bicarbonate and carbonate when it is purged through alkaline solutions.[5] During reaction, because of the proton consumption, the pH near the electrode surface is expected to be higher than in the bulk electrolyte.[72] Mathematical calculations show that local pH (at the electrode surface) during CO_2RR can be up to 6 units higher than in the bulk of non-buffered solution. This parameter is determined by the thickness of the diffusion layer, the current density and the electrolyte buffer capacity.[100] Thus the mechanism of CO_2RR can be influenced by both bulk pH and buffer concentration. Figure 3.11 shows pH dependent and pH independent reaction pathways of CO_2RR.[6] In the electrolytes with low buffer capacity (*e.g.* $KClO_4$) high pH occurs locally near the electrode which enhance the selectivity of C_2 products (ethylene). In buffered solutions (bicarbonate or phosphate buffer), with local pH close to neutral, formation of CH_4 and CO is favored.[5,72]

http://rcin.org.pl

Electrochemical CO_2RR is mainly studied in aqueous electrolytes. CO_2 dissolves poorly in water (34 mM under 1 bar, at 25^0C) what leads to low concentrations of the substrate. However, one can change the solubility of CO_2 by changing composition of the solution. In salted water the solubility of CO_2 decreases.[101] In alkaline media more CO_2 can be dissolved. CO_2 dissolves in water forming carbonic acid (H_2CO_3). This reaction is reversible and rapid:

$$CO_{2(g)} \rightleftarrows CO_{2(aq)} \quad \text{(Eq. 3.2)}$$

$$H_2O_{(l)} + CO_{2(aq)} \rightleftarrows H_2CO_{3(aq)} \quad \text{(Eq. 3.3)}$$

$$K = [\ H_2O_{(l)}]\ K_{eq} = [H_2CO_{3(aq)}] / [CO_{2(aq)}] \quad \text{(Eq. 3.4)}$$

$$K = 1.70 \times 10^{-3} \quad \text{(Eq. 3.5)}$$

H_2CO_3 reacts with bases present in the solution and is converted to bicarbonate (HCO_3^-) and carbonate (CO_3^{2-}) what pulls the equilibrium of equation 3.3 to the right and allows more CO_2 to be dissolved.

Besides CO_2RR, HER occurs at the same potential range and contributes to the Faradaic efficiency. These difficulties can be overcome by using solvents with increased CO_2 solubility and lower proton concentration. Organic solvents provide wider potential window in comparison to aqueous solutions, allowing application of higher cathodic overpotentials. CO_2 can be then reduced more selectively because of the suppression or even elimination of HER. By using a specific electrode materials the potential window of aqueous electrolytes can be increased up to around 2 V. However, it is still not enough to eliminate the contribution of HER.[102] It results from the difficulty of breaking of the C-H bonds comparing to O-H bonds between water molecules.[5,103]

The mechanism of CO_2RR in nonaqueous solvents has been described in the literature since the early 1980s.[104] The actual path that the reaction follows depends on the material of the working electrode: Sn, Pb, In, and Hg lead to the formation of oxalate, whereas Pt, Pd, Au, and Cu to carbon monoxide.[103] A broader spectrum of products can be obtained using mixture of water and nonaqueous solvents. Using water/acetonitrile mixtures one can control proton availability by adjusting the amount of water. For example, product selectivity for CO_2 electroreduction on the Pt catalyst is dependent on the amount of water in the electrolyte. In the absence of water oxalic acid is formed. Small amounts of water lead to the formation of formic acid and high content of water favors HER.[5,105]

http://rcin.org.pl

Because of the high CO_2 solubility, good ionic conductivity and wide potential window, room temperature ionic liquids (RTILs) have recently gained attention as electrolytes for CO_2RR. The effects of electrode material and type of RTIL on the mechanism of CO_2RR were studied by Compton group. They investigated CO_2RR on Au, Ag, Pt and GC microelectrodes in 1-butyl-3-methylimidazolium bis (trifluoromethylsulfonyl) imide ([Bmim][NTf_2]), using cyclic voltammetry (Chapter 7.1). They observed a diffusion-limited reductive peak current on Ag electrodes. For Au the peak current density was 6 times smaller, while for Pt and GC electrodes no appreciable reduction was observed. Moreover, the overpotential required for reduction was reduced on Ag by *ca.* 1.5 V as compared with Au. There was a shift in the potential of the reductive wave upon changing the cation, with the reduction occurring at the most positive potential in [Bmim][NTf_2]. This work has thus demonstrated that there is an inner-sphere, silver-specific mechanism of CO_2RR involving desorption of the cation prior to electron transfer: $CO_2 + e^- \rightarrow CO_2^{\bullet -}$.[106]

Anions and cations present in the electrolyte (traditional or RTIL) have big impact on the CO_2RR. Cations may specifically adsorb on the surface of cathodically polarized electrode, influencing the potential at the outer Helmholtz plane. They can also deliver water molecules from their solvation shells to the electrode influencing competitive CO_2RR and HER. Moreover, electrolyte cations may interact with negatively charged reaction intermediates. For example, on Cu electrode, the correlation between the Stokes radii of the hydrated cations and the production of ethylene over methane has been found.[5]

3.5. Summary

The mechanism of the electrochemical CO_2RR is very complicated and still not well understood. There are several theoretical reaction pathways proposed by the researchers. The mechanism of CO_2RR is influenced by a variety of parameters such as catalyst material, electrolyte composition, applied overpotential and pH value. Various products of CO_2RR as formate, acetate, aldehydes, alcohols, hydrocarbons and CO can be obtained. Due to their high energy density most favorable as combustible fuels are hydrocarbons. Formic acid and CO can be generated at low cathodic overpotentials and are easily electrooxidized at mild conditions. This makes formate and CO valuable for electrochemical energy storage devices.

To reduce CO_2 to desirable products researchers should focus on two strategies: adjusting the material of the catalyst or changing the composition of the electrolyte. Manipulating the pH and other components of the electrolyte, *e.g.* by using nonaqueous electrolytes, influences the product selectivity. Alloying different metals, **changing metal morphology**, and using new

http://rcin.org.pl

materials, *e.g.* conductive polymers, can optimize the binding energies of the reaction intermediates and leads to development of new, stable, selective, efficient, and cheap catalyst for CO_2RR.[5]

http://rcin.org.pl

4. Electrodeposition of metallic nanostructures

4.1. Introduction

In 1772 Giovanni Battista Beccaria performed the first electroplating experiment. He successfully deposited metal by discharging a Leyden jar and using the spark to decompose metal salts.[107] The development of galvanic cell by Volta (*ca.* 1800) led to use electrodeposition technique as a cost-effective process to produce coatings.[108]

Among the diverse deposition processes, *e.g.* Physical Vapor Deposition (PVD),[109] Molecular Beam Epitaxy (MBE),[110] Chemical Vapor Deposition (CVD),[111] and hydrothermal techniques,[112] electrodeposition has certain advantages. It is a simple, fast and inexpensive technique to produce a wide range of various nanostructures (NS) directly on a conductive substrate.

The electrodeposition technique setup (Figure 4.1) uses a galvanostat that applies controlled current through the cell. Potentiostatic polarization can be also applied. The cell consist of cathode as a support for electrodeposited material, an anode and electrolyte containing deposit precursor. The electrodeposited NS are formed at the cathode substrate that can be made of either metallic or nonmetallic material.[113]

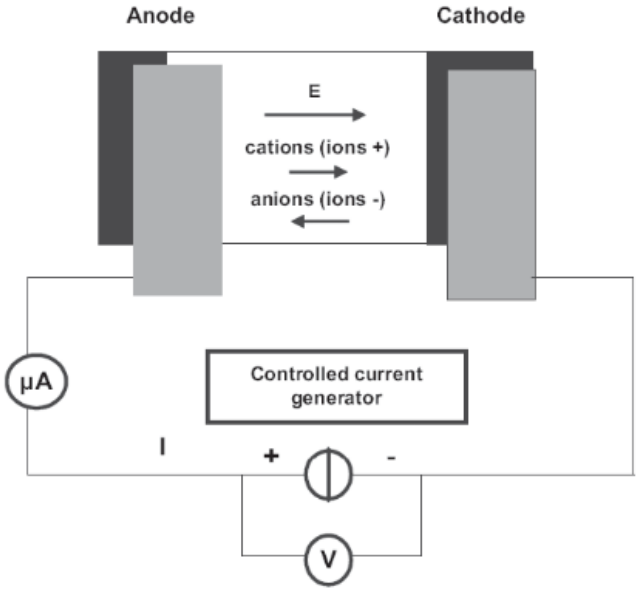

Fig. 4.1. General scheme of electrodeposition process.[113]

http://rcin.org.pl

During the process metal from the anode is oxidized what means that is losing electrons. Obtained cations, or their complexes, are transported to the cathode where they are reduced to metal by gaining electrons (Equation 4.1):

$$M(L)_p^{n+} + ne^- \rightarrow M^0 + pL \qquad \text{(Eq. 4.1)}$$

and form a deposit which morphology depends on various parameters.[114] The crystal structure of the substrate, lattice orientation of the electrode surface, type of the substrate (*e.g.* amorphous cathodes made of glassy carbon; GC), specific surface energy, adhesion energy and crystallographic lattice mismatch at the nucleus-substrate interface determines the parameters of the nucleation at the electrode. The final size distribution of the electrodeposited structures strongly depends on the kinetics of the nucleation and growth. Concerning the type of nucleation during electrodeposition one can distinguish progressive and instantaneous nucleation. In the case of progressive nucleation the number of nuclei that is formed, is a function of the time of electrolysis. Progressive nucleation produces zones of reduced nucleation rate around the growing nuclei because of depletion of substrate concentration around the growing nuclei. During instantaneous nucleation, all the nuclei are formed instantaneously on the cathode substrate and subsequently grow with time of electrodeposition.[113] This type of mechanism can be achieved by application of appropriate voltage or current pulse program.

The process of electrodeposition can be performed with direct current (DCE) and pulse current (PCE) modes, (Figure 4.2).[115]

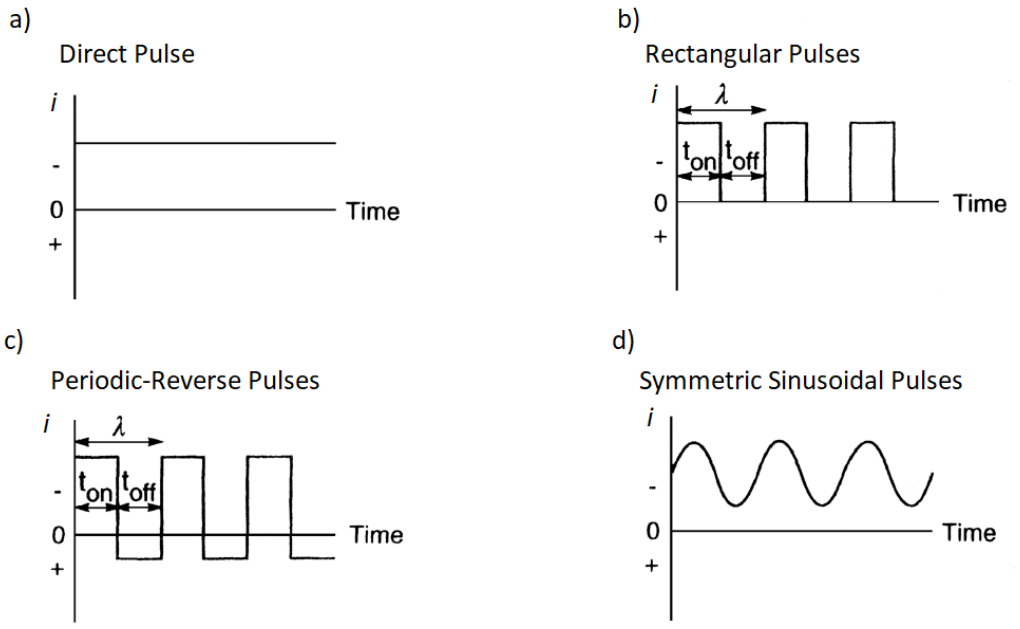

Fig. 4.2 a) Current program in DCE; b – d)Waveforms used in PCE: t_{on}, the on period of a pulse; t_{off}, the off period; λ, the cycle time; t_c, the cathodic pulse period; t_a, the anodic pulse period.[115]

http://rcin.org.pl

The oldest and most conventional method is DCE, where current is continuously applied to the system (Figure 4.2-a). It is a simple process with the sufficient technological knowledge.[108] In PCE a serious modification of the diffusion layer occurs. The Nernst diffusion layer is split into two: pulsating and stationary (Figure 4.3). The pulsating diffusion layer occurs in the closest region of the cathode and the metal ion concentration pulsates with the frequency of the pulsating current in this region.[115,116]

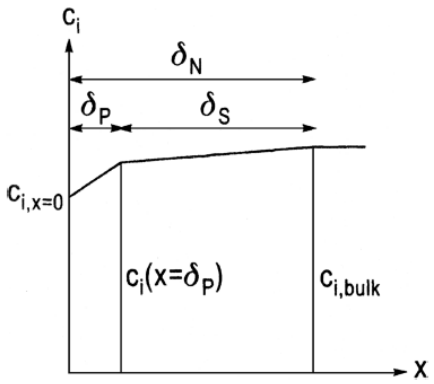

Fig. 4.3. Schematic concentration profile at the cathode for pulse plating conditions: δ_p, pulsating diffusion layer thickness; δ_s, stationary diffusion layer thickness; δ_N, Nernst diffusion layer thickness; x, distance from electrode; C_i, concentration of the reactant.[115]

The waveform in the rectangular-PCE technique consists of pulses of a rectangular shaped current and the intervals of zero current. (Figure 4.2-b). In the waveform of periodic reverse deposition the applied current is periodically switched from cathodic to anodic polarization (Figure 4.2-c). A symmetric sinusoidal deposition waveform is presented in (Figure 4.2-d). It is a sum of the sinusoidal alternating (AC) and direct cathodic current (DC). The waveform consists of both cathodic and anodic portion, when the amplitude of the sine wave is greater than the DC offset.[115]

The process of electrodeposition can be controlled by changing the electroplating bath parameters, *e.g.* temperature, convection, composition and pH value, as well as the parameters of pulses: peak current density, potential, pulse on-time and off-time.[108]

There are several advantages of PCE in comparison to DCE. Pulse deposition techniques are used to improve the distribution of the deposit (current distribution), the leveling, and the brightness of the deposit in case of electroplating. The microstructure, chemical composition and properties of coatings can be managed by changing the pulse parameters that controls adsorption and desorption of various species in the electrolyte, *e.g.* peak current, and frequency.[108,115,117,118]

http://rcin.org.pl

The examples of electrodeposited nanomaterials and their applications are shown in the table 4.1.[113]

Table 4.1. Examples of electrodeposited nanomaterials and their applications.[113]

Materials	Application
Pd, Ni–Pd	Hydrogen storage and purification, electrodes for hydrogen evolution and fuel cells
Ni–Al_2O_3, Ni–SiC	Corrosion protection, wear resistance
Co, Co–W, Co–P	Hard coatings, magnetic materials
Ni, Ni–P, Ni–Mo, Ni–Zn, Ni–Fe, Ni–Fe–Cr	Corrosion protection, stress corrosion, cracking resistance, soft magnets, catalysts

Electrodeposition can be used to prepare thin film NS (nanofilms), nanoparticles, nanowires, nanotubes, core-shell and porous NS. Having a mixture of salts in the electrolyte one can also easily obtain nanostructured alloys. Electrodeposition can be performed from a wide range of electrolytes: aqueous, organic, ionic liquids or their mixtures. Some materials obtained by electrodeposition have enhanced solderability, tribology, electrical conductance, corrosion resistance, wear and thermal resistance. The main advantage of nanomaterials obtained by electrodeposition is that the nanoparticles and NS are attached directly to the surface of the substrate and their size, morphology, crystallographic orientation, mass, thickness and composition can be controlled by adjusting the operating conditions and bath composition.[108,113,119–121]

4.2. Copper nanostructures

Copper nanostructures (CuNS) are very promising catalysts for the electrochemical applications, *e.g.* conversion of CO_2.[94,122,123] In comparison to noble metals such as Au, Pt, and Pd, copper yields valuable, high energy density products as hydrocarbons,[5,124–126] alcohols,[5,124,127] formic acid, and other carbonyls (Chapter 3).[5,124,127,128] Cu can also acts as a catalyst for ORR.[129–131] It

http://rcin.org.pl

exhibits photocatalytic, antibacterial,[132] superhydrophobic, and self-cleaning properties.[133] CuNS due to their low cost, high stability and good electrical conductivity[134] can also find promising applications *e.g.* in heat transfer systems,[135] sensors,[136] and surface enhanced Raman scattering.[121,137]

The most useful materials for electrocatalysis are deposited on the conductive surfaces without any assistance of surfactants in the solution. CuNS can be obtained on that kind of substrates by laser ablation of copper,[138] plasma etching,[139] dealloying,[125] electrochemical polishing,[140] thermal annealing,[141] and electrodeposition.[121,142–145] In some cases appropriate surface ligands promote catalytic properties of metallic nanoparticles by steric interaction and electronic modifications.[146,147] However, their presence may decrease the catalytic activity of the NS because the access of reactants to the metal surface is hindered.[148] There is a plenty of surfactant-free[132,133,137,138,142,149,150] methods to obtain CuNS such as precipitation of Cu(II) complex nanocrystals and their further calcination,[132] microwave assisted synthesis,[137] simple redox replacement by immersing of iron plate in Cu(II) salt solution,[150] and thermal annealing of Cu_2O-dopped glasses in hydrogen atmosphere.[149]

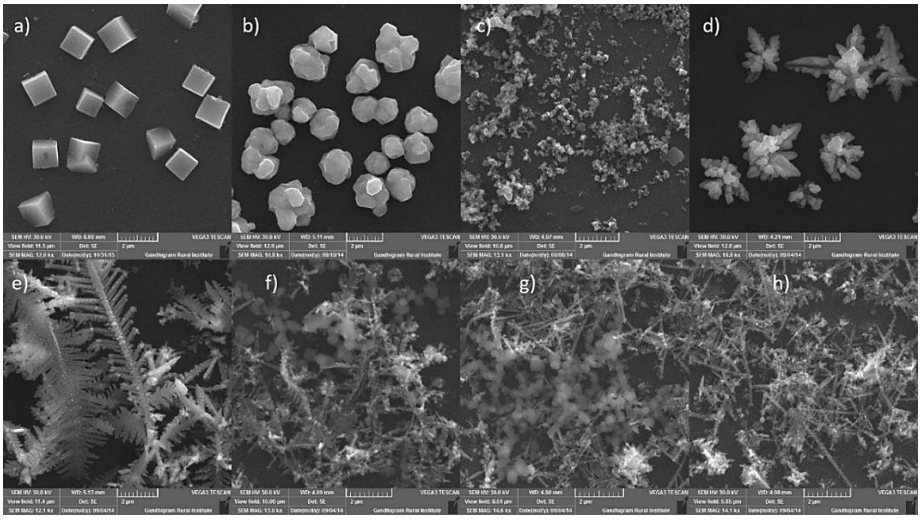

Fig. 4.4. SEM images of ITO/CuNS at different deposition potential of a) +0.10 V, b) 0 V, c) -0.10 V, d) -0.20 V, e) -0.30 V, f) -0.40 V, g) -0.50 V and h) -0.60 V at 400 s using $CuSO_4$.[121]

Copper is a popular metal processed by electrodeposition (Figure 4.4). It is relatively inert in most plating solutions of other common metals. Its high plating efficiency and high conductivity results in a good coverage of difficult to plating parts, coating for printed wiring boards and coating on steel wires are used to conduct electricity.[115]

http://rcin.org.pl

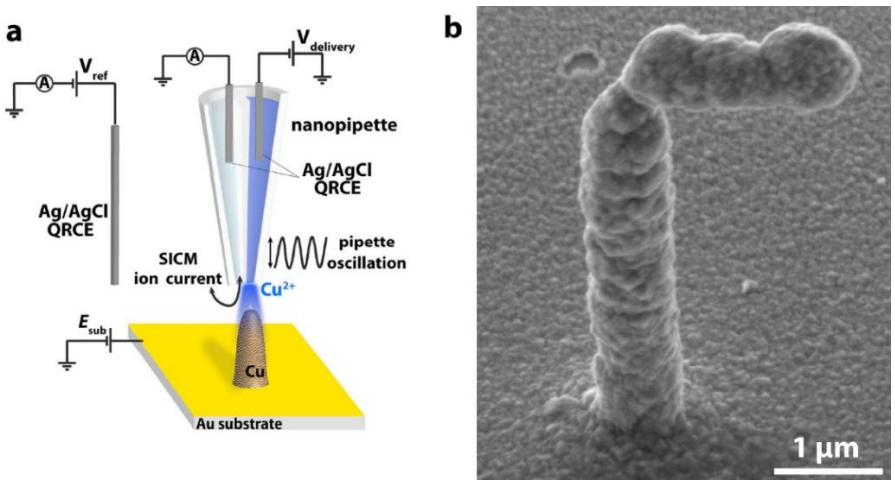

Fig. 4.5. a) Schematic representation of the experimental setup employed for deposition of 3D high aspect ratio Cu features on a gold electrode surface. b) SEM images of complex 3D features fabricated with a dual-channel nanopipette. Fabricated Γ-like feature (image taken at a 45° angle). The top bar of the Γ was deposited by translating the nanopipette probe laterally at 40 nm s^{-1} without SICM positional feedback. The substrate was held at a potential E_{sub} = -0.75 V throughout. SICM barrels in both deposition experiments were biased at 0.2 V vs. quasi-reference counter electrode (QRCE) in the solution bulk.[151]

There is a wide range of CuNS electrodeposition methods based on scanning probe techniques (Chapter 6). One of them is based on scanning ion conductance microscopy (SICM).[151–153] A micropipette with Cu salt solution and Cu anode inside serves as a source of copper. Two-dimensional Cu microcircuits were fabricated by lateral scanning over cathodically polarized support electrode in a Cu-free electrolyte.[152,153] To obtain a 3D Cu nanocolumns a modification of the SICM method was used. In a dual-barrel nanopipettes one channel served as a metal precursor delivery and second for maintaining the constant distance between the nanopipette and electrodeposited metal (Figure 4.5).[151] Another method, similar to SICM, which has been used to local electrodeposition of Cu is scanning electrochemical cell microscopy (SECCM). The pipette filled with Cu salt solution and equipped with counter and reference electrode is moved close to the substrate working electrode to provide contact between electrode and the electrolyte inside the pipette.[154]

http://rcin.org.pl

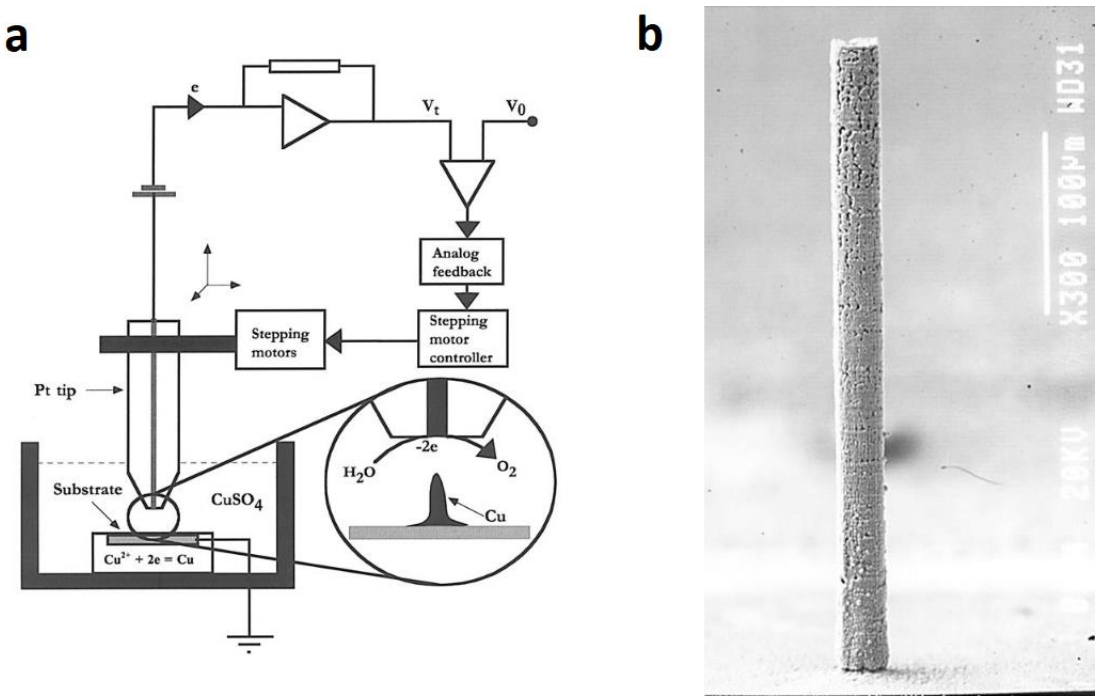

Fig. 4.6. a) A block diagram of the apparatus used for the deposition. When the circuit detects current over a preset threshold, it activates the stepper motor controller and withdraws the tip. This produces highly localized growth and deposits a column of approximately the diameter of the wire used in the tip. b) SEM image of copper column deposited on a copper substrate. Experimental parameters: E = 3.8 V (tip negatively biased), tip electrode 25 µm diam Pt, deposition solution 1.0 M $CuSO_4$.[155]

SECM is also a powerful method for localized electrodeposition of microarrays of metallic NS and their catalytic electroanalysis. Using direct mode of SECM localized electrodeposition of 3D Cu microstructures can be performed. Pt microelectrode which served as a SECM tip was also used as a positionable counter electrode. Cu^{2+} ions were present in the electrolyte. Retracting of the microelectrode with a feedback loop maintaining constant current of electrolysis resulted in a formation of micrometer-sized Cu columns (Figure 4.6).[155] SECM chemical lens concept was used to deposit microstructures of copper from a solution of its stable complexes. Electroless or galvanic deposition of Cu was caused by the local acidification of electrolyte beneath the SECM tip by electrogeneration of protons, which caused the local decomposition of complexes.[156] A micropatterns made of CuNS can also be obtained by localized electrorefining of polycrystalline Cu wire from a microelectrode which serves as a sacrificial SECM tip, under various conditions influencing catalytic properties of obtained nanomaterials.

4.3. Summary

The surface structure influences mechanical, thermal, chemical and electrochemical properties of materials, that can serve *e.g.* as catalysts. Besides obtaining homogenous surfaces with low number of defects, electrodeposition is one of the most common and efficient methods of

http://rcin.org.pl

preparation of nanomaterials with controlled properties, *e.g.* dispersion, morphology and structure. It can be used to synthesize thin film NS (nanofilms), nanoparticles, nanowires, nanotubes, core-shell, and porous NS that can be further applied *e.g.* as catalysts in energy storage devices.[108]

http://rcin.org.pl

5. pH sensing

5.1. Introduction

According to the International Union of Pure and Applied Chemistry (IUPAC) definition: "the quantity pH is defined in terms of the activity of H^+ ions in solution."[157] In aqueous media, the free acid cation is mostly present as the hydrated proton $(H_3O)^+$ thus pH is also defined as:

$$\mathrm{pH} = -\log\left(a_{\mathrm{H_3O^+}}\right) \qquad \text{(Eq. 5.1)}$$

Water molecules are able to take or donate protons and the phenomenon called water self-ionization (autodissociation) occurs:

$$2\mathrm{H_2O} \rightleftarrows \mathrm{H_3O^+} + \mathrm{OH^-} \qquad \text{(Eq. 5.2)}$$

K' and $K^{a\prime}$ are a stoichiometric and thermodynamic equilibrium constants and are equal:

$$K'_W = \frac{[\mathrm{H_3O^+}][\mathrm{OH^-}]}{[\mathrm{H_2O}]^2} \qquad K_W{}^{a\prime} = \frac{a_{\mathrm{H_3O^+}} \cdot a_{\mathrm{OH^-}}}{a^2_{\mathrm{H_2O}}} \qquad \text{(Eq. 5.3a,b)}$$

$[\mathrm{H_2O}]$ and $a_{\mathrm{H_2O}}$ are constant and equal: $[\mathrm{H_2O}] = \frac{1000}{18} = 55{,}5\ \mathrm{mol/L}$ and $a_{\mathrm{H_2O}} = 1$. Thus one can obtain equations for stoichiometric and thermodynamic dissociation constants, known also as the ionic product of water (stoichiometric and thermodynamic) which are constant at a given temperature:

$$K'_W[\mathrm{H_2O}]^2 = K_W = [\mathrm{H_3O^+}][\mathrm{OH^-}] \qquad K_W^{a\prime} a^2_{\mathrm{H_2O}} = K_W^a = a_{\mathrm{H_3O^+}} \cdot a_{\mathrm{OH^-}} \qquad \text{(Eq. 5.4a,b)}$$

Because of the high dilution of ions in the solution they are assumed to be equal, so in 22^0C:

$$K_W = K_W^a = 1 \cdot 10^{-14} \qquad \text{(Eq. 5.5)}$$

Equation 5.4 a can be presented in logarithmic form:

$$\log K_W = \log[\mathrm{H_3O^+}] + \log[\mathrm{OH^-}] \qquad \text{(Eq. 5.6)}$$

Defining $-\log[\mathrm{OH^-}] = \mathrm{pOH}$, $-\log[\mathrm{H_3O^+}] = \mathrm{pH}$, and $-\log[K_W] = \mathrm{p}K_W$, equation 5.6, can be rewritten:

$$\mathrm{p}K_W = \mathrm{pH} + \mathrm{pOH} \text{ and } \mathrm{p}K_W^a = \mathrm{p}\left(a_{H_3O^+}\right) + \mathrm{p}(a_{OH^-}) \qquad \text{(Eq. 5.7a,b)}$$

In the pure water and in the 22^0C:

http://rcin.org.pl

$$[H_3O^+] = [OH^-] = a_{H_3O^+} = a_{OH^-} \approx \sqrt{K_W} \approx 10^{-7} \quad \text{(Eq. 5.8)}$$

$$pH = pOH = p(a_{H_3O^+}) + p(a_{OH^-}) = 7 \quad \text{(Eq. 5.9)}$$

it is usually assumed that the pH scale can take values from 0 to 14.[158,159]

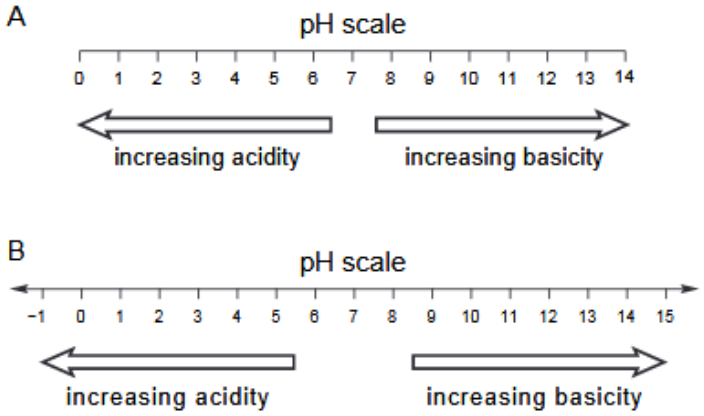

Fig. 5.1. Two pH scales: a) a typical textbook diagram; b) arrows on the axis show that pH is measured on an open-ended scale.[160]

However, commercially available concentrated HCl solution (37% by mass) has pH ≈ -1.1, and saturated NaOH solution has pH ≈ 15.0. Thus negative and higher than 14 pH values are possible and easy to calculate but are difficult to measure experimentally (Figure 5.1). The actual thermodynamic value of $p(a_{H_3O^+})$ differs from the stoichiometric one because under these conditions (highly concentrated acids and bases) the activity coefficient $(f_{H_3O^+})$ is significantly different from unity.[161]

pH is one of the most important parameters of chemical and biochemical reactions that has to be carefully controlled and monitored. It influences a number of processes that occur in aqueous solutions or at their interfaces. Even a small fluctuations of pH can influence kinetics, mechanisms and thermodynamics of the processes where protons and hydroxyl ions are the reactants. Even if they are not involved in the reaction mechanism they may affect the properties of (bio)catalysts or reacting substances and reaction intermediates (Chapter 3.4).[8]

There is a wide range of pH sensors that can be potentiometric,[162–164] voltammetric[165–169] and spectrometric[170–172] in their nature. Some of them will be further described.

5.2. Potentiometric sensors

Potentiometric glass electrode is the most common approach for pH detection due to its high sensitivity, selectivity, durability and commercial availability.[8]

http://rcin.org.pl

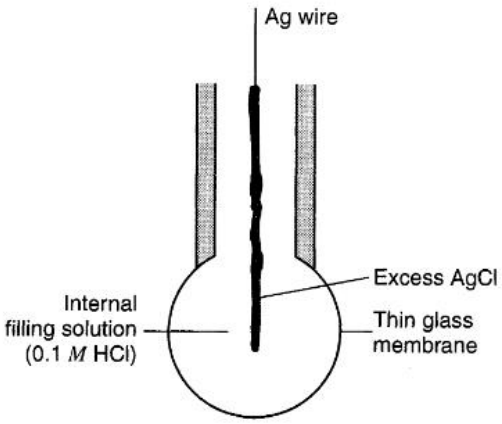

Fig. 5.2. A typical glass electrode.[173]

Figure 5.2 shows the construction of a typical glass electrode. Inside a bulb or membrane made of a thin glass containing metal salts, a silver wire covered with AgCl and a reference solution (0.1 M HCl) is fixed. During measurements, the glass electrode is fully immersed in the tested solution and its potential is registered with record to a reference electrode, *e.g.* saturated calomel electrode (SCE). A notation of the structure of the overall electrochemical cell can be written as:[173]

$$Hg/Hg_2Cl_2/KCl(sat.)//\ \text{tested solution/glass membrane}\ /\ HCl(0.1\ M)/AgCl/Ag$$

Glass electrode's internal reference

SCE

Glass electrode

The major part of its voltage comes from a tested solution and its effects on the glass electrode. The potential difference between the SCE and tested solution also influences the overall cell voltage, however it is negligible. So the overall cell voltage alterations caused by changing composition of the tested solution are only attributed to the junction between the glass electrode and tested solution.[173] During pH measurement a potential difference is created at the interface between the glass membrane and the solution containing H^+ ions. The hydrogen ions from the tested solution replace the metal ions inside the outer surface of the glass electrode. The equilibrium between the hydrogen ions in the glass network and the hydrogen ions in the solution affects the potential of the glass electrode (half-cell), and thus the voltage of the cell, which is converted to pH value on the calibrated pH-meter device.[161]

http://rcin.org.pl

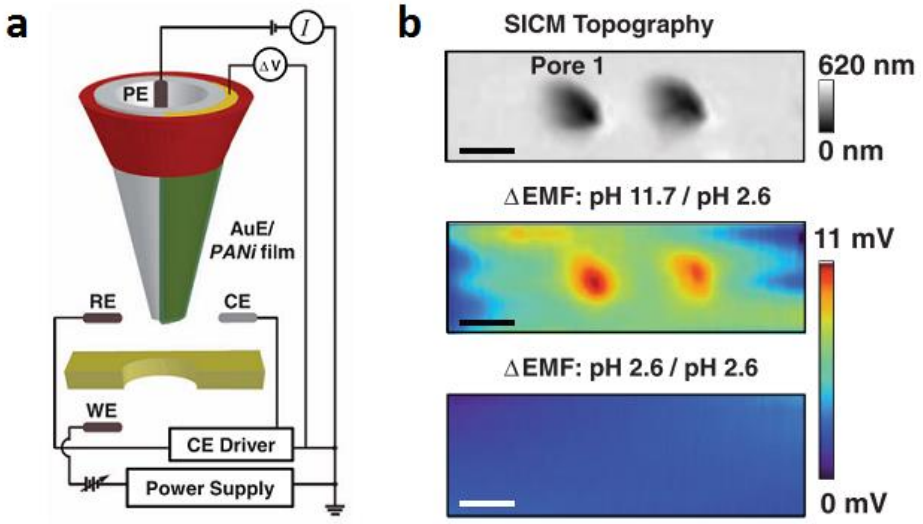

Fig. 5.3. a) Instrument schematic for pH detection with SICM. b) Upper image: SICM topography image of two pores in a polyimide membrane. Middle image: ΔEMF image obtained reports local pH differences induced by the pH gradient of 0.1 M KCl, pH = 11.7 (top chamber) / 2.6 (bottom chamber). Bottom image: No significant EMF difference is observed without pH gradient (0.1 M KCl, pH = 2.6 in both chambers). Scale bars equal 2 μm.[174]

Potentiometric pH sensors can suffer from alkali errors, instability, potential drift and has to be frequently calibrated before use. Their response time is long, because of the long time for the open circuit potential (OCP) equilibration. They are also fragile and difficult in miniaturization, thus are not suitable to perform pH measurements in the femtoliter volumes, or to visualize local changes of the pH with nanometer resolution (*e.g.* in biological cells or close to catalytic nanoparticles).[8,164,175] There are some pH potentiometric sensors to working in microscale,[163,174,176] however they are still not useful for nanoscale experiments. Figure 5.3 shows an example of a potentiometric microsensor consisting of a thin gold layer deposited on the one side of a nanopipette and covered by polyaniline (PANI) thin film. This microscale pH probe was used to map porous polyimide membranes. Potential difference between the PANI modified microsensor and reference electrode was measured when scanning the microsensor above the membrane pores. 11 mV of the probe potential difference was registered for almost 9 pH units.[174]

Some compounds that are present in tested solution may be electrochemically active and can exhibit fast electron transfer kinetics. Moreover, they can adsorb on the sensor surface, so the OCP in such cases is a mixed potential and the sensor is not selective.[177] Not only the electrolyte composition makes potentiometric pH sensors useless in nanoscale measurements but also the apparatus itself. The finite input impedance of voltage meters causes a potential drift, resulting in nonzero leakage current. For example, for a 1 μm diameter disk microsensor, 1 pA of leakage current (1 TΩ input resistance, 1 V) corresponds to a current density of *ca.* 130 μA cm^{-2} which is incompatible with the measurement of an OCP.[175]

http://rcin.org.pl

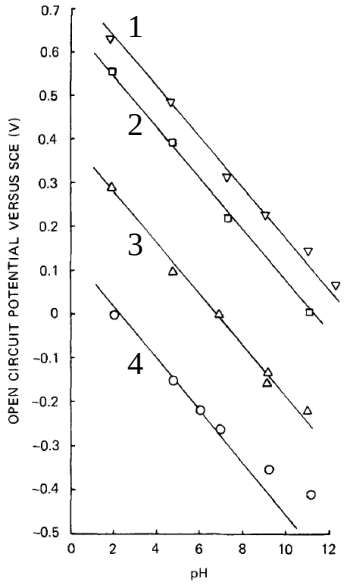

Fig. 5.4. Open-circuit potential of metal oxide electrodes in different pH buffers. Metal oxides of (1) Pt, (2) Ir, (3) Ti, and (4) Zr. Solid lines have slope of -59 mV/pH.[178]

Figure 5.4 presents a plot of the pH dependence of OCP for the various oxide electrodes. Except Zr oxide electrode at alkaline pH, they appear to show a Nernstian behavior with a slope of -59 mV/pH. In the case of Pt and Ir oxides, which are good electronic conductors, OCP can be used to monitor pH. OCP = $C - 0.059 \cdot \mathrm{pH}$, where C depends on the sensor type and reference electrode. C value is usually found by calibration.[178]

5.3. Voltammetric sensors

Voltammetric pH sensors are mainly based on carbon materials which are commercially available, versatile, cheap and have relatively large potential window. Moreover, carbon surfaces can possess large number of carbonyl and hydroxyl functional groups which redox reactions involve protons. Therefore thermodynamics of these reactions are pH dependent.[8,9,179]

When the oxo-groups, that are involved in redox process, undergoes electrochemically reversible reaction, the Nernst equation (Equation 5.10)[180] can be used to quantify this process:

$$E_{\mathrm{p}} = E^{0}_{\mathrm{formal}} - \frac{2.3\,RTm}{nF}\mathrm{pH} \qquad \text{(Eq. 5.10)}$$

where m is the number of protons, and n represents the number of electrons. There is a direct relationship between the peak potential (Ep) and pH (Figure 5.5-a).[8]

In the literature there is a lot of examples of carbon-based voltammetric pH sensors, mostly developed and studied by Compton's group.[8,9,165] They studied voltammetry of surface

http://rcin.org.pl

functional groups on graphitic carbon surfaces and various carbon-oxygen compounds, such as 9,10-diphenylanthracene (DPA), 9,10-phenanthraquinone (PAQ) (Figure 5.5).

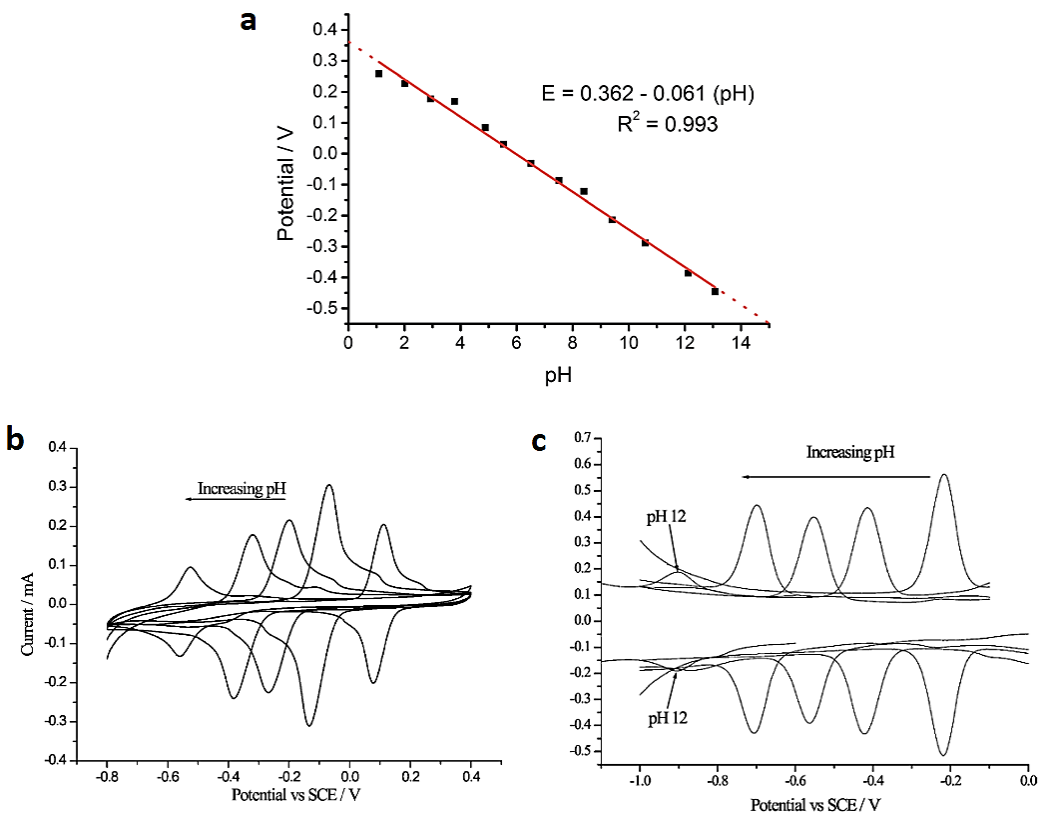

Fig. 5.5. a) Calibration plot of SWV peak potential against pH for a GC electrode in 0.01 M buffer solutions (with 0.1 M HCL/KCL and NaOH buffer solutions at pH = 1.09 and pH = 13.0, respectively), showing a linear response with gradient of 61.0 mV per pH corresponding to a Nernstian behavior at T = 310 K. b) Cyclic voltammograms of PAQ at each pH studied (pH = 1, 4.6, 6.8, 9.2 and 12). Step potential 2 mV, scan rate 100 mVs^{-1}. c) Base-line corrected oxidative and reductive square wave voltammograms of DPA at each pH studied (pH = 1, pH = 4.6, pH = 6.8, pH = 9.2 and pH = 12).[165]

Voltammetric pH sensors are suitable for the measurements in the micro- and nanoscale. They are based on modified carbon microelectrodes.[7,166,181] Contrary to optical methods they can be used in opaque solutions and suspensions. They exhibit fast response time, limited by the time required for recording a voltammogram (proportional to the potential range and inversely proportional to the scan rate). The potential drift problem is eliminated by imposing a potential by an external amplifier (voltage clamp, potentiostat). Figure 5.6 shows SECM pH map, obtained with a 25 μm diameter carbon-based pH sensor above the 1 mm lactate-producing *S. mutans* biofilm after addition of 30 mM sucrose in artificial saliva (pH = 6.0) at 37 ^{o}C. The pH above the biofilm surface created a low pH zone and dropped from 6.0 to 5.4.[181] Nanoscale voltammetric pH sensing is described in ref.[175] and Chapter 12.

http://rcin.org.pl

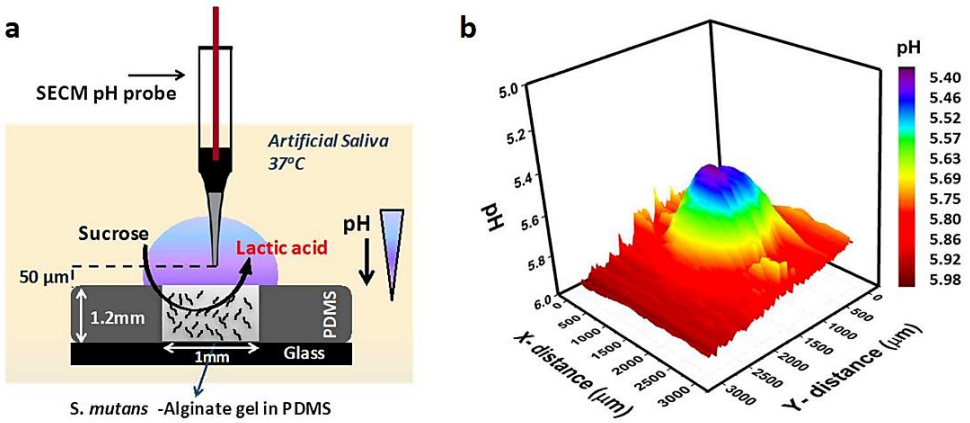

Fig 5.6. a) Schematic of S. mutans bacteria gel biofilm substrate and pH microprobe used in SECM experiments. b) 3D pH image recorded 60 µm above the biofilm with pH microprobe (scan speed, 30 µm/s) after addition of 30 mM sucrose in artificial saliva (pH = 6.0) at 37 °C.[181]

5.4. Summary

pH determination and control is indispensable in different fields, such as food, biopharmaceutical, and medical industry, water treatment, and environment protection. pH is a fundamental parameter in studies of chemical and biochemical reactions in the industry and in the environment. It is a challenge to develop a fast, sensitive and reliable sensor to detect small pH changes in fluids containing various organic compounds. Carbon-based voltammetric sensors seem to be the best candidates for these applications, since they are biocompatible, conductive, appropriate for surface modification and suitable for experiments in nanoscale. The future of carbon based sensors lies not only in their use as a pH sensors but also in the possibility of simultaneous measurements of other substances.[7–9]

http://rcin.org.pl

6. Scanning electrochemical microscopy

6.1. Introduction

SECM is one of the scanning probe microscopies (SPM) among which the most popular are atomic force microscopy (AFM, Chapter 7.4.), scanning electron microscopy (SEM, Chapter 7.3.) and scanning tunneling microscopy (STM).[182] In this technique the current, caused by an electrochemical reaction, at the tip is usually measured as its position over the sample. First SECM-like experiment results were published in 1986 by Engstrom, *et al.*[183] and then, in 1989, was developed by Bard group.[184]

In SECM experiment the probe (tip) and the sample (substrate) are immersed in a solution containing supporting electrolyte and most often electroactive species.[185] Using SECM technique one is able to evaluate material flux from a surface with a high spatial and temporal resolution.[186] SECM has been also used to study ion transport in channels and cellular or enzyme activity in biological systems (*e.g.* single cells[187]). One can also evaluate the (electro)catalytic activity of varied materials towards useful reactions, such as ORR or CO_2RR and hydrogen oxidation. SECM is also a powerful electrochemical tool for studies of the local properties and reactivity of a wide range of materials (metals, insulators, semiconductors). It can be also combined with other non-electrochemical scanning probe techniques, *e.g.* AFM, to provide constant distance imaging and independent information on the topography of studied sample.[188] The variety of SECM application areas has been shown in figure 6.1.

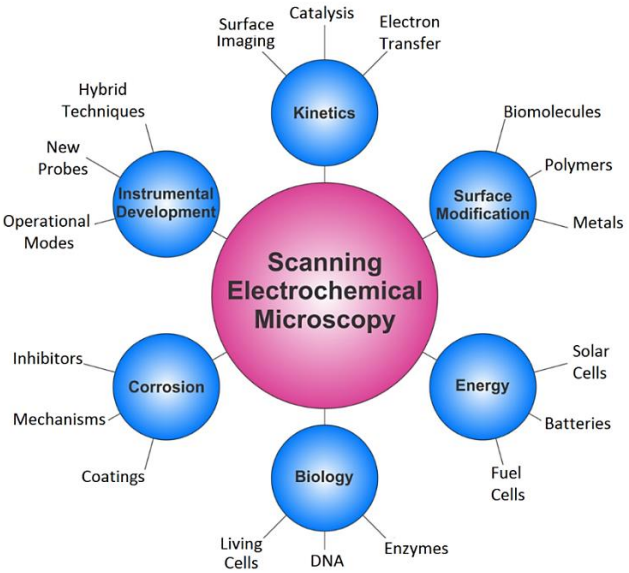

Fig. 6.1. SECM applications.[186]

http://rcin.org.pl

6.2. Instrumentation

The setup of SECM (Figure 6.2) consist of a mono- or bipotentiostat that can apply a bias and measure the currents at the probe (first working electrode, WE1) and the substrate (second working electrode, WE2) simultaneously. The potentials are always applied with respect to a non-polarizable reference electrode (RE) or polarizable quasi-reference electrode and the measured currents flow between individual working electrodes and common counter (auxiliary) electrode (CE).[173,189]

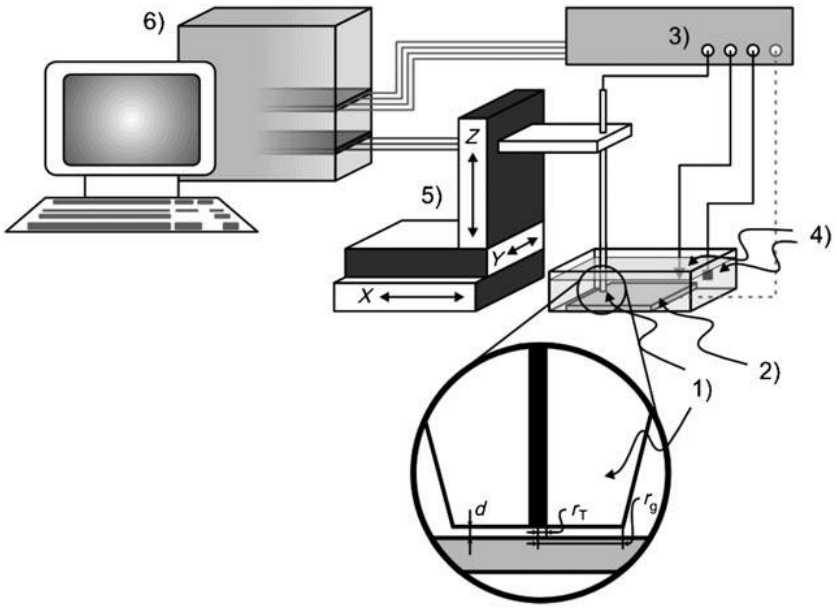

Fig. 6.2. Components of SECM setup. 1) Disk-shaped amperometric ultramicroelectrode (called probe or tip), 2) sample (substrate), 3) mono- or bipotentiostat, 4) reference and counter electrodes, 5) positioning system, 6) control PC.[189]

SECM employs microelectrodes as probes and typically large electrodes as substrates. Microelectrode is mounted to the microscope high resolution three-dimensional (3D) positioning system which allows to move it in three dimensions (*X*, *Y*, and *Z*) over the substrate electrode, using stepper and/or piezoelectric motors. To synchronize and coordinate each SECM component a control unit (PC) equipped with data acquisition system is required together with appropriate SECM software.[186] To get additional information on studied sample or to maintain constant probe-to-sample distance one can add additional instruments to SECM setup like inverted optical microscope, fluorescence detection systems or constant distance unit.

6.3. Micro- and nanoelectrodes

An important part of the SECM setup is the probe (micro- or nanoelectrode). In 1939 Laitinen and Kolthoff used the term microelectrode to describe the role of the electrode under small

http://rcin.org.pl

A (electrode area) / V (solution volume) conditions. In this case A is small enough and V is large enough to not alter the bulk concentrations of electroactive species by the passage of current, so microelectrodes probe a system rather than effect compositional change.

There is no broadly accepted definition of ultramicroelectrode (UME). In the literature microelectrodes with radius of a disk (or the width of a band) smaller than 25 μm are very often called UMEs. However, a definition specifying a certain geometric dimension is rather arbitrary. Not only the electrode size and shape must be considered, but also a kinetic parameter of the employed electroanalytical technique, that governs the thickness of the diffusion layer developed (*e.g.* the potential scan rate for cyclic voltammetry). Relatively large electrodes may, under certain conditions, respond like a microelectrodes. Microelectrode is any electrode whose characteristic dimension is, under the given experimental conditions, comparable to or smaller than the diffusion layer thickness. Under these conditions, a steady state or a pseudo steady state (cylindrical electrodes) is attained.[190]

The dimensions of the tip determine the spatial resolution of a SECM measurement. Researches continuously develop smaller working electrodes of dimensions not only in the micrometer but also in the nanometer range.[173] The most popular cores for microelectrodes are platinum, gold, other noble metals, and carbon.[186] To less-common cores one can count tungsten, cobalt,[191] aluminum,[192] gallium,[193] manganese.[194] There are many reviews concerning design, fabrication and preparation of SECM probes.[195–198] The procedures of preparation of microelectrodes used in experiments described in this thesis are described in chapter 10.2. The most popular geometries of commonly used microelectrodes are: disks, rings, ring-disks, hemispherical, and conical.[197] The examples of SECM tips geometries are shown in figure 6.3.

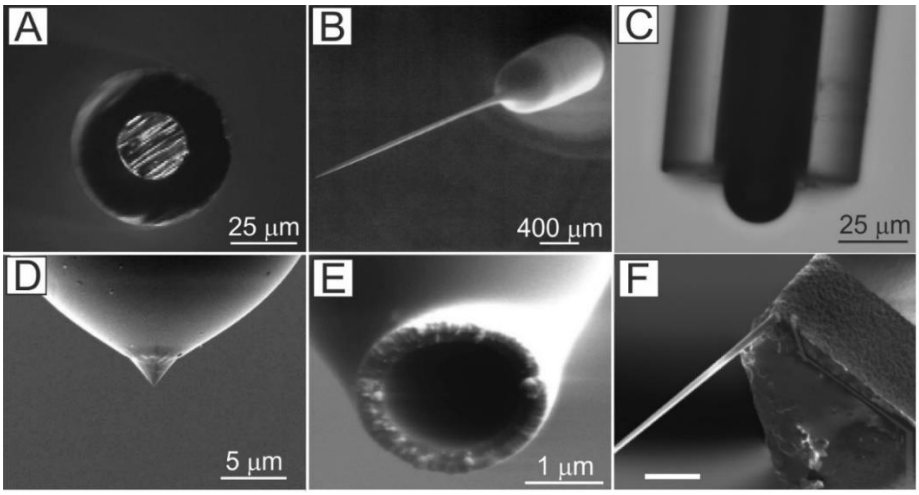

Fig. 6.3. Examples of SECM tip geometries. (A) 25 μm Pt disk microelectrode.[199] *(B) 200 nm Pt disk nanoelectrode.*[198] *(C) 25 μm Hg hemispherical microelectrode.*[199] *(D) Au conical microelectrode.*[200] *(E) 1.4 μm Au ring microelectrode.*[201] *(F) AFM-SECM tip with 100 nm Au layer.*[202]

http://rcin.org.pl

From the operational point, there are two kinds of SECM tips: amperometric and potentiometric. Majority of SECM measurements have been performed using amperometric probes (>90%) because of their advantages, such as relative ease in preparation, positioning, high robustness and fast response time. In amperometric probes the recorded signal is a current correlated with a Faradaic reaction occurring at the SECM tip. However, they can suffer from low selectivity – the measured signal can be a convolution of several different Faradaic processes.[186]

The most critical geometric parameter of SECM tip is the ratio between the radius of conductive core, r_T, and the total tip radius (r_T plus insulating sheath thickness), r_g, defined as a dimensionless parameter *RG* (Figure 6.4, equation 6.1).[203]

$$RG = \frac{r_g}{r_T} \qquad \text{(Eq. 6.1)}$$

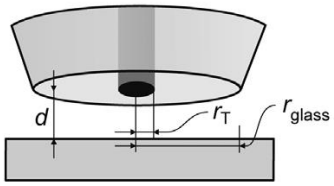

Fig. 6.4. Dimensions of microelectrode.[203]

Although the geometrical RG parameter is crucial for microdisk tips, other geometries (beveled, conical, hemispherical) needs different parameters for their characterization, such as recession/protrusion, aspect ratio, insulation angle, off-centered positioning of the metal wire, uneven insulation, insulation gaps, and cracks.[186]

The microelectrode can be characterized by optical microscopy, cyclic voltammetry (CV) (Chapter 7.1.), and by recording approach curves using positive or negative feedback mode of SECM (Chapter 6.4.1, Figure 6.5).

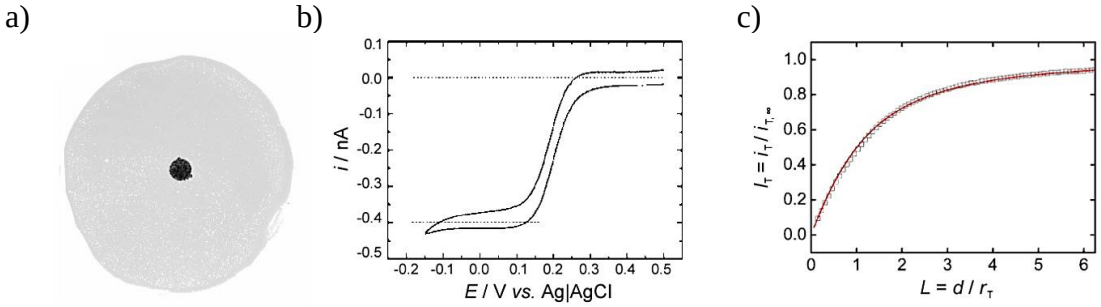

Fig. 6.5. a) Optical image of the Au microelectrode: r_T = 12.5 µm and RG = 9.97, b) CV of the same microelectrode resulted in a r_T ≈ 13.4 µm according to equation 6.2 (redox probe: 0.1 mM $[Fe(CN)_6]^{3-}$ in 0.1 M phosphate buffer pH = 4.8, v = 10 mV s^{-1}), c) SECM approach curve to a glass surface using the same microelectrode. The theoretical parameters fit with RG = 9.97 yields r_T = 12.48 µm.[204]

http://rcin.org.pl

As it was mentioned earlier, in the literature, microelectrodes with radius smaller than 25 μm are very often called "ultramicroelectrodes".[173] The biggest advantage of the UME is rapid formation of a hemispherical diffusion field (Figure 6.6-a). It allows more efficient mass transfer (manifested by larger current density) than at macroscopic electrodes, where the planar diffusion occurs. It also provides a number of advantages like fast steady-state response, low capacitance and low "ohmic" (iR) drop. These special properties of diffusion leads to establishment of a steady-state diffusion-limited current $i_{\mathrm{T},\infty}$[A]:[189]

$$i_{\mathrm{T},\infty} = gnFDC^{*}r_{\mathrm{T}} \qquad \text{(Eq. 6.2)}$$

where n is the number of electrons exchanged in the redox reaction, F is the Faraday constant (96 485 $[\mathrm{A\,s\,mol^{-1}}]$), D is the diffusion coefficient of the redox mediator (probe) in solution $[\mathrm{cm^2\ s^{-1}}]$, C^{*} is the concentration of the redox mediator in solution $[\mathrm{mol\ cm^3}]$, r_T is the radius of the electroactive surface of the electrode [cm], and g is a dimensionless geometry-dependent factor that assumes different values of RG (Table 6.1).[186, 205-206]

Table 6.1. Selected values of the parameter g with respect to RG:[206]

RG	∞	10	2	1.2
g	4	4.07	4.44	4.95

6.4. Modes of operation

SECM measurements are performed using different operational modes. The most common are: feedback, generation/collection, redox competition, direct, potentiometric (Figure 6.6), surface interrogation (Figure 6.9), and ion transfer/electron transfer (also called micropipette delivery/substrate collection modes, Figure 6.11). Historically, feedback and generation/collection modes were introduced as first.[184,207]

http://rcin.org.pl

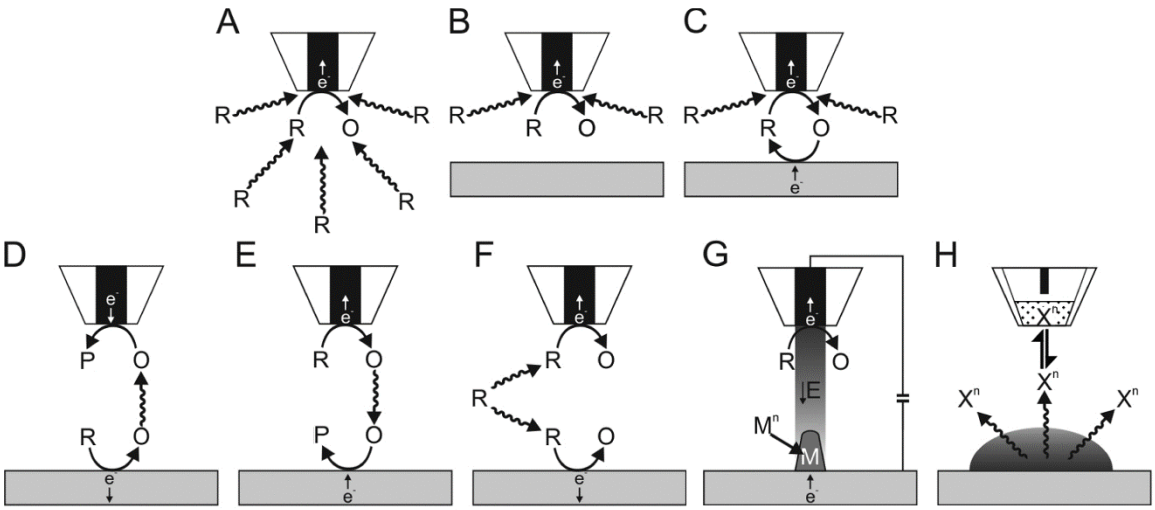

Fig. 6.6. Schematic explanation of selected examples of SECM operational modes. (A) Steady-state behavior (diffusion-limited) in bulk solution. (B) Feedback over an inert substrate (negative feedback). (C) Feedback over a conducting substrate (positive feedback). (D) Substrate-Generation/Tip-Collection (SG/TC). (E) Tip-Generation/Substrate-Collection (TG/SC). (F) Redox competition (RC) mode. (G) Direct mode, where "M^{n+}" is a metal precursor in solution with charge n (n = integer) and M is a solid metal. (H) Potentiometric mode with an ion-selective electrode, where "X" is an ion with charge n (n = integer generated at the sample).[186]

To simplify approach curves analysis, the probe current and the tip-to-sample distance are normalized versus infinite distance current $i_{T,\infty}$ and tip radius r_T, respectively. As it is shown in figure 6.5, in SECM measurements lowercase *i* means raw current, uppercase *I* means normalized current which is calculated by dividing the measured tip current i_T by the steady-state current recorded at large distance $i_{T,\infty}$. *L* is reported as normalized distance, where tip-to-substrate distance (*d*) is normalized by the probe radius r_T. All of these normalizations enable comparison between measurements performed using different probe dimensions, mediator diffusion coefficients and concentrations.[186]

6.4.1. Feedback Mode

Feedback mode (FB) is the most versatile operational mode of SECM. In this mode, both the tip and the substrate are immersed in a solution containing supporting electrolyte and redox species.[185] On an example of mediator reduction reaction at the sample, an anodically biased probe is approached to a substrate of interest. Only the reduced form of mediator (R) is present in the electrolyte bulk, which is oxidized at the probe, according to the following tip reaction:[186]

$$R - ne^- \rightarrow O \qquad \text{(Eq. 6.3)}$$

When the tip is far away from the substrate, in a bulk solution (at a distance greater than 10 times the radius of the electroactive probe core; $d > 10\ r_T$) the UME current is in accordance

http://rcin.org.pl

with the mass-transfer limited steady-state current $i_{T,\infty}$ (Figure 6.6-a, Equation 6.2). If the sample is an insulating (inert) surface where no reaction occurs, the absolute tip current decreases upon approaching ($i_T < i_{T,\infty}$) to shorter distances, as a result of hindered diffusion of the mediator (Figure 6.6-b). This is called SECM negative feedback. If the substrate electrode is able to regenerate the redox mediator (Figure 6.6-c) according to the following substrate reaction:

$$O + ne^- \rightarrow R \qquad \text{(Eq. 6.4)}$$

an increased current at shorter tip-to-sample distances is recorded, because of an increase of the local flux of R beneath the probe ($i_T > i_{T,\infty}$). This behavior is called SECM positive feedback.[186,188,189,208]

The pure positive and pure negative feedback (Figure 6.7) currents are limited by diffusion. For finite kinetics of regeneration of mediator at the sample an approach curve falls between pure positive and pure negative feedback behaviors.[186]

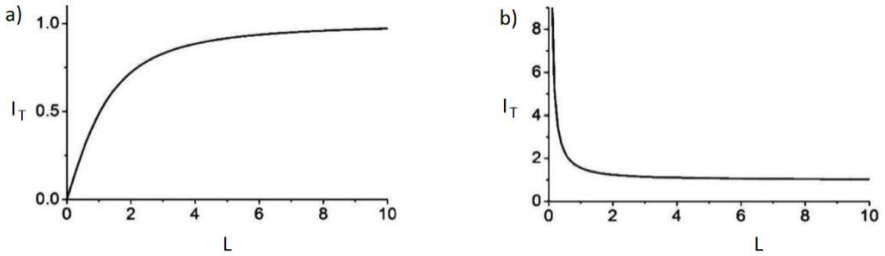

Fig. 6.7. Normalized SECM approach curves to (a) an insulating substrate and (b) a conductive substrate. I_T (normalized tip current) = $i_T/i_{T,\infty}$; L (normalized distance) = d/r_t; RG ≈10.[209]

6.4.2. Generation/Collection Modes

There are two kinds of generation/collection modes: substrate generation/tip collection mode (SG/TC) and tip generation/substrate collection mode (TG/SC). The main difference between them is the locus of the redox reaction, where the form of electroactive species which is initially absent in electrolyte is generated. This process occurs either at the substrate or at the tip.[210]

In SG/TC mode electroactive species are generated at the substrate (*e.g.* at the substrate electrode) and collected at the biased tip electrode (Figure 6.6-d).[186] The following reactions occur at the substrate:

$$S \rightarrow O \qquad \text{(Eq. 6.5)}$$

and at the tip:

$$O + ne^- \rightarrow P \qquad \text{(Eq. 6.6)}$$

http://rcin.org.pl

In SG/TC mode the electrolyte above the sample surface is probed by the microelectrode during generating a redox-active species. The product of the reaction at the sample electrode (O) is electrolyzed at the tip and, as a result, a non-electroactive product P is generated. When the UME is placed close to the active sample region (where the redox-active species are generated), the i_T depends on the local concentration of these species.[189] The reaction at the tip can be the same as in the FB mode (equation 6.4). To avoid feedback one must establish the distance between electrodes to $L > 10$. Usually the relation between the linear size of the substrate a_s and the size of the tip r_T is $a_s/r_T \gg 1$, so the diffusion layer of the substrate is much larger than that of the tip. Using this mode one can perform measurements of chemical flux from the sample, or the concentration profiles of sample products[186] also in corrosion or in heterogeneous enzymatic processes. This method offers much better sensitivity than FB mode but, unfortunately, SG/TC suffers from some disadvantages:

- lack of steady-state concentration profile at the large substrate electrode,
- interference between substrate and tip reactions (to minimalize the feedback effect one must use microelectrode with smaller r_T and *RG*),
- microelectrode movement can disturb the diffusion layer of the sample electrode through convection,
- the hindered diffusion of reagents to the sample region can occur.[189]

In TG/SC mode electroactive species are generated at the tip and collected by the biased substrate electrode (Figure 6.6-e). The following reactions occur at the tip:

$$R - ne^- \rightarrow O \qquad \text{(Eq. 6.7)}$$

and at the substrate:

$$O + ne^- \rightarrow P \qquad \text{(Eq. 6.8)}$$

When the electrode is close to the substrate (which has a larger area) and when O is stable, almost all reactive species are collected (*e.g.* reduced) by the substrate. Under these conditions the steady-state cathodic substrate current, i_S, is equal to the tip current, i_T. It means that the collection efficiency $|i_T/i_S|$ is close to unity. If O reacts before it diffuses across the tip/substrate gap, the collection efficiency will be smaller than 1 and, for a very rapid decomposition, can approach zero. To study the kinetics of decomposition of O one can determine $|i_T/i_S|$ as a function of *d* and concentration of R. Using this mode one can perform kinetic studies of electrode reactions that are inaccessible to the feedback mode.[173,211]

http://rcin.org.pl

6.4.3. Redox Competition Mode

The use of redox competition mode (RC) was introduced by Eckhard *et al.*[212] In this mode the SECM tip competes with the sample for the same redox species (Figure 6.6-f). For instance the sample is biased at a reductive potential, whereas the tip is pulsed anodically to generate the substrate species (*e.g.* O_2) for the sample reaction (*e.g.* ORR). Next, a reductive potential pulse is applied to the tip for consuming previously generated species (Figure 6.8).[203]

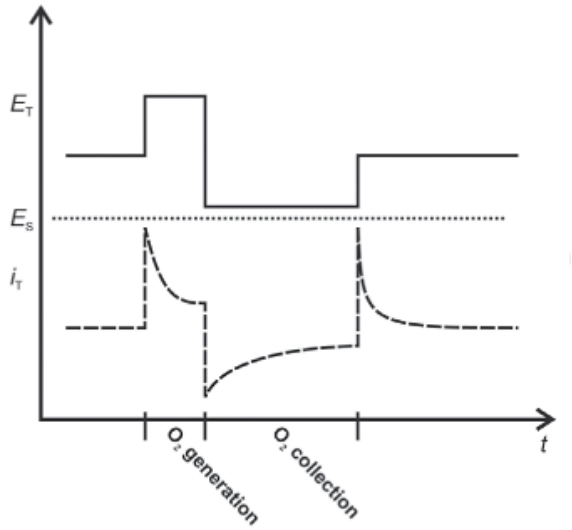

Fig. 6.8. General principle of the RC mode: pulse program at the UME from ref [203] *with corrections.*

When the tip electrode is scanning over a flat inactive region of the substrate, the tip current recorded upon its cathodic pulses remains constant. When an active region of the sample is scanned (where the reduction process competing for the same substrate occurs), the reducible species are consumed by both the SECM tip and the substrate at the same time. It leads to decrease in measured current at the SECM tip. Decreased cathodic tip current regions in SECM plot indicate increased substrate activity.[186] Using this mode one can map local catalytic activity of samples.

6.4.4. Direct Mode

In the direct SECM mode the configuration of electrochemical cell is different. The microelectrode tip serves as a counter electrode and the substrate as a working electrode (Figure 6.6-g). An amplified electric field is localized between the tip and the substrate, when the current flow between WE and CE is enforced by voltage polarization. The current flow is partly limited to the gap between the microelectrode and the sample. One can achieve a high patterning resolution with small tip-to-substrate distance.[186] The direct SECM mode is used for surface modification, semiconductor etching, enzyme deposition, and micropatterning.[213,214] Current

http://rcin.org.pl

flow through the sample is mainly restricted to the region underneath the microelectrode, especially when low conductivity electrolyte is applied.

6.4.5. Potentiometric Mode

In the potentiometric SECM mode potential is usually measured at an ion selective microelectrode (ISME) versus a reference electrode positioned in the SECM cell. Typical ISME for SECM measurements is composed of an internal reference electrode inserted into a glass capillary, filled with a defined activity solution containing the ion of interest and an ion-selective membrane at the tip. The sample solution can contain the ions of interests, so when the ISME is immersed into a sample solution the chemical recognition of the analyte at the ion-selective membrane causes the formation of a junction potential (Figure 6.6-h). A junction potential is created because of the difference in chemical activities of ions in the internal and external solutions, and it can be measured due to stable internal and external reference electrodes. This potential depends on the activity of the ion of interest.

The use of potentiometric mode of SECM provides several advantages including determination of nonelectroactive and electroactive ions with standard redox potentials outside the solvent window.

Because no Faradaic reaction is required to perform potentiometric experiments, the concentration and oxidation state of the analyte is not affected by the ISME. One can also use different probes than ISME membranes, but still, they require the presence of a component which is capable of differentiating species.[215] Potentiometric probes have many advantages, however they can suffer from relatively slow response times (~milliseconds to seconds), short lifetimes and difficult probe positioning.[186]

http://rcin.org.pl

6.4.6. Surface Interrogation Mode

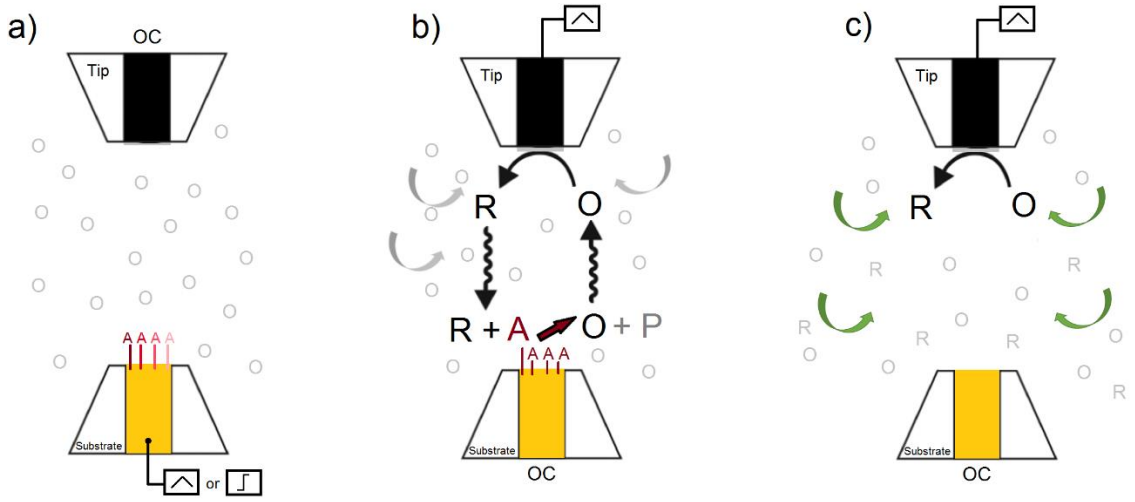

Fig. 6.9. SI-SECM of an adsorbed species. a) A reactive species (A) is chemically or electrochemically adsorbed at the substrate during a potential scan or step while the tip is at open circuit (OC). b) The substrate is switched to OC, and the tip generates the titrant (R), which reacts at the surface of the substrate to support positive feedback at the same tip. (C) After the adsorbate (A) is consumed at the substrate, the tip experiences negative feedback.[209]

Surface-interrogation mode of SECM (SI-SECM) was developed by Rodríguez-López *et al.* to study adsorbed surface species on an electrode. This new approach to SECM methodology is developing rapidly.[216–219] In this mode two microelectrodes (sample and tip) are immersed in a solution which contains only one form of mediator *e.g.* its oxidized state (O). This mediator must be stable under these conditions and does not participate in any reaction. At the beginning of the experiment a reactive species A are formed at the substrate microelectrode by pulse or by scan to a potential where oxidation occurs, and are adsorbed at a substrate electrode. During this time the tip is kept at OC or polarized at potential stabilizing oxidized form of mediator (Figure 6.9-a). Then the substrate electrode is switched to OC and the tip is scanned or pulsed to generate titrant R (produced by reduction of O). The titrant R diffuses to the substrate electrode, reaches the adsorbed reducible species A and reacts with it to re-generate O and to produce positive feedback. (Figure 6.9-b) Species A are consumed during this reaction exhaustively (transformed to a final product P) so the regeneration of redox mediator is terminated and negative feedback is detected (Figure 6.9-c). In the final stage system shows negative feedback and only O reacts at the tip electrode at the rate governed by the hindered diffusion into the tip–substrate gap. Figure 6.10 shows the expected voltammetric response for the SI-SECM system.[186,220]

http://rcin.org.pl

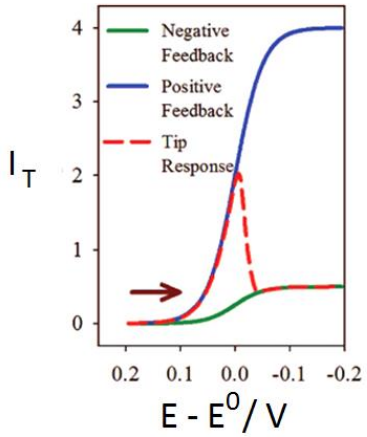

Fig. 6.10. Expected current response at the tip following the events depicted in figure 6.9 for SI-SECM mode at an arbitrary electrode setup.[221]

The SI-SECM mode relies on a specific application of the transient feedback mode which allows the quantification of reacting species adsorbed on a surface of a substrate electrode. The tip must be placed parallel to the substrate and approach to $L \leq 0.3$. The tip and the substrate should be small enough for easiest approaching and to prevent OC feedback.[186,209,220]

6.4.7. Ion Transfer/Electron Transfer Mode

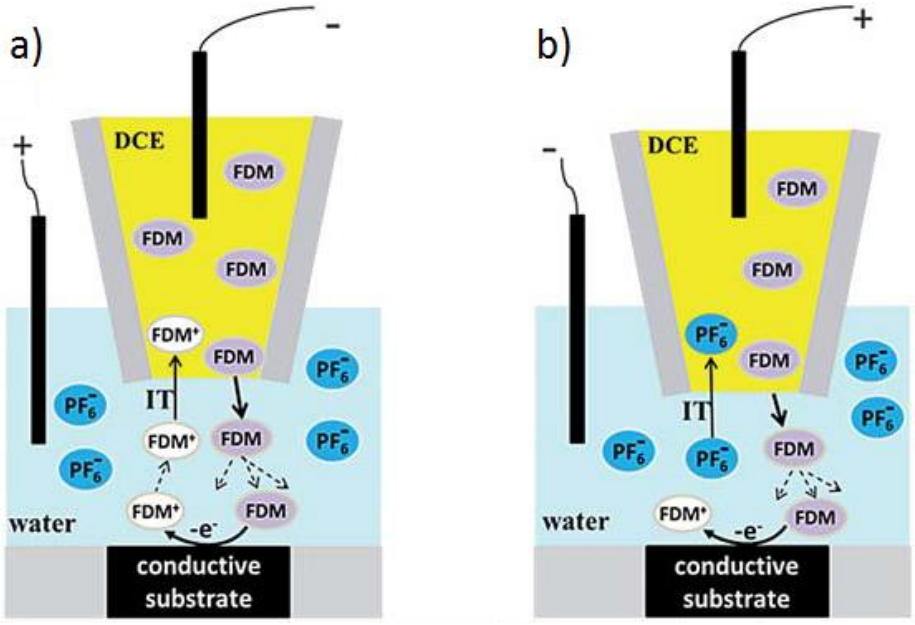

Fig. 6.11. Schematic representation of ET/IT mode with positive a) and negative b) IT feedback.[222]

Ion transfer/electron transfer mode of SECM (IT/ET) was introduced by Mirkin and co-workers.[222] It enables topography-independent reaction rate imaging in the nanoscale. In this mode a nanometer sized pipette probe served as a tip and is filled with a liquid phase (*e.g.* 1,2-dichloroethane; DCE), immiscible with external solution (*e.g.* aqueous). Inside the pipette solution a neutral redox species (*e.g.* ferrocendimethanol; FDM) is initially presented. During the experiment these redox species can partition from organic to the aqueous phase. They diffuse to

http://rcin.org.pl

the active substrate surface and can be oxidized at a significant fraction at the sample (Figure 6.11-a). The recorded substrate (oxidation) current represents the local ET rate at the microscopic portion of the substrate surface facing the tip.

The ionic product of the substrate reaction (FDM^+) can be transferred to the organic solution inside the nanopipette by applying suitable voltage (negative) between the reference electrode inside the pipette and the external reference. An IT tip current is then detected (Figure 6.11-a). Similarly to the conventional SECM feedback mode (Chapter 6.4.1) this current increases with the decreasing tip-substrate separation distance – positive IT feedback occurs. The FDM^+ localized within the tip-substrate gap does not need to diffuse from a bulk solution, which provides a high spatial resolution of this method.

The negative IT feedback (Figure 6.11-b) occurs when the RE inside the pipette is biased to a positive potential versus external RE. It prevents the transfer of FDM^+ ions to the organic solution inside the nanopipette. Instead, the transfer of anions from the external solution to DCE occurs (*e.g.* PF_6^-, ClO_4^- or any other hydrophobic ions present in aqueous solution). This process results in negative feedback – the IT current decreases with the decreasing tip-substrate separation distance. One can use the negative IT feedback of ET/IT SECM mode for positioning of the nanopipette and for the distance controlling, because it is independent of the surface reactivity.[222–224]

The fundamental limitations of the SECM feedback and substrate generation/tip collection modes (Chapters: 6.4.1 and 6.4.2) are difficulties in probing low signal sources in the nanoscale. When the positive feedback, produced by low signal sources, is much lower that the magnitude of the tip current in the bulk solution ($i_{T,\infty}$) the sample activity will not be probed. Bard and co-workers shown[225] that in the feedback mode of the SECM an active spot feature on the insulating planar substrate can be detected only if its radius is $\geq 0.1\ r_T$. Also, when the kinetics of the regeneration of a mediator is slow, the substrate electrode may not produce measurable feedback current. For measuring slow kinetics and imaging a small surface features, alternative to feedback is the substrate generation/tip collection mode. Much higher sensitivity of this method results from the fact that reactant is generated at the substrate and collected at the tip, therefore low $i_{T,\infty}$ flows. However there is limitation caused by significant diffusion broadening effect (the apparent size of an object in the SECM image is larger than its actual dimensions) and elevated background signal.[226-227] The ET/IT mode of the SECM operation combines the advantages of conventional feedback and generation/collection experiments without being plagued by their shortcomings. One can probe electrochemical activity under the conditions

http://rcin.org.pl

which involves very high fluxes by the reactant delivery directly to the electrode surface from a pipette positioned in close proximity to the sample. This mode also allows to mimic the conditions attained in industrial electrolyzers while avoiding problems caused by high concentrations. The ET/IT experiments are performed under steady state conditions, that is why this method can be viewed as an alternative to ultrafast cyclic voltammetry and high-speed flow in nanofluidic channels because it eliminates sophisticated electronics or high pressures.[222–224]

A wide range of experiments employs SECM with a nano- or micropipette tip filled with organic phase and immersed in aqueous solution including catalysis studies,[228] imaging surface topography[229] and ion transport,[230] local electrodeposition,[231] surface patterning[232] and studies of biomembranes.[233] ET/IT mode of SECM has recently been used for detection and identifying superoxide intermediate released from the Pt catalyst surface during ORR.[234]

6.5. Combined electrochemical – topographical imaging

The applications of SECM expanded since its introduction. During the last years SECM has been strengthened by the introduction of new probes (nanometer-sized tips),[235] commercially available instrumentation, and new practical applications at a variety of fields:[210,216,236] biology, enzymes, living cell studies,[224] corrosion, energy, surface modification and kinetics.[186] The development of numerous hybrid techniques has greatly enhanced SECM application. The common aspect for SECM and its combined techniques is the development and fabrication of miniaturized electrodes. The main limitation of nanoelectrodes application in SECM results from the fact that the smaller the imaging electrode is, the closer it has to be positioned to and scanned at the sample surface.[235]

The use of positional feedback during electrochemical imaging provides access to an additional information – surface topography. Therefore one can acquire topographical and electrochemical images simultaneously to understand structure – activity relationships. Moreover, maintenance of constant tip-sample distance eliminates common convolution of the sample topography and its activity in constant height SECM imaging. A wide range of positional feedback methods have been proposed but the most popular are combined SECM-AFM and combined SECM-SICM techniques.[237]

6.5.1. SECM-AFM

AFM (Chapter 7.4) is one of the most popular among the SPMs. To probe the surface, a nm-sharp tip is attached to a flexible cantilever and is controlled by monitoring the deflection or oscillation amplitude of the cantilever using an optical feedback mechanism (Figure 6.12-a). Using AFM

http://rcin.org.pl

one can obtain a high resolution topographical images of conducting and non-conducting samples in different environments - air, liquids or vacuum. AFM measurements also provides unique information about electrical, chemical and mechanical properties of the surface.[237]

Combining AFM with SECM provides not only a direct information on the topography of examined sample but also about its surface reactivity. The first SECM-AFM experiment with contact-mode imaging (Figure 6.12-b) was reported by MacPherson and co-workers in 2000[238] and using lift mode (Figure 6.12-c) in 2001.[239] Since that time a wide range of probe geometries have been implemented such as: nanowires, needles,[240] conical,[241] and recessed.[242] One can also integrate SECM with AFM using nanoelectrodes as AFM probes. The following fabrication methods of SECM-AFM tips have been recently reported:[235]

- nanoprobes with electrodes located directly at the apex of the AFM tip;[243,244]
- microfabricated probes with the conductive electrode also constituting the AFM tip;
- insulated carbon nanotubes at the end of the AFM tip with an exposed electroactive area;
- microfabricated bifunctional nanoprobes which consist a sharp non-conductive AFM probe and an nanoelectrode that is located at a certain distance above the top of the tip.[245]

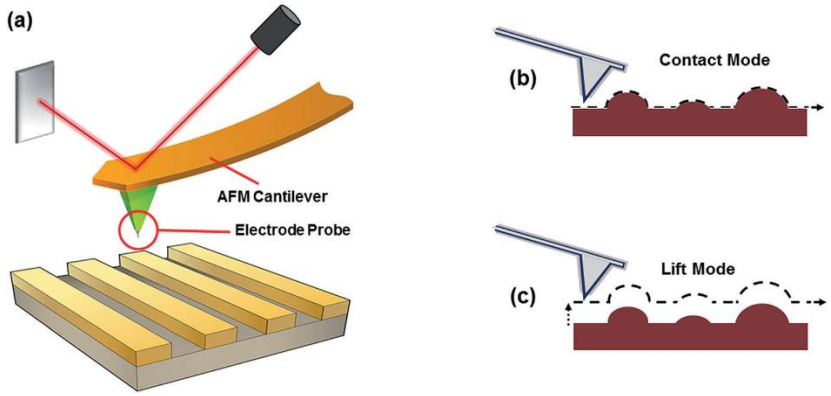

Fig. 6.12. a) Schematic depiction of dual SECM-AFM operation, b) contact mode imaging, c) lift mode imaging.[237]

Performing SECM-AFM experiment one can use other modes of the SECM. For example in SG/TC mode, during a brief time of electrolysis, an electroactive species are present in its relevant oxidation state not in a bulk solution but at the interface, so the probe essentially maps the diffusion profile of these species. In SECM-AFM feedback mode the electrochemical response is very sensitive to tip geometry and to the durability and quality of the insulation of the probe. Because of their geometries, conical and spherical tips have low SECM feedback responses making them less suitable for feedback mode experiments.[202,237]

http://rcin.org.pl

On figure 6.13 a topography and electrochemistry images were recorded simultaneously using noncontact mode of AFM and feedback mode of SECM, using a 50 nm-diameter probe tip and a tip potential at which ferrocenemethanol oxidation occurred at a diffusion-controlled rate.[202]

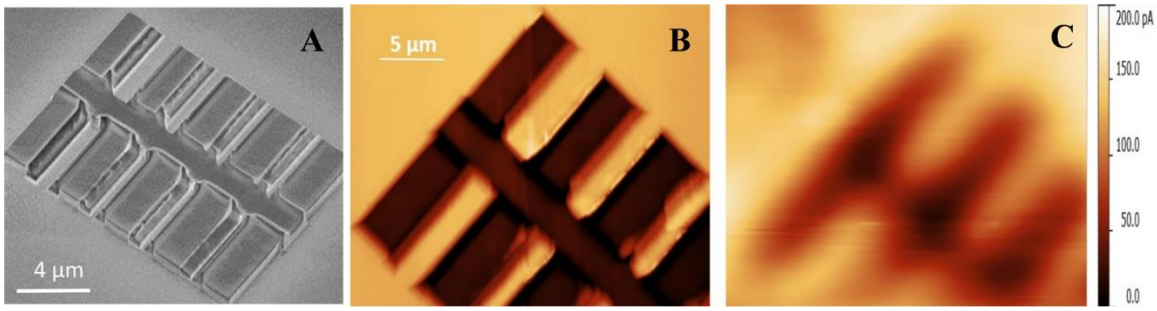

Fig. 6.13. a) SEM image of calibration standard (Pt on SiO_2) for lateral resolution determination; b) Topography and c) electrochemistry AFM-SECM images recorded with a Pt probe (electrode size, 50 nm diameter; tip length, 3 mm; scan speed, 0.3 line s^{-1}). Solution conditions, 1 mmol L^{-1} FcMeOH; tip potential = 0.4 V vs. Ag/AgCl.[202]

SECM-AFM technique is a powerful tool to obtain a high resolution combined topographical-electrochemical imaging rapidly. Its main advantage is a good topographic resolution and quality of obtained images. It is also suitable for fundamental studies in bioelectrochemistry, biocorrosion, fuel cell research, electrochemical nanotechnology, sensor technology, and materials science.[235] The major weakness of combined SECM-AFM is the cost of the probes which also suffer from reliability and durability.[237]

6.5.2. SECM-SICM

SICM is one of a non-contact SPMs, introduced in 1989 by Hansma *et al.*[246] In comparison with SECM, SICM uses a much simpler tip and employs distance control to position the probe. SICM is used for probing samples which are immersed in an electrochemical cell filled with ionically conducting solution. In a typical set-up a single-channel nanopipette is filled with an electrolyte and detects the ionic current between a quasi-reference counter electrode (QRCE) inserted inside the pipette and a second QRCE located in a bulk solution. Due to the voltage applied between electrodes the ionic current flows through the edge of the nanopipette. The distance between the pipette and the sample is regulated by maintaining the ionic current used as feedback signal. When the SICM probe approaches the sample surface due to hindered migration of ions the resistance between two QRCEs increases, thus the ionic current decreases (Figure 6.14).[208,247]

http://rcin.org.pl

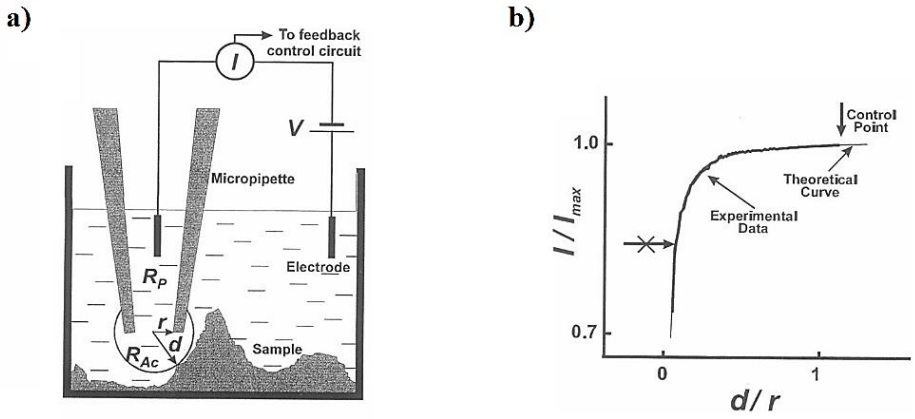

Fig.6.14. Diagram of sensing mechanism of the SICM. a) The micropipette tip/surface interaction. b) Comparison of expected and actual values of tip current (I) as a function of the sample/tip separation (d). The vertical arrow indicates the value of current (control point) used for the scanning protocol in the feedback control circuit.[248]

SICM was combined with SECM to obtain the relationship between the localized topography/electrochemical properties without physical contact. Two types of SECM–SICM probes have been described: dual-barrel theta pipette where one barrel serves as the SICM channel and the other is a solid SECM electrode (Figure 6.15-a,b)[249–252] and ring, where metal and insulator are deposited on the walls of the SICM channel, and subsequently exposed by gentle polishing or focused ion beam milling (Figure 6.15-c,d).[253–255]

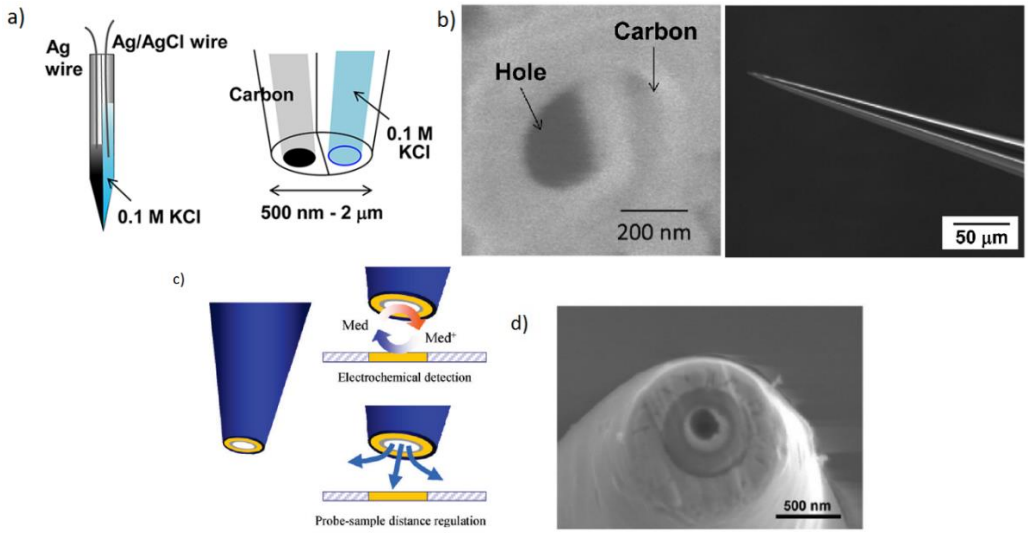

Fig.6.15. a) Schematic illustration and b) SEM image of SECM-SICM dual-barrel nanoprobe.[256] *c) Schematic illustration and d) SEM image of the SECM/SICM ring probe.*[255]

In 2011 Takahashi *et al.*[249] developed bifunctional nanoelectrodes. A quartz dual-barrel (theta-shaped cross-section) capillary was pulled by a laser puller. Next, one barrel was blocked inside and the back side of the obtained nanopipette was connected to a petroleum gas fed which was pyrolyzed by gas torch flame. The open capillary served for SICM distance control while the carbon-filled electrode was used for local electrochemical measurements. This new, cheap and

http://rcin.org.pl

quick method of fabrication of dual-barrel nanoprobes makes a huge progress in electrochemical imaging. Results of combined electrochemical and topographical imaging with high spatial resolution are demonstrated in figure 6.16.[257]

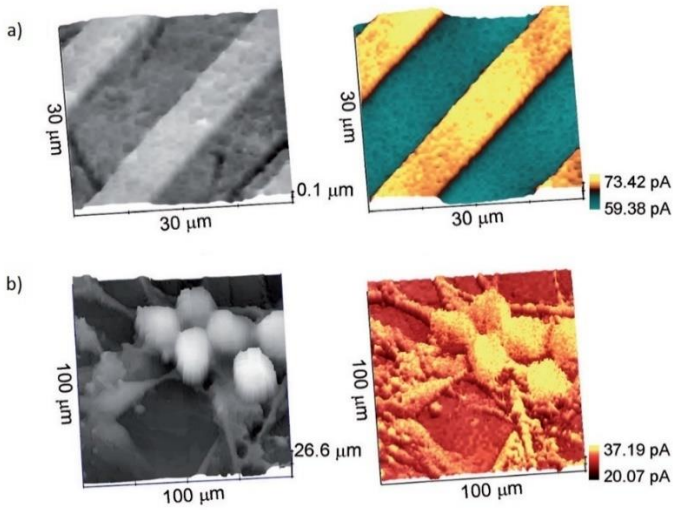

Fig.6.16. Simultaneous topographical (left) and electrochemical (right) images a) Pt interdigitated array in 1.0 mm $FcCH_2OH$ + PBS. b) Living sensory neurons in 0.5 mm $FcCH_2OH$ + HBSS.[249]

6.5.3. AC-SECM

In alternating current SECM (AC-SECM)[258–260] the tip-to-sample distance is maintained independently of the redox current. In 1993 Horrocks *et al.*[261] applied alternating potential to an SECM tip for the first time. Authors presented the H_2O_2 diffusion profile over gold and carbon electrodes during ORR. Experiment was carried out in a two-electrode arrangement. The solution resistance between the tip and the reference-counter electrode was detected in a conductometric measurement and increased as the tip approached an insulator, because the ionic pathway was hindered by the surface. Similar phenomenon occurs in SICM (Chapter 6.5.2). AC-SECM setup contains a function generator or the internal oscillator of a lock-in amplifier (LIA). It sends a sinusoidal wave of low amplitude superimposed on DC offset to the potential input of the potentiostat. AC component of the resulting current (alternating at the same frequency) is detected and the current output of the potentiostat is fed into the signal input of the LIA. Because of the frequency-selective amplification of the lock-in technique, the AC detection schemes decreases noise level. The LIA output signal represents the alternating current signal. Consists of one value for the alternating current amplitude $|I|$ and one value for the phase angle θ by which the sinusoidal current wave is shifted with respect to the perturbation voltage. Thus, the current can be considered as a vector in the complex plane with real I' and imaginary part I''. AC current is directly proportional to the conductance Y and inversely proportional to the impedance Z. DC

http://rcin.org.pl

component of the resulting current at the potentiostat output is extracted by a low-pass filter. It corresponds to the rate of Faradaic processes at the tip.

In the AC-SECM technique obtained AC-signal at the UME depends on tip-to-sample distance, thus this method can be used in positioning or topographic imaging with sensor tips exhibiting a distance-independent DC signal (*e.g.* in SG/TC mode). It can be also utilized to adjust the tip distance to insulating surfaces. AC-SECM also delivers information of differences in the local electrochemical surface properties. Thus, obtained signal simultaneously carries information not only about the topography but also of the local electrochemical activity of the sample.[260] The main disadvantage of AC-SECM is perturbation of AC component of the tip current by electrolyte alterations (ionic conductivity) and variations in redox activity and conductivity of the sample, *e.g.* the AC response is not sensitive exclusively to the distance. This imposes difficulties in maintaining constant distance upon scanning over samples with inhomogeneous activity.

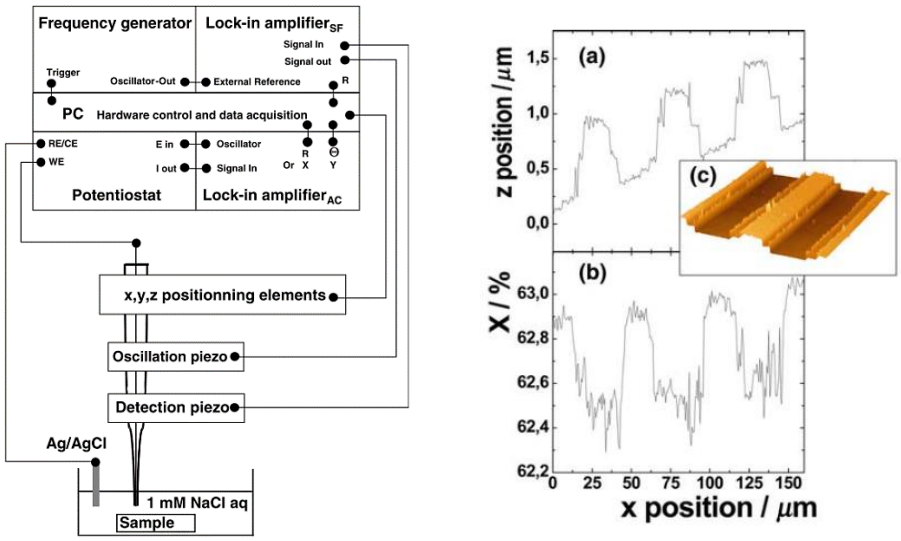

Fig. 6.17. Left side) Schematic illustration of the instrumentation used for constant-distance mode AC-SECM. Right side) topography (a) and AC current (b) line scans acquired during scanning the tip of a sub-µm Pt electrode (350 nm radius) in constant distance across three Pt-micro bands of a microfabricated band electrode array. (c) shows an AFM image of one band of the microelectrode array for comparison.[262]

The first combined electrochemical – topographical imaging using AC-SECM was performed by Etienne *et al.* in 2004 (Figure 6.17). The measurements were performed in 1 mM NaCl by applying an alternating potential of 100 mV at a frequency of 1 kHz between the SECM tip (350 nm radius PtUME) and the counter electrode.[262]

http://rcin.org.pl

6.5.4. SF-SECM

Another technique providing simultaneously topographic and electrochemical information is shearforce SECM (SF-SECM). SF response is sensitive to the tip-to-substrate distance and probe geometry.[263] In 1995 Ludwig *et al.* introduced SF control for SECM using a laser detection of the shearforce-induced tip vibration dampening.[264] Later, the modification of SF-SECM were developed by using non-optical shearforce control by tuning fork[265] or piezoelectric plates[266] and is still in the interest of researchers. Figure 6.18 presents a typical SECM setup with shearforce detector.[267] Several types of SF methodologies have been reported in the literature,[268,269] however the typical SF-SECM setup involves a UME fastened to two piezoelectric plates: dither and receiver. To maintain a constant probe-to-substrate distance, SF-SECM employs a feedback signal based on changes of SF tip-to-substrate interactions attributed to hydrodynamic forces, Van der Waals interactions, direct mechanical contact or capillary forces. A sinusoidal lateral mechanical oscillation of the UME is induced by the dither piezoelectric plate and is detected by the receiver plate. The lateral oscillation of the UME is damped when it is close to the surface, because of the SF interactions between the tip and the sample. The *Z* position of the UME can be adjusted by maintaining a constant SF amplitude and the constant tip-to-substrate separation can be achieved. From the *Z* motion of the probe the height profile or the topographic variation of the surface can be constructed.[263]

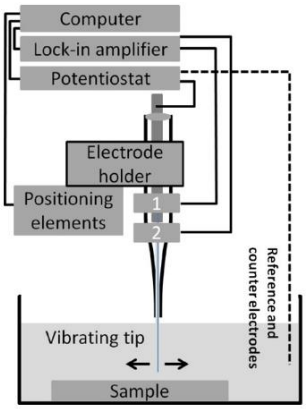

Fig.6.18. Scheme of the SECM setup equipped with an electrode holder allowing shearforce detection.[267]

SF-SECM is used to study the topography and activity of a variety of surfaces including live cells,[270,271] large and complex metal samples[272] or to monitor local activities of ions in proximity of a solid/liquid interface.[273]

6.6. Nanoscale electrochemical imaging

It is well known that adjusting the NPs shape, size and structure has a significant influence at their overall electrocatalytic activity.[274] Unfortunately, the characterization of electrocatalytic

http://rcin.org.pl

reactions at individual nanoparticles is still challenging because the macroscopic, "bulk" voltammetric techniques are not suitable to analyze the non-uniform fluxes at complex electrochemical interfaces. Using a highly sensitive methods with good spatial resolution like SPMs and electrochemical scanning probe microscopies (EC-SPMs) resolve this problem. To EC-SPMs one can count for instance electrochemical scanning tunneling microscopy (EC-STM), electrochemical atomic force microscopy (EC-AFM), scanning electrochemical potential microscopy (SECPM), and SECM. They are able to perform measurements in the nanoscale between the structure of catalytic systems under reaction conditions.[275–277]

The biggest disadvantage in the commonly used constant high SECM mode is the fact that the response of the tip is influenced not only by the activity of the sample but also by its topography. That is why the positioning and scanning in the nanometer region above the surface, without positional feedback, limits the types of studied substrates. One can overcome this problem using dual redox mediators,[187] by changing the scanning probe to pipette (SICM,[278] SECM-SICM,[279] SECCM[276]) or by the integration of SECM with other scanning probe techniques (SECM-AFM).[237,276]

Figure 6.19 shows an example of simultaneously activity and topography SICM mapping at individual nanoparticles using a single channel probe. In this experiment the electrocatalytic oxidation of borohydride was studied at AuNPs on a carbon fiber support, in alkaline media. Occurring reaction caused the depletion of hydroxide ions and release of water, what causes the change in the ionic composition around NPs. Thus, the ion conductance inside nanopipette probe was also changed when it approached active sites of the sample (NPs) where the composition of the electrolyte was different than in the bulk solution.[275]

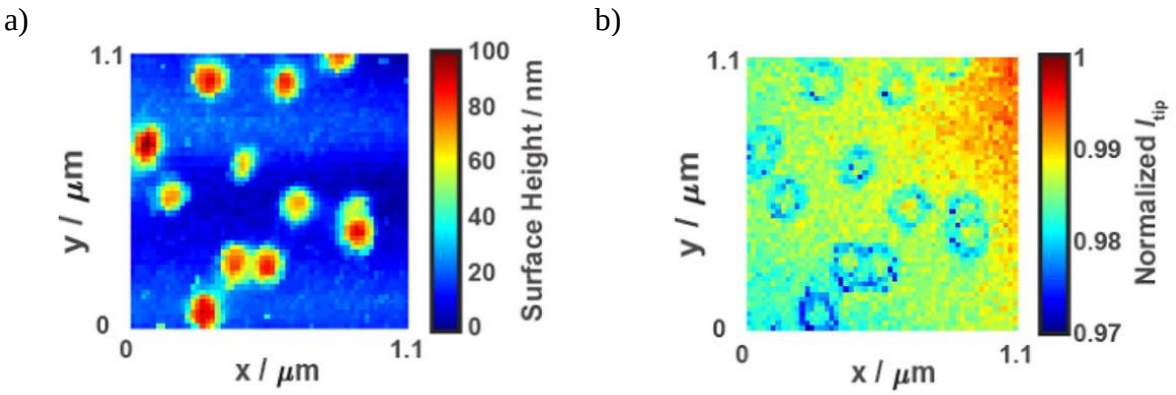

Fig. 6.19. a) SICM topography maps and b) simultaneously recorded activity images of AuNPs on a 7 μm diameter CF UME, obtained in a solution containing 3 mM $NaBH_4$ and 30 mM NaOH, at V = 0.75 V.[275]

Besides the surface structure imaging, EC-STM allows mapping of relative local activity. EC-STM is a combination of traditional STM and a classical electrochemical setup where the

http://rcin.org.pl

sample acts as main working electrode. The side-insulated tip is connected as the second working electrode to allow application of a bias voltage between the tip and the sample. Figure 6.20-a presents the EC-STM setup. It contains a bipotentiostat that controls the potentials of the sample and the STM tip independently, reference and counter electrodes.[277]

a) b)

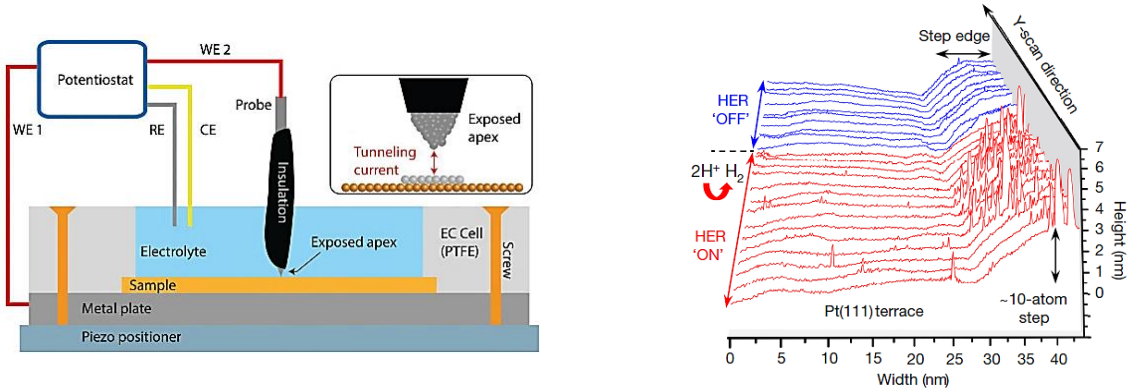

Fig. 6.20. a) Schematic diagram of the EC-STM setup (RE: reference electrode; CE: counter electrode) and the working principle.[277] b)EC-STM line scans (constant-current mode) obtained over a Pt(111) surface in 0.1 M $HClO_4$, when the potential of the sample is either sufficiently negative or too positive to initiate the HER ('ON' or 'OFF').[280]

Figure 6.20-b shows EC-STM line scans obtained for a platinum(111) electrode with flat terraces and step-like surface defects in an aqueous 0.1 M $HClO_4$ electrolyte. It reveals that over different surface sites (terraces and steps) that are active for the HER, different 'noise levels' occurs. Terraces and steps exhibit different catalytic activities, thus are expected to contribute differently to the temporal changes in the tunneling barriers. If the electrode potential is negative enough to initiate the HER (but not sufficient to produce gas bubbles) then the STM signal reveals noticeable differences: under reaction conditions the detected noise level is systematically higher at step-like defects than at terraces.[280]

6.7. Summary

SECM is one of the most important scientific tools. Its application continuously expands to many domains, *e.g.* charge transfer reactions at the solid/liquid and liquid/liquid interface, electrocatalysis, local properties (*e.g.* local activity, pH) and reactivity of all kinds of materials: insulators, metals, semiconductors, and to biological cells and enzymes. It was also applied in the studies of photovoltaic conversion, solar cells, and bioanalysis. Because of the progress of technology and equipment, nowadays SECM has improved sensitivity, high spatial resolution, and the position of the probe is more precisely controlled. It can be combined with other techniques, such as SICM, AFM, electrochemiluminescence (ECL), surface plasmon resonance (SPR). Using nano-sized SECM tips, local detection in nanoscale is possible allowing new discoveries and deeper insight into various phenomena and their better understanding.[224]

http://rcin.org.pl

Experimental

7. Methods

7.1 Cyclic voltammetry

Cyclic voltammetry (CV) is one of the most widely used electroanalytical techniques. It provides significant information about the thermodynamics of redox processes, the kinetics of heterogeneous electron transfer reactions, kinetics of preceding and following homogeneous reactions and on chemical adsorption and physisorption processes.[281] A basic experimental setup for the CV technique is composed of a potentiostat or patch-clamp amplifier, function generator and an electrochemical, three- or two-electrode cell (Figure 7.1). Potentiostat controls the voltage between the working electrode (WE) and the counter (auxiliary) electrode (CE), to maintain the potential difference between the WE and non-polarizable reference electrode (RE) in accordance with the program generated by a function generator (Figure 7.2-a).[173]

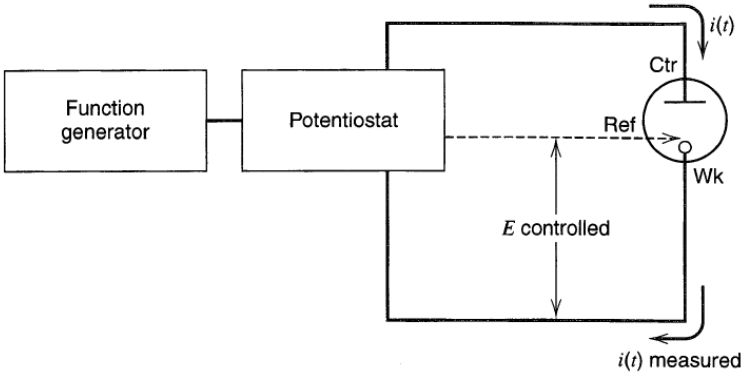

Fig.7.1. An experimental setup for controlled-potential experiments.[173]

Most electrochemical experiments are carried out in electrolytes containing analyte in millimolar concentration and supporting electrolyte in a concentration at least one order of magnitude higher. It provides sufficient electrolyte conductivity and minimizes the migration of charged analyte molecules. By using supporting electrolyte one can restrict mass transfer of an electroactive species near the electrode to the diffusive mode.[173]

During a CV experiment the linear potential sweep is applied to the WE using a triangular potential waveform (Figure 7.2-a). The potentiostat measures the currents resulting from the applied potentials. When the vertex potential (E_λ) is reached, the sweep is reversed. The obtained current–potential plot is named cyclic voltammogram. An example of a single potential cycle is shown in the Figure 7.2-b. Here, only oxidizable species (R) are present in electrolyte and the

http://rcin.org.pl

redox couple undergo reversible electrochemical process. The size of the electrode used in this example is larger than the diffusion layer of the analyte. Therefore peak-shape CV is obtained. When the electrode size is comparable or smaller than the diffusion layer the steady-state is seen (Chapter 6.3).

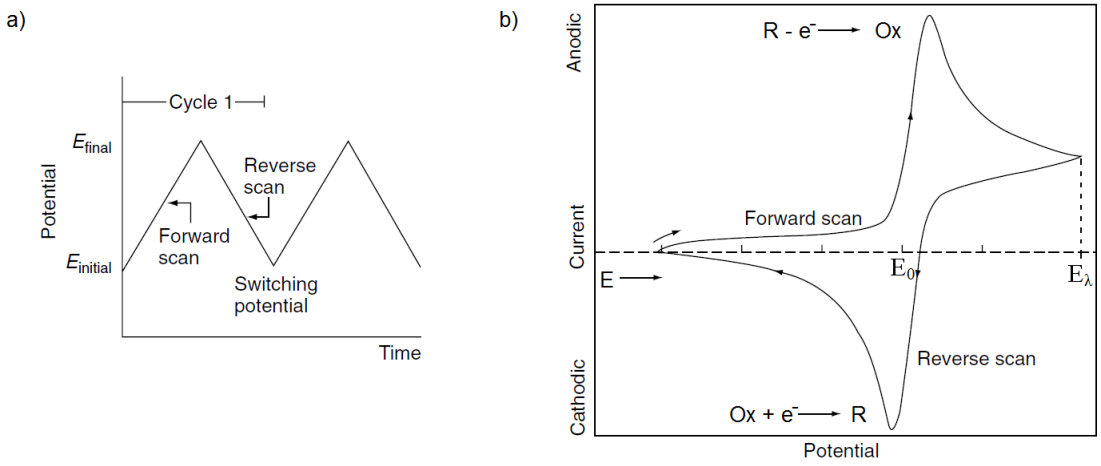

Fig.7.2.a) Potential–time program in a cyclic voltammetry experiment. b)Typical cyclic voltammogram for a reversible redox process. From ref. [281] *modified to be in accordance with IUPAC recommendations.*

The shape of obtained cyclic voltammogram depends on chemical reversibility, adsorption, kinetics, coupled homogeneous reactions and diffusion coefficients of reactants. For fast reactions (when standard heterogeneous rate constant $k^0 > 10^{-1}[\mathrm{cm \cdot s^{-1}}]$) the peaks separation is close to 57/*n* mV at 25 °C where *n* is a number of electrons involved in an electrode reaction. For slower reactions peak separation is larger.[173]

An important parameter of CV is the scan rate (*v*):

$$v = \frac{\mathrm{d}E}{\mathrm{d}t} \qquad \text{(Eq. 7.1)}$$

The scan rate controls the time scale of the experiment and capacitive current. According to the Randles-Sevcik equation (Equation 7.2), when a substrate is diffusing from the bulk of the electrolyte the peak current i_p [A] is proportional to the square root of scan rate:

$$i_p = (2.69 \cdot 10^5) \cdot n^{3/2} \cdot A \cdot D_R^{1/2} \cdot C_R^* \cdot v^{1/2} \qquad \text{(Eq. 7.2)}$$

where *A* is the surface area [$\mathrm{cm^2}$], *D* is the diffusion coefficient [$\mathrm{cm^2\ s^{-1}}$], C^* is the concentration [$\mathrm{mol\ cm^3}$], *v* is a scan rate [$\mathrm{V\ s^{-1}}$]. In the case of restricted diffusion length or when the substrate is adsorbed on the electrode, i_p is proportional to *v*.[281,173]

http://rcin.org.pl

7.2 Chronoamperometry

Chronoamperometry (CA) is an example of a potential-step technique. The potential step is applied to the working electrode (WE) and current is recorded as a function of time. The potential is applied from a value E_1, at which no Faradaic reaction occurs, to the potential E_2, high enough to cause the diffusion-controlled, *e.g.* oxidation of R species presented in the electrolyte. The resulting current–time dependence reflects the change in the concentration gradient close to the surface of the electrode.

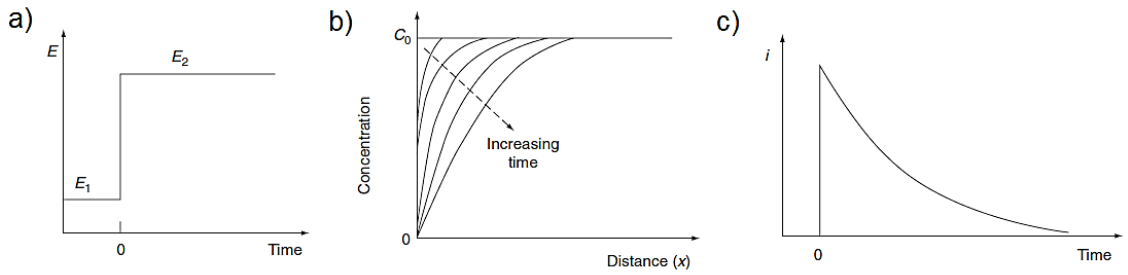

Fig. 7.3. Chronoamperometric experiment: (a) potential–time program; (b) change in concentration profiles as time progresses; (c) the resulting current–time response.[281]

During CA experiment the reactant is eliminated from electrolyte at the electrode surface, thus the slope of the concentration profile during the time of the experiment is decreased (Figure 7.3-b). Consequently the Faradaic current drops with time (Figure 7.3-c) and it is given by the Cottrell equation:

$$i(t) = \frac{n \cdot F \cdot A \cdot D_R^{1/2} \cdot C_R^*}{\pi^{1/2} \cdot t^{1/2}} \qquad \text{(Eq. 7.3)}$$

CA is usually used for measuring the diffusion coefficients of electroactive species or the surface area of the working electrode.[281,173]

7.3 Scanning Electron Microscopy

Scanning electron microscopy (SEM) allows to characterize solid sample surfaces. The electron beam does not produce an image directly but serves to excite the sample. An electron gun (cathode) emits electrons beam with an energy of 0.2-40 keV. In the vacuum column of the microscope electrons are accelerated in the direction of the anode and focused by a set of magnetic lenses so that the final beam diameter reaches a few nm. Focused electron beam hits the selected area of the sample and scans its surface line by line. Obtained signal is collected by the dedicated detector (Figure 7.4).

http://rcin.org.pl

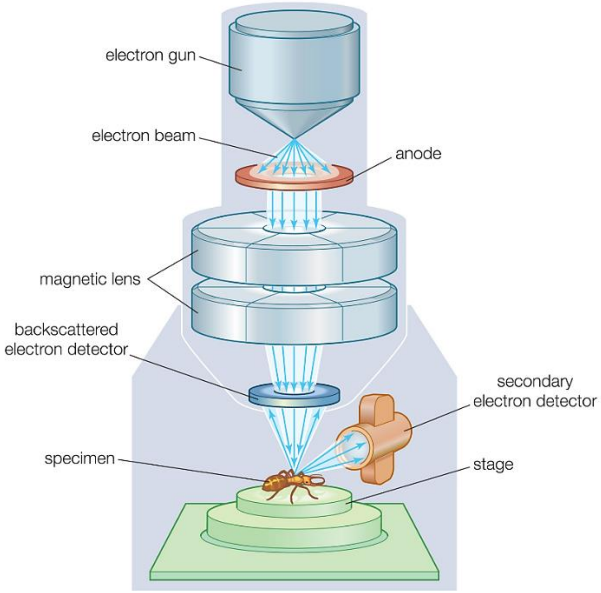

Fig.7.4. Scheme of the Scanning Electron Microscope.[282]

When the energy of electrons emitted from the sample is almost equal to the energy of the beam electrons the emission is called backscattered electrons emission. When lower energy electrons are emitted from the sample surface the emission is called secondary electrons emission. The interaction between electron beam and the sample surface results also in the emission of characteristic X-ray radiation. The use of the energy dispersive X-ray spectroscopy (EDX) provides valuable information about the qualitative and quantitative composition of the sample.[283,284]

7.3.1. Energy Dispersive X - Ray Spectroscopy

SEM equipped with an energy dispersive X-ray spectroscopy (EDX) detector allows the characterization of solid sample surfaces. It provides simultaneously examination of the morphology and the elemental composition of studied object. EDX can be used for qualitative analysis as reveals information about type of elements, as well as for quantitative analysis – provides information about the percentage of the concentration of each element of the sample.

X-rays in SEM measurement are generated by the electron gun – the electron beam hits the sample and transfers part of its energy to sample atoms. It causes the transition of the electrons, as they can be moved to a higher energy shells or they can be knocked out from the atom, what results in a formation of positively charged holes. The electron from higher energy shell can fill the positively charged hole and the difference of the energy, which corresponds to this transition, can be released in the form of an X-ray. Its energy is unique to every element because it depends on its atomic number. X-rays are electromagnetic radiation and consist of photons. To detect them, the energy dispersive X-ray spectroscopy detector is placed under an

http://rcin.org.pl

angle, very close to the sample. It has an ability to measure the energy of the incoming photons. The higher the solid angle between the detector and the sample is, the higher is the X-rays' detection probability. The data generated by EDX analysis consists of spectra with peaks corresponding to different elements presented in the sample. Every element has its characteristic peaks of unique energy. EDX analysis enables also the creation of elemental maps that illustrate the distribution of elements over the sample area.[285]

7.4 Atomic Force Microscopy

Atomic Force Microscopy (AFM) is one of the scanning probe techniques which allows to obtain atomic resolution topography images of conductive and insulating sample surfaces. The advantage of this method is that the sample can be measured in air or in liquid, what is especially important in the case of biological samples.

In the AFM technique, usually the force between the probe and the sample is measured. The probe consists of a sharp tip attached to a flexible cantilever. Using piezoelectric scanner, the tip scans across the analyzed sample surface. The cantilever deflects in response to the force, *e.g.* of van der Waals interactions between the tip and the substrate. This deflection is monitored by a signal from a photodetector illuminated by laser beam reflected from the backside of the cantilever (Figure 7.5). The photodetector's output is an input signal to the feedback-loop maintaining this value constant by changing vertical position of the cantilever holder.

The most common AFM operating modes, which depends on the type of the contact between the probe and the scanned surface, are: contact (Figure 7.5-a) and tapping mode (Figure 7.5-b).

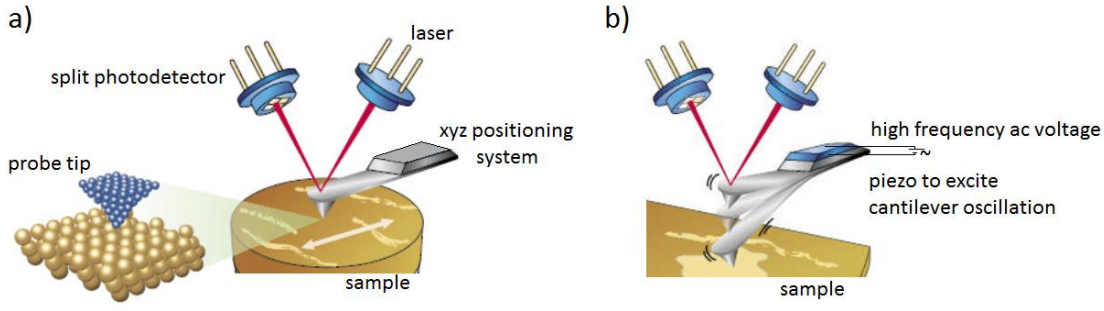

Fig. 7.5. A schematic diagram of a) contact mode and b) tapping mode of the AFM setup.[286]

In the contact mode, a constant cantilever deflection is kept to maintain a constant force exerted on the sample surface. Using this mode, one can obtain a high resolution images but unfortunately there is a possibility of damaging the sample surface or the probe tip. This mode is commonly used for hard surfaces. To study soft surfaces without their damage one can use the

http://rcin.org.pl

tapping mode. In this mode, an additional piezoelectric element is connected to the cantilever and oscillates in the vertical direction. When the tip approaches the surface the amplitude of the oscillation decreases when the tip taps the surface.[281,287] This amplitude is used as an input signal to the feedback loop maintaining its constant value during scanning by changing the vertical position of the cantilever holder.

http://rcin.org.pl

8. Chemicals and materials

Material	Source
4-Hydroxy-3,5-dimethoxybenzaldehyde azine, syringaldazine	Sigma-Aldrich
50 nm grade alumina lapping tape	Buehler
Ag|AgCl|3M NaCl	ALS
Argon N 5.0	Multax
Au wire, 25 and 100 μm diameter	Mint of Poland
Cu wire, 100 μm diameter	Alfa Aesar
Ethanol	POCh
FcMeOH	Sigma
GC plate	Alfa Aesar
H_2SO_4	Chempur
HCl	Chempur
HCOOH	Sigma-Aldrich
ITO coated glass (sheet resistance 8-12 Ω $sq.^{-1}$)	Delta Technologies
KCl	Sigma-Aldrich
Na_2HPO_4	POCh
NaH_2PO_4	Sigma
$NaNO_3$	Chempur
NaOH	Fluka
PBS	Sigma-Aldrich
P2000 grit silicon carbide sand paper	
petroleum gas (*ca.* 60 vol % butane, *ca.* 40 vol % propane)	
Pt wire, 25 μm diameter	Mint of Poland
quartz capillary (o.d. 1.0 mm, i.d. 0.7 mm)	Sutter Instruments

All water solution were prepared with deionized water purified by Elix system (Millipore).

http://rcin.org.pl

9. Instrumentation

Laser puller

P-2000, Sutter Instruments.

Micropipette puller

PC-10 micropipette puller, Narishige.

Potentiostat

Axon Multiclamp 700B patch-clamp amplifier with the automatic cell capacitance compensation controlled by the DigiData 1440 acquisition system, (Molecular Devices).

Scanning electrochemical microscopes

- CHI900B, (CH Instruments).
- Home built:
    - VA-10X patch-clamp amplifier, npi (Electronic Instruments),
    - CHI900B positioning system, (CH Instruments).

In this setup PCI – DAS1602/16 analog-digital (AD) and digital-analog (DA) and PCI-DDA04 DA cards (Measurement Computing) were used.

- Home built:
    - Ivium CompactStat potentiostat (Ivium Technologies),
    - mechOnics XYZ positioning system (mechOnics AG).

Motors positioning and data acquisition in all home-built SECMs were controlled by the SECMx software.[288] Data analysis was performed with the in house developed package MIRA.[289]

Optical microscopes

- Specwell 10 x 30,
- Inverted optical microscope, MA200, (Nikon),
- Nikon Eclipse LV150.

Scanning electron microscope

FEI Nova NanoSEM 450 equipped with an EDAX energy dispersive X-ray spectroscopy (EDX) detector and GENESIS software.

http://rcin.org.pl

Atomic force microscope

MultiMode AFM instrument using a Nanoscope V controller (Bruker).

pH-meter

Glass-electrode pH meter, CG 837, (Schott).

Other

- Mass flow controller (SmartTrak 2, Sierra Instruments).
- Micromanipulator (PT3/M, Thorlabs).
- Butane-air gas torch (Miniset 1450°C, Rothenberger Industrial).
- All electrochemical experiments were perform in a home-built Faraday cages.

http://rcin.org.pl

10. Local deposition of nanostructures by electrorefining of polycrystalline metals

10.1. Introduction

In this chapter the process of controlled and local electrodeposition will be described. Micropatterns of bare (ligand-free), metallic nanostructures (NS) were obtained by localized electrorefining of polycrystalline metal wires from the microelectrodes, in a controlled manner, using scanning electrochemical microscopy (SECM).

Copper and gold nanostructures (CuNS and AuNS) were selected as a model materials to study their electrocatalytic properties. Because of the limited availability of noble metal catalysts, such as platinum and palladium, substitution with abundant non-platinum metals, *e.g.* gold and copper is highly desirable. Controlled and reproducible synthesis of stable non-platinum metallic NS with accessible active sites is considerably challenging. In described method the precursor is just a raw, polycrystalline metal, which is the most economically viable source.

10.2 Preparation of metallic microelectrodes

Microelectrodes were fabricated using PC-10 micropipette puller (Narishige). A 100 μm diameter wires of Au or Cu were inserted into the borosilicate glass capillary (o.d. 2.1 mm, i.d. 0.43 mm) and then mounted into the micropipette puller. Capillary was pre-pulled for 1 mm length in its middle to facilitate melting and to obtain a smaller RG parameter. Then the heat from the coil melted the glass, thus the wire was sealed tightly inside the capillary. This process requires vacuum conditions to avoid gas bubbles created in the melted glass. After melting, capillary was broken in the necking, so the glass surrounding the conductive disk was beveled, results in small RG value. The end of the microelectrode was then polished with silicon carbide sand paper to obtain a flat surface without any scratches or additional glass sticking out from the surface (Figure 10.1). This makes the tip easier to place so that it can be moved close to the sample (substrate) without the insulator touching the sample surface.[173]

http://rcin.org.pl

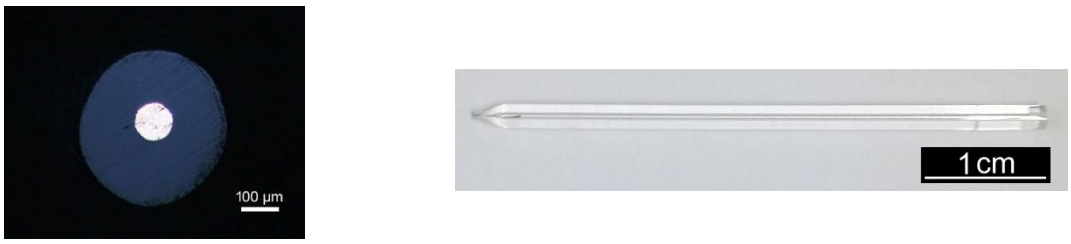

Fig.10.1. Micrographs of the Au microelectrode. Left image shows front view, right image – side view.

10.3 Cell assembly

All electrochemical experiments were performed using homemade scanning electrochemical microscope controlled and operated under SECMx software. SECM setup consisted of Ivium CompactStat bipotentiostat and mechOnics *XYZ* positioning system. Ag|AgCl|3M NaCl and a Pt wire served respectively as a reference and counter electrodes. If not otherwise stated, all potentials in this chapter are provided versus this type of reference electrode. Microelectrode of appropriate metal was used as a first working electrode (tip) and indium tin oxide coated glass (ITO) or glassy carbon (GC) plate was applied as a second working electrode (substrate). The ITO can be polarized only to *ca.* -0.75V.[290] That is why also a GC, which can be polarized to more negative potentials, was used as the substrate electrode.

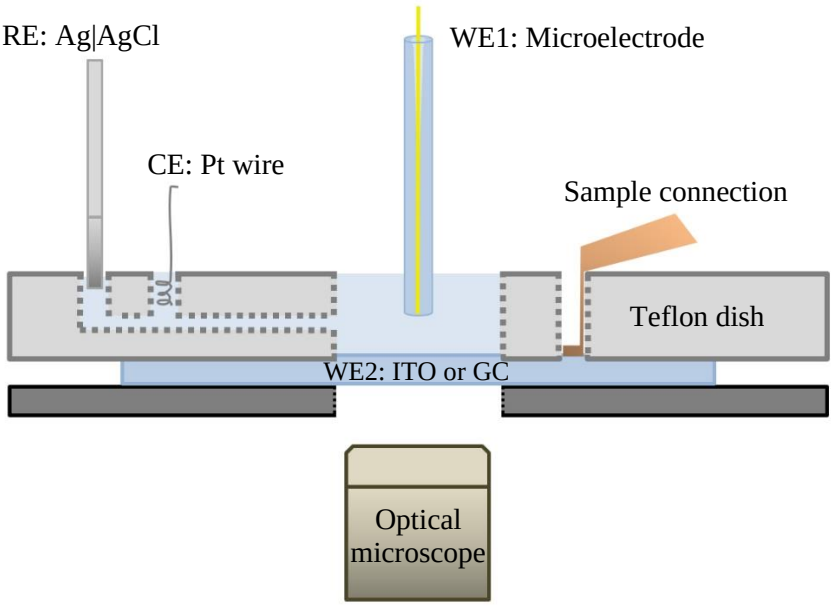

Fig. 10.2. Scheme of the electrochemical cell (not to scale).

The electrochemical cell (Figure 10.2) was filled with an electrolyte which enables the electrodissolution of the microelectrode's wire. When the transparent ITO was used as the sample the electrochemical cell was mounted on an inverted optical microscope (Nikon MA200) to see the progress of electrodeposition and to estimate the distance between two working electrodes.[291]

http://rcin.org.pl

In the case of nontransparent GC, the distance between the electrodes was estimated using approaching with ORR driven at the tip.

10.4 Electrorefining of Cu

Electrodissolution of Cu microelectrode (CuUME) was carried out in three different aqueous solutions: 0.5 M H_2SO_4, 0.5 M H_2SO_4 + 0.1 M KCl, and 1 M KCl + 10 mM HCl. In 0.5 M H_2SO_4 the dissolution of Cu wire was driven at 0.15 V. In the electrolytes containing chlorides at -0.06 V.

A 100 µm diameter CuUME was positioned 30 µm above the ITO or GC support. Before the electrorefining, the negative potential equal -0.4 V was applied to CuUME to prevent the spontaneous dissolution of Cu in acidic electrolyte. Cathodically polarized ITO (or GC) substrate (~3.14 cm^2) exhibits residual background current of few tens of µA (depending on applied potential) due to sluggish reduction of oxygen. Since there is no redox mediator in the electrolyte, the amount of deposited metal can be determined from the measured Faradaic charge, because it's not affected by the cycling between the microelectrode and the substrate during deposition. The Faradaic current recorded at the CuUME upon its anodic polarization corresponds to electrodissolution of Cu (Figure 10.3). Once electrodissolution of CuUME starts, cathodic current at ITO support starts to grow accordingly yielding, under the quiescent condition (without Cu-tip movement), nearly 100 % of coulombic collection efficiency.

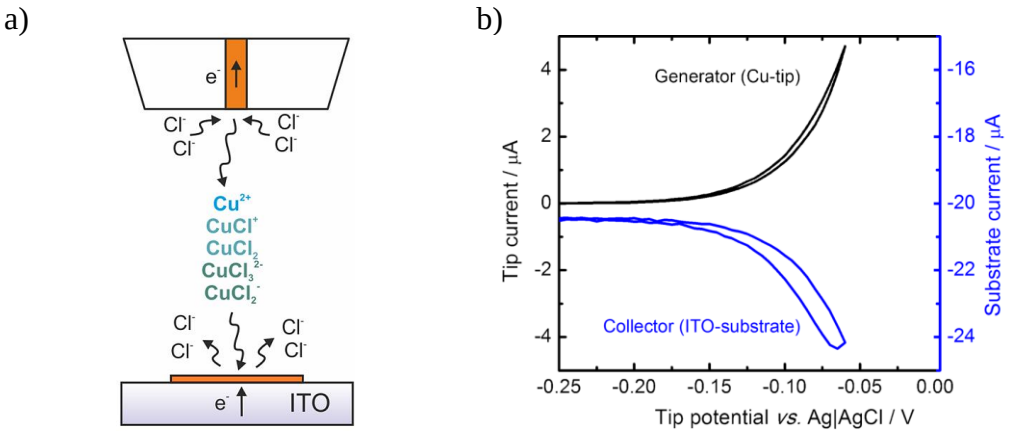

Fig. 10.3. a) General scheme of localized electrorefining of Cu with SECM (not to scale). b) Cyclic voltammogram of a 100 µm diameter CuUME (tip, black line) positioned 30 µm above the ITO electrode (substrate) polarized at -0.5 V. The blue line is the substrate current vs. tip potential. Electrolyte: 1 M KCl + 10 mM HCl; scan rate: 50 mV s^{-1}.

http://rcin.org.pl

Figure 10.4 shows processed data from figure 10.3. Substrate current (cathodic) modulus is corrected by subtraction of constant background to get zero values for potential range, where no electrodissolution of copper occurs.

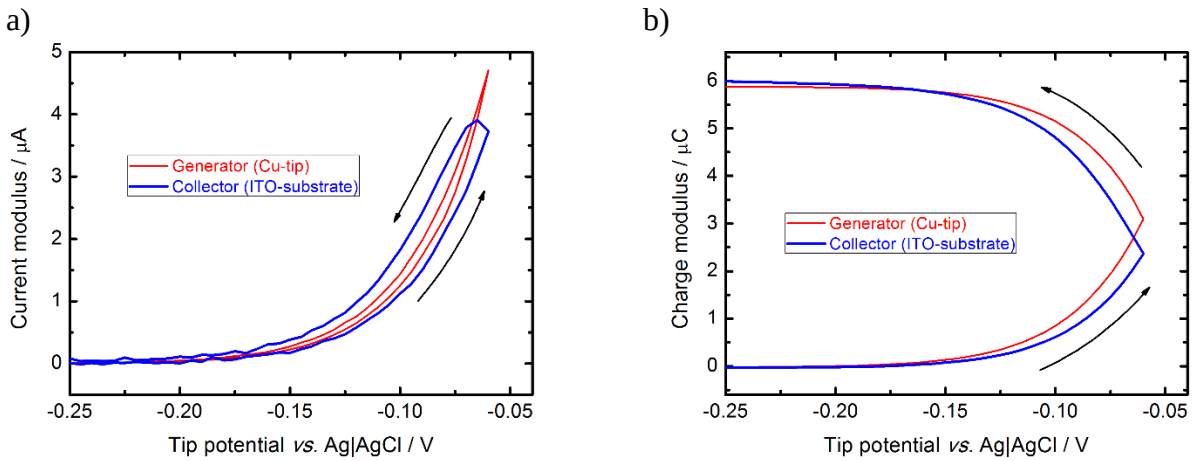

Fig.10.4. a) Cyclic voltammogram of a 100 µm diameter CuUME (tip, red line) positioned 30 µm above the ITO electrode (substrate) polarized at -0.5 V. The blue line is the substrate current corrected by subtraction of constant background. Electrolyte: 1 M KCl + 10 mM HCl; scan rate: 50 mV s^{-1}. b) Cyclic voltammograms from the a) integrated over time to get charge-potential plots.

The moduli of charges are very similar for tip and for the substrate, although the tip current reaches slightly higher values at -0.06 V. This is caused by the diffusion time of generated copper ions from the CuUME to the ITO (or GC). Slightly higher cathodic charge recorded at the sample is most probably caused by electroreduction of oxygen on freshly prepared CuNS.

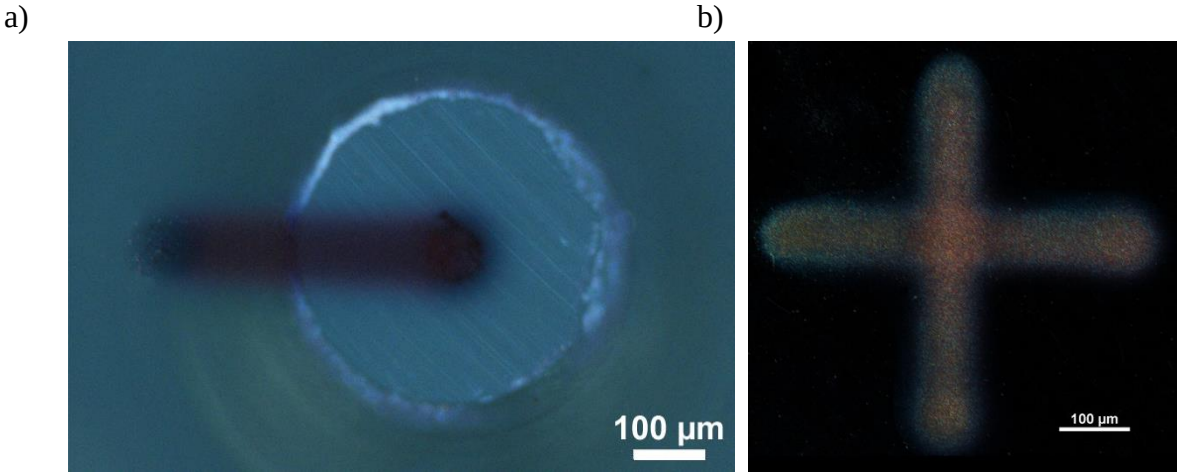

Fig. 10.5. a) Optical micrograph presenting local electrodeposition of CuNS on ITO. b) Optical microscope image presenting micropatterns of CuNS on GC.

It is also possible to “print” micropatterns or continuous layers composed of metallic NS using SECM. The source microelectrode can be mounted into the three dimensional positioning

http://rcin.org.pl

system that allows to move it *X*, *Y* and *Z* directions. The potential of the UME can be switched during the movement to the value that electrodissolution of the wire occurs and then switched back to the values when no electrodissolution occurs (Figure 10.5).

For the SECM analysis the electrolyte in the electrochemical cell was exchanged gradually under continuous cathodic polarization of the sample. Special attention was kept to prevent the electrodes (sample, reference and counter) from losing their contact with the electrolyte. For SEM and AFM analysis, before the removal of CuNS samples from the cell, an acidic electrolyte was exchanged gradually to 0.1 M phosphate buffer (pH = 7.2) under continuous cathodic polarization. The samples were rinsed with deionized water and dried with argon.

As a result of the process of local electrodeposition, micrometer wide stripes composed of CuNS were obtained (Figure 10.6).

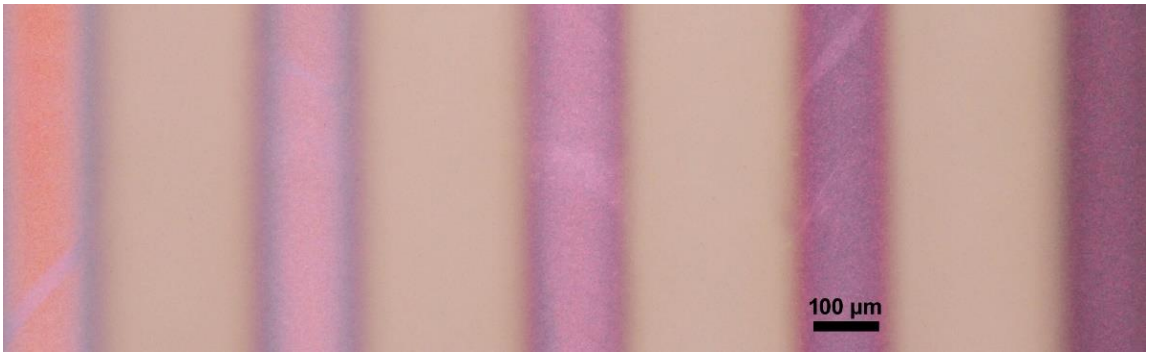

Fig. 10.6. Optical micrograph presenting electrodeposited stripes of CuNS, obtained under the following conditions; substrate electrode: ITO; electrolyte: 0.5 M H_2SO_4; CuUME translation rate: 50 µm s^{-1}, substrate potentials marked on the picture.

The surface morphology and chemical composition of deposited CuNS were observed/examined with the use of a SEM equipped with an EDAX energy dispersive X-ray spectroscopy (EDX) detector and GENESIS software. EDX analysis was performed at a primary beam energy of 20 kV (Figure 10.7).

http://rcin.org.pl

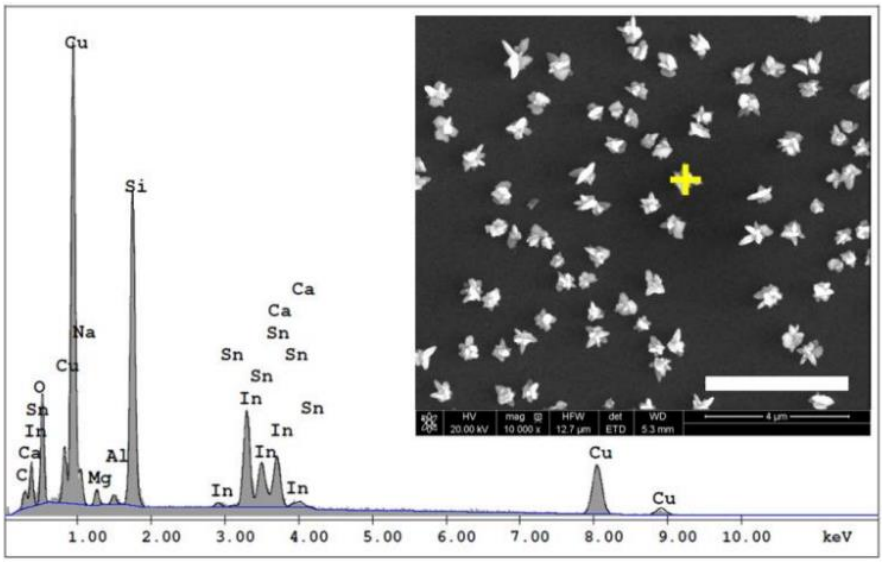

Fig. 10.7. EDX spectrum of CuNS deposited on the ITO support obtained under the following conditions; Electrolyte: 1 M KCl + 10 mM HCl; Electrodeposition potential: -0.5 V; CuUME translation rate: 100 µm s^{-1}. The inset provides the SEM image with marked point of EDX analysis, scale bar: 4 µm.

Optical micrograph presented in Figure 10.6 shows that there is a difference in the reflected light between each microstrip of CuNS obtained on the ITO from 0.5 M H_2SO_4. SEM micrographs show that CuNS electrodeposited in these conditions are always rounded, without distinct edges or sharp corners, regardless of potential value applied to the substrate. However, the potential applied to the substrate electrode during the process of electrodeposition influences the size of CuNS: the lower the potential is applied, the smaller CuNS are obtained (Figure 10.8) what influences the changes in reflected light.

a) b)

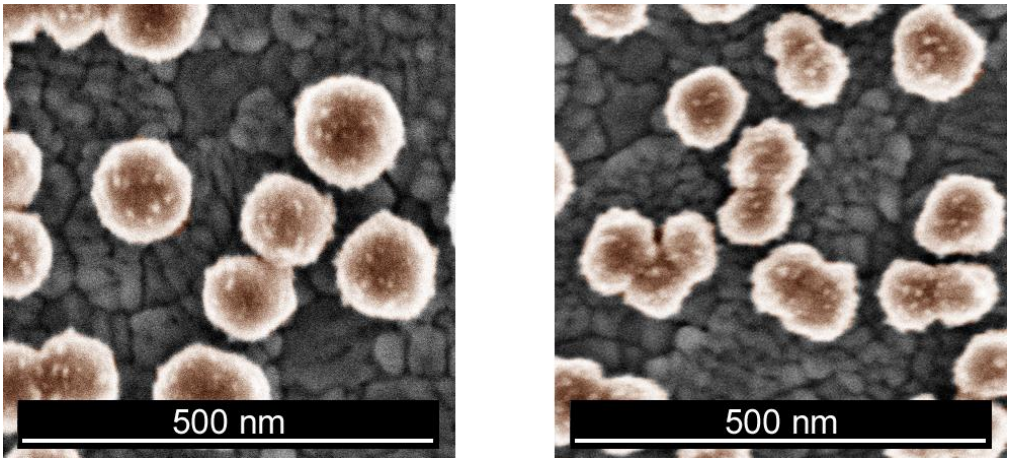

Fig. 10.8. CuNS obtained under the following conditions; substrate electrode: ITO; electrolyte: 0.5 M H_2SO_4; CuUME translation rate: 50 µm s^{-1}, substrate potentials: a) -0.3 V, b) -0.5 V.

http://rcin.org.pl

The size of obtained CuNS depends also on the translation rate of electrodissolving CuUME. Faster translation rate results in smaller NS (Figure 10.9), because the time of exposure of certain area of ITO support to Cu^{2+} flux is shorter.

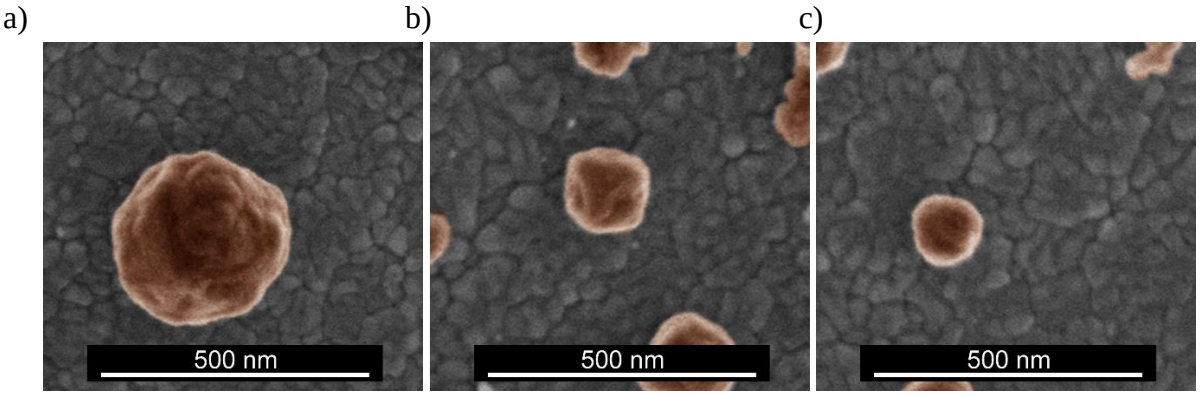

Fig. 10.9. CuNS obtained under the following conditions; substrate electrode: ITO; electrolyte: 0.5 M H_2SO_4; substrate potential: -0.2 V; CuUME translation rates: a) 50 µm s^{-1}, b) 100 µm s^{-1}, c) 200 µm s^{-1}.

Figure 10.10 shows that the mechanism of electrodeposition of CuNS is significantly affected by hydrodynamic conditions caused by electrode motion. The morphology of CuNS obtained under quiescent conditions (without translating of CuUME) differs from that obtained with translating microelectrode.

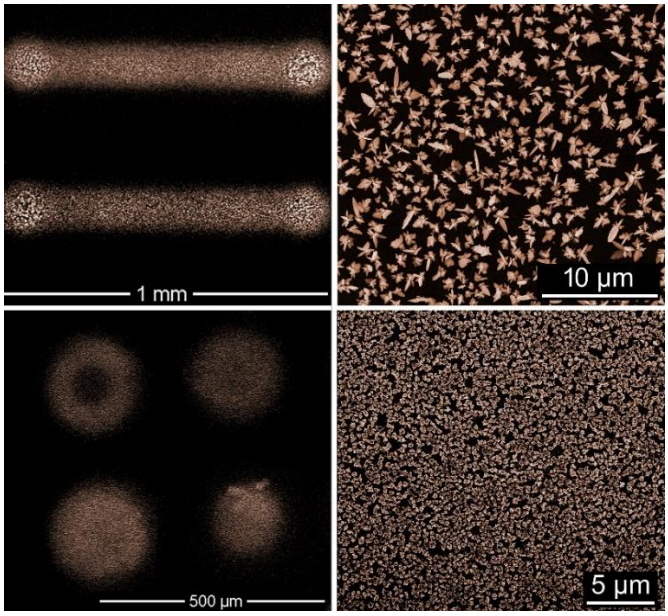

Fig. 10.10. CuNS obtained under the following conditions; substrate electrode: ITO; electrolyte: 1 M KCl + 10 mM HCl; substrate potential: -0.4 V. Upper images show CuNS electrodeposited under dynamic conditions, CuUME translation rate: 50 µm s^{-1}; lower images - under stationary conditions.

Another factor that influences the morphology of CuNS is the composition of the electrolyte. Addition of KCl to H_2SO_4 solution, as well as complete substitution of H_2SO_4 by solution containing only Cl^- anions (1 M KCl acidified with 10 mM HCl) prevents hydrolysis of

http://rcin.org.pl

Cu^{2+}, facilitates electrodissolution of Cu and alters the shape of the CuNS substantially (Figure 10.11).

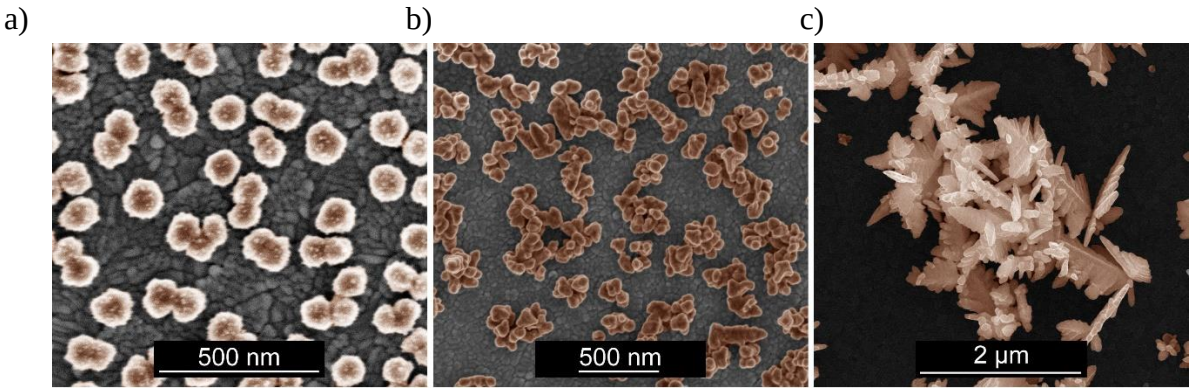

Fig. 10.11. CuNS obtained under the following conditions; substrate electrode: ITO; substrate potential: -0.6 V; microelectrode translation rate: 50 µm s^{-1}; electrolytes: a) 0.5 M H_2SO_4, b) 0.5 M H_2SO_4 + 0.1 M KCl, c) 1 M KCl + 10 mM HCl.

Cl^- at 1 M concentration causes formation of stable $CuCl^+$ and $CuCl_2$ complexes.[292,293] Moreover, Cu(I) complexes ($CuCl_3^{2-}$, $CuCl_2^-$) are also stable under these experimental conditions, thus electrorefining of Cu can occur with one electron per Cu atom stoichiometry. CuNS obtained with acidified KCl electrolyte are larger and exhibit number of sharp edges and corners (Figure 10.11). This is caused by slower kinetics of nucleation and growth of Cu deposits from chloride-complexed copper ions. Negatively charged complexes are repelled from the electrical double layer at the ITO upon its cathodic polarization. Inhibited nucleation on the substrate surface causes larger separation of formed nuclei. Further growth of NS causes depletion of copper ions around them preventing nucleation around. Kinetics of outer sphere electroreduction of stable complexes depends on the type of crystallographic facet, therefore electrodeposition on certain surface facets occurs faster than on others. This causes symmetry breaking and growth of prickly shape CuNS. Preferential adsorption of Cl^- on certain crystallographic facets can also play a role in formation of peaky NS.

The type of the substrate electrode also influences the morphology of CuNS. Electrodeposition of Cu on GC support from solution containing copper-chloride complexes forms CuNS with plenty of edges and corners (Figure 10.12-a), however when more negative potential is applied to GC during the process, smaller CuNS starts to aggregate. Although similar amount of Cu is deposited, its larger surface is exposed with possibly large number of low coordination Cu atoms at edges, corners and defects (Figure 10.12-b,c).

http://rcin.org.pl

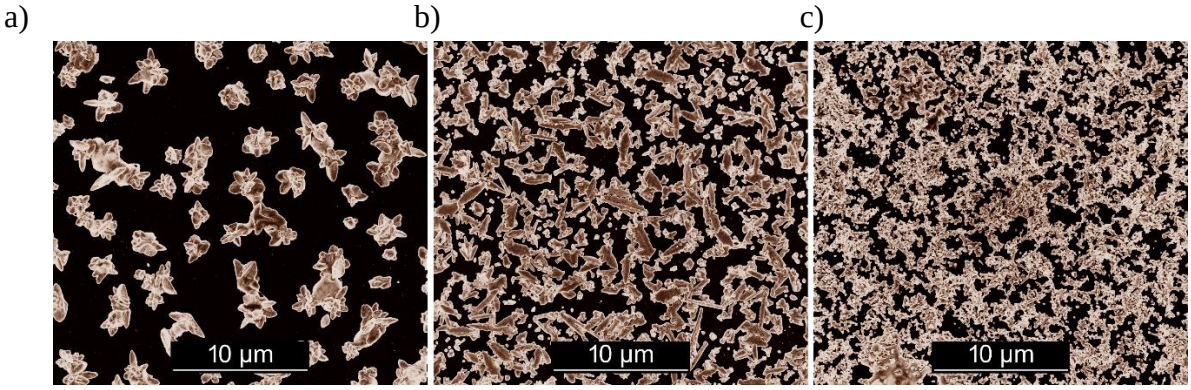

Fig. 10.12. CuNS obtained under the following conditions; substrate electrode: GC; electrolyte: 1 M KCl + 10 mM HCl; CuUME translation rate: 50 µm s^{-1}; substrate potentials: a) -0.3V, b) -0.5 V, c) -0.9V.

Amount of deposited copper estimated by analysis of SEM images is in good accordance with Faradaic charge passed for 2 electron reaction in H_2SO_4 solution and 1 electron process in the presence of chlorides. Application of chloride electrolyte decreases electricity consumption required for electrorefining of Cu. This is especially important for large scale industrial processes.

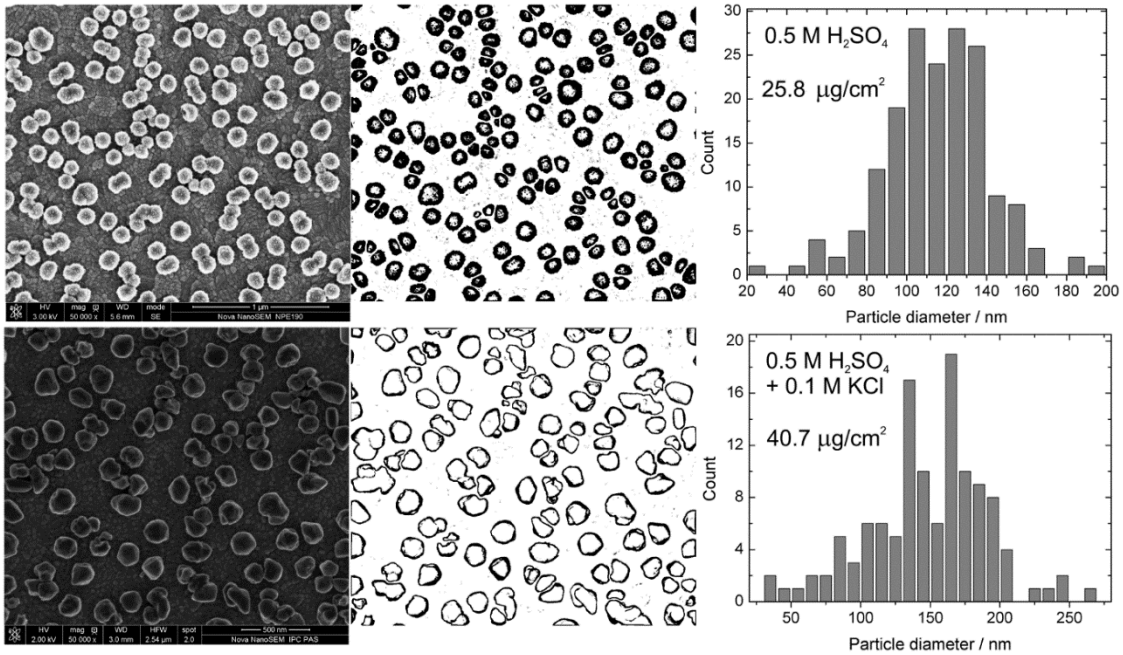

Fig. 10.13. Nanostructure size estimation by microscopic analysis. Raw SEM images (left column) calibrated to real distance was converted to particles mask (center column). CuNS size distribution histograms (right column) estimated as hypothetical spheres with the same projected area. CuNS were obtained by electrorefining of a 100 µm diameter CuUME translating horizontally 30 µm above the ITO electrode polarized at -0.4 V. Microelectrode translation rate: 50 µm s^{-1}. Electrolytes: 0.5 M H_2SO_4 (upper row), 0.5 M H_2SO_4 + 0.1 M KCl (bottom row).

To estimate size distribution of electrodeposited CuNS selected gray-scale SEM images were converted to 1-bit monochrome ones with a threshold adjusted to get black projections of CuNS on a white background. Some particles were connected together into bigger aggregates. In order to minimize the particles size estimation errors, their projected areas were separated by intuitive manual cutting in the graphics software. The separated and manually-separated NS were

http://rcin.org.pl

counted and the projected area of each spot was calculated by pixel area integration (Figure 10.13). The projected areas of each particle were evaluated using the ImageJ free software. The 'diameters' ($d = (4A/\pi)^{1/2}$) and volumes (Equation 10.1) of CuNS were estimated under the assumption of spherical shape:

$$V = \frac{4A^{3/2}}{3\pi^{1/2}} \qquad \text{(Eq. 10.1)}$$

where A is the projected area of the nanostructure.

Surface concentration of electrodeposited metal is calculated as a sum of volumes of all the particles visible in the SEM image divided by the image area (5.56 μm^2) and multiplied by the volumetric mass density of Cu (8.95 g/cm^3). This method of volume estimation is accurate exclusively for ideal spheres.

Figure 10.14 presents a SEM side view image of CuNS obtained in 1 M KCl + 10 mM HCl on the ITO support. It reveals that they are grown perpendicularly to the ITO surface, because of precursor concentration gradient normal to the substrate surface upon electrorefining.

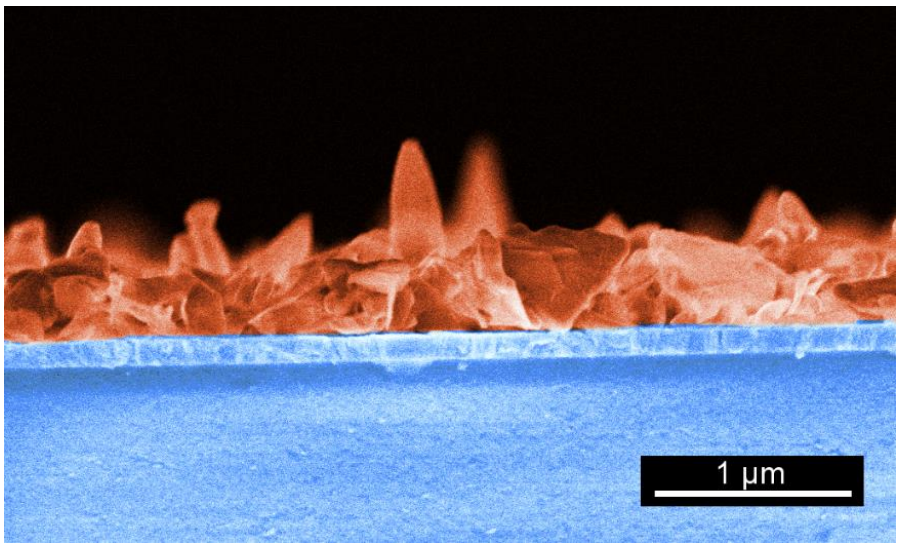

Fig. 10.14. SEM micrograph of CuNS obtained by localized electrorefining under the following conditions; Supporting material: ITO; Electrolyte: 1 M KCl + 10 mM HCl; Electrodeposition potential: -0.5 V; Cu source: 100 µm diameter Cu disk microelectrode; Source translation velocity: 50 µm s^{-1}. The sample was broken manually to allow side view SEM imaging.

Figure 10.15 shows an AFM image (after tip deconvolution) of CuNS obtained in 0.5 M H_2SO_4 on the ITO support.

http://rcin.org.pl

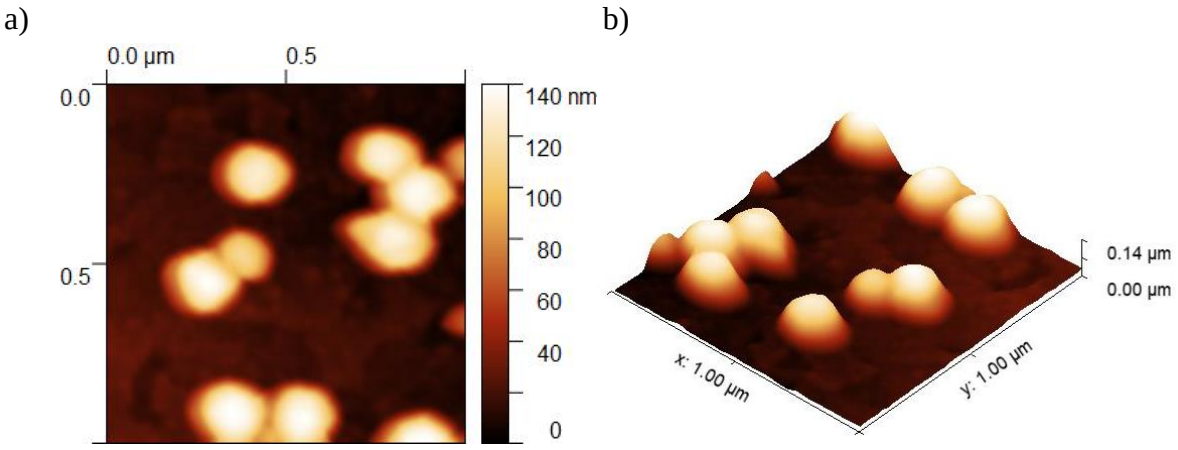

Fig. 10.15. a) AFM image and b) its 3D projection of CuNS obtained by localized electrorefining under the following conditions; Supporting material: ITO; Electrolyte: 0.5 M H_2SO_4; Electrodeposition potential: -0.5 V; Cu source: 100 µm diameter CuUME; Source translation rate: 50 µm s^{-1}.

Figure 10.16 reveals that CuNS obtained in these conditions are *c.a.* 130 nm high.

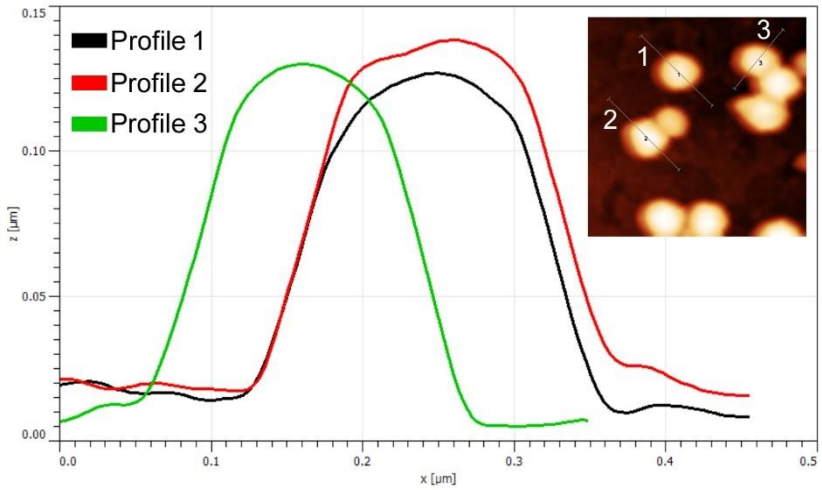

Fig. 10.16. AFM profile picture of CuNS obtained in the same conditions as in figure 10.15. Inset shows which particles were taken into account.

Application of Equation 10.1 to assess the volume of CuNS on the basis of their projected area should therefore result in values close to actual volumes. The theoretical surface concentration of metal in deposited Cu microstripes (assuming that the majority of Cu is deposited beneath the CuUME), can be calculated using the Faraday laws of electrolysis and simple geometry (Equation 10.2):

$$\Gamma = \frac{i_T \theta}{zF\phi_T v} \qquad \text{(Eq. 10.2)}$$

where Γ is the surface concentration (mol cm^{-2}), i_T is the tip current (A), θ is the collection efficiency (Figure 10.4-a, $|q_S/q_T| = 0.8$ for v = 50 µm s^{-1}), z is the number of electrons transferred per atom (or ion), F is the Faraday constant (96485 C mol^{-1}), Φ_T is the tip diameter (cm), and v is the tip translation velocity (cm s^{-1}).

http://rcin.org.pl

Table 10.1 summarizes the parameters of deposited CuNS. The surface concentration of Cu obtained with electrolyte without chloride anions, estimated by analysis of SEM images (25.8 μg cm^{-2}) is in good accordance with the value calculated using Equation 10.2 and two-electron stoichiometry (24 μg cm^{-2}). Analysis of SEM image of CuNS deposited with electrolyte containing 0.1 M KCl results in the amount of Cu (40.7 μg cm^{-2}), which is closer to the theoretic value calculated for one-electron stoichiometry (47.8 μg cm^{-2}). This shows that addition of chloride ions at concentration as low as 0.1 M stabilizes Cu(I) complexes ($CuCl_3^{2-}$ and $CuCl_2^-$) facilitating 1-electron electrorefining.

Table 10.1. Geometric parameters of CuNS obtained by analysis of SEM images and Faradaic charge.

Electrolyte	Particle diameter (nm)	Γ_{SEM} (μg cm^{-2})	i_T (μA)	z	$\Gamma_{Faradaic}$ (μg cm^{-2})
0.5 M H_2SO_4	115 ±26	25.8	4.55	2	24
0.5 M H_2SO_4 + 0.1 M KCl	148 ±42	40.7	4.54	1	47.8

10.5 Electrorefining of Au

Electrodissolution of 100 μm diameter Au microelectrode (AuUME) was carried out in a similar manner as electrodissolution of Cu. In this case, the electrolyte was 3 M KCl and the potential applied to AuUME: +0.95 V. AuUME was positioned 30 μm above the substrate electrode. The distance was estimated using the same methods as in the case of electrodeposition of CuNS.

At moderate potentials, when no other processes (*e.g.* ORR or chlorine evolution) occur, the Faradaic currents recorded at the source and the support are related to gold electrodissolution rate,

$$Au^0 + 4Cl^- - 3e^- \rightarrow AuCl^{4-} \quad \text{(Eq. 10.3)}$$

and electrodeposition,

$$AuCl^{4-} + 3e^- \rightarrow Au^0 + 4Cl^- \quad \text{(Eq. 10.4)}$$

respectively (Figure 10.17-a).

During the electrodeposition of the micrometer sized stripes of AuNS the electrode was moving parallel to the substrate surface and the observed current was also stable

http://rcin.org.pl

(Figure 10.17-b). The sample treatment after the deposition was carried out in the same manner as it was in the case of Cu electrodeposition.

a) b)

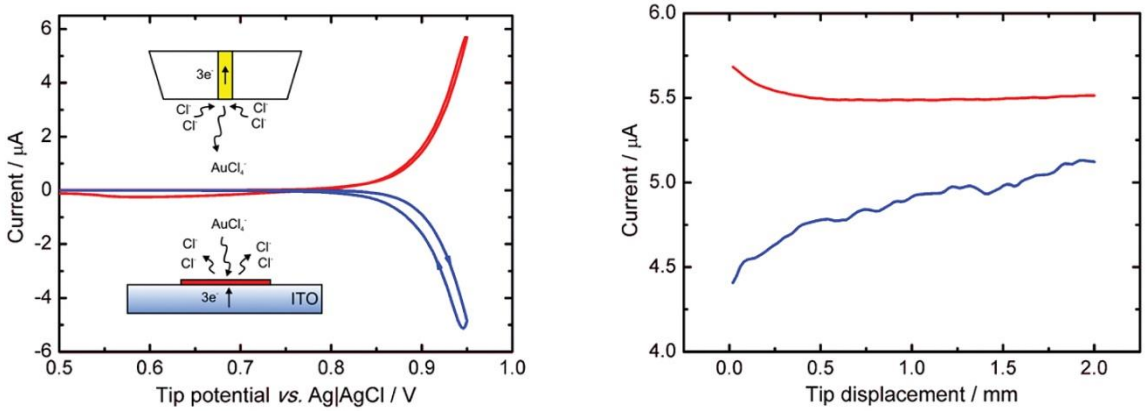

Fig. 10.17. a) Cyclic voltammogram of a 100 µm diameter AuUME (tip, red line) positioned 20 µm above the ITO electrode (substrate) polarized at +0.5 V. The blue line is the substrate current vs. tip potential. Electrolyte: 3 M KCl; scan rate: 10 mV s^{-1}. The inset in a) is a scheme of occurring processes (not to scale) b) Tip current (anodic, red line) and inverse of the substrate current (cathodic, blue line) recorded during the lateral tip movement 20 µm above the ITO substrate. Translation speed: 100 µm s^{-1}; tip potential: +0.95 V; substrate potential: −0.3 V.

Electrodissolution of the AuUME (as well as CuUME) causes progressive recession of the metal surface. However, the flux of $AuCl_4^-$ ions remains unchanged (Figure 10.18).

a) b)

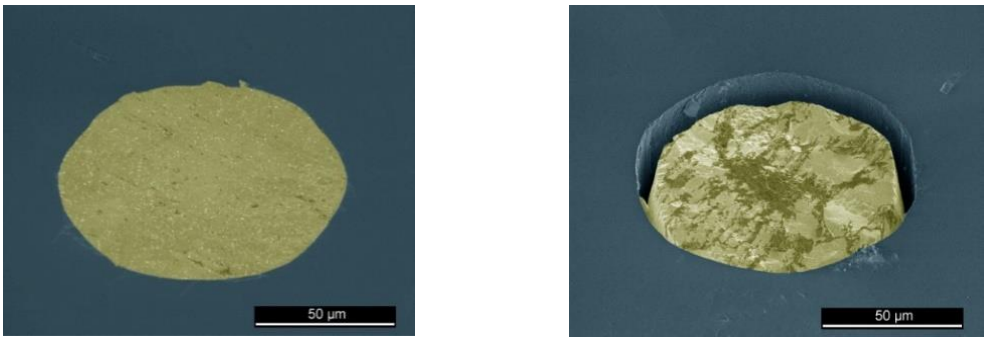

Fig. 10.18. SEM images of Au microelectrode before a) and after b) electrochemical etching at 0.95 V for 5 min. Electrolyte: 3 M KCl. Samples are tilted by 45°.

During 20 minutes of the experiment that produces recessed microelectrode the tip current didn't change. This is probably caused by self-compensation of two effects. The first one is diffusion length extension for electrogenerated $AuCl_4^-$ ions between recessing metallic surface and the negatively polarized ITO substrate, where these ions are consumed by electrodeposition at diffusion limiting rate (surface concentration is zero). The second effect is increasing surface concentration of $AuCl_4^-$ close to source electrode. This helps keeping its concentration gradient unchanged despite growing diffusion length. Due to kinetic limitation of Au electrodissolution

http://rcin.org.pl

(Figure 10.17-a), increasing surface concentration of the dissolution product results in decreasing current density when the electrode is polarized at constant potential. A constant current can be maintained by growing surface area of dissolving electrode. In fact, we observed faster dissolution of Au near the circumference of the disk microelectrode resulting in formation of a gap between the metal and the glass sheath (Figure 10.18-b).[291]

As a result of electrodeposition micro-bands of AuNS were obtained, using a 100 μm diameter AuUME moving 20 μm above the support. They are about the same width as the source diameter. Their edges are slightly blurred due to diffusion of the precursor ions generated at the microelectrode (Figure 10.19). This effect is more visible for longer tip-to-sample distances. However, morphologies of the deposited AuNS within the centers of stripes are uniform.

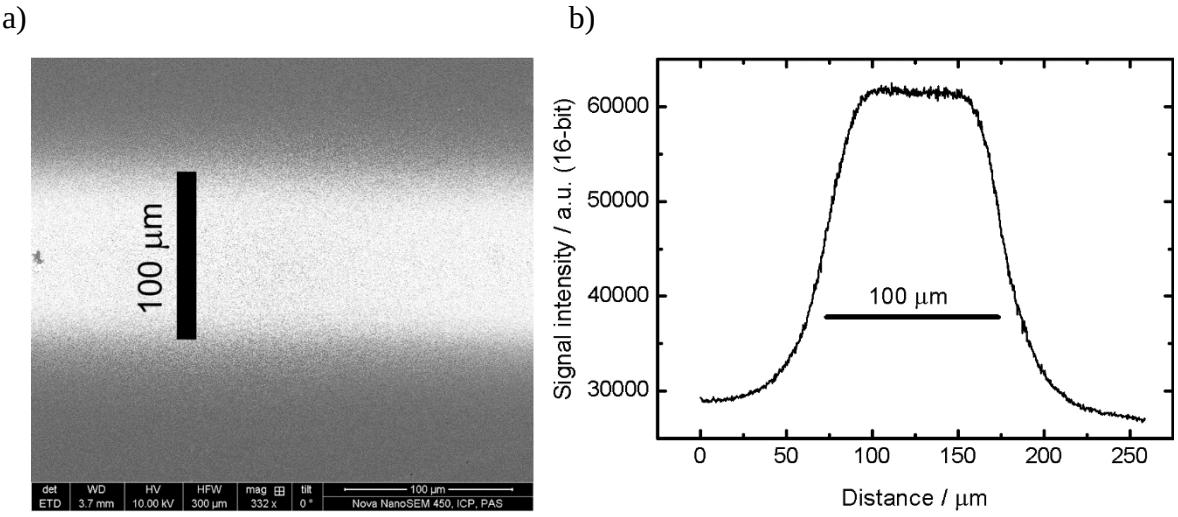

Fig. 10.19. a) SEM image of a micro-band of AuNS obtained by localized electrorefining using a 100 um diameter AuUME moving 20 μm above the ITO support. Translation rate: 50 μm s^{-1}, Substrate potential: -0.6 V. b) The chart represents averaged signal intensity of vertical lines of SEM image.

The majority of the metal is deposited just beneath the source when the tip-to-sample distance is much shorter than the tip diameter. Assuming that the metal is deposited mainly beneath the tip source, one can calculate the surface concentration of metal in deposited micro-bands using Equation 10.2.

Collection efficiencies and surface concentrations of gold in electrorefined microbands are listed in Table 10.2.

http://rcin.org.pl

Table 10.2. Collection efficiencies and surface concentrations of Au in microbands obtained by localized electrorefining from a 100 µm diameter AuUME translated 20 µm above the cathodically polarized ITO substrate. Tip potential: +0.95 V (corresponding current: 5.5 µA). Electrolyte: 3 M NaCl.

v (µm s^{-1})	Θ	Γ_{Au} (nmol cm^{-2})	Γ_{Au} (µg cm^{-2})
50	0.799 (±0.076)	304 (±29)	59.8 (±5.7)
100	0.712 (±0.037)	135 (±7)	26.6 (±1.4)
200	0.688 (±0.068)	65 (±6.5)	12.9 (±1.3)

SEM micrographs show that also in the case of AuNS, the potential applied to the substrate electrode influences the size and shape of obtained structures. AuNS obtained at the ITO substrate from 3 M KCl solution at moderately cathodic potentials are more separated than these obtained when more negative potential was applied (Figure 10.20).

a) b)

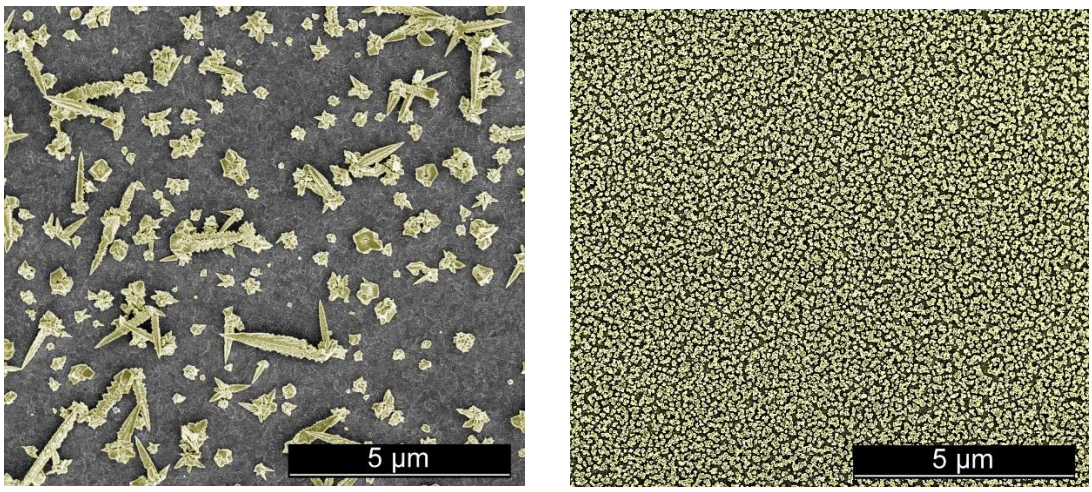

Fig. 10.20. AuNS obtained under the following conditions: electrolyte: 3 M KCl; substrate electrode: ITO; AuUME translation rate: 50 µm s^{-1}; ITO potentials: a) -0.3 V, b)-0.8 V.

AuNS obtained at moderate overpotentials are larger and possess number of sharp edges and corners. The same effect is visible when the substrate electrode is changed to GC (Figure 10.21). However the shape of obtained structures is different. Polarization of the substrate at higher potentials leads to lower number of nucleation sites, thus lower number of bigger particles.

http://rcin.org.pl

a) b)

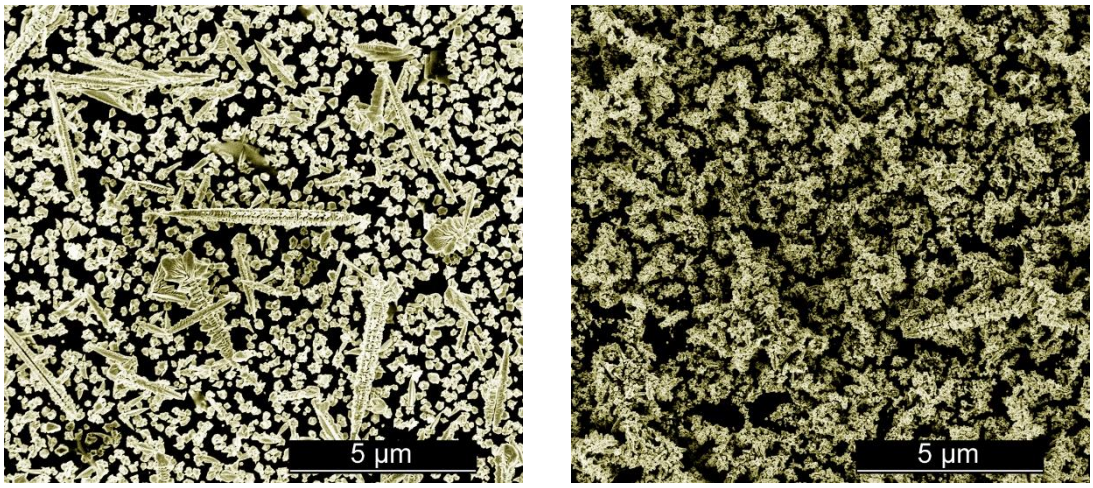

Fig. 10.21. AuNS obtained under the following conditions: electrolyte: 3 M KCl; substrate electrode: GC; AuUME translation rate: 50 µm s^{-1}; GC potentials: a) -0.3 V, b)-0.8 V.

10.6 Electrorefining of bi-metallic Cu and AuNS

It is also possible to obtain bimetallic NS by electrorefining of polycrystalline metals. First, the electrodeposition of AuNS was performed in a manner described in the chapter 10.5. Then, the electrolyte and the source microelectrode were exchanged to CuUME and the process of CuNS deposition was performed (Chapter 10.4). As a result, a pattern with crossed Au-Cu microstripes was obtained (Figure 10.22).

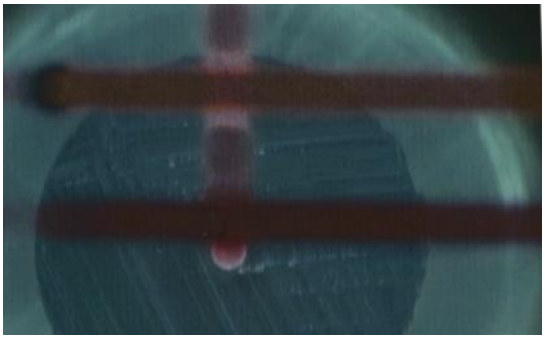

Fig. 10.22. Optical micrograph presenting local electrodeposition of CuNS on predeposited AuNS on the ITO substrate.

Figure 10.23-a shows SEM images of AuNS obtained on the ITO support in 3 M KCl. As it was described in section 10.5 these parameters of electrodeposition lead to separated deposits with lower number of bigger particles. Figure 10.23-b shows CuNS obtained on the ITO support, in 0.5 M H_2SO_4, which are rounded and deposited densely on the substrate electrode. Figure 10.23-c shows SEM image at the intersection of Cu stripe deposited on predeposited Au stripe. Stripes were deposited with the same parameters as it was described in figure 10.23-a and -b.

http://rcin.org.pl

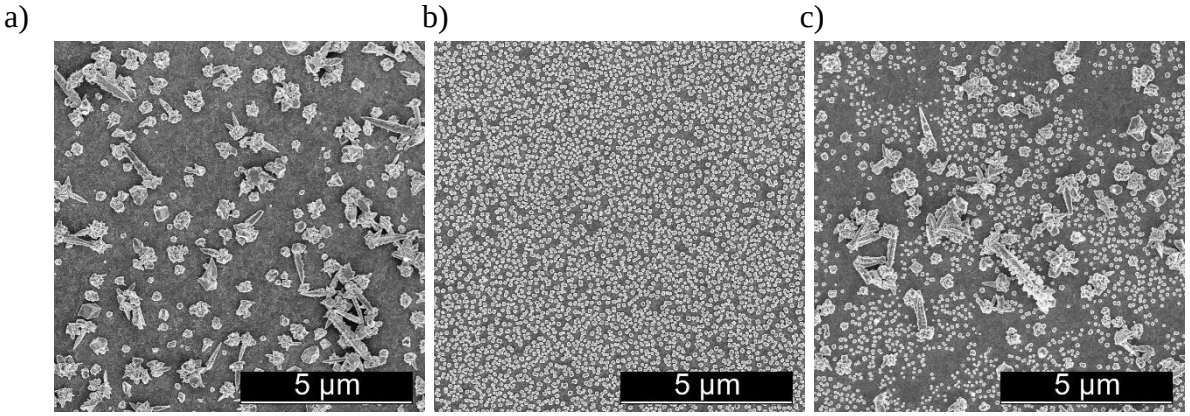

Fig. 10.23. SEM micrographs presenting a) AuNS, b) CuNS obtained under the following conditions: substrate electrode: ITO; tip translation rate: 50 µm s^{-1}; electrolytes: a) 3 M KCl; b) 0.5M H_2SO_4; ITO potentials: a) -0.2 V, b) -0.5 V; c) CuNS electrodeposited on predeposited AuNS.

One can clearly see that CuNS were deposited in the free spaces at the ITO electrode, between AuNS. However, the close up SEM pictures (Figure 10.24) reveal, that the structure of AuNS was also changed - before CuNS deposition AuNS were sharper.

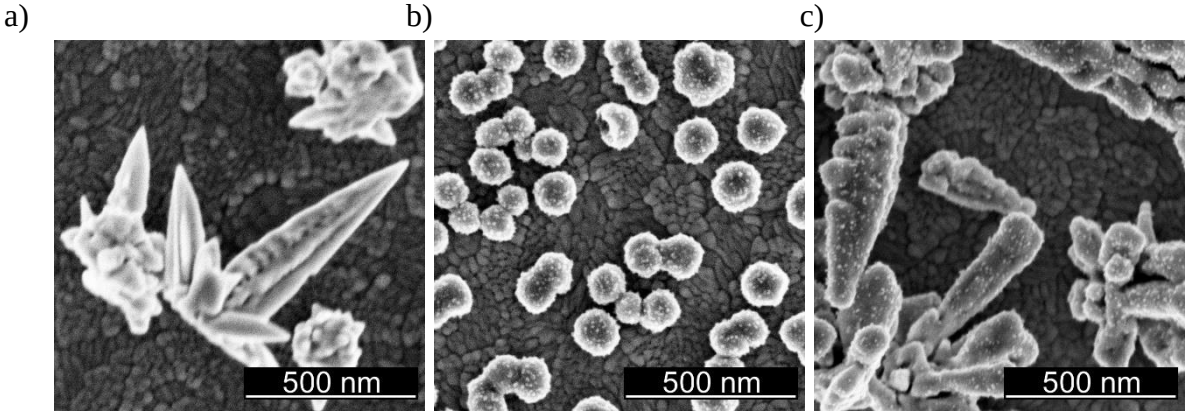

Fig. 10.24. SEM micrographs presenting a) AuNS, b) CuNS obtained under the following conditions: substrate electrode: ITO; tip translation rate: 50 µm s^{-1}; electrolytes: a) 3 M KCl; b) 0.5M H_2SO_4; ITO potentials: a) -0.3 V, b)-0.4 V; c) CuNS electrodeposited on predeposited AuNS.

The surface morphology and chemical composition of obtained intersections of Cu- and AuNS stripes were characterized under the SEM equipped with an EDX detector and GENESIS software. It reveals that at the intersections bimetallic NS are obtained. Figure 10.25 and 10.26 show EDX spectra of CuNS deposited on predeposited AuNS and AuNS deposited on predeposited CuNS on the GC substrate respectively.

http://rcin.org.pl

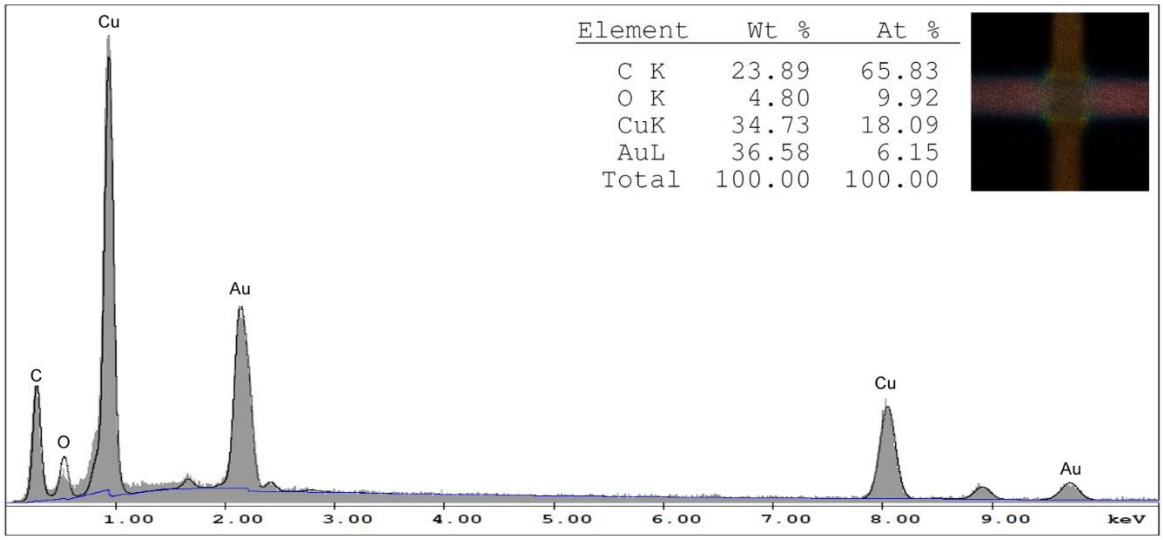

Fig. 10.25. EDX spectrum of CuNS deposited on predeposited AuNS on the GC support. Insets: table provides the information about atomic and weight percentage of each element and optical micrograph of studied sample.

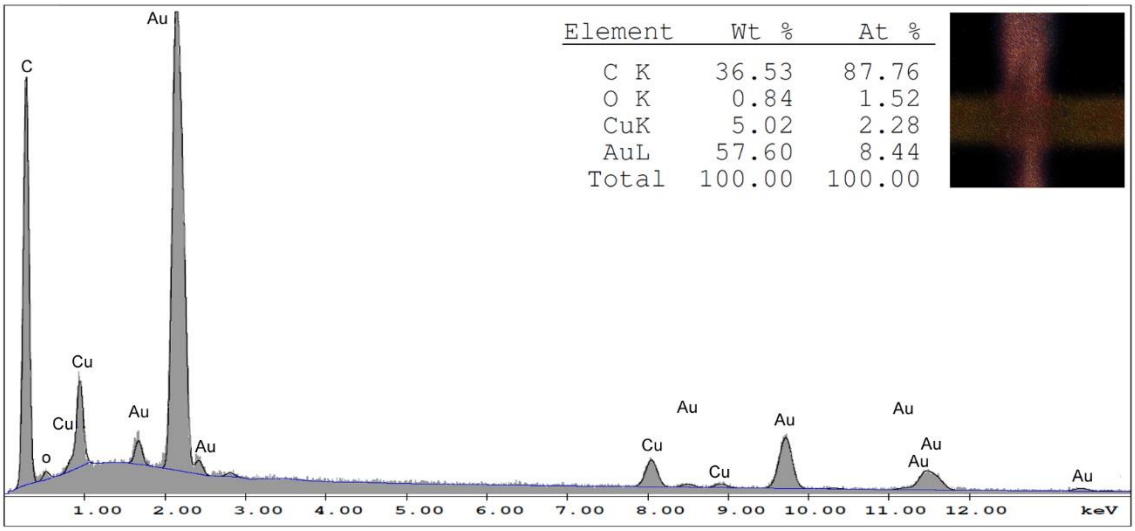

Fig. 10.26. EDX spectrum of AuNS deposited on predeposited CuNS on the GC support. Insets: table provides the information about atomic and weight percentage of each element and optical micrograph of studied sample.

There are significant differences in the intensity of the peaks corresponding to Au and Cu, depending on the order in which the NS were deposited. Insets in Figures 10.25 and 10.26 show correlations in weight and atomic percentage between individual elements of the samples. When CuNS were deposited on predeposited AuNS the weight percentage of Cu and Au were similar, but atomic percentage of Cu was higher. The phenomenon of underpotential deposition (UPD) of Cu at Au occurs,[294,295] which means that the Au surface was covered with Cu. When AuNS were deposited on predeposited CuNS, both the weight and atomic percentage of Au were greater than Cu. Figure 10.27 presents SEM images and EDX maps of described samples.

http://rcin.org.pl

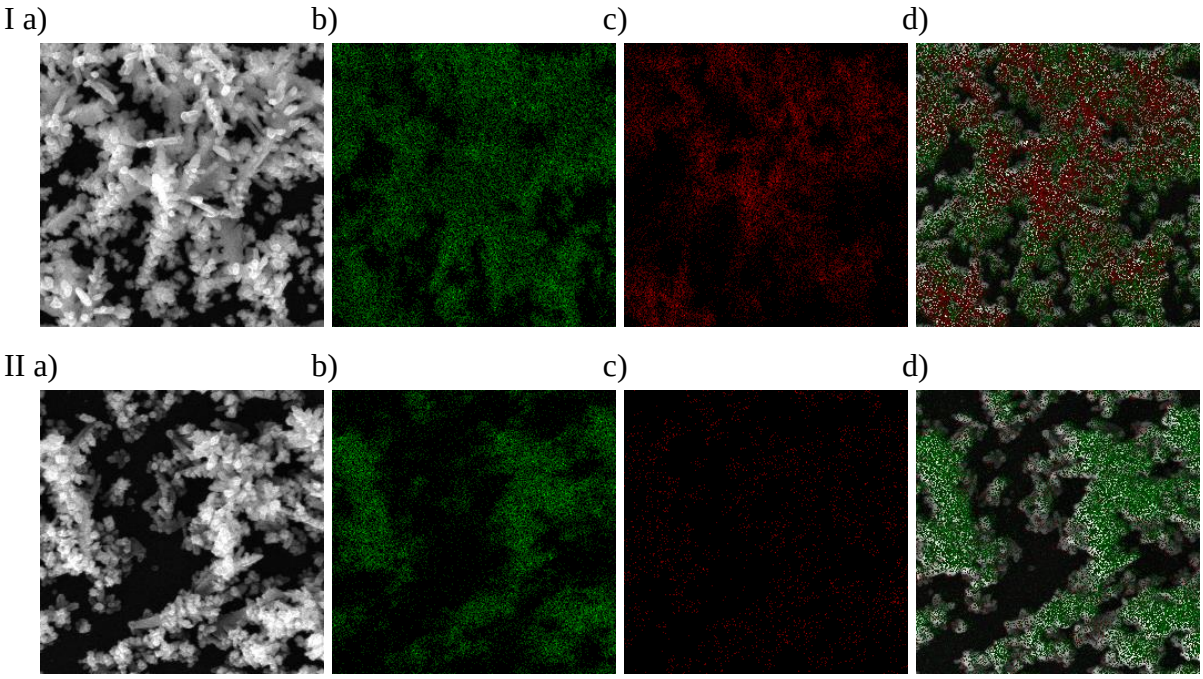

Fig. 10.27. I a) SEM image of CuNS deposited on predeposited AuNS on the GC support; b) EDX map of Au in the sample presented in a); c) EDX map of Cu in the sample presented in a); d) EDX map of Au and Cu in the sample presented in a) overlayed on SEM image. II a) SEM image of AuNS deposited on predeposited CuNS on the GC support; b) EDX map of Au in the sample presented in a); c) EDX map of Cu in the sample presented in a); d) EDX map of Au and Cu in the sample presented in a) overlayed on SEM image.

10.7 Summary and conclusions

This chapter described application of SECM to obtain micropatterns of ligand-free Au-, Cu-, and bimetallic NS, by localized electrorefining of polycrystalline metal wires from the microelectrodes, in a controlled manner.

Bare NS are desirable in catalysis as their activity is not affected by ligands. Their presence may decrease catalytic activity and hinder access of the analyte to the metal surface. Localized electrorefining allows quick fabrication of microscopic patterns where only a small amount of raw metal is used. A number of various NS can be prepared on a single support and studied instantaneously for their catalytic activity by SECM. An additional advantage of NS preparation directly from a polycrystalline metallic source is the cost-efficiency of this approach. This is because, *e.g.* metallic gold is much cheaper than gold in the chemical compounds used for AuNS synthesis.

Presented researches have shown that by adjusting the electrorefining parameters one can control the morphology of obtained NS. Changing the substrate electrode – using GC instead of ITO – allows to apply more negative potentials of electrodeposition, what influences the size and shape of obtained nanocomposites. Faster horizontal translation rate of the metal source during

http://rcin.org.pl

the process results in smaller NS. Electrodeposition performed in quiescent conditions (without tip movement) also influences their morphology, as well as the composition of supporting electrolyte.

http://rcin.org.pl

11. Electrocatalysis on metallic nanostructures

11.1 Introduction

Catalytic properties of prepared bare metallic NS were examined using feedback mode of SECM, by carrying out oxygen reduction reaction (ORR) in alkaline media and carbon dioxide reduction reaction (CO_2RR). These kinetically sluggish processes are important in the industry and described in Chapters 2 and 3.

Au- and CuNS have gained recently high importance as catalysts. Their catalytic activity depends on their morphology. Low coordinated surface atoms, such as those occupying edges and corners of NS, are supposedly the sites of increased electrocatalytic activity.

11.2 Cell assembly

All electrochemical experiments were performed using homemade SECM controlled and operated under SECMx software. SECM setup consisted of Ivium CompactStat bipotentiostat and mechOnics *XYZ* positioning system. Ag|AgCl|3M NaCl and a Pt wire served respectively as a reference and counter electrodes. If not otherwise stated, all potentials in this chapter are provided versus this type of reference electrode. 25 μm diameter AuUME was used as a first working electrode (tip) during ORR studies and 25 μm diameter platinum microelectrode (PtUME) in the case of CO_2RR. ITO coated glass or GC plate with deposited NS served as a second working electrode (substrate).

A horizontal SECM line scans were used to examine activity of microstripes composed of metallic NS towards CO_2RR or ORR (Figure 11.1). In the case of ORR study, AuUME was positioned ~30 μm above the ITO surface and moved perpendicularly to the stripes, which were obtained by localized electrorefining at various substrate potentials. Electrochemical cell was filled with alkaline media: 0.1 M $NaNO_3$ + 0.01 M NaOH electrolyte. During the time of the experiment +1.6 V was applied to the tip, to produce O_2 locally by electrooxidation of OH^- at diffusion controlled rate. The substrate electrode was polarized at moderately cathodic potential to drive ORR on studied NS at kinetically limited rate. In the case of CO_2RR study, PtUME was used in the same way as in the case of ORR, however, the electrochemical cell was filled with 30 mM HCOOH + 0.1 M phosphate buffer (pH = 7), and +0.7 V was applied to PtUME to produce CO_2 by oxidation of HCOOH at the tip and to reduce it at the sample. In both cases tip translation rate was 10 μm s^{-1}.

http://rcin.org.pl

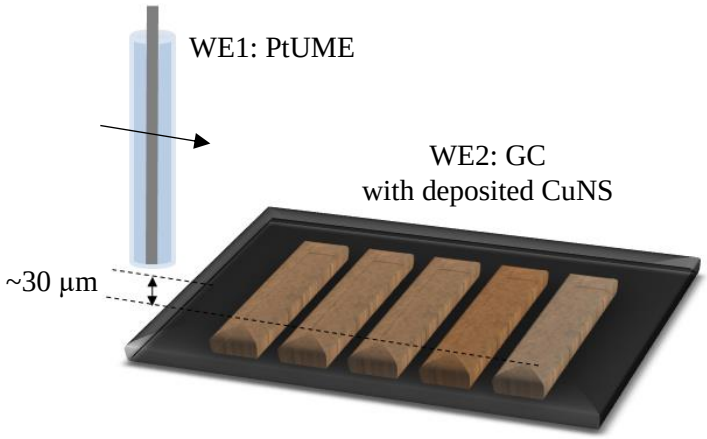

Fig. 11.1. Scheme of the CuNS deposited on the GC substrate and examination of their activity toward CO_2RR during horizontal SECM line scan experiment (not to scale).

A SECM mapping experiment was used to study the catalytic properties towards CO_2RR and ORR of metallic NS which were obtained by localized electrorefining at various substrate potentials under quiescent conditions (Figure 11.2) and mixed stripes of Au- and CuNS (Figure 11.3).

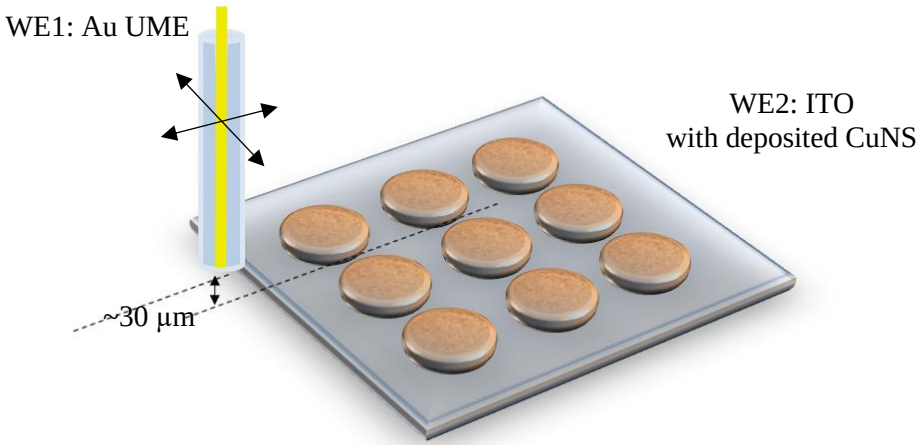

Fig. 11.2. Scheme of the CuNS deposited under quiescent conditions on the ITO substrate and examination of their activity toward ORR during SECM mapping experiment (not to scale).

Au or PtUME was mounted into a 3D positioning system and positioned ~30 µm above the substrate electrode. For recording of activity maps the microelectrode was scanning in *X* and *Y* directions whereas ORR or CO_2RR were driven at the sample. The conditions of the reactions were the same as it was described in the case of a horizontal line scan technique.

http://rcin.org.pl

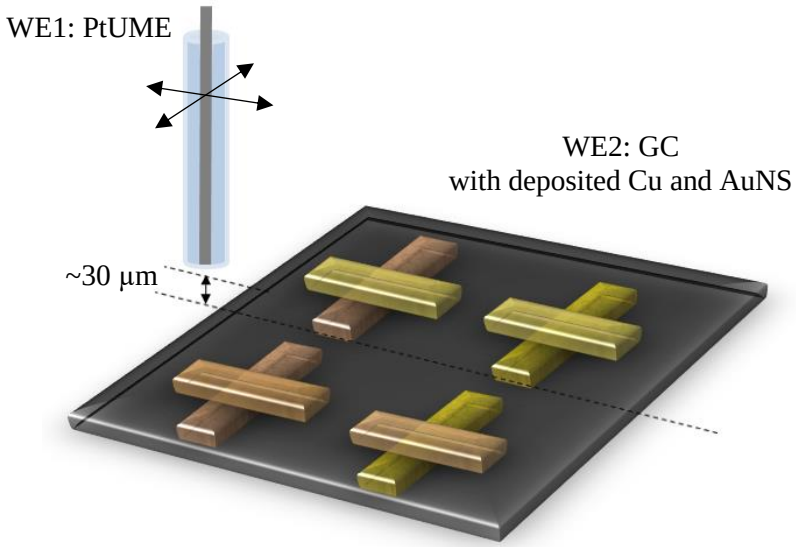

Fig. 11.3. Scheme of the mixed Cu- and AuNS deposited on the GC substrate and examination of their activity toward CO_2RR during SECM mapping experiment (not to scale).

11.3 Oxygen reduction reaction

ORR in alkaline media can be studied by SECM in feedback mode, as ORR is chemically reversible. In this method O_2 is generated at the SECM tip. To a 25 µm diameter AuUME potential of +1.6 V was applied to perform the oxidation of OH^- to O_2 (Figure 11.4-a). Generated oxygen diffused to the sample electrode, polarized at -0.7 V, where it was reduced, generating additional flux of hydroxide ions. Thus, the SECM feedback mode experiment was possible to carry out (Figure 11.4-b).

a) b)

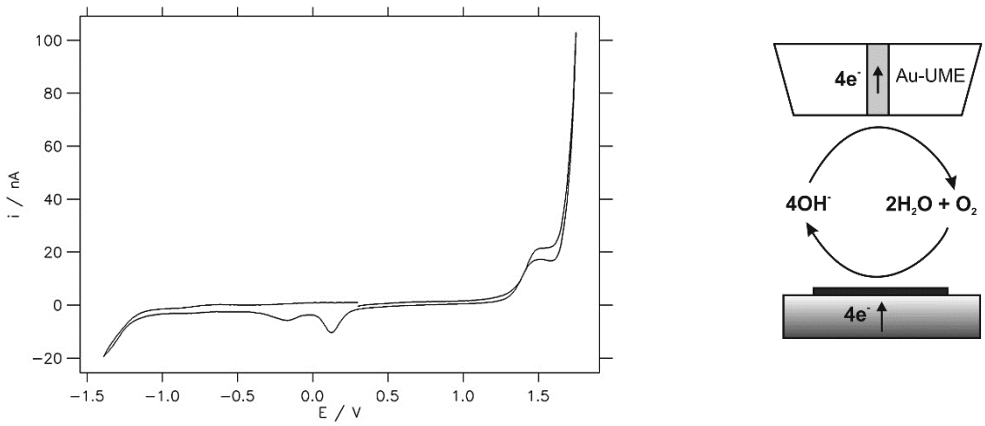

Fig. 11.4. a) Cyclic voltammogram recorded at the 25µm AuUME in 0.1 M $NaNO_3$ + 10 mM NaOH. Scan rate: 20 mV s^{-1}. Oxidation of OH^- occurs at +1.6 V. b) A scheme of feedback mode SECM study of ORR in alkaline solution (not to scale).

http://rcin.org.pl

11.3.1 ORR of CuNS deposited under dynamic conditions

First, the influence of the electrodeposition substrate potential on the catalytic activity of the obtained CuNS was studied. AuUME was translated 30 μm above the sample perpendicular to micro bands of CuNS (Figure 11.1, Figure 11.5, inset) at 10 μm s^{-1}. When SECM tip was crossing above the copper stripes, the corresponding anodic tip current was enhanced as a result of more efficient regeneration of OH^- at a surface exhibiting higher catalytic activity towards ORR. This feedback current at a constant tip-to-sample distance is proportional to the reaction rate at the sample and provides direct information about the sample catalytic activity.

Figure 11.5 shows the response of a tip current versus its horizontal position, recorded during scanning across a set of Cu stripes. CuNS were prepared by electrorefining at different sample potentials, on GC and on ITO support, in 10 mM HCl + 1M KCl electrolyte. It reveals that each stripe exhibits different activity towards ORR in applied alkaline medium, although each sample contains the same amount of Cu per unit area of the support. The decrease of the background current is due to probe deactivation caused by the formation of an oxide film on the Au tip polarized at constant potential.[291] Feedback currents are at a similar level, however the contrast is higher for the sample deposited on GC support. Lower current contrast for ITO supported sample is due to higher residual activity of ITO towards ORR than residual activity of GC.

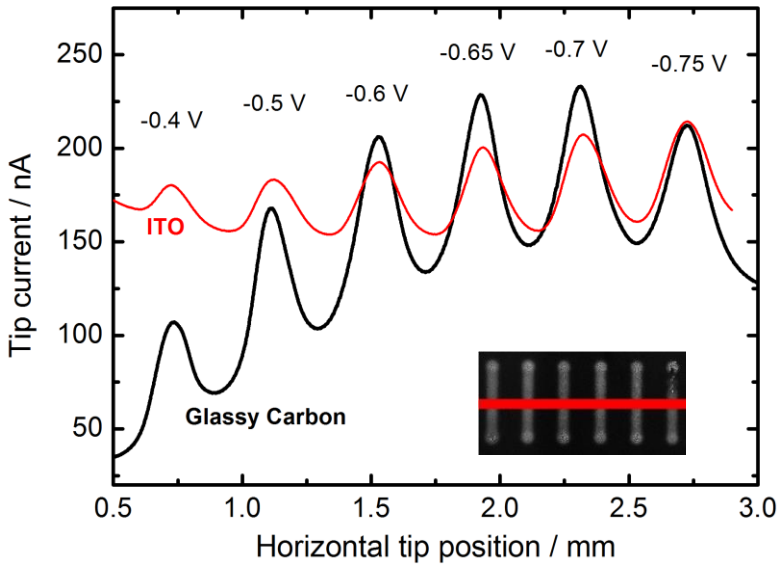

Fig. 11.5. Feedback mode SECM line scan analysis results of ORR occurring on the microstripes of CuNS obtained by localized electrorefining at various substrate potentials and materials (marked in the figure). ITO and GC potential: -0.7 V.

http://rcin.org.pl

The catalytic activity of obtained CuNS depends on the electrorefining potential. For CuNS obtained on the ITO support, the activity reaches maximum for the stripe deposited at −0.75 V (Figure 11.5, red line). The stripes obtained at less cathodic potentials exhibit lower activity. This is in accordance with the morphology of the obtained structures (Figure 11.6). A lower number of larger particles per unit area contain a lower number of exposed Cu atoms and defects (see Chapter 10.4).

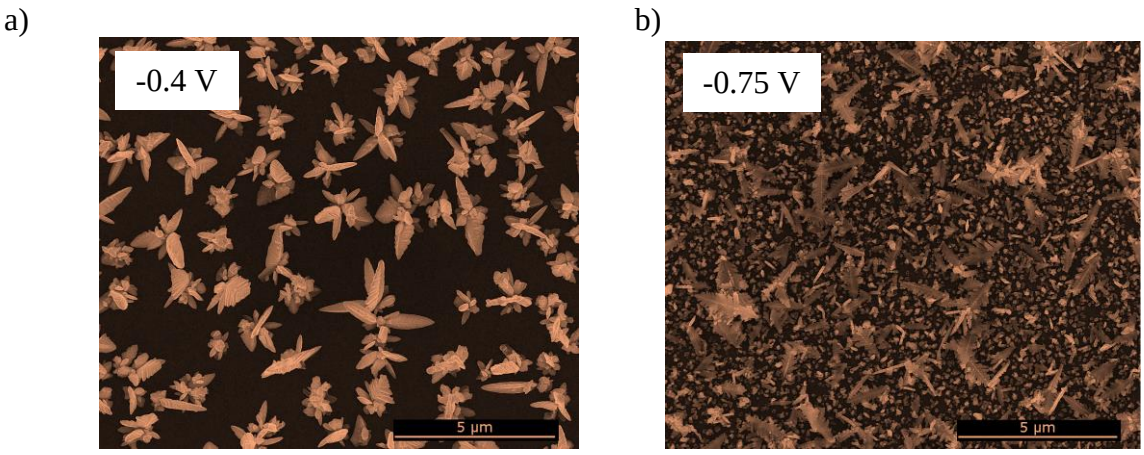

Fig. 11.6. CuNS obtained on the ITO electrode, in 10 mM HCl + 1M KCl electrolyte, potential of electrodeposition marked in the micrographs.

For CuNS deposited on the GC electrode, the activity reaches maximum for the stripe deposited at −0.7 V (Figure 11.5, black line). As in the case of ITO support, Cu stripes deposited on GC at less cathodic potentials are also composed of a lower number of larger particles. Interestingly, the stripe made of CuNS deposited at the most negative potential (−0.75 V) is less active than that deposited at −0.7 V. CuNS deposited at −0.7 V are small and separated, whereas these deposited at -0.75 V constitute aggregates (Figure 11.7).

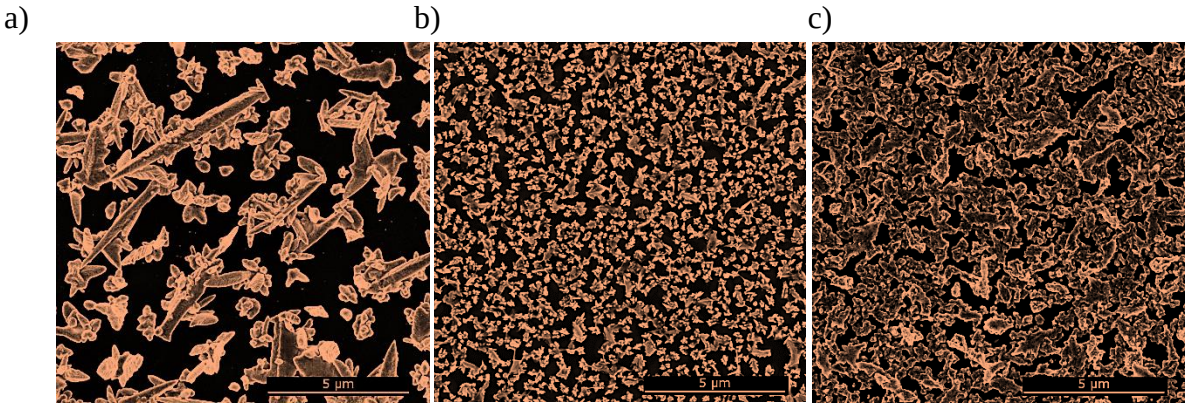

Fig. 11.7. CuNS obtained on the GC electrode, in 10 mM HCl + 1M KCl electrolyte, potentials of electrodeposition: a) -0.4 V, b) -0.7 V, c) -0.75 V.

http://rcin.org.pl

11.3.2 ORR of CuNS deposited under quiescent conditions

Another parameter that can influence the catalytic properties of obtained NS is the composition of the electrolyte that was used during the experiment. The sample for further activity studies was obtained by localized electrorefining of CuUME under quiescent conditions, without translation of the tip. It was performed in three different electrolytes: 0.5 M H_2SO_4, 0.5 M H_2SO_4 + 0.1 M KCl, and 1 M KCl + 10 mM HCl, at three different potentials applied to the ITO: -0.3 V, -0.4 V, and -0.5 V.

Figure 11.8 presents a SECM map of ORR (and its 3D representation) at the microspots of CuNS carried out in 0.1 M $NaNO_3$ + 10 mM NaOH solution. The lowest catalytic activity was obtained for the rounded nanoparticles, deposited from the 0.5 M H_2SO_4 electrolyte. As it was described in the Chapter 10.4, these NS are circular, thus they contain smaller number of edges and corners which are supposedly catalytic active sites. The highest enhancement of the current, so the best catalytic activity toward ORR, was recorded for CuNS samples prepared using 1 M KCl + 10 mM HCl solution. Figure 11.9 shows the cross-section of the microspots of CuNS exhibiting the best catalytic properties. SEM micrographs reveal, that also among these NS, the highest catalytic activity presents CuNS with more developed structure.

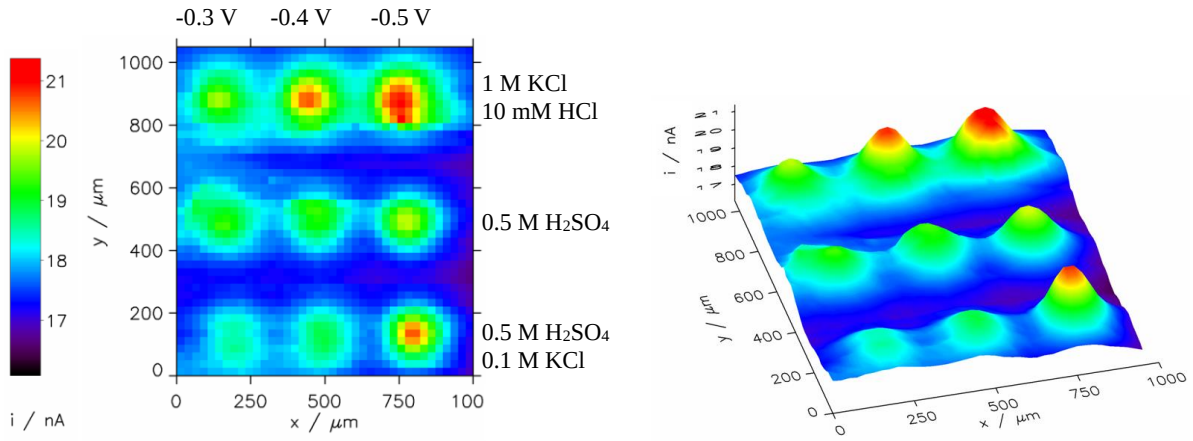

Fig. 11.8. Feedback mode SECM image of ORR (and its 3D representation) at microspots of CuNS deposited on ITO support at various deposition potentials applied to the support and with use of various electrolytes (parameters marked in the figure).

http://rcin.org.pl

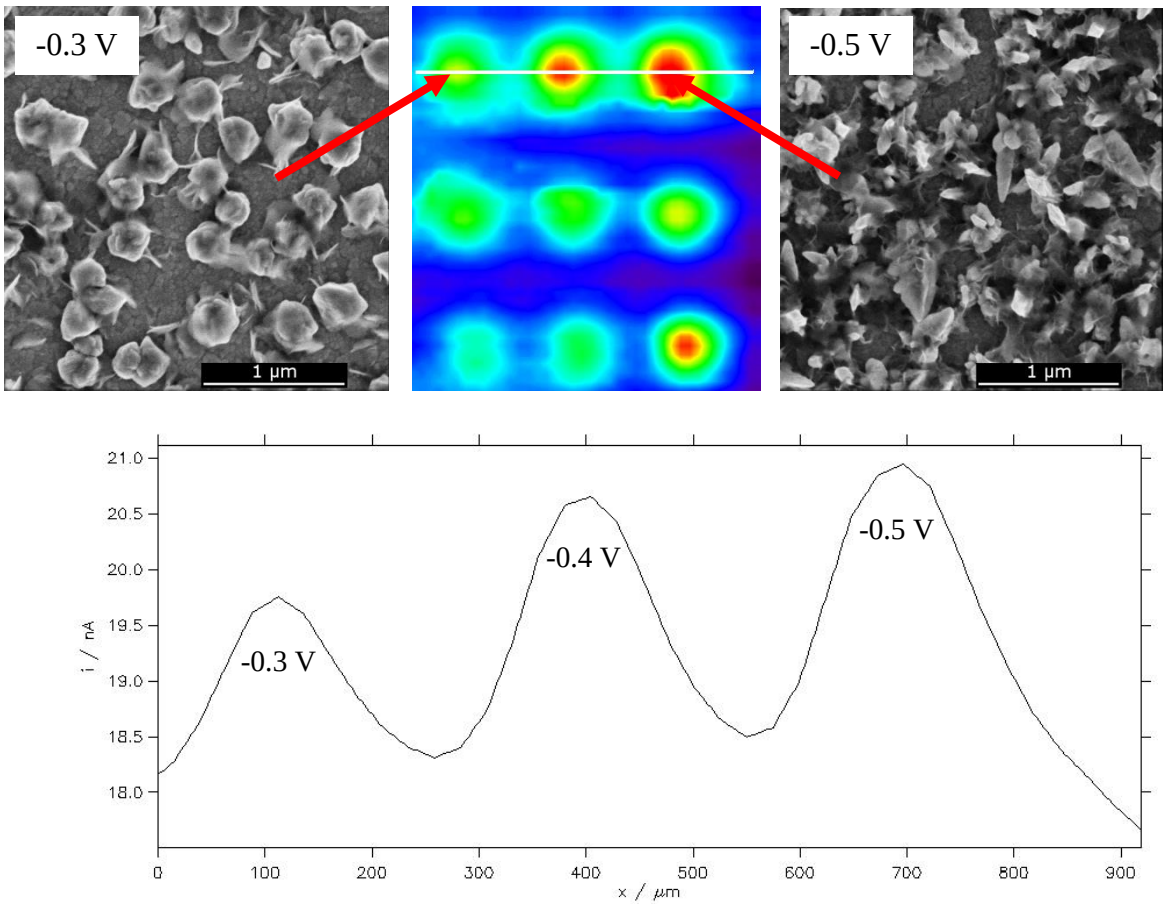

Fig. 11.9. A cross-section of the microspots of CuNS with the highest catalytic activity toward ORR (from figure 11.8.) and their SEM micrographs.

11.3.3 ORR of bimetallic Cu- and AuNS

SECM map of feedback mode ORR in 0.1 M $NaNO_3$ + 10 mM NaOH solution was also performed over bimetallic Cu- and AuNS deposited on the ITO substrate electrode (Figure 11.10). The results show the highest activity of the spot, where CuNS were obtained on predeposited AuNS. This suggests synergistic catalytic effect in such bimetallic NS. Due to known phenomenon of underpotential deposition of copper on gold,[295] the surface concentration of adjacent Au and Cu surface atoms is expected to be little, however such a loci can exist at corners and vertexes of Cu@Au bimetallic NS. Possible locations of active sites towards ORR can be Cu atoms deposited on Au facets of AuNS. The structure of such a surface differs significantly from either bare Au or bare Cu facets.[296] Morphology of such a surface can be favorable for promoting ORR in alkaline media.

http://rcin.org.pl

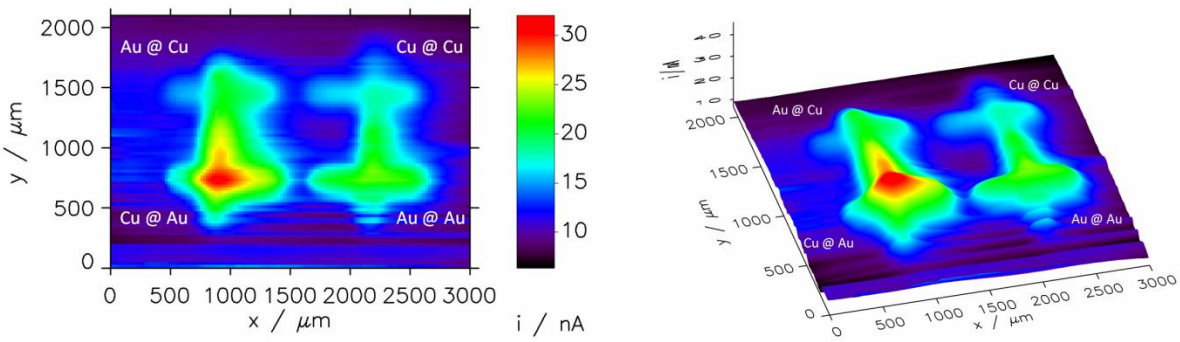

Fig. 11.10. SECM map of feedback mode ORR in 0.1 M $NaNO_3$ + 10 mM NaOH solution over crossed copper and gold nanoparticles on the ITO electrode and its 3D representation. E_{ITO} = -0.75V.

11.4 Carbon dioxide reduction reaction

Catalytic properties of electrodeposited NS towards CO_2RR were also studied using feedback mode SECM. CO_2 was electrogenerated by oxidation of formic acid (HCOOH) on PtUME at the potential +0.7 V. Then it diffused to the sample and was reduced (Figure 11.11). At the neutral pH (pH = 7) it is reduced mainly to HCOOH,[297] generating additional flux of tip reaction substrate. In neutral buffered solution hydrolyzed CO_2 ($pK_{a1}(H_2CO_3)$ = 6.35) and HCOOH (pK_a = 3.75) occurs as bicarbonate (HCO_3^-) and formate ($HCOO^-$), respectively. The electrodeposition of CuNS, and their further studies, were performed only on GC support, as the ITO is instable under strong cathodic polarization required to drive CO_2RR.

a) b)

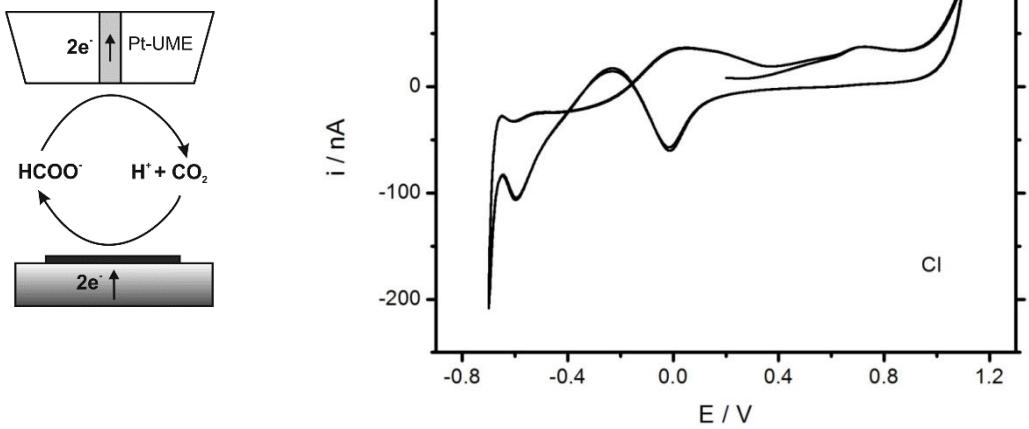

Fig. 11.11. a) A scheme of feedback mode SECM study of CO_2RR in 30 mM HCOOH + 0.1 M phosphate buffer (pH = 7) solution. b) A cyclic voltammogram recorded at the 25 μm diameter PtUME in the same electrolyte. Scan rate: 20 mV s^{-1}. Oxidation of HCOOH occurs at +0.7 V.

http://rcin.org.pl

11.4.1 CO_2RR of CuNS deposited under dynamic conditions

First, the study of the influence of the electrodeposition potential on the catalytic properties of obtained stripes of CuNS was carried out. As it was in the case of ORR study, parallel microstripes of CuNS were deposited at various potentials applied to the GC substrate. The sample was analyzed with a 25 μm PtUME, in buffered solution of HCOOH, by performing a horizontal line scan perpendicular to the axes of CuNS microstripes, 30 μm above the sample. Figure 11.12 shows the tip current *vs.* its horizontal position. It reveals that there is a strong influence of electrodeposition potential on electrocatalytic activity of CuNS. At the electrodeposition potentials less than -0.2 V, CuNS growth rate is limited by diffusion. That is why all stripes of CuNS contains approximately the same amount of Cu per unit area of the support, because, at constant parameters such as electrodissolution current, tip translation rate, tip-to-sample distance, the same amount of Cu ions is delivered per unit area of the substrate. For CO_2RR carried out at moderate potentials, down to -1.1 V, the optimal value of electrodeposition potential is *c.a.* -0.7 V. When CO_2RR is driven at more extreme cathodic polarizations, CuNS obtained at -0.4 V acquire maximum activity, instead.

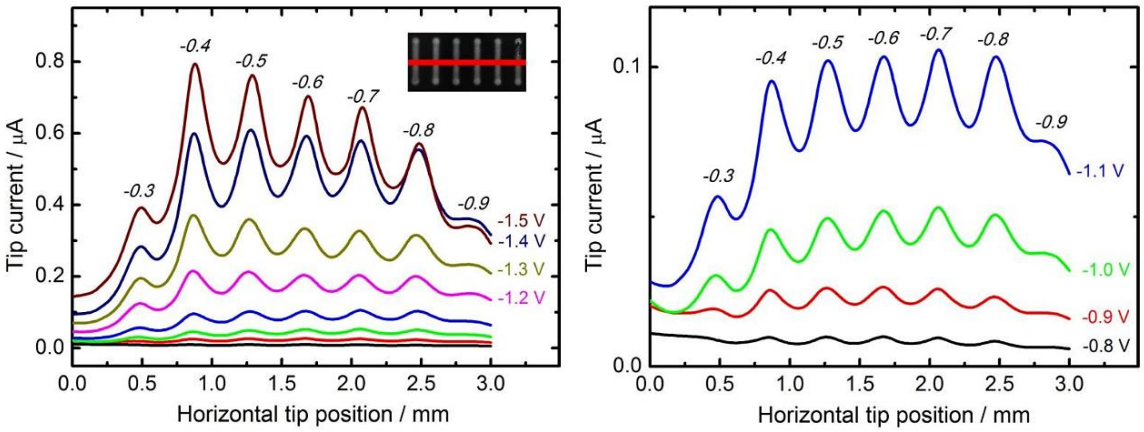

Fig. 11.12. Feedback mode SECM line scan analysis result of CO_2RR driven on the microstripes of CuNS obtained by localized electrorefining at various substrate potentials on GC electrode.

At potentials below -1.1 V applied to the CuNS sample, hydrogen evolution reaction (HER, by electroreduction of water) may occur simultaneously with CO_2RR and contribute to the SECM feedback current. This result shows that HER occurs faster at other types of active sites at CuNS than CO_2RR. Because CuNS deposited at more negative potentials possess more developed surface and less exposed flat crystallographic facets (see Chapter 10.4), one could conclude that chemically reversible CO_2RR, contrary to HER, occurs preferentially at low coordination sites (edges and corners) rather than at crystallographic facets of CuNS.

http://rcin.org.pl

11.4.2 CO_2RR on CuNS deposited under quiescent conditions

To analyze the influence of the electrolyte composition on the catalytic properties of obtained CuNS, a SECM mapping of CuNS prepared at the GC electrode with three different solution compositions was performed. Feedback mode SECM image of CO_2RR on CuNS deposits was obtained using 25 µm PtUME polarized to +0.7 V. Sample potential during imaging was -0.9 V (Figure 11.13).

Figure 11.13 shows that CuNS obtained in the absence of SO_4^{2-} ions exhibit the highest catalytic activity towards CO_2RR. CuNS obtained with 0.5 M H_2SO_4 and H_2SO_4 with an addition of 0.1 M KCl exhibit similar activities substantially lower than these obtained with acidified electrolyte containing only chloride anions.

When stable, negatively charged complexes of Cu and Cl are formed, which require higher cathodic polarization for nucleation and growth of CuNS, then CuNS with exposed crystallographic facets are deposited. Such structures are preferred as catalysts for CO_2RR at high overpotentials, when HER is also possible. In order to prevent hydrolysis of Cu^+/Cu^{2+} ions and precipitation of $Cu(OH)_2$ pH has to be kept around 2 (10 mM HCl). Further pH decrease shifts hydrogen evolution potential to higher values affecting electrodeposition of CuNS.

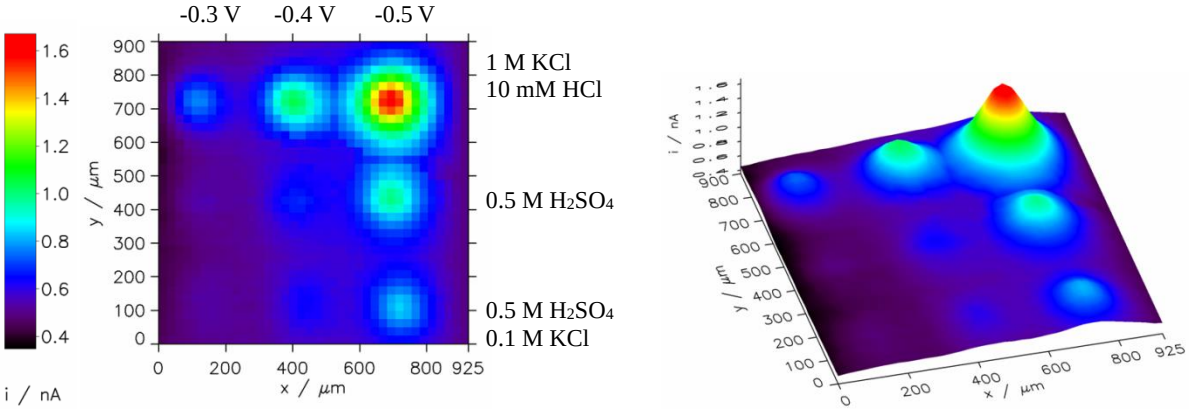

Fig. 11.13. Feedback mode SECM image of CO_2RR at microspots of CuNS deposited on GC support at various deposition potentials applied to the support and with use of various compositions of electrorefining electrolyte (parameters marked in the figure). Sample potential during imaging: -0.9 V.

Figure 11.14 shows the cross-section of the SECM map of microspots of CuNS deposited in 1 M KCl + 10 mM HCl solution, exhibiting the best catalytic properties toward CO_2RR. Among these NS the largest feedback current, thus the highest catalytic activity, exhibit the smallest CuNS, with well-developed structure, deposited at -0.5 V. Their exposed surface area is the largest per amount of Cu deposited. Contrary to the spherical CuNS obtained without chloride ions in electrolyte, crystallographic planes are visible at their surfaces. This result confirms that

http://rcin.org.pl

CO_2RR with generation of electrooxidizable compounds and possible contribution of HER under strong cathodic polarization besides spots with low coordination surface atoms, occurs also at flat crystallographic planes.

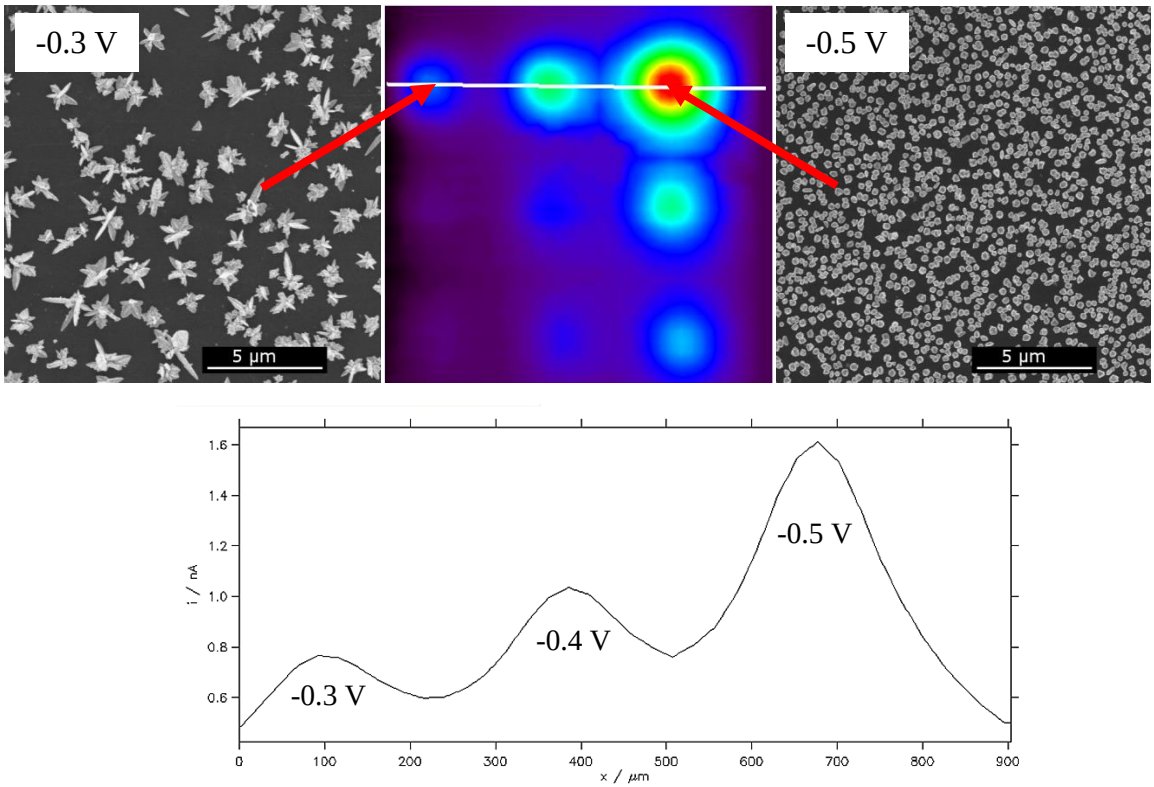

Fig. 11.14. A cross-section of the microspots of CuNS with the highest catalytic activity toward CO_2RR (from Fig. 11.13.) and their SEM micrographs.

11.4.3 CO_2RR of mixed Cu and AuNS

SECM map of feedback mode CO_2RR in 30 mM HCOOH + 0.1 M phosphate buffer (pH = 7) solution was also performed over crossed Cu- and AuNS microstripes deposited on a GC electrode. Both structures were deposited at -0.4 V with 50 µm s^{-1} translation rates (Figure 11.16).

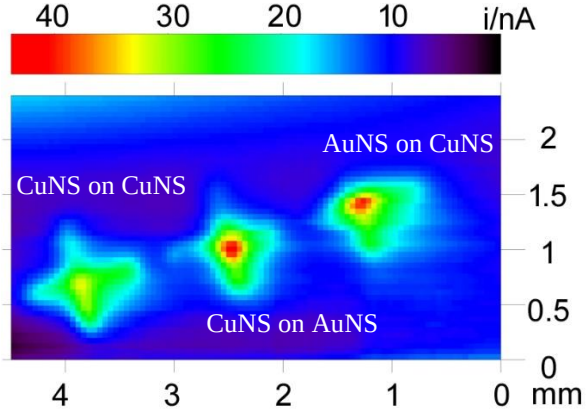

Fig. 11.16. SECM map of feedback mode CO_2RR in 30 mM HCOOH + 0.1 M phosphate buffer (pH = 7) solution over crossed Cu- and AuNS on the GC electrode. Sample potential during imaging: -0.9 V.

http://rcin.org.pl

Obtained results reveal the synergetic activity of bimetallic NS toward CO_2RR. Figure 11.17 shows that in the intersection of a stripe with CuNS deposited on predeposited AuNS, the enhancement of the current was higher than when AuNS were deposited on CuNS (Figure 11.17-b,c). In the intersection of two CuNS stripes the current was enhanced because of the highest amount of deposited material (Figure 11.17-a).

a)

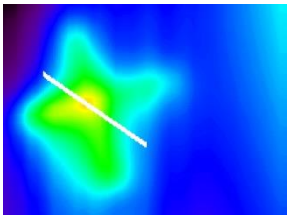

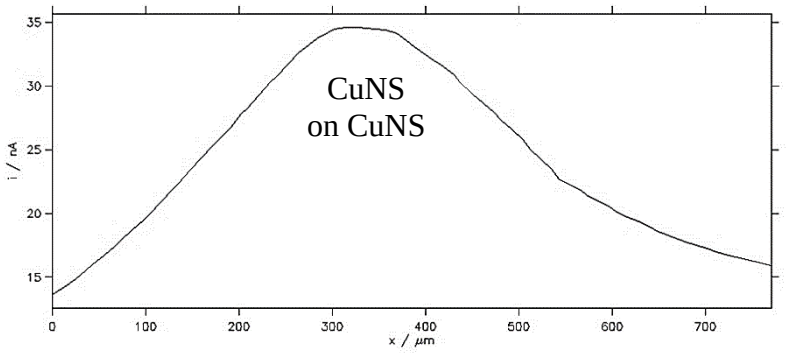

b)

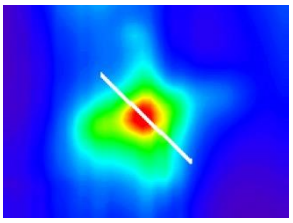

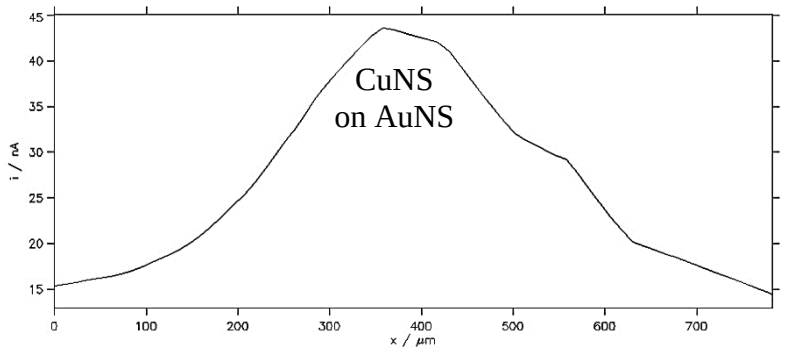

c)

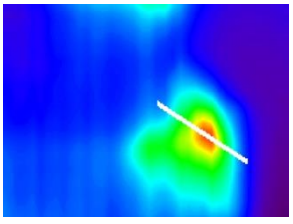

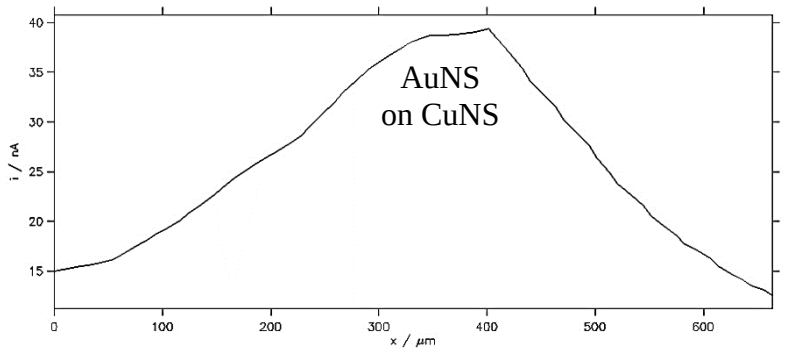

Fig. 11.17. Current enhancements above a) CuNS deposited on CuNS, b) CuNS deposited on AuNS, c) AuNS deposited on CuNS, extracted from the intersection of crossed stripes from figure 11.16.

http://rcin.org.pl

11.6 Summary and conclusions

The studies of the catalytic activity toward CO_2RR and ORR in alkaline media of electrodeposited Cu- and bimetallic NS were performed using SECM feedback mode. Horizontal SECM line scans experiments and SECM maps reveal that each stripe (or spot) of metallic NS exhibits different catalytic activity toward CO_2RR and ORR. The activity depends on the electrorefining parameters: potential applied during deposition, substrate electrode, source translation rate, and the composition of the electrolyte, thus the shape and structure of obtained NS.

Presented results show that programmable fabrication of NS microarrays followed by SECM analysis allows the quick optimization and characterization for newly designed catalysts for CO_2RR and ORR in alkaline media.

http://rcin.org.pl

12. Voltammetric pH nanosensing

12.1 Introduction

In this chapter the preparation, calibration and use of 50 nm diameter voltammetric pH nanosensor will be described. The sensor consists of a carbon nanoelectrode (CNE) with preadsorbed 4-hydroxy-3,5-dimethoxybenzaldehyde azine (syringaldazine, Syr). Its midpeak potential (E_{mp}) is linearly dependent on the pH because of the protons that are involved in its electrode reaction. Obtained nanosensor was used to acquire pH map over a PtUME, generating hydroxide ions (OH^-) by the ORR at a diffusion-controlled rate in aerated phosphate buffered saline (PBS).

12.2 Nanosensor preparation and calibration

Preparation of pyrolytic CNEs was performed by the chemical vapor deposition (CVD) in a similar manner as it is described in the literature.[251,298,299] A quartz capillary (o.d. 1.0 mm, i.d. 0.7 mm) was mounted into a laser puller and pulled using dedicated program (Figure 12.1-a, upper image): line 1: HEAT = 700, FIL = 4, VEL = 55, DEL = 130, PUL = 55; line 2: HEAT = 700, FIL = 4, VEL = 45, DEL = 132, PUL = 150, where: HEAT parameter specifies the output power of the laser, and consequently the amount of energy supplied to the glass; FIL (filament) indicates the scanning pattern of the laser beam that is used to supply heat to the glass; VEL (velocity) specifies the velocity at which the puller bar must be moving before the hard pull is executed; DEL (delay) controls the timing of the start of the hard pull relative to the deactivation of the laser; and PUL (pull) parameter controls the force of the hard pull.

The back side of the obtained nanopipette was connected via silicone tube to the cylinder with petroleum gas (*ca.* 60 vol % butane, *ca.* 40 vol % propane), under the pressure reduced to 1.5 bar. Then it was inserted into a bigger quartz tube (o.d. 3.0 mm, i.d. 2.0 mm), in which the opposite side was fed with a 15 mL min^{-1} argon stream maintained using a gas flow controller. The petroleum gas inside the argon-shielded nanopipette was pyrolyzed three times by direct butane-air gas torch flame at the nanopipette tip for *ca.* 5 s (Figure 12.1-a, middle image, Figure 12.1-b). To remove gaseous products of the pyrolysis and to deliver fresh propane-butane reactant gas, the silicone tube with petroleum gas was disconnected and connected to the pipette several times, between the pyrolysis steps. To provide an electrical connection, a 0.5 mm diameter copper wire was inserted into the pipette with a carbonized interior.

http://rcin.org.pl

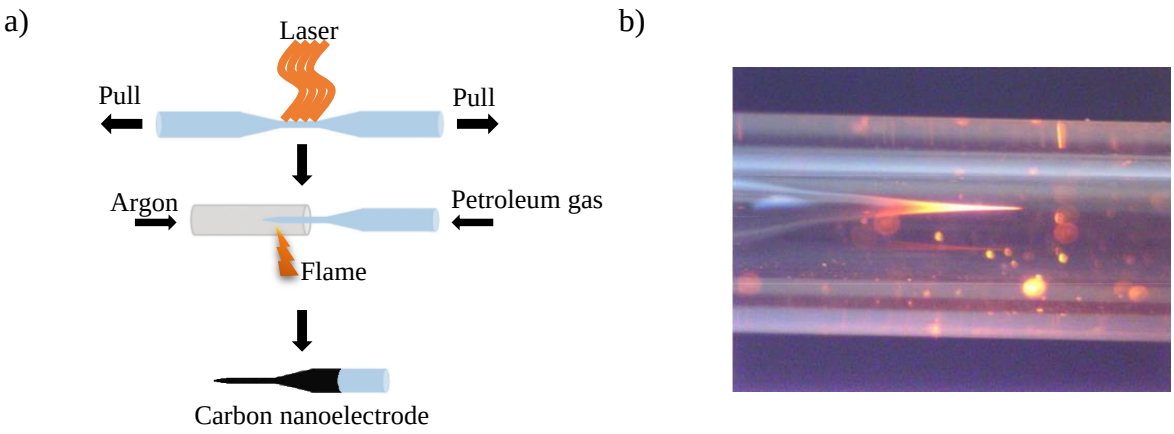

Fig. 12.1. a) Probe fabrication.[300] *b) An image presenting CVD of carbon.*

Such prepared nanoelectrodes (Figure 12.1-a, lower image) were examined by CV in an aqueous 1 mM ferrocenemethanol (FcMeOH) and 0.1 M KCl. A 0.5 mm diameter silver wire served as a quasi-reference and counter electrode. Its potential was assumed to be stable during the experiment when sub-nanoampere currents were recorded. Two types of CNEs were obtained: completely filled with carbon and recessed (Figure 12.2-a and 12.2-b, insets). The type of obtained CNE influences the shape of corresponded CVs. A peak-shaped voltammogram observed in the presence of the used redox mediator indicates a recessed electrode (Figure 12.2-b). Wave-shaped (sigmoidal) CV (Figure 12.2-a), even at scan rates as high as 10 V s^{-1} (Figure 12.3) proves that the nanopipette is filled completely with carbon and the aqueous electrolyte does not penetrate into its interior.[299]

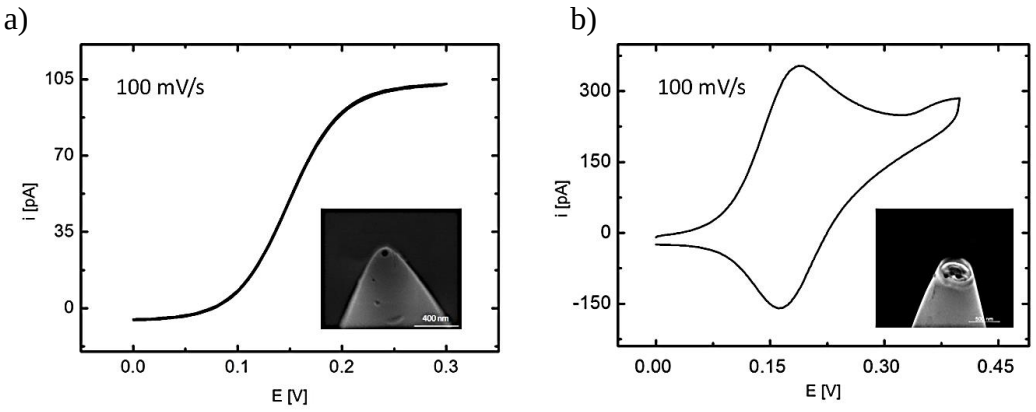

Fig. 12.2. Cyclic voltammograms of a) fully-filled and b) recessed CNEs recorded in 1 mM ferrocenemethanol in 0.1 M KCl at a scan rate: 0.1 V s^{-1}. Inset: SEM micrographs of the analyzed electrodes.

At the disk UME, diffusion limiting current at is given by the equation 6.2:[205]

$$i_T = 4nFDr_T c^* \beta \qquad \text{(Eq. 6.2)}$$

where: n = 1 is the number of electrons exchanged with FcMeOH, F is the faraday constant, D (7.6×10^{-6} cm^2 s^{-1})[301] is the diffusion coefficient of FcMeOH, r_T is the radius of active UME

http://rcin.org.pl

area, c^* is the bulk concentration of mediator, and β is a parameter dependent on the radius of the glass sheath of the UME.

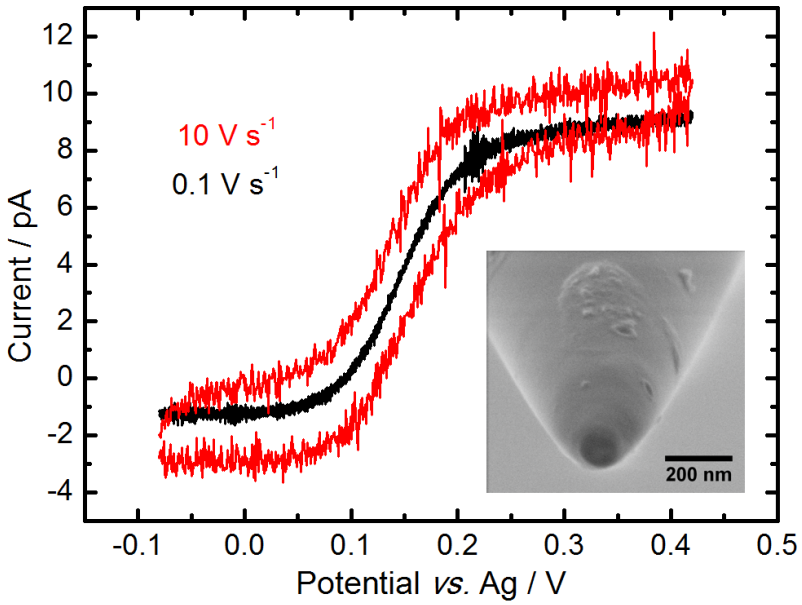

Fig. 12.3. Cyclic voltammograms of CNE recorded in 1 mM ferrocenemethanol in 0.1 M KCl at various scan rates: 0.1 V s^{-1} (black) and 10 V s^{-1} (red). Inset: SEM micrograph of the analyzed electrode.

The measured diffusion-limited current (Figure 12.3), which corresponds to the oxidation of 1 mM FcMeOH, is in accordance with the calculated one. For a 50 nm diameter UME (Figure 12.3, inset), with a glass sheath thickness of 25 nm, the calculated steady-state current is *ca.* 8 pA. It is a prove that no electrically connected carbon layer is deposited on the exterior of the pipette. In such a case, the measured current would exceed the calculated value for the UME geometry derived from SEM micrographs.

CNEs were modified with syringaldazine (4-Hydroxy-3,5-dimethoxybenzaldehyde azine, Syr) by immersion in its 0.5 mg mL^{-1} solution in ethanol for 20 s, and dried under ambient conditions. Syr is a water-insoluble compound and undergoes 2-proton, 2-electron reaction which makes it sensitive to the pH changes (Figure 12.4).[302]

a)

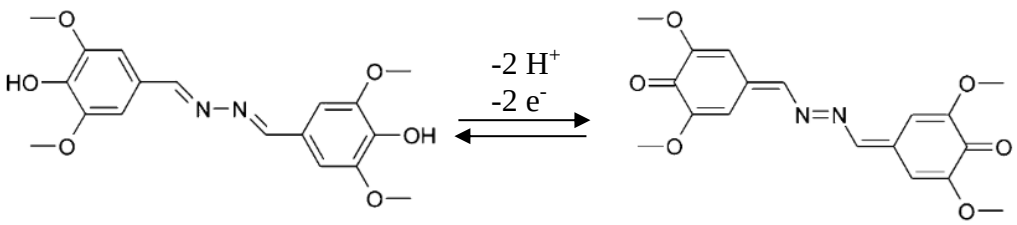

http://rcin.org.pl

b)

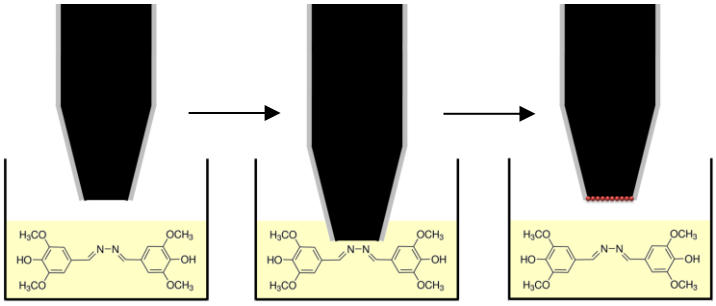

Fig. 12.4. a) Mechanism of the electrode reaction of syringaldazine. b) A scheme of modification of CNE with syringaldazine.

CVs were recorded in a two-electrode configuration system, with reference and counter electrode immersed into 0.1 M phosphate buffer solutions of various pH. Figure 12.5 shows that Syr-modified CNEs exhibit stable, quasi-reversible cyclic voltammograms, with peaks characteristic of exhaustive electrolysis of the adsorbate. A linear relation between peak current and scan rate also confirms the adsorption of Syr (Figure 12.5, inset).

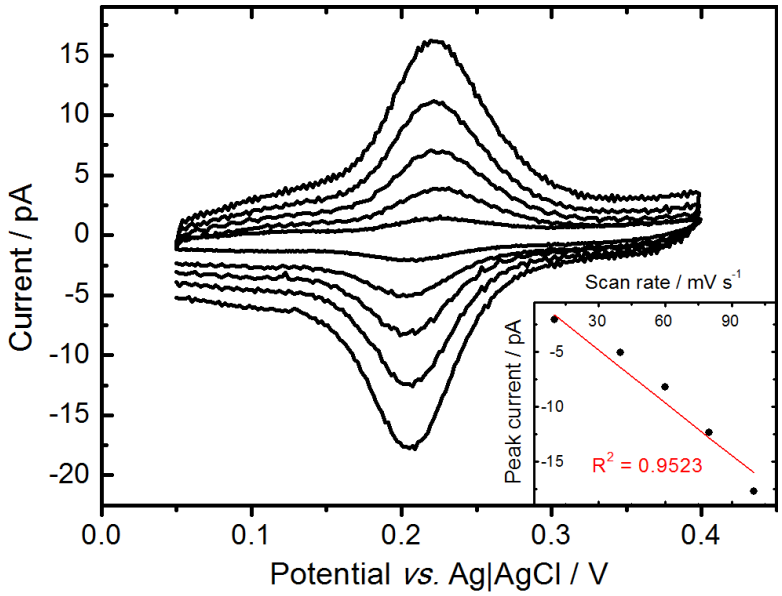

Fig. 12.5. Cyclic voltammograms of CNE with preadsorbed syringaldazine recorded in 0.1 M phosphate buffer, pH = 7.05, at various scan rates: 10, 40, 60, 80, and 100 mV s^{-1}. Inset: plot of cathodic peak current vs. scan rate.

The amount of adsorbed syringaldazine was estimated on the basis of the Faradaic charge for its electrooxidation. This charge was calculated by integration of positive-going sweeps of CVs presented in figure 12.5.

http://rcin.org.pl

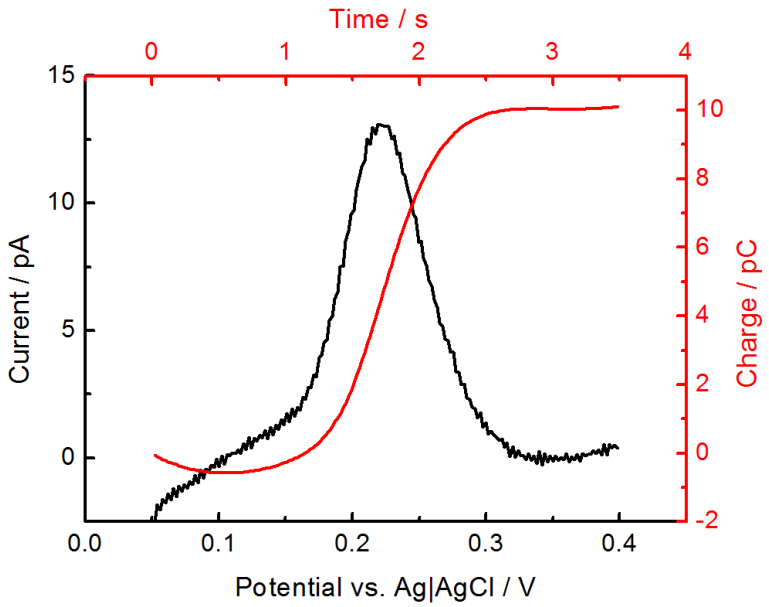

Fig. 12.6. Linear sweep voltammogram corrected by constant capacitive current baseline subtraction (black) of CNE with preadsorbed syringaldazine recorded in 0.1 M phosphate buffer pH = 7.05 and its integration result (red).

Figure 12.6 shows a linear sweep voltammogram corrected by constant capacitive current baseline subtraction of Syr-modified CNE and its integration result. Using Faraday laws of electrolysis for a two electrons process, one can calculate the molar amount of adsorbed Syr:

$$n = \frac{Q}{zF} = \frac{10^{-11}}{2 \cdot 96485} \approx 5.18 \cdot 10^{-17}\text{mol} \qquad \text{(Eq. 12.1)}$$

Multiplying this value by the Avogadro constant one obtains *ca.* 3×10^7 molecules, *e.g.* around 15,000 molecules per square nanometer of geometric area of 50 nm diameter disc electrode. Such a high adsorbate loading is probably caused by the microporosity of pyrolytic carbon[303] and possible multilayer adsorption. Moreover, after removing CNEs from the adsorption solution, some excess of Syr could precipitate upon evaporation of ethanol, and undergo complete electrooxidation/electroreduction as previously found for bulk electrolysis of solid-state Syr microcrystals.[304] Depletion of redox-active adsorbate, *e.g.* partial dissolution of previously deposited Syr, has been observed after further immersion of Syr-modified CNE in ethanolic Syr solution.

The calibration curve of the voltammetric pH nanosensor was constructed by plotting the mid peak potential of CVs of the Syr-CNEs recorded in a series of buffered solutions versus pH of these buffers. pH values of the tested solutions were determined by a glass-electrode pH meter, calibrated using standard buffer solutions. In order to evaluate midpeak potential accurately from noisy CVs, they were smoothed using the Savitzky-Golay algorithm implemented in OriginPro8 software. Mid-peak potential evaluation from CVs with noise would contain significant error when performed by a simple computerized search for the maximum and minimum current values.

http://rcin.org.pl

Figure 12.7 represents an example of the smoothing result. Importantly the mid-peak potential of original and smoothed curves are identical.

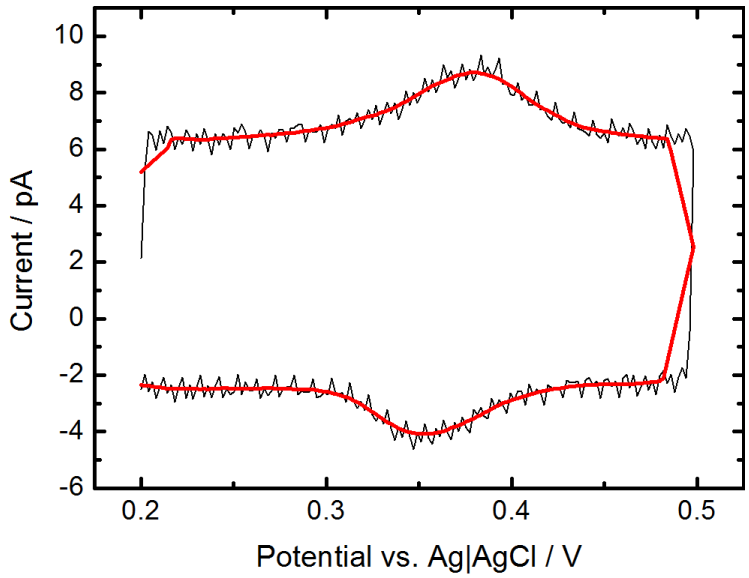

Fig. 12.7. A noisy CV (black) of CNE with preadsorbed syringaldazine recorded in 0.1 M phosphate buffer, pH = 4.45 at a scan rate of 0.5 V s^{-1} and the same measurement after smoothing (red).

As it was mentioned before, the electrode reaction of Syr is a two electron/two proton process, therefore its formal potential (E°′) is proportional to pH with a theoretical slope of −59 mV pH^{-1}.[302] The midpeak potential (E_{mp}) is linearly dependent on the pH. This is in agreement with the found dependence of the E_{mp} on pH dependency (Figure 12.8-a). There is a slight difference between the theoretical and experimental slope value (−59 mV pH^{-1} *vs.* −54 mV pH^{-1}) which can be caused by hindered access of protons to redox-active Syr molecules adsorbed inside the micropores of carbon or inside precipitated nanocrystal. A least-squares fit of a linear calibration function yields:

$$pH = -\frac{E_{mp}}{0.0538} + 11.27 \qquad \text{(Eq. 12.2)}$$

with a Pearson correlation coefficient R^2 = 0.99 (Figure 12.8-b). The voltammetric response signal can be distorted by the filtering of the current signal, because the cut off frequency of the analog low-pass filter is set to a value below the data acquisition rate. It is visible as an enlargement of the peak-to-peak separation. However, the accurate evaluation of the E_{mp} is unaffected by such “overfiltering”, providing a convenient way for its accurate evaluation.

http://rcin.org.pl

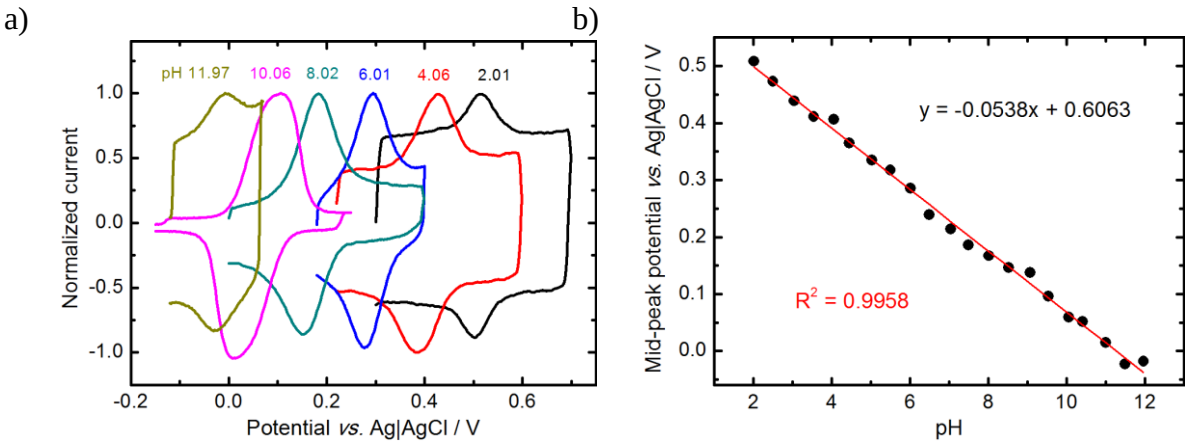

Fig. 12.8. a) Selected CVs of CNEs with preadsorbed syringaldazine recorded at various pH values (labeled) of 0.1 M phosphate buffers. Current is normalized versus anodic peak current. b) Plot of midpeak potential of CVs at various pH values.

Described nanosensor requires careful handling. The most important is to eliminate the electromagnetic noise. When the nanoelectrode is in contact with the electrolyte, including the moments of its immersion and removal, the Faraday cage has to be closed all the time. Otherwise, the external alternating electromagnetic field induces parasitic currents, which shifts the nanoelectrode potential to extreme values and may damage them irreversibly.

12.3 Cell assembly and nanosensor positioning

The pH mapping experiment was performed in a four-electrode system (Figure 12.9). Syr-modified CNE was employed as a first working electrode (tip probe). Second working electrode – PtUME – was used as a model substrate. It was prepared by sealing a 10 μm diameter Pt wire into a borosilicate glass capillary and polished finally with 50 nm grade alumina lapping tape. The electrochemical cell was filled with the examined solution of known pH. All electrodes were connected to the SECM setup.

http://rcin.org.pl

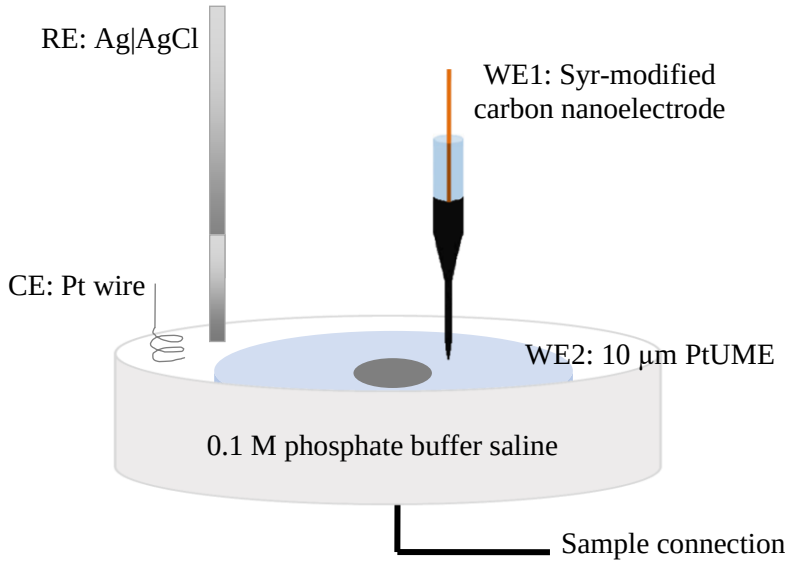

Fig. 12.9. A scheme of the SECM electrochemical cell with two working electrodes (not to scale).

A Syr-modified CNE was mounted into a piezo positioning system that allows to move it in a three dimensions *X*,*Y*, and *Z*. It was positioned *ca.* 10 µm above the Pt substrate, using an optical microscope, in air. After retracting the probe by 1 cm (further above the electrolyte level), the electrolyte was gently poured into the cell and the Faraday cage was closed. By using SECM motors, the probe returned to the position optimized in air. Then it was polarized at a potential of −0.7 V, to reduce oxygen at a quasi-steady-state rate, however the slow rise of the cathodic current with time was observed. This could be caused by a slow increase of the electrode area affected by electrodeposition of metallic clusters by reduction of metal ion traces present in the electrolyte. With larger microelectrodes this effect is not observed, because the deposited NS do not increase their size significantly. Moreover, in case of kinetically sluggish process, such as ORR, deposited metallic NS can possess catalytic properties, causing an additional acceleration of the studied process.

12.4 pH mapping

Figure 12.10 shows the approach curve of a pH-probe to the polished insulating glass sheath of the PtUME (sample), with 9.77 nm steps. The movement was interrupted automatically when an ORR current decreased by 20% of its initial value. What is important, the polarization of Syr-modified CNE to the potential where ORR occurs allows its controlled approach to the sample surface without losing its pH-sensing function.

http://rcin.org.pl

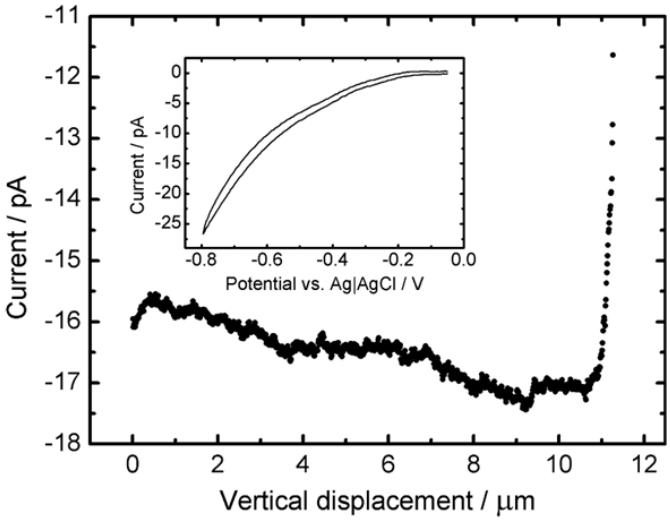

Fig. 12.10. Approach curve of CNE with preadsorbed syringaldazine to polished glass surface. Probe potential: -0.7 V, electrolyte: aerated PBS. Inset: CV of the nanoelectrode under the same conditions.

Approach curve allowed the positioning of the pH probe *ca.* 2.5 µm from the sample surface. After that, PtUME was polarized at −0.8 V to reduce the oxygen (Figure 12.11). Then the pH mapping was performed, at constant height, with a 0.66 V s^{-1} scan rate of a single CV recorded in every grid point of the scanning raster. From the obtained CVs, the map of midpeak potentials was extracted and rearranged to a map of local pH using MIRA software.

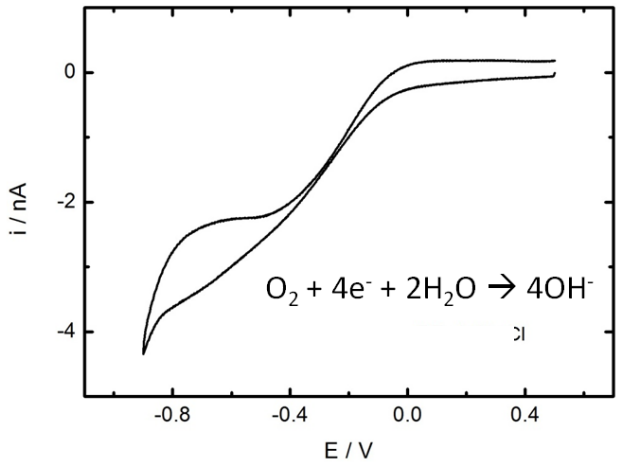

Fig. 12.11. Cyclic voltammogram of on 10 µm diameter PtUME in aerated 0.1M KCl. Inset: the mechanism of the 4-electron ORR reaction in neutral electrolyte, [Chapter 2.2]

The first pH mapping attempt over an oxygen reducing PtUME was performed with non-buffered 0.1 M KCl solution, using recessed carbon nanosensor. Each point in the obtained pH map, presented in Figure 12.12, was calculated from the E_{mp} of CV. Detected pH values above the Pt substrate electrode were higher than in the bulk solution, due to the local alkalization of the electrolyte, caused by hydroxide anions generation at the sample (Figure 12.11, inset), however, no sharp peak appeared in a pH map of 75× 75 μm^2 scanning area that would reveal the dimension

http://rcin.org.pl

of the active sample (Figure 12.12-a). The second mapping was performed using fully filled Syr-modified CNE, also in non-buffered 0.1 M KCl solution, what results in better resolution image, but still not good enough to reveal the sample dimension (Figure 12.12-b).

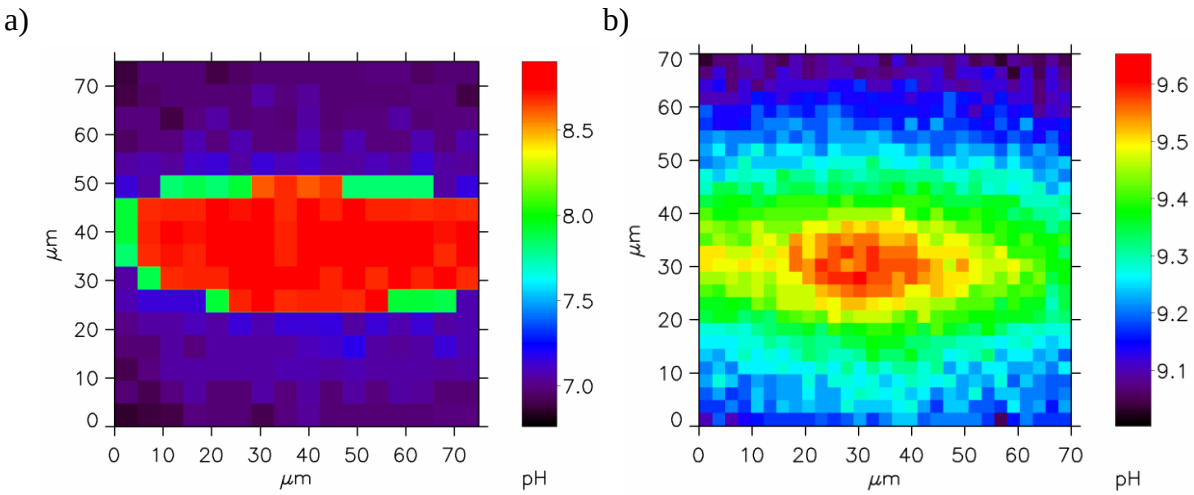

Fig. 12.12. pH maps recorded above a 10µm diameter PtUME polarized at -0.8 V to reduce oxygen in non-buffered 0.1M KCl using a) recessed, b) fully filled CNEs.

In nonbuffered solution, such as used 0.1 M KCl, OH^- ions generated by the ORR at the diffusion-limited rate of the sample, diffuse toward the bulk electrolyte. In the hemispherical diffusion regime, the product concentration is close to its bulk concentration already at a distance of *ca.* 10 times the microelectrode radius.[173] Here, the bulk pH is found at a distance of *ca.* 50 µm. Mapping of a whole diffusion profile would require a large scanning area and corresponding long imaging times. Moreover in this experiment, the type of used Syr-modified CNE was crucial. Recessed electrodes that can be penetrated with the electrolyte should be excluded, because the diffusion of solution components in and out of the pipette cavity through its tiny orifice prolongs its response time and causes image blurring,[305] which is more important than the potential advantage from larger amount of redox-active adsorbate in the sensor, and which results in a blurred image (Figure 12.12-a).

To obtain a higher resolution image of low local pH changes, the electrolyte was changed to a buffered solution – PBS (pH = 7.4). It is commonly applied in the biological studies and its considerable, but finite, buffer capacity causes depression of pH changes around the OH^- source. Each point in the obtained pH map, presented in Figure 12.13, was calculated from the E_{mp} of CV, recorded with a 2 mV potential step, at a scan rate of 0.66 V s^{-1}, within the potential range of 0 to 0.32 V. The time required for an individual CV was 0.97 s. Recording of all CVs of the image took 20 min. Another 20 min was spent on probe translation. The time of the experiment depends on the scan rate and potential range of the single CV experiment, probe translation rate,

http://rcin.org.pl

and the total number of image points. The scan rate of recorded CVs was restricted by specification of the digital-analog and analog-digital converters, that were used in the experiment. The scan rate could be increased with an increased potential step at the expense of lower precision of midpeak potential and pH evaluation. An increase of scan rate requires higher acquisition rates of the current signal, which usually causes noise enhancement. Because Faradaic currents corresponding to adsorbed Syr oxidation/reduction are proportional to scan rate (Figure 12.5), current noise would not be a problem. This enables further improvement of the presented technique by faster CV acquisition.

Obtained results show that pH reaches *ca.* 8 over the center of UME, which means that even in buffered solution the pH close to ORR catalyst can be significantly shifted locally.

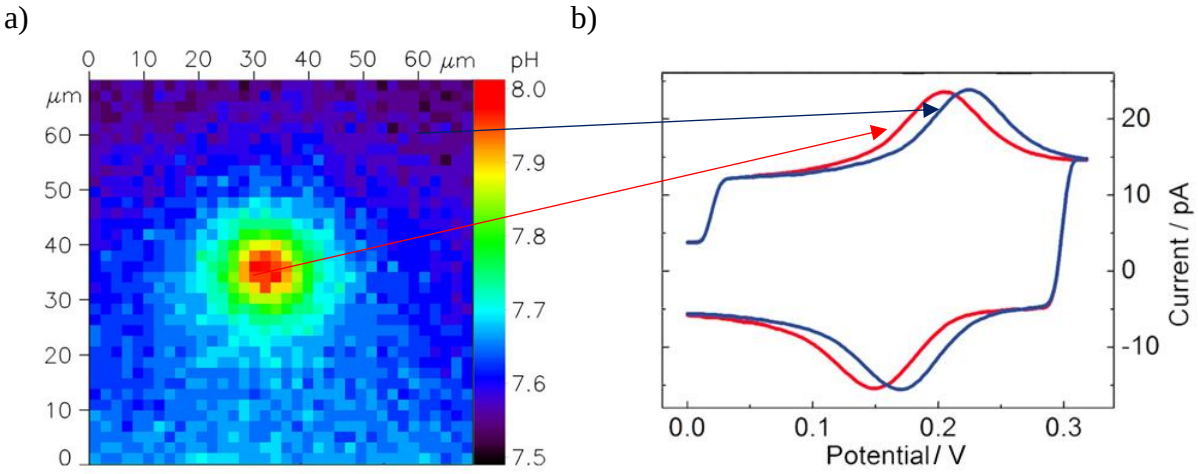

Fig. 12.13. a) pH map recorded ca. 2.5 μm above a 10μm diameter PtUME polarized at -0.8 V to reduce oxygen in aerated PBS (pH = 7.4). b) CVs recorded at the marked points within the pH map at a scan rate 0.66 V s^{-1}.

12.5 Summary and conclusions

A nanoprobe for pH imaging with fast response and high spatial resolution was obtained using Syr-modified CNEs. It was based on the determination of the E_{mid} of a cyclic voltammogram of an adsorbed redox-active organic compound (Syr) with pH dependent electrode potential. A CNE with preadsorbed water-insoluble syringaldazine exhibits a stable quasi-reversible voltammetric response within the pH range of 2 − 12. It was successfully applied to map of local alkalization of PBS above a model sample – 10 μm PtUME during ORR.

The ability to monitor changes in the acidity or alkalinity of solutions at the nanoscale is an important step towards a better understanding of many chemical processes, *e.g.* in corrosion studies, that begins within very small surface fragments. Another important advantage of the Syr-modified CNE nanosensors, even for imaging of larger sample features, is the avoidance of hindered diffusion of reactants to the sample in the sample-generation/tip-collection mode.[306]

http://rcin.org.pl

Obtained results show that the larger amount of redox-active adsorbate in the sensor made of recessed CNE is not desired as it prolongs its response time and causes image blurring. They also indicate that even in buffered solution and using CNEs filled fully with carbon, the pH at an ORR catalyst can be significantly shifted locally, what may affect the mechanisms of the reactions.

http://rcin.org.pl

13. Summary, conclusions and outlook

Local deposition and electrocatalysis of metallic nanostructures (NS):

- Ligand-free Au-, Cu-, and bimetallic NS were obtained by localized electrorefining of polycrystalline metal wires from the microelectrodes, using scanning electrochemical microscopy (SECM).
- Localized electrorefining allows quick micro-sample fabrication, directly from a polycrystalline metallic source, with only a small amount of raw metal used. The proposed procedures could be scaled up to obtain larger amounts of NS and make the process more cost-efficient as metallic wires are much cheaper than the chemical compounds used for NS synthesis.
- Presented researches have shown that one can control the morphology of obtained NS by adjusting the electrorefining parameters:
    - changing the substrate electrode (using glassy carbon instead of indium tin oxide) allows to apply more negative potentials of electrodeposition what influences their size and shape;
    - faster horizontal translation rate of the metal source results in smaller NS;
    - hydrodynamic conditions of electrodeposition influences NS morphology what may be the subject of further researches;
    - composition of supporting electrolyte influences their size and shape – addition of complexing ions (Cl^-) into the electrolyte breaks the symmetry of the obtained NS which has a positive effect on their catalytic properties.
- Amount of deposited copper estimated by the analysis of SEM images is in good accordance with Faradaic charge passed for 2 electron reaction in H_2SO_4 solution and 1 electron process in the presence of chlorides. Application of chloride electrolyte decreases electricity consumption required for electrorefining of Cu.
- Programmable fabrication of NS microarrays prepared on a single support followed by immediate SECM analysis allows quick optimization and characterization for newly designed catalysts for carbon dioxide reduction reaction (CO_2RR) and oxygen reduction reaction (ORR) in alkaline media.
- NS activity depends on their morphology. Obtained results indicate that ORR in alkaline media and CO_2RR are catalyzed more efficiently in those places of NS where low coordination number atoms are present, however hydrogen evolution reaction can occur

http://rcin.org.pl

effectively on undefined crystallographic planes. In future studies it would appear interesting to elucidate these phenomena using nanoscale activity mapping.

- One can apply the proposed method to obtain NS of other metals. The choice of electrolyte must allow the electrodissolution of metal (by applying appropriate potential) and eliminate its passivation or other Faradaic reactions leading to the evolution of gaseous products.

Voltammetric pH nanosensing:

- A method of obtaining nanoprobe for pH imaging with fast response and high spatial resolution was developed by using syringaldazine-modified carbon nanoelectrode (Syr-modified CNE). Voltammetric pH nanosensor exhibits a stable response within the pH range 2 − 12.
- Obtained results show that the larger amount of redox-active adsorbate in the sensor made of recessed CNEs is not desired as it prolongs its response time and causes image blurring.
- Even in buffered solutions, the pH at an ORR catalyst can be significantly shifted locally what can affect the mechanisms of the catalytic reactions.

Outlook:

- In the future studies it would appear interesting to develop methods of preparation of other ligand-free monometallic NS and multimetallic NS by localized electrorefining of pure metals and alloys.
- More advanced research focused on verification of the hypothesis of possible electrocatalytic synergy of bimetallic Cu- and AuNS can be performed.
- There is still a room for improvement in lateral resolution of developed voltammetric pH nanosensor. One can obtain CNEs as small as 10 nm in diameter and modify them with Syr. Such electrodes can be applied for localization of active sites on the surfaces of NS. One can scan samples with nano-structured topographic features (*e.g.* obtained by localized SECM electrorefining) during reactions involving H^+ or OH^- reactants using pH nanosensor combined with a vertical position control based on a distance-dependent signal.

http://rcin.org.pl

14. Published papers

The results presented in this thesis are partially published in following papers:

1. "Tailored gold nanostructure arrays as catalysts for oxygen reduction in alkaline media and a single molecule SERS platform",

   Nogala, W., Kannan, P., Gawinkowski, S., Jönsson-Niedziolka, M., **Kominiak, M**., Waluk, J., Opallo, M.,

   Nanoscale, (2015, 7, 10767-10774).

2. "Voltammetric pH Nanosensor",

   Michalak, M., Kurel, M., Jedraszko, J., Toczydlowska, D., Wittstock, G., Opallo, M., Nogala, W.,

   Analytical Chemistry, (2015, 87, 11641−11645)

3. "Patterning Cu nanostructures tailored for CO_2 reduction to electrooxidizable fuels and oxygen reduction in alkaline media."

   Michalak, M., Roguska, A., Nogala, W., Opallo, M.

   Nanoscale Advances, (2019,1, 2645-2653)

Others papers with my co-authorship:

1. "Carbon Nanoparticulate Film Electrode Prepared by Electrophoretic Deposition. Electrochemical oxidation of Thiocholine and Topography Imaging with SECM Equipment in Dry Conditions",

   Celebanska, A., Lesniewski, A., Niedziolka-Jonsson, J., **Kominiak, M**., Nogala, W., Wittstock, G., Opallo, M.,

   Electrochimica Acta, (2014, 144, 136-140).

2. "The role of butylbenzene carbenium ions in the acid catalyzed cracking of polystyrene. Transformation of n-butylbenzene, sec-butylbenzene, iso-butylbenzene, tert-butylbenzene, 4-phenyl-1-butene, n-propylbenzene and n-hexylbenzene over silicaalumina and alumina acid catalysts"

   Marczewski, M., **Kominiak, M.**, Dul, M., Marczewska, H.

   Reaction Kinetics, Mechanisms and Catalysis, (2016, 119, 107-120)

3. "Hopping mode SECM imaging of redox activity in ionic liquid with glass-coated inlaid platinum nanoelectrodes prepared using a heating coil puller"

   Jedraszko, J., **Michalak, M**., Jönsson-Niedziolka, M., Nogala, W.

   Journal of Electroanalytical Chemistry, (2018, 815, 231–237)

http://rcin.org.pl

15. Bibliography

(1) Kommenda, N. The power switch: tracking Britain's record coal-free run https://www.theguardian.com/environment/ng-interactive/2019/may/25/the-power-switch-tracking-britains-record-coal-free-run.

(2) Sui, S.; Wang, X.; Zhou, X.; Su, Y.; Riffat, S.; Liu, C. jun. A Comprehensive Review of Pt Electrocatalysts for the Oxygen Reduction Reaction: Nanostructure, Activity, Mechanism and Carbon Support in PEM Fuel Cells. *J. Mater. Chem. A* **2017**, *5* (5), 1808–1825. https://doi.org/10.1039/C6TA08580F.

(3) Carmo, M.; Doubek, G.; Sekol, R. C.; Linardi, M.; Taylor, A. D. Development and Electrochemical Studies of Membrane Electrode Assemblies for Polymer Electrolyte Alkaline Fuel Cells Using FAA Membrane and Ionomer. *J. Power Sources* **2013**, *230*, 169–175. https://doi.org/10.1016/j.jpowsour.2012.12.015.

(4) Nørskov, J. K.; Rossmeisl, J.; Logadottir, A.; Lindqvist, L.; Kitchin, J. R.; Bligaard, T.; Jo´nsson, H. Origin of the Overpotential for Oxygen Reduction at a Fuel-Cell Cathode. *J. Phys. Chem. B* **2004**, *108*, 17886–17892. https://doi.org/10.1021/jp047349j.

(5) Kortlever, R.; Shen, J.; Schouten, K. J. P.; Calle-Vallejo, F.; Koper, M. T. M. Catalysts and Reaction Pathways for the Electrochemical Reduction of Carbon Dioxide. *J. Phys. Chem. Lett.* **2015**, *6* (20), 4073–4082. https://doi.org/10.1021/acs.jpclett.5b01559.

(6) Kas, R.; Kortlever, R.; Yilmaz, H.; Koper, M. T. M.; Mul, G. Manipulating the Hydrocarbon Selectivity of Copper Nanoparticles in CO_2 Electroreduction by Process Conditions. *ChemElectroChem* **2015**, *2* (3), 354–358. https://doi.org/10.1002/celc.201402373.

(7) Makos, M. A.; Omiatek, D. M.; Ewing, A. G.; Heien, M. L. Development and Characterization of a Voltammetric Carbon-Fiber Microelectrode PH Sensor. *Langmuir* **2010**, *26* (12), 10386–10391. https://doi.org/10.1021/la100134r.

(8) Lu, M.; Compton, R. G. Voltammetric PH Sensing Using Carbon Electrodes: Glassy Carbon Behaves Similarly to EPPG. *Analyst* **2014**, *139* (18), 4599. https://doi.org/10.1039/C4AN00866A.

(9) Lu, M.; Compton, R. G. Voltammetric PH Sensor Based on an Edge Plane Pyrolytic Graphite Electrode. *Analyst* **2014**, *139* (10), 2397–2403. https://doi.org/10.1039/c4an00147h.

(10) Stacy, J.; Regmi, Y. N.; Leonard, B.; Fan, M. The Recent Progress and Future of Oxygen Reduction Reaction Catalysis: A Review. *Renew. Sustain. Energy Rev.* **2017**, *69* (July 2015), 401–414. https://doi.org/10.1016/j.rser.2016.09.135.

(11) Kulkarni, A.; Siahrostami, S.; Patel, A.; Nørskov, J. K. Understanding Catalytic Activity Trends in the Oxygen Reduction Reaction. *Chem. Rev.* **2018**, *118* (5), 2302–2312. https://doi.org/10.1021/acs.chemrev.7b00488.

(12) Li, M.; Zhao, Z.; Cheng, T.; Fortunelli, A.; Chen, C. Y.; Yu, R.; Zhang, Q.; Gu, L.; Merinov, B. V; Lin, Z. Ultrafine Jagged Platinum Nanowires Enable Ultrahigh Mass Activity for the Oxygen Reduction Reaction. *Science* **2016**, *354* (6318), 1414–1419. https://doi.org/10.1126/science.aaf9050.

(13) Guerrero Moreno, N.; Cisneros Molina, M.; Gervasio, D.; Pérez Robles, J. F. Approaches to Polymer Electrolyte Membrane Fuel Cells (PEMFCs) and Their Cost. *Renew. Sustain. Energy Rev.* **2015**, *52*, 897–906. https://doi.org/10.1016/j.rser.2015.07.157.

(14) Sheng, W.; Gasteiger, H. A.; Shao-Horn, Y. Hydrogen Oxidation and Evolution Reaction Kinetics on Platinum: Acid *vs.* Alkaline Electrolytes. *J. Electrochem. Soc.* **2010**, *157* (11), B1529. https://doi.org/10.1149/1.3483106.

(15) Goenaga, G. A.; Roy, A. L.; Cantillo, N. M.; Foister, S.; Zawodzinski, T. A. A Family of Platinum Group Metal-Free Catalysts for Oxygen Reduction in Alkaline Media. *J. Power Sources* **2018**, *395* (February), 148–157. https://doi.org/10.1016/j.jpowsour.2018.05.025.

(16) Sekol, R. C.; Li, X.; Cohen, P.; Doubek, G.; Carmo, M.; Taylor, A. D. Silver Palladium Core-

http://rcin.org.pl

Shell Electrocatalyst Supported on MWNTs for ORR in Alkaline Media. *Appl. Catal. B Environ.* **2013**, *138–139*, 285–293. https://doi.org/10.1016/j.apcatb.2013.02.054.

(17) Antolini, E. Catalysts for Direct Ethanol Fuel Cells. *J. Power Sources* **2007**, *170*, 1–12. https://doi.org/doi:10.1016/j.jpowsour.2007.04.009.

(18) Meng, H.; Shen, P. K. Novel Pt-Free Catalyst for Oxygen Electroreduction. *Electrochem. Commun.* **2006**, *8* (4), 588–594. https://doi.org/10.1016/j.elecom.2006.01.020.

(19) Chatenet, M.; Genies-Bultel, L.; Aurousseau, M.; Durand, R.; Andolfatto, F. Oxygen Reduction on Silver Catalysts in Solutions Containing Various Concentrations of Sodium Hydroxide - Comparison with Platinum. *J. Appl. Electrochem.* **2002**, *32* (10), 1131–1140. https://doi.org/10.1023/A:1021231503922.

(20) Hansen, H. A.; Viswanathan, V.; NØrskov, J. K. Unifying Kinetic and Thermodynamic Analysis of 2 E- and 4 e- Reduction of Oxygen on Metal Surfaces. *J. Phys. Chem. C* **2014**, *118* (13), 6706–6718. https://doi.org/10.1021/jp4100608.

(21) Thorseth, M. A.; Tornow, C. E.; Tse, E. C. M.; Gewirth, A. A. Cu Complexes That Catalyze the Oxygen Reduction Reaction. *Coord. Chem. Rev.* **2013**, *257* (1), 130–139. https://doi.org/10.1016/j.ccr.2012.03.033.

(22) Katsounaros, I.; Cherevko, S.; Zeradjanin, A. R.; Mayrhofer, K. J. J. Oxygen Electrochemistry as a Cornerstone for Sustainable Energy Conversion. *Angew. Chemie - Int. Ed.* **2014**, *53* (1), 102–121. https://doi.org/10.1002/anie.201306588.

(23) Cheng, J.; Hu, P. Utilization of the Three-Dimensional Volcano Surface to Understand the Chemistry of Multiphase Systems in Heterogeneous Catalysis. *J. Am. Chem. Soc.* **2008**, *130* (33), 10868–10869. https://doi.org/10.1021/ja803555g.

(24) Flyagina, I. S.; Hughes, K. J.; Pourkashanian, M.; Ingham, D. B. DFT Study of the Oxygen Reduction Reaction on Iron, Cobalt and Manganese Macrocycle Active Sites. *Int. J. Hydrogen Energy* **2014**, *39* (36), 21538–21546. https://doi.org/10.1016/j.ijhydene.2014.09.075.

(25) Wellendorff, J.; Silbaugh, T. L.; Garcia-Pintos, D.; Nørskov, J. K.; Bligaard, T.; Studt, F.; Campbell, C. T. A Benchmark Database for Adsorption Bond Energies to Transition Metal Surfaces and Comparison to Selected DFT Functionals. *Surf. Sci.* **2015**, *640*, 36–44. https://doi.org/10.1016/j.susc.2015.03.023.

(26) Hansen, H. A.; Rossmeisl, J.; Nørskov, J. K. Surface Pourbaix Diagrams and Oxygen Reduction Activity of Pt, Ag and Ni(111) Surfaces Studied by DFT. *Phys. Chem. Chem. Phys.* **2008**, *10*, 3722–3730. https://doi.org/10.1039/b803956a.

(27) Siahrostami, S.; Verdaguer-Casadevall, A.; Karamad, M.; Deiana, D.; Malacrida, P.; Wickman, B.; Escudero-Escribano, M.; Paoli, E. A.; Frydendal, R.; Hansen, T. W.; et al. Enabling Direct H_2O_2 Production through Rational Electrocatalyst Design. *Nat. Mater.* **2013**, *12* (12), 1137–1143. https://doi.org/10.1038/nmat3795.

(28) Keith, J. A.; Jacob, T. Theoretical Studies of Potential-Dependent and Competing Mechanisms of the Electrocatalytic Oxygen Reduction Reaction on Pt(111). *Angew. Chemie - Int. Ed.* **2010**, *49* (49), 9521–9525. https://doi.org/10.1002/anie.201004794.

(29) Tripković, V.; Skúlason, E.; Siahrostami, S.; Nørskov, J. K.; Rossmeisl, J. The Oxygen Reduction Reaction Mechanism on Pt(111) from Density Functional Theory Calculations. *Electrochim. Acta* **2010**, *55* (27), 7975–7981. https://doi.org/10.1016/j.electacta.2010.02.056.

(30) Karlberg, G. S.; Rossmeisl, J.; Nørskov, J. K. Estimations of Electric Field Effects on the Oxygen Reduction Reaction Based on the Density Functional Theory. *Phys. Chem. Chem. Phys.* **2007**, *9* (37), 5158–5161. https://doi.org/10.1039/b705938h.

(31) Gasteiger, H. A.; Kocha, S. S.; Sompalli, B.; Wagner, F. T. Activity Benchmarks and Requirements for Pt, Pt-Alloy, and Non-Pt Oxygen Reduction Catalysts for PEMFCs. *Appl. Catal. B Environ.* **2005**, *56* (1-2 SPEC. ISS.), 9–35. https://doi.org/10.1016/j.apcatb.2004.06.021.

(32) Noël, J.-M.; Latus, A.; Lagrost, C.; Volanschi, E.; Hapiot, P. Evidence for OH Radical Production during Electrocatalysis of Oxygen Reduction on Pt Surfaces: Consequences and

http://rcin.org.pl

Application. *J. Am. Chem. Soc.* **2012**, *134* (5), 2835–2841. https://doi.org/10.1021/ja211663t.

(33) Li, D.; Lv, H.; Kang, Y.; Markovic, N. M.; Stamenkovic, V. R. Progress in the Development of Oxygen Reduction Reaction Catalysts for Low-Temperature Fuel Cells. *Annu. Rev. Chem. Biomol. Eng.* **2016**, *7* (1), 509–532. https://doi.org/10.1146/annurev-chembioeng-080615-034526.

(34) Lv, H.; Li, D.; Strmcnik, D.; Paulikas, A. P.; Markovic, N. M.; Stamenkovic, V. R. Recent Advances in the Design of Tailored Nanomaterials for Efficient Oxygen Reduction Reaction. *Nano Energy* **2016**, *29*, 149–165. https://doi.org/10.1016/j.nanoen.2016.04.008.

(35) Stephens, I. E. L.; Bondarenko, A. S.; Perez-Alonso, F. J.; Calle-Vallejo, F.; Bech, L.; Johansson, T. P.; Jepsen, A. K.; Frydendal, R.; Knudsen, B. P.; Rossmeisl, J.; et al. Tuning the Activity of Pt(111) for Oxygen Electroreduction by Subsurface Alloying. *J. Am. Chem. Soc.* **2011**, *133* (14), 5485–5491. https://doi.org/10.1021/ja111690g.

(36) Stamenkovic, V. R.; Mun, B. S.; Arenz, M.; Mayrhofer, K. J. J.; Lucas, C. A.; Wang, G.; Ross, P. N.; Markovic, N. M. Trends in Electrocatalysis on Extended and Nanoscale Pt-Bimetallic Alloy Surfaces. *Nat. Mater.* **2007**, *6* (3), 241–247. https://doi.org/10.1038/nmat1840.

(37) Mukerjee, S.; Srinivasan, S.; Soriaga, M. P. Role of Structural and Electronic Properties of Pt and Pt Alloys on Electrocatalysis of Oxygen Reduction. *J. Electrochem. Soc.* **1995**, *142* (5), 1409. https://doi.org/10.1149/1.2048590.

(38) Simonsen, S. B.; Chorkendorff, I.; Dahl, S.; Skoglundh, M.; Sehested, J.; Helveg, S. Direct Observations of Oxygen-Induced Platinum Nanoparticle Ripening Studied by In Situ TEM. *J. Am. Chem. Soc.* **2010**, *132* (23), 7968–7975. https://doi.org/10.1021/ja910094r.

(39) Yeo, K. M.; Choi, S.; Anisur, R. M.; Kim, J.; Lee, I. S. Surfactant-Free Platinum-on-Gold Nanodendrites with Enhanced Catalytic Performance for Oxygen Reduction. *Angew. Chemie - Int. Ed.* **2011**, *50* (3), 745–748. https://doi.org/10.1002/anie.201005775.

(40) Shao, M.; Peles, A.; Shoemaker, K.; Gummalla, M.; Njoki, P. N.; Luo, J.; Zhong, C. J. Enhanced Oxygen Reduction Activity of Platinum Monolayer on Gold Nanoparticles. *J. Phys. Chem. Lett.* **2011**, *2* (2), 67–72. https://doi.org/10.1021/jz1015789.

(41) Karan, H. I.; Sasaki, K.; Kuttiyiel, K.; Farberow, C. A.; Mavrikakis, M.; Adzic, R. R. Catalytic Activity of Platinum Monolayer on Iridium and Rhenium Alloy Nanoparticles for the Oxygen Reduction Reaction. *ACS Catal.* **2012**, *2* (5), 817–824. https://doi.org/10.1021/cs200592x.

(42) Kuttiyiel, K. A.; Sasaki, K.; Choi, Y.; Su, D.; Liu, P.; Adzic, R. R. Bimetallic IrNi Core Platinum Monolayer Shell Electrocatalysts for the Oxygen Reduction Reaction. *Energy Environ. Sci.* **2012**, *5* (1), 5297–5304. https://doi.org/10.1039/c1ee02067f.

(43) Jukk, K.; Alexeyeva, N.; Ritslaid, P.; Kozlova, J.; Sammelselg, V.; Tammeveski, K. Electrochemical Reduction of Oxygen on Heat-Treated Pd Nanoparticle/Multi-Walled Carbon Nanotube Composites in Alkaline Solution. *Electrocatalysis* **2013**, *4* (1), 42–48. https://doi.org/10.1007/s12678-012-0117-y.

(44) Qiao, J.; Lin, R.; Li, B.; Ma, J.; Liu, J. Kinetics and Electrocatalytic Activity of Nanostructured Ir-V/C for Oxygen Reduction Reaction. *Electrochim. Acta* **2010**, *55* (28), 8490–8497. https://doi.org/10.1016/j.electacta.2010.07.069.

(45) Zaikovskii, V. I.; Nagabhushana, K. S.; Kriventsov, V. V.; Loponov, K. N.; Cherepanova, S. V.; Kvon, R. I.; Bonnemann, H.; Kochubey, D. I.; Savinova, E. R. Synthesis and Structural Characterization of Se-Modified Carbon-Supported Ru Nanoparticles for the Oxygen Reduction Reaction. *J. Phys. Chem. B* **2006**, *110* (13), 6881–6890. https://doi.org/10.1021/jp056715b.

(46) Zhou, R.; Qiao, S. Z. Silver/Nitrogen-Doped Graphene Interaction and Its Effect on Electrocatalytic Oxygen Reduction. *Chem. Mater.* **2014**, *26* (20), 5868–5873. https://doi.org/10.1021/cm502260m.

(47) Goenaga, G. A.; Foister, S.; Belapure, A.; Byrne, K.; Hawks, S.; Papandrew, A. B.; Zawodzinski, T. Pyrolyzed Copper-Based Catalyst with High Oxygen Reduction Activity for PEM Fuel Cell Applications. *ECS Electrochem. Lett.* **2014**, *3* (11), F68–F71. https://doi.org/10.1016/j.ifacol.2015.08.147.

http://rcin.org.pl

(48) Nie, Y.; Li, L.; Wei, Z. Recent Advancements in Pt and Pt-Free Catalysts for Oxygen Reduction Reaction. *Chem. Soc. Rev.* **2015**, *44* (8), 2168–2201. https://doi.org/10.1039/c4cs00484a.

(49) Shao, M. Palladium-Based Electrocatalysts for Hydrogen Oxidation and Oxygen Reduction Reactions. *J. Power Sources* **2011**, *196* (5), 2433–2444. https://doi.org/10.1016/j.jpowsour.2010.10.093.

(50) Wei, Y. C.; Liu, C. W.; Wang, K. W. Improvement of Oxygen Reduction Reaction and Methanol Tolerance Characteristics for PdCo Electrocatalysts by Au Alloying and CO Treatment. *Chem. Commun.* **2011**, *47* (43), 11927–11929. https://doi.org/10.1039/c1cc15110j.

(51) Serov, A.; Robson, M. H.; Halevi, B.; Artyushkova, K.; Atanassov, P. Highly Active and Durable Templated Non-PGM Cathode Catalysts Derived from Iron and Aminoantipyrine. *Electrochem. Commun.* **2012**, *22* (1), 53–56. https://doi.org/10.1016/j.elecom.2012.04.029.

(52) Material, S. O.; Web, S.; York, N.; Nw, A. High-Performance Electrocatalysts for Oxygen Reduction Derived from Polyaniline, Iron, and Cobalt. *Science* **2011**, *332* (6028), 443–447. https://doi.org/10.1126/science.1200832.

(53) Thorum, M. S.; Yadav, J.; Gewirth, A. A. Oxygen Reduction Activity of a Copper Complex of 3,5-Diamino-1,2,4-Triazole Supported on Carbon Black. *Angew. Chemie - Int. Ed.* **2009**, *48* (1), 165–167. https://doi.org/10.1002/anie.200803554.

(54) Chong, L.; Goenaga, G. A.; Williams, K.; Barkholtz, H. M.; Grabstanowicz, L. R.; Brooksbank, J. A.; Papandrew, A. B.; Elzein, R.; Schlaf, R.; Zawodzinski, T. A.; et al. Investigation of Oxygen Reduction Activity of Catalysts Derived from Co and Co/Zn Methyl-Imidazolate Frameworks in Proton Exchange Membrane Fuel Cells. *ChemElectroChem* **2016**, *3* (10), 1541–1545. https://doi.org/10.1002/celc.201600163.

(55) Gong, K.; Du, F.; Xia, Z.; Durstock, M.; Dai, L. Nitrogen-Doped Carbon Nanotube Arrays with High Electrocatalytic Activity for Oxygen Reduction. *Science* **2009**, *323* (5915), 760–764. https://doi.org/10.1126/science.1168049.

(56) Qu, L.; Liu, Y.; Baek, J.; Dai, L. Nitrogen-Doped Graphene as Efficient Metal-Free Electrocatalyst for Oxygen Reduction in Fuel Cells. *ACS Nano* **2010**, *4* (3), 1321–1326.

(57) Nagaiah, T. C.; Kundu, S.; Bron, M.; Muhler, M.; Schuhmann, W. Nitrogen-Doped Carbon Nanotubes as a Cathode Catalyst for the Oxygen Reduction Reaction in Alkaline Medium. *Electrochem. Commun.* **2010**, *12* (3), 338–341. https://doi.org/10.1016/j.elecom.2009.12.021.

(58) National Energy Technology Laboratory https://www.netl.doe.gov/research/coal/carbon-storage/carbon-storage-faqs/what-are-the-primary-sources-of-co2%0A.

(59) Rohde, R. A. Global Warming Art http://www.globalwarmingart.com/.

(60) Betts, R. A.; Jones, C. D.; Knight, J. R.; Keeling, R. F.; Kennedy, J. J. El Niño and a Record CO 2 Rise. *Nat. Clim. Chnage* **2016**, doi:10.1038/nclimate3063. https://doi.org/10.1038/nclimate3063.

(61) Le Quéré, C.; Moriarty, R.; Andrew, R. M.; Canadell, J. G.; Sitch, S.; Korsbakken, J. I.; Friedlingstein, P.; Peters, G. P.; Andres, R. J.; Boden, T. A.; et al. Global Carbon Budget 2015. *Earth Syst. Sci. Data* **2015**, *7* (2), 349–396. https://doi.org/10.5194/essd-7-349-2015.

(62) Gao, T.; Shen, L.; Shen, M.; Chen, F.; Liu, L.; Gao, L. Analysis on Differences of Carbon Dioxide Emission from Cement Production and Their Major Determinants. *J. Clean. Prod.* **2015**, *103*, 160–170. https://doi.org/10.1016/j.jclepro.2014.11.026.

(63) Coskun, H.; Aljabour, A.; De Luna, P.; Farka, D.; Greunz, T.; Stifter, D.; Kus, M.; Zheng, X.; Liu, M.; Sargent, E. H.; et al. Biofunctionalized Conductive Polymers Enable Efficient CO_2 Electroreduction. *Sci. Adv.* **2017**, No. August, 1–9. https://doi.org/10.1126/sciadv.1700686.

(64) Xie, M. S.; Xia, B. Y.; Li, Y.; Yan, Y.; Yang, Y.; Sun, Q.; Chan, S. H.; Fisher, A.; Wang, X. Amino Acid Modified Copper Electrodes for the Enhanced Selective Electroreduction of Carbon Dioxide towards Hydrocarbons. *Energy Environ. Sci.* **2016**, *9* (5), 1687–1695. https://doi.org/10.1039/C5EE03694A.

(65) Dunwell, M.; Lu, Q.; Heyes, J. M.; Rosen, J.; Chen, J. G.; Yan, Y.; Jiao, F.; Xu, B. The Central

http://rcin.org.pl

Role of Bicarbonate in the Electrochemical Reduction of Carbon Dioxide on Gold. *J. Am. Chem. Soc.* **2017**, *139* (10), 3774–3783. https://doi.org/10.1021/jacs.6b13287.

(66) Dumesic, J. A.; Huber, G. W.; Boudart, M. *Handbook of Heterogeneous Catalysis*; Ertl, G., Knözinge, H., Schüth, F., Weitkamp, J., Eds.; Wiley-VCH: Wienheim, 2008.

(67) Koper, M. T. M. Theory of Multiple Proton–Electron Transfer Reactions and Its Implications for Electrocatalysis. *Chem. Sci.* **2013**, *4* (7), 2710. https://doi.org/10.1039/c3sc50205h.

(68) Koper, M. T. M. Thermodynamic Theory of Multi-Electron Transfer Reactions: Implications for Electrocatalysis. *J. Electroanal. Chem.* **2011**, *660* (2), 254–260. https://doi.org/10.1016/j.jelechem.2010.10.004.

(69) Kuhl, K. P.; Hatsukade, T.; Cave, E. R.; Abram, D. N.; Kibsgaard, J.; Jaramillo, T. F. Electrocatalytic Conversion of Carbon Dioxide to Methane and Methanol on Transition Metal Surfaces. *J. Am. Chem. Soc.* **2014**, *136* (40), 14107–14113. https://doi.org/10.1021/ja505791r.

(70) Feaster, J. T.; Shi, C.; Cave, E. R.; Hatsukade, T.; Abram, D. N.; Kuhl, K. P.; Hahn, C.; Nørskov, J. K.; Jaramillo, T. F. Understanding Selectivity for the Electrochemical Reduction of Carbon Dioxide to Formic Acid and Carbon Monoxide on Metal Electrodes. *ACS Catal.* **2017**, *7* (7), 4822–4827. https://doi.org/10.1021/acscatal.7b00687.

(71) Hori, Y.; Kikuchi, K.; Shin, S. Production of CO and CH4 in Electrochemical Reduction of CO_2 at Metal Electrodes in Aqueous Hydrogencarbonate Solution. *Chem. Lett* **1985**, *11*, 1695–1698.

(72) Varela, A. S.; Kroschel, M.; Reier, T.; Strasser, P. Controlling the Selectivity of CO_2 Electroreduction on Copper: The Effect of the Electrolyte Concentration and the Importance of the Local PH. *Catal. Today* **2016**, *260*, 8–13. https://doi.org/10.1016/j.cattod.2015.06.009.

(73) Kas, R.; Hummadi, K. K.; Kortlever, R.; de Wit, P.; Milbrat, A.; Luiten-Olieman, M. W. J.; Benes, N. E.; Koper, M. T. M.; Mul, G. Three-Dimensional Porous Hollow Fibre Copper Electrodes for Efficient and High-Rate Electrochemical Carbon Dioxide Reduction. *Nat. Commun.* **2016**, *7*, 10748. https://doi.org/10.1038/ncomms10748.

(74) Roberts, F. S.; Kuhl, K. P.; Nilsson, A. High Selectivity for Ethylene from Carbon Dioxide Reduction over Copper Nanocube Electrocatalysts. *Angew. Chemie - Int. Ed.* **2015**, *54* (17), 5179–5182. https://doi.org/10.1002/anie.201412214.

(75) Reske, R.; Mistry, H.; Behafarid, F.; Roldan Cuenya, B.; Strasser, P. Particle Size Effects in the Catalytic Electroreduction of CO_2 on Cu Nanoparticles. *J. Am. Chem. Soc.* **2014**, *136* (19), 6978–6986. https://doi.org/10.1021/ja500328k.

(76) Monzó, J.; Malewski, Y.; Kortlever, R.; Vidal-Iglesias, F. J.; Solla-Gullón, J.; Koper, M. T. M.; Rodriguez, P. Enhanced Electrocatalytic Activity of Au@Cu Core@shell Nanoparticles towards CO_2 Reduction. *J. Mater. Chem. A* **2015**, *3* (47), 23690–23698. https://doi.org/10.1039/C5TA06804E.

(77) Garza, A.; Bell, A. T.; Head-Gordon, M. Is Subsurface Oxygen Necessary for the Electrochemical Reduction of CO_2 on Copper? *J. Phys. Chem. Lett.* **2018**, acs.jpclett.7b03180. https://doi.org/10.1021/acs.jpclett.7b03180.

(78) Kuhl, K. P.; Cave, E. R.; Abram, D. N.; Jaramillo, T. F. New Insights into the Electrochemical Reduction of Carbon Dioxide on Metallic Copper Surfaces. *Energy Environ. Sci.* **2012**, *5* (5), 7050. https://doi.org/10.1039/c2ee21234j.

(79) Hatsukade, T.; Kuhl, K. P.; Cave, E. R.; Abram, D. N.; Jaramillo, T. F. Insights into the Electrocatalytic Reduction of CO_2 on Metallic Silver Surfaces. *Phys. Chem. Chem. Phys.* **2014**, *16* (27), 13814–13819. https://doi.org/10.1039/C4CP00692E.

(80) Zhang, S.; Kang, P.; Meyer, T. J. Nanostructured Tin Catalysts for Selective Electrochemical Reduction of Carbon Dioxide to Formate. *J. Am. Chem. Soc.* **2014**, *136* (5), 1734–1737. https://doi.org/10.1021/ja4113885.

(81) Qiao, J.; Jiang, P.; Liu, J.; Zhang, J. Formation of Cu Nanostructured Electrode Surfaces by an Annealing-Electroreduction Procedure to Achieve High-Efficiency CO_2 Electroreduction. *Electrochem. Commun.* **2014**, *38*, 8–11. https://doi.org/10.1016/j.elecom.2013.10.023.

http://rcin.org.pl

(82) Chen, C. S.; Handoko, A. D.; Wan, J. H.; Ma, L.; Ren, D.; Yeo, B. S. Stable and Selective Electrochemical Reduction of Carbon Dioxide to Ethylene on Copper Mesocrystals. *Catal. Sci. Technol.* **2015**, *5* (1), 161–168. https://doi.org/10.1039/C4CY00906A.

(83) Kim, C.; Jeon, H. S.; Eom, T.; Jee, M. S.; Kim, H.; Friend, C. M.; Min, B. K.; Hwang, Y. J. Achieving Selective and Efficient Electrocatalytic Activity for CO_2 Reduction Using Immobilized Silver Nanoparticles. *J. Am. Chem. Soc.* **2015**, *137* (43), 13844–13850. https://doi.org/10.1021/jacs.5b06568.

(84) Gao, D.; Zhou, H.; Wang, J.; Miao, S.; Yang, F.; Wang, G.; Wang, J.; Bao, X. Size-Dependent Electrocatalytic Reduction of CO_2 over Pd Nanoparticles. *J. Am. Chem. Soc.* **2015**, 4288–4291. https://doi.org/10.1021/jacs.5b00046.

(85) Watanabe, M.; Shibata, M.; Kato, A. Design of Alloy Electrocatalysts for C02 Reduction. Improved Energy Efficiency, Selectivity, and Reaction Rate for the CO_2 Electroreduction on Cu Alloy Electrodes. *J. Electrochem. Soc.* **1991**, *138*, 3382–3389. https://doi.org/10.1149/1.2085417.

(86) Hori, Y.; Wakebe, H.; Tsukamoto, T.; Koga, O. Electrocatalytic Process of CO Selectivity in Electrochemical Reduction of CO_2 at Metal Electrodes in Aqueous Media. *Electrochim. Acta* **1994**, *39*, 1833–1839. https://doi.org/10.1016/0013-4686(94)85172-7.

(87) Kim, D.; Resasco, J.; Yu, Y.; Asiri, A. M.; Yang, P. Synergistic Geometric and Electronic Effects for Electrochemical Reduction of Carbon Dioxide Using Gold-Copper Bimetallic Nanoparticles. *Nat. Commun.* **2014**, *5* (May), 1–8. https://doi.org/10.1038/ncomms5948.

(88) Hoffman, Z. B.; Gray, T. S.; Moraveck, K. B.; Gunnoe, T. B.; Zangari, G. Electrochemical Reduction of Carbon Dioxide to Syngas and Formate at Dendritic Copper-Indium Electrocatalysts. *ACS Catal.* **2017**, *7* (8), 5381–5390. https://doi.org/10.1021/acscatal.7b01161.

(89) Sarfraz, S.; Garcia-Esparza, A. T.; Jedidi, A.; Cavallo, L.; Takanabe, K. Cu-Sn Bimetallic Catalyst for Selective Aqueous Electroreduction of CO_2 to CO. *ACS Catal.* **2016**, *6* (5), 2842–2851. https://doi.org/10.1021/acscatal.6b00269.

(90) Li, M.; Wang, J.; Li, P.; Chang, K.; Li, C.; Wang, T.; Jiang, B.; Zhang, H.; Liu, H.; Yamauchi, Y.; et al. Mesoporous Palladium-Copper Bimetallic Electrodes for Selective Electrocatalytic Reduction of Aqueous CO_2 to CO. *J. Mater. Chem. A* **2016**, *4* (13), 4776–4782. https://doi.org/10.1039/c6ta00487c.

(91) He, J.; Johnson, N. J.; Huang, A.; Berlinguette, C. Electrocatalytic Alloys for CO_2 Reduction. *ChemSusChem* **2018**, *11* (1), 48–57. https://doi.org/10.1002/cssc.201701825.

(92) Choi, S. Y.; Jeong, S. K.; Kim, H. J.; Baek, I. H.; Park, K. T. Electrochemical Reduction of Carbon Dioxide to Formate on Tin-Lead Alloys. *ACS Sustain. Chem. Eng.* **2016**, *4* (3), 1311–1318. https://doi.org/10.1021/acssuschemeng.5b01336.

(93) Luc, W.; Collins, C.; Wang, S.; Xin, H.; He, K.; Kang, Y.; Jiao, F. Ag–Sn Bimetallic Catalyst with a Core–Shell Structure for CO_2 Reduction. *J. Am. Chem. Soc.* **2017**, *139* (5), 1885–1893. https://doi.org/10.1021/jacs.6b10435.

(94) Kortlever, R.; Peters, I.; Koper, S.; Koper, M. T. M. Electrochemical CO_2 Reduction to Formic Acid at Low Overpotential and with High Faradaic Efficiency on Carbon-Supported Bimetallic Pd-Pt Nanoparticles. *ACS Catal.* **2015**, *5* (7), 3916–3923. https://doi.org/10.1021/acscatal.5b00602.

(95) Hahn, C.; Abram, D. N.; Hansen, H. A.; Hatsukade, T.; Jackson, A.; Johnson, N. C.; Hellstern, T. R.; Kuhl, K. P.; Cave, E. R.; Feaster, J. T.; et al. Synthesis of Thin Film AuPd Alloys and Their Investigation for Electrocatalytic CO_2 Reduction. *J. Mater. Chem. A* **2015**, *3* (40), 20185–20194. https://doi.org/10.1039/c5ta04863j.

(96) Meshitsuka, S.; Ichikawa, M.; Tamaru, K. Electrocatalysis by Metal Phthalocyanines in the Reduction of Carbon Dioxide. *J. Chem. Soc. Chem. Commun.* **1974**, No. 0, 158–159.

(97) Shen, J.; Kortlever, R.; Kas, R.; Birdja, Y. Y.; Diaz-Morales, O.; Kwon, Y.; Ledezma-Yanez, I.; Schouten, K. J. P.; Mul, G.; Koper, M. T. M. Electrocatalytic Reduction of Carbon Dioxide to Carbon Monoxide and Methane at an Immobilized Cobalt Protoporphyrin. *Nat. Commun.* **2015**,

http://rcin.org.pl

6, 1–8. https://doi.org/10.1038/ncomms9177.

(98) Froehlich, J. D.; Kubiak, C. P. The Homogeneous Reduction of CO_2 by $[Ni(Cyclam)]^+$: Increased Catalytic Rates with the Addition of a CO Scavenger. *J. Am. Chem. Soc.* **2015**, *137* (10), 3565–3573.

(99) Zhang, X.; Wu, Z.; Zhang, X.; Li, L.; Li, Y.; Xu, H.; Li, X.; Yu, X.; Zhang, Z.; Liang, Y.; et al. Highly Selective and Active CO_2 Reduction Electrocatalysts Based on Cobalt Phthalocyanine/Carbon Nanotube Hybrid Structures. *Nat. Commun.* **2017**, *8* (March), 1–8. https://doi.org/10.1038/ncomms14675.

(100) Gupta, N.; Gattrell, M.; MacDougall, B. Calculation for the Cathode Surface Concentrations in the Electrochemical Reduction of CO_2 in $KHCO_3$ Solutions. *J. Appl. Electrochem.* **2006**, *36* (2), 161–172. https://doi.org/10.1007/s10800-005-9058-y.

(101) Weiss, R. F. Carbon Dioxide in Water and Seawater: The Solubility of a Non - Ideal Gas. *Mar. Chem.* **1974**, *2*, 203–215. https://doi.org/https://doi.org/10.1016/0304-4203(74)90015-2.

(102) Tomiyasu, H.; Shikata, H.; Takao, K.; Asanuma, N.; Taruta, S.; Park, Y. Y. An Aqueous Electrolyte of the Widest Potential Window and Its Superior Capability for Capacitors. *Sci. Rep.* **2017**, *7*, 1–12. https://doi.org/10.1038/srep45048.

(103) Figueiredo, M. C.; Ledezma-Yanez, I.; Koper, M. T. M. In Situ Spectroscopic Study of CO_2 Electroreduction at Copper Electrodes in Acetonitrile. *ACS Catal.* **2016**, *6* (4), 2382–2392. https://doi.org/10.1021/acscatal.5b02543.

(104) Amatore, C.; Savéant, J. M. Mechanism and Kinetic Characteristics of the Electrochemical Reduction of Carbon Dioxide in Media of Low Proton Availability. *J. Am. Chem. Soc.* **1981**, *103* (17), 5021–5023. https://doi.org/10.1021/ja00407a008.

(105) Tomita, Y.; Hori, Y. Electrochemical Reduction of Carbon Dioxide at a Platinum Electrode in Acetonitrile-Water Mixtures. **2000**, *147*, 4164–4167.

(106) Tanner, E. E. L.; Batchelor-McAuley, C.; Compton, R. G. Carbon Dioxide Reduction in Room-Temperature Ionic Liquids: The Effect of the Choice of Electrode Material, Cation, and Anion. *J. Phys. Chem. C* **2016**, *120* (46), 26442–26447. https://doi.org/10.1021/acs.jpcc.6b10564.

(107) Raub, C. *The History of Electroplating*; Butterworth-Heinemann Ltd, 1993. https://doi.org/10.1016/B978-0-7506-1611-9.50027-3.

(108) Torabinejad, V.; Aliofkhazraei, M.; Assareh, S.; Allahyarzadeh, M. H.; Rouhaghdam, A. S. Electrodeposition of Ni-Fe Alloys, Composites, and Nano Coatings–A Review. *J. Alloys Compd.* **2017**, *691*, 841–859. https://doi.org/10.1016/j.jallcom.2016.08.329.

(109) Wu, Y.; Wang, L.; Chen, M.; Jin, Z.; Zhang, W.; Cao, R. Preparation of Cobalt-Based Electrodes by Physical Vapor Deposition on Various Nonconductive Substrates for Electrocatalytic Water Oxidation. *ChemSusChem* **2017**, *10* (23), 4699–4703. https://doi.org/10.1002/cssc.201701576.

(110) Zhuang, J.; Xu, X.; Peleckis, G.; Hao, W.; Dou, S. X.; Du, Y. Silicene: A Promising Anode for Lithium-Ion Batteries. *Adv. Mater.* **2017**, *29* (48). https://doi.org/10.1002/adma.201606716.

(111) Hou, Q.; Cao, G.; Wang, P.; Zhao, D.; Cui, X.; Li, S.; Li, C. Carbon Coating Nanostructured-LiNi1/3Co1/3Mn1/3O2cathode Material Synthesized by Chemical Vapor Deposition Method for High Performance Lithium-Ion Batteries. *J. Alloys Compd.* **2018**, *747*, 796–802. https://doi.org/10.1016/j.jallcom.2018.03.115.

(112) Zhang, R.; Wang, Y.; Jia, M.; Xu, J.; Pan, E. One-Pot Hydrothermal Synthesis of ZnS Quantum Dots/Graphene Hybrids as a Dual Anode for Sodium Ion and Lithium Ion Batteries. *Appl. Surf. Sci.* **2018**, *437*, 375–383. https://doi.org/10.1016/j.apsusc.2017.12.110.

(113) Gurrappa, I.; Binder, L. Electrodeposition of Nanostructured Coatings and Their Characterization - A Review. *Sci. Technol. Adv. Mater.* **2008**, *9* (4). https://doi.org/10.1088/1468-6996/9/4/043001.

(114) Asa Deepthi, K.; Balachandran, R.; Ong, B. H.; Tan, K. B.; Wong, H. Y.; Yow, H. K.; Srimala, S. Physical and Electrical Characteristics of NiFe Thin Films Using Ultrasonic Assisted Pulse Electrodeposition. *Appl. Surf. Sci.* **2016**, *360*, 519–524.

http://rcin.org.pl

https://doi.org/10.1016/j.apsusc.2015.10.181.

(115) Schlesinger, M.; Paunovic, M. *Modern Electroplating*, 5th ed.; John Wiley & Sons, Inc.: Hoboken, New Jersey, 2010.

(116) Ibl, N. Some Theoretical Aspects of Pulse Electrolysis. *Surf. Technol.* **1980**, *10*, 81–104.

(117) Sohrabi, A.; Dolati, A.; Ghorbani, M.; Monfared, A.; Stroeve, P. Nanomechanical Properties of Functionally Graded Composite Coatings: Electrodeposited Nickel Dispersions Containing Silicon Micro- and Nanoparticles. *Mater. Chem. Phys.* **2010**, *121* (3), 497–505. https://doi.org/10.1016/j.matchemphys.2010.02.014.

(118) Frade, T.; Siopa, D.; Martins, A. F.; Carreira, J. F. C.; Rodrigues, J.; Sedrine, N. Ben; Correia, M. R.; Monteiro, T.; Tena-Zaera, R.; Gomes, A. Optoelectronic Characterization of ZnO Nanorod Arrays Obtained by Pulse Electrodeposition. *J. Electrochem. Soc.* **2018**, *165* (13), D595–D603. https://doi.org/10.1149/2.0131813jes.

(119) Lahiri, A.; Endres, F. Review—Electrodeposition of Nanostructured Materials from Aqueous, Organic and Ionic Liquid Electrolytes for Li-Ion and Na-Ion Batteries: A Comparative Review. *J. Electrochem. Soc.* **2017**, *164* (9), D597–D612. https://doi.org/10.1149/2.1011709jes.

(120) Mohanty, U. S. Electrodeposition: A Versatile and Inexpensive Tool for the Synthesis of Nanoparticles, Nanorods, Nanowires, and Nanoclusters of Metals. *J. Appl. Electrochem.* **2011**, *41* (3), 257–270. https://doi.org/10.1007/s10800-010-0234-3.

(121) Gowthaman, N. S. K.; John, S. A. Fabrication of Different Copper Nanostructures on Indium-Tin-Oxide Electrodes: Shape Dependent Electrocatalytic Activity. *CrystEngComm* **2016**, *18* (44), 8696–8708. https://doi.org/10.1039/c6ce01846g.

(122) Bai, X. F.; Chen, W.; Zhao, C. C.; Li, S. G.; Song, Y. F.; Ge, R. P.; Wei, W.; Sun, Y. H. Exclusive Formation of Formic Acid from CO_2 Electroreduction by a Tunable Pd-Sn Alloy. *Angew. Chemie-International Ed.* **2017**, *56* (40), 12219–12223. https://doi.org/10.1002/anie.201707098.

(123) Jiang, B.; Zhang, X. G.; Jiang, K.; Wu, D. Y.; Cai, W. B. Boosting Formate Production in Electrocatalytic CO_2 Reduction over Wide Potential Window on Pd Surfaces. *J. Am. Chem. Soc.* **2018**, *140* (8), 2880–2889. https://doi.org/10.1021/jacs.7b12506.

(124) Hori, Y. Electrochemical CO_2 Reduction on Metal Electrodes. In *Modern Aspects of Electrochemistry*; Vayenas, C. G., White, R. E., Gamboa-Aldeco, M. E., Eds.; Springer, 2008; Vol. 42, pp 89–189.

(125) Egle, T.; Barroo, C.; Janvelyan, N.; Baumgaertel, A. C.; Akey, A. J. Y.; Biener, M. M.; Friend, C. M.; Bell, D. C.; Biener, J. Multiscale Morphology of Nanoporous Copper Made from Intermetallic Phases. *ACS Appl. Mater. Interfaces* **2017**, *9* (30), 25615–25622. https://doi.org/10.1021/acsami.7b05648.

(126) Peng, Y. C.; Wu, T.; Sun, L. B.; Nsanzimana, J. M. V; Fisher, A. C.; Wang, X. Selective Electrochemical Reduction of CO_2 to Ethylene on Nanopores-Modified Copper Electrodes in Aqueous Solution. *ACS Appl. Mater. Interfaces* **2017**, *9* (38), 32782–32789. https://doi.org/10.1021/acsami.7b10421.

(127) Le Duff, C. S.; Lawrence, M. J.; Rodriguez, P. Role of the Adsorbed Oxygen Species in the Selective Electrochemical Reduction of CO_2 to Alcohols and Carbonyls on Copper Electrodes. *Angew. Chemie-International Ed.* **2017**, *56* (42), 12919–12924. https://doi.org/10.1002/anie.201706463.

(128) Zhao, J.; Sun, L. B.; Canepa, S.; Sun, H. Y.; Yesibolati, M. N.; Sherburne, M.; Xu, R.; Sritharan, T.; Loo, J. S. C.; Ager, J. W.; et al. Phosphate Tuned Copper Electrodeposition and Promoted Formic Acid Selectivity for Carbon Dioxide Reduction. *J. Mater. Chem. A* **2017**, *5* (23), 11905–11916. https://doi.org/10.1039/c7ta01871a.

(129) Brisard, G.; Bertrand, N.; Ross, P. N.; Markovic, N. M. Oxygen Reduction and Hydrogen Evolution-Oxidation Reactions on Cu(Hkl) Surfaces. *J. Electroanal. Chem.* **2000**, *480* (1–2), 219–224. https://doi.org/Doi 10.1016/S0022-0728(99)00463-5.

http://rcin.org.pl

(130) Liu, K.; Song, Y.; Chen, S. Electrocatalytic Activities of Alkyne-Functionalized Copper Nanoparticles in Oxygen Reduction in Alkaline Media. *J. Power Sources* **2014**, *268*, 469–475. https://doi.org/10.1016/j.jpowsour.2014.06.054.

(131) Li, Z. X.; Ma, Z. Z.; Wen, Y. Y.; Ren, Y.; Wei, Z. T.; Xing, X. F.; Sun, H.; Zhang, Y. W.; Song, W. Y. Copper Nanoflower Assembled by Sub-2 Nm Rough Nanowires for Efficient Oxygen Reduction Reaction: High Stability and Poison Resistance and Density Functional Calculations. *ACS Appl. Mater. Interfaces* **2018**, *10* (31), 26233–26240. https://doi.org/10.1021/acsami.8b06722.

(132) Gao, F.; Pang, H.; Xu, S.; Lu, Q. Copper-Based Nanostructures: Promising Antibacterial Agents and Photocatalysts. *Chem. Commun.* **2009**, No. 24, 3571–3573. https://doi.org/10.1039/b904801d.

(133) He, Z.; He, J.; Zhang, Z. Selective Growth of Metallic Nanostructures on Microstructured Copper Substrate in Solution. *CrystEngComm* **2015**, *17* (38), 7262–7269. https://doi.org/10.1039/c5ce01093d.

(134) Gawande, M. B.; Goswami, A.; Felpin, F. X.; Asefa, T.; Huang, X.; Silva, R.; Zou, X.; Zboril, R.; Varma, R. S. Cu and Cu-Based Nanoparticles: Synthesis and Applications in Catalysis. *Chem. Rev.* **2016**, *116* (6), 3722–3811. https://doi.org/10.1021/acs.chemrev.5b00482.

(135) Poulomi, R.; Srivastava, S. K. Nanostructured Copper Sulfides: Synthesis, Properties and Applications. *CrystEngComm* **2015**, *17* (41), 7801–7815. https://doi.org/10.1039/C5CE01304F.

(136) Hwang, D. W.; Lee, S.; Seo, M.; Chung, T. D. Recent Advances in Electrochemical Glucose Biosensors: A Review. *RSC Adv.* **2013**, *3*, 4473–4491. https://doi.org/DOI: 10.1039/c2ra22351a.

(137) Dar, M. I.; Sampath, S.; Shivashankar, S. A. Microwave-Assisted, Surfactant-Free Synthesis of Air-Stable Copper Nanostructures and Their SERS Study. *J. Mater. Chem.* **2012**, *22* (42), 22418–22423. https://doi.org/10.1039/c2jm35629e.

(138) Fan, P.; Wu, H.; Zhong, M.; Zhang, H.; Bai, B.; Jin, G. Large-Scale Cauliflower-Shaped Hierarchical Copper Nanostructures for Efficient Photothermal Conversion. *Nanoscale* **2016**, *8* (30), 14617–14624. https://doi.org/10.1039/c6nr03662g.

(139) Vilaro, I.; Yague, J. L.; Borros, S. Superhydrophobic Copper Surfaces with Anticorrosion Properties Fabricated by Solventless CVD Methods. *ACS Appl. Mater. Interfaces* **2017**, *9* (1), 1057–1065. https://doi.org/10.1021/acsami.6b12119.

(140) Pham, Q. N.; Shao, B.; Kim, Y.; Won, Y. Hierarchical and Well-Ordered Porous Copper for Liquid Transport Properties Control. *ACS Appl. Mater. Interfaces* **2018**, *10* (18), 16015–16023. https://doi.org/10.1021/acsami.8b02665.

(141) Ke, X.; Cheng, Y. F.; Liu, J.; Liu, L. Y.; Wang, N. G.; Liu, J. P.; Zhi, C. Y.; Shi, Z. C.; Guo, Z. P. Hierarchically Bicontinuous Porous Copper as Advanced 3D Skeleton for Stable Lithium Storage. *ACS Appl. Mater. Interfaces* **2018**, *10* (16), 13552–13561. https://doi.org/10.1021/acsami.8b01978.

(142) Qiu, R.; Cha, H. G.; Noh, H. B.; Shim, Y. B.; Zhang, X. L.; Qiao, R.; Zhang, D.; Kim, Y. Il; Pal, U.; Kang, Y. S. Preparation of Dendritic Copper Nanostructures and Their Characterization for Electroreduction. *J. Phys. Chem. C* **2009**, *113* (36), 15891–15896. https://doi.org/10.1021/jp904222b.

(143) Mignani, A.; Ballarin, B.; Boanini, E.; Cassani, M. C. Simple One Step Electrochemical Preparation of Copper Nanostructures. *Electrochim. Acta* **2014**, *115*, 537–545. https://doi.org/10.1016/j.electacta.2013.10.207.

(144) Nam, D. H.; Taitt, B. J.; Choi, K. S. Copper-Based Catalytic Anodes To Produce 2,5-Furandicarboxylic Acid, a Biomass-Derived Alternative to Terephthalic Acid. *Acs Catal.* **2018**, *8* (2), 1197–1206. https://doi.org/10.1021/acscatal.7b03152.

(145) Han, Y. J.; Zhang, X.; Leach, G. W. Shape Control of Electrodeposited Copper Films and Nanostructures through Additive Effects. *Langmuir* **2014**, *30* (12), 3589–3598. https://doi.org/10.1021/la500001j.

http://rcin.org.pl

(146) Liu, P.; Qin, R.; Fu, G.; Zheng, N. Surface Coordination Chemistry of Metal Nanomaterials. *J. Am. Chem. Soc.* **2017**, *139* (6), 2122–2131. https://doi.org/10.1021/jacs.6b10978.

(147) Kunz, S. Supported, Ligand-Functionalized Nanoparticles: An Attempt to Rationalize the Application and Potential of Ligands in Heterogeneous Catalysis. *Top. Catal.* **2016**, *59* (19–20), 1671–1685. https://doi.org/10.1007/s11244-016-0687-7.

(148) Huang, W.; Hua, Q.; Cao, T. Influence and Removal of Capping Ligands on Catalytic Colloidal Nanoparticles. *Catal. Letters* **2014**, *144* (8), 1355–1369. https://doi.org/10.1007/s10562-014-1306-5.

(149) Pereira, A. J.; Gomes, J. P.; Lenz, G. F.; Schneider, R.; Chaker, J. A.; De Souza, P. E. N.; Felix, J. F. Facile Shape-Controlled Fabrication of Copper Nanostructures on Borophosphate Glasses: Synthesis, Characterization, and Their Highly Sensitive Surface-Enhanced Raman Scattering (SERS) Properties. *J. Phys. Chem. C* **2016**, *120* (22), 12265–12272. https://doi.org/10.1021/acs.jpcc.6b02881.

(150) Wei, F.; Li, L.; Liu, L. Facile Synthesis of Copper Nanostructures through Simple Replacement Reaction. *2015 IEEE 10th Int. Conf. Nano/Micro Eng. Mol. Syst. NEMS 2015* **2015**, 160–163. https://doi.org/10.1109/NEMS.2015.7147400.

(151) Momotenko, D.; Page, A.; Adobes-Vidal, M.; Unwin, P. R. Write-Read 3D Patterning with a Dual-Channel Nanopipette. *ACS Nano* **2016**, *10* (9), 8871–8878. https://doi.org/10.1021/acsnano.6b04761.

(152) Zhang, H.; Wu, L.; Huang, F. Electrochemical Microprocess by Scanning Ion-Conductance Microscopy. *J. Vac. Sci. Technol. B Microelectron. Nanom. Struct.* **1999**, *17* (2), 269. https://doi.org/10.1116/1.590549.

(153) Müller, A. D.; Müller, F.; Hietschold, M. Localized Electrochemical Deposition of Metals Using Micropipettes. *Thin Solid Films* **2000**, *366* (1–2), 32–36. https://doi.org/10.1016/S0040-6090(99)01117-7.

(154) Staemmler, L.; Suter, T.; Böhni, H. Nanolithography by Means of an Electrochemical Scanning Capillary Microscope. *J. Electrochem. Soc.* **2004**, *151* (11), G734. https://doi.org/10.1149/1.1803834.

(155) El-Giar, E. M.; Said, R. A.; Bridges, G. E.; Thomson, D. J. Localized Electrochemical Deposition of Copper Microstructures. *J. Electrochem. Soc.* **2000**, *147* (2), 586. https://doi.org/10.1149/1.1393237.

(156) Radtke, V.; Heß, C.; Souto, R. M.; Heinze, J. Electroless, Electrolytic and Galvanic Copper Deposition with the Scanning Electrochemical Microscope (SECM). *Zeitschrift fur Phys. Chemie* **2006**, *220* (4), 393–406. https://doi.org/10.1524/zpch.2006.220.4.393.

(157) McNaught, A. D.; Wilkinson, A. *IUPAC. Compendium of Chemical Terminology, 2nd Ed. (the "Gold Book")*; Blackwell Scientific Publications: Oxford, 1997. https://doi.org/https://doi.org/10.1351/goldbook.

(158) Crow, D. R. Principles and Applications of Electrochemistry; Springer: Wolverhampton, 1974. https://doi.org/10.1007/978-1-4899-7154-8.

(159) Bielański, A. *Podstawy Chemii Nieorganicznej*, 5th ed.; Wydawnictwo naukowe PWN: Warsaw, 2007.

(160) Lim, K. F. Negative PH Does Exist. *J. Chem. Educ.* **2009**, *83* (10), 1465. https://doi.org/10.1021/ed083p1465.

(161) Minczewski, J.; Marczenko, Z. *Chemia Analityczna. 1, Podstawy Teoretyczne i Analiza Jakościowa.*, 9th ed.; Wydawnicto Naukowe PWN: Warszawa, 2004.

(162) Flis-Kabulska, I.; Sun, Y.; Flis, J. Monitoring the Near-Surface PH to Probe the Role of Nitrogen Incorrosion Behaviour of Low-Temperature Plasma Nitrided 316L Stainless Steel. *Electrochim. Acta* **2013**, *104*, 208–215. https://doi.org/10.1016/j.electacta.2013.04.111.

(163) Serrapede, M.; Pesce, G. L.; Ball, R. J.; Denuault, G. Nanostructured Pd Hydride Microelectrodes: In Situ Monitoring of PH Variations in a Porous Medium. *Anal. Chem.* **2014**,

http://rcin.org.pl

86, 5758−5765. https://doi.org//10.1021/ac500310j.

(164) Zuaznabar-Gardona, J. C.; Fragoso, A. A Wide-Range Solid State Potentiometric PH Sensor Based on Poly-Dopamine Coated Carbon Nano-Onion Electrodes. *Sensors Actuators, B Chem.* **2018**, *273* (January), 664–671. https://doi.org/10.1016/j.snb.2018.06.103.

(165) Leventis, H. C.; Streeter, I.; Wildgoose, G. G.; Lawrence, N. S.; Jiang, L.; Jones, T. G. J.; Compton, R. G. Derivatised Carbon Powder Electrodes: Reagentless PH Sensors. *Talanta* **2004**, *63* (4), 1039–1051. https://doi.org/10.1016/j.talanta.2004.01.017.

(166) Munteanu, R. E.; Stănică, L.; Gheorghiu, M.; Gáspár, S. Measurement of the Extracellular PH of Adherently Growing Mammalian Cells with High Spatial Resolution Using a Voltammetric PH Microsensor. *Anal. Chem.* **2018**, *90* (11), 6899–6905. https://doi.org/10.1021/acs.analchem.8b01124.

(167) Herdman, K. M.; Breslin, C. B.; Finnerty, N. J. Physiological Monitoring of Tissue PH: In Vitro Characterisation and in Vivo Validation of a Quinone-Modified Carbon Paste Electrode. *Electrochim. Acta* **2019**, *298*, 484–495. https://doi.org/10.1016/j.electacta.2018.12.110.

(168) Finnerty, N. J.; Bolger, F. B. A Platinum Oxide-Based Microvoltammetric PH Electrode Suitable for Physiological Investigations. *Analyst* **2018**, *143* (13), 3124–3133. https://doi.org/10.1039/c8an00631h.

(169) Botz, A.; Clausmeyer, J.; Öhl, D.; Tarnev, T.; Franzen, D.; Turek, T.; Schuhmann, W. Local Activities of Hydroxide and Water Determine the Operation of Silver-Based Oxygen Depolarized Cathodes. *Angew. Chemie - Int. Ed.* **2018**, *57* (38), 12285–12289. https://doi.org/10.1002/anie.201807798.

(170) Chen, D.-J.; Tong, Y. Y. J. In Situ Raman Spectroscopic Measurement of Near-Surface Proton Concentration Changes during Electrochemical Reactions. *ChemCommun.* **2015**, No. 51, 5683–5686. https://doi.org/DOI: 10.1039/c5cc00427f.

(171) Hardcastle, C. D.; Harris, J. M. Confocal Raman Microscopy for PH-Gradient Preconcentration and Quantitative Analyte Detection in Optically Trapped Phospholipid Vesicles. *Anal. Chem.* **2015**, *87* (15), 7979–7986. https://doi.org/10.1021/acs.analchem.5b01905.

(172) Müller, J. D.; Schneider, B.; Aßmann, S.; Rehder, G. Spectrophotometric PH Measurements in the Presence of Dissolved Organic Matter and Hydrogen Sulfide. *Limnol. Oceanogr. Methods* **2018**, *16* (2), 68–82. https://doi.org/10.1002/lom3.10227.

(173) Bard, A. J.; Faulkner, L. R. Electrochemical Methods Fundamentals and Applications; Wiley: New York, 2001.

(174) Morris, C.; Chen, C.-C.; Ito, T.; Baker, L. Local PH Measurement with Scanning Ion Conductance Microscopy. *J. Electrochem. Soc.* **2013**, *160* (8), H430–H435. https://doi.org/10.1149/2.028308jes.

(175) Michalak, M.; Kurel, M.; Jedraszko, J.; Toczydlowska, D.; Wittstock, G.; Opallo, M.; Nogala, W. Voltammetric PH Nanosensor. *Anal. Chem.* **2015**, *87* (23), 11641–11645. https://doi.org/10.1021/acs.analchem.5b03482.

(176) Mani, G. K.; Morohoshi, M.; Yasoda, Y.; Yokoyama, S.; Kimura, H.; Tsuchiya, K. ZnO-Based Microfluidic PH Sensor: A Versatile Approach for Quick Recognition of Circulating Tumor Cells in Blood. *ACS Appl. Mater. Interfaces* **2017**, *9* (6), 5193–5203. https://doi.org/10.1021/acsami.6b16261.

(177) Serrapede, M.; Denuault, G.; Sosna, M.; Pesce, G. L.; Ball, R. J. Scanning Electrochemical Microscopy: Using the Potentiometric Mode of SECM to Study the Mixed Potential Arising from Two Independent Redox Processes. *Anal. Chem.* **2013**, *85* (17), 8341–8346. https://doi.org/10.1021/ac4017055.

(178) Kinoshita, K.; Madou, M. J. Electrochemical Measurements on Pt, Ir, and Ti Oxides as PH Probes. *J. Electrochem. Soc.* **1984**, *131* (5), 1089–1094. https://doi.org/10.1149/1.2115755.

(179) Kahlert, H. Functionalized Carbon Electrodes for PH Determination. *J. Solid State Electrochem.* **2008**, *12* (10), 1255–1266. https://doi.org/10.1007/s10008-008-0566-7.

http://rcin.org.pl

(180) Compton, R. G.; Banks, C. E. Understanding Voltammetry; Imperial College Press: London, 2011.

(181) Joshi, V. S.; Sheet, P. S.; Cullin, N.; Kreth, J.; Koley, D. Real-Time Metabolic Interactions between Two Bacterial Species Using a Carbon-Based PH Microsensor as a Scanning Electrochemical Microscopy Probe. *Anal. Chem.* **2017**, *89* (20), 11044–11052. https://doi.org/10.1021/acs.analchem.7b03050.

(182) Kutz, M. *Handbook of Measurement in Science and Engineering*; WILEY & SONS, INC., PUBLICATION, 2016.

(183) Engstrom, R. C.; Weber, M.; Wunder, D. J.; Burgess, R.; Winquist, S. Measurements within the Diffusion Layer Using a Microelectrode Probe. *Anal. Chem.* **1986**, *58* (4), 844–848. https://doi.org/10.1021/ac00295a044.

(184) Bard, A. J.; Fan, F.-R. F.; Kwak, J.; Lev, O. Scanning Electrochemical Microscopy. Introduction and Principles. *Anal. Chem.* **1989**, *61* (2), 132–138. https://doi.org/10.1021/ac00177a011.

(185) Bard, A. J.; Mirkin, M. V. *Scanning Electrochemical Microscopy*; CRC Press: New York, 2012.

(186) Polcari, D.; Dauphin-Ducharme, P.; Mauzeroll, J. Scanning Electrochemical Microscopy: A Comprehensive Review of Experimental Parameters from 1989 to 2015. *Chem. Rev.* **2016**, *116* (22), 13234–13278. https://doi.org/10.1021/acs.chemrev.6b00067.

(187) Takahashi, Y.; Shevchuk, A. I.; Novak, P.; Babakinejad, B.; Macpherson, J.; Unwin, P. R.; Shiku, H.; Gorelik, J.; Klenerman, D.; Korchev, Y. E.; et al. Topographical and Electrochemical Nanoscale Imaging of Living Cells Using Voltage-Switching Mode Scanning Electrochemical Microscopy. *Proc. Natl. Acad. Sci.* **2012**, *109* (29), 11540–11545. https://doi.org/10.1073/pnas.1203570109.

(188) Amemiya, S.; Bard, A. J.; Fan, F. F.; Mirkin, M.; Unwin, P. Scanning Electrochemical Microscopy. *Annu. Rev. Anal. Chem.* **2008**, *1* (May), 95–131. https://doi.org/10.1146/annurev.anchem.1.031207.112938.

(189) Wittstock, G.; Burchardt, M.; Pust, S. E.; Shen, Y.; Zhao, C. Scanning Electrochemical Microscopy for Direct Imaging of Reaction Rates. *Angew. Chem. Int. Ed.* **2007**, *46* (10), 1584–1617. https://doi.org/10.1002/anie.200602750.

(190) Stulik, K.; Amatore, C.; Holub, K.; Marecek, V.; Kutner, W. Microelectrodes. Definitions, Characterization, and Applications. *Pure Appl. Chem.* **2000**, *72* (8), 1483–1492.

(191) Sauter, S.; Wittstock, G. Local Deposition and Characterisation of K2Co[Fe(CN)6] and $K_2Ni[Fe(CN)_6]$ by Scanning Electrochemical Microscopy. *J. Solid State Electrochem.* **2001**, *5* (3), 205–211. https://doi.org/10.1007/s100080000137.

(192) Blanc, C.; Pébère, N.; Tribollet, B.; Vivier, V. Galvanic Coupling between Copper and Aluminium in a Thin-Layer Cell. *Corros. Sci.* **2010**, *52* (3), 991–995. https://doi.org/10.1016/j.corsci.2009.11.023.

(193) Wei, C.; Bard, A. J.; Kapui, I.; Nagy, G.; Tóth, K. Scanning Electrochemical Microscopy. 32. Gallium Ultramicroelectrodes and Their Application in Ion-Selective Probes. *Anal. Chem.* **1996**, *68* (15), 2651–2655. https://doi.org/10.1021/ac9512362.

(194) Leonard, K. C.; Bard, A. J. The Study of Multireactional Electrochemical Interfaces via a Tip Generation/Substrate Collection Mode of Scanning Electrochemical Microscopy: The Hydrogen Evolution Reaction for Mn in Acidic Solution. *J. Am. Chem. Soc.* **2013**, *135* (42), 15890–15896. https://doi.org/10.1021/ja407395m.

(195) Lee, Y.; Amemiya, S.; Bard, A. J. Scanning Electrochemical Microscopy. 41. Theory and Characterization of Ring Electrodes. *Anal. Chem.* **2011**, *73* (10), 2261–2267.

(196) Mauzeroll, J.; Hueske, E. A.; Bard, A. J. Scanning Electrochemical Microscopy. 48. Hg / Pt Hemispherical Ultramicroelectrodes: Fabrication and Characterization. *Anal. Chem.* **2003**, *75* (15), 3880–3889.

(197) Zoski, C. G. Ultramicroelectrodes: Design, Fabrication, and Characterization. *Electroanalysis* **2002**, *14* (15–16), 1041–1051. https://doi.org/10.1002/1521-4109(200208)14:15/16<1041::AID-

http://rcin.org.pl

ELAN1041>3.0.CO;2-8.

(198) Katemann, B. B.; Schuhmann, W. Fabrication and Characterization of Needle-Type Pt-Disk Nanoelectrodes. *Electroanalysis* **2002**, *14* (1), 22–28. https://doi.org/10.1002/1521-4109(200201)14:1<22::AID-ELAN22>3.0.CO;2-F.

(199) Danis, L.; Polcari, D.; Kwan, A.; Gateman, S. M.; Mauzeroll, J. Fabrication of Carbon, Gold, Platinum, Silver, and Mercury Ultramicroelectrodes with Controlled Geometry. *Anal. Chem.* **2015**, *87* (5), 2565–2569. https://doi.org/10.1021/ac503767n.

(200) Xiong, H.; Guo, J.; Kurihara, K.; Amemiya, S. Fabrication and Characterization of Conical Microelectrode Probes Templated by Selectively Etched Optical Fibers for Scanning Electrochemical Microscopy. *Electrochem. Commun.* **2004**, *6* (6), 615–620. https://doi.org/10.1016/j.elecom.2004.04.016.

(201) Walsh, D. a; Ferna, L.; Mauzeroll, J.; Bard, A. J. Scanning Electrochemical Microscopy. 55. Fabrication and Characterization of Micropipet Probes. *Anal. Chem.* **2005**, *77* (16), 5182–5188.

(202) Velmurugan, J.; Agrawal, A. K.; An, S.; Choudhary, E.; Szalai, V. A. Fabrication of Scanning Electrochemical Microscopy-Atomic Force Microscopy (SECM-AFM) Probes to Image Surface Topography and Reactivity at the Nanoscale. *Anal. Chem.* **2017**, *89*, 2687–2691.

(203) Pust, S. E.; Maier, W.; Wittstock, G. Investigation of Localized Catalytic and Electrocatalytic Processes and Corrosion Reactions with Scanning Electrochemical Microscopy (SECM). *Zeitschrift für Phys. Chemie* **2008**, *222* (10), 1463–1517. https://doi.org/10.1524/zpch.2008.5426.

(204) Nogala, W. Dioxygen Electroreduction on Enzyme Modified Carbon Ceramic Electrodes, Institute of Physical Chemistry, Polish Academy of Sciences, 2010.

(205) Lefrou, C.; Cornut, R. Analytical Expressions for Quantitative Scanning Electrochemical Microscopy (SECM). *ChemPhysChem* **2010**, *11* (3), 547–556. https://doi.org/10.1002/cphc.200900600.

(206) Zoski, C. G.; Mirkin, M. V. Steady-State Limiting Currents at Finite Conical Microelectrodes. *Anal. Chem.* **2002**, *74* (9), 1986–1992. https://doi.org/10.1021/ac015669i.

(207) Engstrom, R. C.; Pharr, C. M. Scanning Electrochemical Microscopy. *Anal. Chem.* **1989**, *61* (19), 1099–1104.

(208) Takahashi, Y.; Kumatani, A.; Shiku, H.; Matsue, T. Scanning Probe Microscopy for Nanoscale Electrochemical Imaging. *Anal. Chem.* **2016**, *89*, 342–357.

(209) Zoski, C. G. Review—Advances in Scanning Electrochemical Microscopy (SECM). *J. Electrochem. Soc.* **2016**, *163* (4), 3088–3100. https://doi.org/10.1149/2.0141604jes.

(210) Sun, P.; Laforge, F. O.; Mirkin, M. V. Scanning Electrochemical Microscopy in the 21st Century. *Phys. Chem. Chem. Phys.* **2007**, *9* (7), 802–823. https://doi.org/10.1039/B612259K.

(211) Fernández, J. L.; Bard, A. J. Scanning Electrochemical Microscopy 50. Kinetic Study of Electrode Reactions by the Tip Generation-Substrate Collection Mode. *Anal. Chem.* **2004**, *76* (8), 2281–2289. https://doi.org/10.1021/ac035518a.

(212) Eckhard, K.; Chen, X.; Turcu, F.; Schuhmann, W. Redox Competition Mode of Scanning Electrochemical Microscopy (RC-SECM) for Visualisation of Local Catalytic Activity. *Phys. Chem. Chem. Phys.* **2006**, *8* (45), 5359. https://doi.org/10.1039/b609511a.

(213) Wittstock, G.; Schuhmann, W. Formation and Imaging of Microscopic Enzymatically Active Spots on an Alkanethiolate-Covered Gold Electrode by Scanning Electrochemical Microscopy. *Anal. Chem.* **1997**, *69* (24), 5059–5066. https://doi.org/10.1021/ac970504o.

(214) Wuu, Y.-M.; Fan, F.-R. F.; Bard, A. J. High Resolution Deposition of Polyaniline on Pt with the Scanning Electrochemical Microscope. *J. Electrochem. Soc.* **1989**, *136* (3), 885–886. https://doi.org/10.1149/1.2096765.

(215) El-Giar, E. E. D. M.; Wipf, D. O. Microparticle-Based Iridium Oxide Ultramicroelectrodes for PH Sensing and Imaging. *J. Electroanal. Chem.* **2007**, *609* (2), 147–154. https://doi.org/10.1016/j.jelechem.2007.06.022.

http://rcin.org.pl

(216) Liang, Z.; Ahn, H. S.; Bard, A. J. A Study of the Mechanism of the Hydrogen Evolution Reaction on Nickel by Surface Interrogation Scanning Electrochemical Microscopy. *J. Am. Chem. Soc.* **2017**, *139* (13), 4854–4858.

(217) Ahn, H. S.; Bard, A. J. Surface Interrogation Scanning Electrochemical Microscopy of $Ni_{1-x}Fe_xOOH$ ($0 < x < 0.27$) Oxygen Evolving Catalyst: Kinetics of the "Fast" Iron Sites. *J. Am. Chem. Soc.* **2016**, *138* (1), 313–318. https://doi.org/10.1021/jacs.5b10977.

(218) Park, H. S.; Leonard, K. C.; Bard, A. J. Surface Interrogation Scanning Electrochemical Microscopy (SI- SECM) of Photoelectrochemistry at a W/Mo-BiVO4 Semiconductor Electrode: Quantification of Hydroxyl Radicals during Water Oxidation. *J. Phys. Chem. C* **2013**, *117*, 12093−12102.

(219) Arroyo-Currás, N.; Bard, A. J. Iridium Oxidation as Observed by Surface Interrogation Scanning Electrochemical Microscopy. *J. Phys. Chem. C* **2015**, *119* (15), 8147–8154. https://doi.org/10.1021/acs.jpcc.5b00106.

(220) Rodríguez-López, J. *Electroanalytical Chemistry, A Series of Advances*; Bard, A. J., Zoski, C. G., Eds.; CRC Press, Taylor & Francis Group, 2012; Vol. 24.

(221) Rodríguez-López, J.; Bard, A. J. Scanning Electrochemical Microscopy: Surface Interrogation of Adsorbed Hydrogen and the Open Circuit Catalytic Decomposition of Formic Acid at Platinum. *J. Am. Chem. Soc.* **2010**, *132* (14), 5121–5129. https://doi.org/10.1021/ja9090319.

(222) Wang, Y.; Kececi, K.; Velmurugan, J.; Mirkin, M. V. Electron Transfer/Ion Transfer Mode of Scanning Electrochemical Microscopy (SECM): A New Tool for Imaging and Kinetic Studies. *Chem. Sci.* **2013**, *4* (9), 3606. https://doi.org/10.1039/c3sc50825k.

(223) Oleinick, A.; Yu, Y.; Svir, I.; Mirkin, M. V.; Amatore, C. A. Theory and Simulations for the Electron Transfer/Ion Transfer Mode of SECM in the Presence or Absence of Homogenous Kinetics. *ChemElectroChem* **2016**, *56*, 607–622. https://doi.org/10.1002/celc.201600583.

(224) Li, Y.; Ning, X.; Ma, Q.; Qin, D.; Lu, X. Recent Advances in Electrochemistry by Scanning Electrochemical Microscopy. *Trends Anal. Chem.* **2016**, *80*, 242–254. https://doi.org/10.1016/j.trac.2016.02.002.

(225) Bard, A. J.; Mirkin, M. V.; Unwin, P. R.; Wipf, D. Scanning Electrochemical Microscopy. 12. Theory and Experiment of the Feedback Mode with Finite Heterogeneous Electron-Transfer Kinetics and Arbitrary Substrate Size. *J. Phys. Chem.* **1992**, *96* (14), 1861–1868.

(226) Minguzzi, A.; Alpuche-Aviles, M. A.; López, J. R.; Rondinini, S.; Bard, A. J. Screening of Oxygen Evolution Electrocatalysts by Scanning Electrochemical Microscopy Using a Shielded Tip Approach. *Anal. Chem.* **2008**, *80* (11), 4055–4064. https://doi.org/10.1021/ac8001287.

(227) Engstrom, R. C.; Small, B.; Kattan, L. Observation of Microscopically Local Electron-Transfer Kinetics with Scanning Electrochemical Microscopy. *Anal. Chem.* **1992**, *64* (3), 241–244. https://doi.org/10.1021/ac00027a001.

(228) Lin, C. L.; Rodríguez-López, J.; Bard, A. J. Micropipet Delivery-Substrate Collection Mode of Scanning Electrochemical Microscopy for the Imaging of Electrochemical Reactions and the Screening of Methanol Oxidation Electrocatalysts. *Anal. Chem.* **2009**, *81* (21), 8868–8877. https://doi.org/10.1021/ac901434a.

(229) Laforge, F. O.; Velmurugan, J.; Wang, Y.; Mirkin, M. V. Nanoscale Imaging of Surface Topography and Reactivity with the Scanning Electrochemical Microscope. *Anal. Chem.* **2009**, *81* (8), 3143–3150. https://doi.org/10.1021/ac900335c.

(230) Shen, M.; Ishimatsu, R.; Kim, J.; Amemiya, S. Quantitative Imaging of Ion Transport through Single Nanopores by High-Resolution Scanning Electrochemical Microscopy. *J. Am. Chem. Soc.* **2012**, *134* (24), 9856–9859. https://doi.org/10.1021/ja3023785.

(231) Yatziv, Y.; Turyan, I.; Mandler, D. A New Approach to Micropatterning: Application of Potential-Assisted Ion Transfer at the Liquid-Liquid Interface for the Local Metal Deposition. *J. Am. Chem. Soc.* **2002**, *124* (20), 5618–5619. https://doi.org/10.1021/ja0257826.

(232) Zhou, M.; Yu, Y.; Blanchard, P. Y.; Mirkin, M. V. Surface Patterning Using Diazonium Ink

http://rcin.org.pl

Filled Nanopipette. *Anal. Chem.* **2015**, *87* (21), 10956–10962. https://doi.org/10.1021/acs.analchem.5b02784.

(233) Kim, J.; Izadyar, A.; Shen, M.; Ishimatsu, R.; Amemiya, S. Ion Permeability of the Nuclear Pore Complex and Ion-Induced Macromolecular Permeation as Studied by Scanning Electrochemical and Fluorescence Microscopy. *Anal. Chem.* **2014**, *86* (4), 2090–2098. https://doi.org/10.1021/ac403607s.

(234) Zhou, M.; Yu, Y.; Hu, K.; Mirkin, M. V. Nanoelectrochemical Approach To Detecting Short-Lived Intermediates of Electrocatalytic Oxygen Reduction. *J. Am. Chem. Soc.* **2015**, *137* (20), 6517–6523. https://doi.org/10.1021/ja512482n.

(235) Kranz, C. Recent Advancements in Nanoelectrodes and Nanopipettes Used in Combined Scanning Electrochemical Microscopy Techniques. *Analyst* **2014**, *139* (2), 336–352. https://doi.org/10.1039/C3AN01651J.

(236) Mirkin, M. V.; Nogala, W.; Velmurugan, J.; Wang, Y. Scanning Electrochemical Microscopy in the 21st Century. Update 1: Five Years After. *Phys. Chem. Chem. Phys.* **2011**, *13* (48), 21196–21212. https://doi.org/10.1039/c1cp22376c.

(237) O'Connell, M. A.; Wain, A. J. Combined Electrochemical-Topographical Imaging: A Critical Review. *Anal. Methods* **2015**, *7* (17), 6983–6999. https://doi.org/10.1039/C5AY00557D.

(238) Macpherson, J. V.; Unwin, P. R. Combined Scanning Electrochemical-Atomic Force Microscopy. *Anal. Chem.* **2000**, *72* (2), 276–285. https://doi.org/10.1021/ac990921w.

(239) Macpherson, J. V.; Unwin, P. R. Noncontact Electrochemical Imaging with Combined Scanning Electrochemical Atomic Force Microscopy. *Anal. Chem.* **2001**, *73*, 550–557. https://doi.org/10.1021/ac001072b.

(240) Comstock, D. J.; Elam, J. W.; Pellin, M. J.; Hersam, M. C. High Aspect Ratio Nanoneedle Probes with an Integrated Electrode at the Tip Apex. *Rev. Sci. Instrum.* **2012**, *83* (11), 113704. https://doi.org/10.1063/1.4767248.

(241) Wain, A. J.; Pollard, A. J.; Richter, C. High-Resolution Electrochemical and Topographical Imaging Using Batch-Fabricated Cantilever Probes. *Anal. Chem.* **2014**, *86* (10), 5143–5149. https://doi.org/10.1021/ac500946v.

(242) Lee, E.; Kim, M.; Seong, J.; Shin, H.; Lim, G. An L-Shaped Nanoprobe for Scanning Electrochemical Microscopy-Atomic Force Microscopy. *Phys. Status Solidi - Rapid Res. Lett.* **2013**, *7* (6), 406–409. https://doi.org/10.1002/pssr.201307120.

(243) Derylo, M. A.; Morton, K. C.; Baker, L. A. Parylene Insulated Probes for Scanning Electrochemical-Atomic Force Microscopy. *Langmuir* **2011**, *27* (22), 13925–13930. https://doi.org/10.1021/la203032u.

(244) Nellist, M. R.; Chen, Y.; Mark, A.; Gödrich, S.; Stelling, C.; Jiang, J.; Poddar, R.; Li, C.; Kumar, R.; Papastavrou, G.; et al. Atomic Force Microscopy with Nanoelectrode Tips for High Resolution Electrochemical, Nanoadhesion and Nanoelectrical Imaging. *Nanotechnology* **2017**, *28* (9), 095711. https://doi.org/10.1088/1361-6528/aa5839.

(245) Eifert, A.; Smirnov, W.; Frittmann, S.; Nebel, C.; Mizaikoff, B.; Kranz, C. Atomic Force Microscopy Probes with Integrated Boron Doped Diamond Electrodes: Fabrication and Application. *Electrochem. Commun.* **2012**, *25*, 30–34.

(246) Hansma, P.; Drake, B.; Marti, O.; Gould, S.; Prater, C. The Scanning Ion-Conductance Microscope. *Science* **1989**, *243* (4891), 641–643. https://doi.org/10.1126/science.2464851.

(247) Page, A.; Perry, D.; Unwin, P. R. Multifunctional Scanning Ion Conductance Microscopy. *Proc. R. Soc. A* **2017**, *473* (2200), 1–34.

(248) Korchev, Y. E.; Bashford, C. L.; Milovanovic, M.; Vodyanoy, I.; Lab, M. J. Scanning Ion Conductance Microscopy of Living Cells. *Biophys. J.* **1997**, *73* (2), 653–658. https://doi.org/10.1016/s0006-3495(97)78100-1.

(249) Takahashi, Y.; Shevchuk, A. I.; Novak, P.; Zhang, Y.; Ebejer, N.; MacPherson, J. V.; Unwin, P. R.; Pollard, A. J.; Roy, D.; Clifford, C. A.; et al. Multifunctional Nanoprobes for Nanoscale

http://rcin.org.pl

Chemical Imaging and Localized Chemical Delivery at Surfaces and Interfaces. *Angew. Chemie - Int. Ed.* **2011**, *50* (41), 9638–9642. https://doi.org/10.1002/anie.201102796.

(250) O'Connell, M. A.; Wain, A. J. Mapping Electroactivity at Individual Catalytic Nanostructures Using High-Resolution Scanning Electrochemical − Scanning Ion Conductance Microcopy. *Anal. Biochem.* **2014**, *86*, 12100–12107.

(251) Nadappuram, B. P.; McKelvey, K.; Al Botros, R.; Colburn, A. W.; Unwin, P. R. Fabrication and Characterization of Dual Function Nanoscale PH-Scanning Ion Conductance Microscopy (SICM) Probes for High Resolution PH Mapping. *Anal. Chem.* **2013**, *85* (17), 8070–8074. https://doi.org/10.1021/ac401883n.

(252) Page, A.; Kang, M.; Armitstead, A.; Perry, D.; Unwin, P. R. Quantitative Visualization of Molecular Delivery and Uptake at Living Cells with Self-Referencing Scanning Ion Conductance Microscopy – Scanning Electrochemical Microscopy. *Anal. Chem.* **2017**, *89*, 3021–3028. https://doi.org/10.1021/acs.analchem.6b04629.

(253) Comstock, D. J.; Elam, J. W.; Pellin, M. J.; Hersam, M. C. Integrated Ultramicroelectrode-Nanopipet Probe for Concurrent Scanning Electrochemical Microscopy and Scanning Ion Conductance Microscopy. *Anal. Chem.* **2010**, *82* (4), 1270–1276. https://doi.org/10.1021/ac902224q.

(254) Morris, C. A.; Chen, C.-C.; Baker, L. A. Transport of Redox Probes through Single Pores Measured by Scanning Electrochemical-Scanning Ion Conductance Microscopy (SECM-SICM). *Analyst* **2012**, *137* (13), 2933. https://doi.org/10.1039/c2an16178h.

(255) Takahashi, Y.; Shevchuk, A. I.; Novak, P.; Murakami, Y.; Shiku, H.; Korchev, Y. E.; Matsue, T. Simultaneous Noncontact Topography and Electrochemical Imaging by SECM/SICM Featuring Ion Current Feedback Regulation. *J. Am. Chem. Soc.* **2010**, *132* (29), 10118–10126. https://doi.org/10.1021/ja1029478.

(256) Ino, K.; Ono, K.; Arai, T.; Takahashi, Y.; Shiku, H.; Matsue, T. Carbon-Ag/AgCl Probes for Detection of Cell Activity in Droplets. *Anal. Chem.* **2013**, *85* (8), 3832–3835. https://doi.org/10.1021/ac303569t.

(257) Clausmeyer, J.; Schuhmann, W. Nanoelectrodes: Applications in Electrocatalysis, Single-Cell Analysis and High-Resolution Electrochemical Imaging. *Trends Anal. Chem.* **2016**, *79*, 46–59. https://doi.org/10.1016/j.trac.2016.01.018.

(258) Alpuche-Aviles, M. A.; Wipf, D. O. Impedance Feedback Control for Scanning Electrochemical Microscopy. *Anal. Chem.* **2001**, *73* (20), 4873–4881. https://doi.org/10.1021/ac010581q.

(259) Ervin, E. N.; White, H. S.; Baker, L. A.; Martin, C. R. Alternating Current Impedance Imaging of High-Resistance Membrane Pores Using a Scanning Electrochemical Microscope. *Anal. Chem.* **2006**, *78* (18), 6535–6541.

(260) Eckhard, K.; Schuhmann, W. Alternating Current Techniques in Scanning Electrochemical Microscopy (AC-SECM). *Analyst* **2008**, *133* (11), 1486–1497. https://doi.org/10.1039/b806721j.

(261) Horrocks, B. R.; Schmidtke, D.; Heller, A.; Bard, A. J. Scanning Electrochemical Microscopy. 24. Enzyme Ultramicroelectrodes for the Measurement of Hydrogen Peroxide at Surfaces. *Anal. Chem.* **1993**, *65* (24), 3605–3614. https://doi.org/10.1021/ac00072a013.

(262) Etienne, M.; Schulte, A.; Schuhmann, W. High Resolution Constant-Distance Mode Alternating Current Scanning Electrochemical Microscopy (AC-SECM). *Electrochem. Commun.* **2004**, *6* (3), 288–293. https://doi.org/10.1016/j.elecom.2004.01.006.

(263) Danis, L.; Snowden, M. E.; Tefashe, U. M.; Heinemann, C. N.; Mauzeroll, J. Development of Nano-Disc Electrodes for Application as Shear Force Sensitive Electrochemical Probes. *Electrochim. Acta* **2014**, *136*, 121–129. https://doi.org/10.1016/j.electacta.2014.05.047.

(264) Ludwig, M.; Kranz, C.; Schuhmann, W.; Gaub, H. E. Topography Feedback Mechanism for the Scanning Electrochemical Microscope Based on Hydrodynamic Forces between Tip and Sample. *Rev. Sci. Instrum.* **1995**, *66* (4), 2857–2860. https://doi.org/10.1063/1.1145568.

(265) Lee, Y.; Ding, Z.; Bard, A. J. Combined Scanning Electrochemical/Optical Microscopy with

http://rcin.org.pl

Shear Force and Current Feedback. *Anal. Chem.* **2002**, *74* (15), 3634–3643.

(266) Cougnon, C.; Bauer-Espindola, K.; Fabre, D. S.; Mauzeroll, J. Development of a Phase-Controlled Constant-Distance Scanning Electrochemical Microscope. *Anal. Chem.* **2009**, *81* (9), 3654–3659. https://doi.org/10.1021/ac802211u.

(267) Etienne, M.; Lhenry, S.; Cornut, R.; Lefrou, C. Optimization of the Shearforce Signal for Scanning Electrochemical Microscopy and Application for Kinetic Analysis. *Electrochim. Acta* **2013**, *88*, 877–884. https://doi.org/10.1016/j.electacta.2012.09.063.

(268) Nebel, M.; Eckhard, K.; Erichsen, T.; Schulte, A.; Schuhmann, W. 4D Shearforce-Based Constant-Distance Mode Scanning Electrochemical Microscopy. *Anal. Chem.* **2010**, *82* (18), 7842–7848. https://doi.org/10.1021/ac1008805.

(269) Ballesteros Katemann, B.; Schulte, A.; Schuhmann, W. Constant-Distance Mode Scanning Electrochemical Microscopy. Part II: High-Resolution SECM Imaging Employing Pt Nanoelectrodes as Miniaturized Scanning Probes. *Electroanalysis* **2004**, *16* (12), 60–65. https://doi.org/10.1002/elan.200302918.

(270) Schulte, A.; Nebel, M.; Schuhmann, W. Single Live Cell Topography and Activity Imaging with the Shear-Force-Based Constant-Distance Scanning Electrochemical Microscope, 1st ed.; Elsevier Inc., 2012; Vol. 504. https://doi.org/10.1016/B978-0-12-391857-4.00012-4.

(271) Takahashi, Y.; Shiku, H.; Murata, T.; Yasukawa, T.; Matsue, T. Transfected Single-Cell Imaging by Scanning Electrochemical Optical Microscopy with Shear Force Feedback Regulation. *Anal. Chem.* **2009**, *81* (23), 9674–9681. https://doi.org/10.1021/ac901796r.

(272) Etienne, M.; Layoussifi, B.; Giornelli, T.; Jacquet, D. SECM-Based Automate Equipped with a Shearforce Detection for the Characterization of Large and Complex Samples. *Electrochem. Commun.* **2012**, *15* (1), 70–73. https://doi.org/10.1016/j.elecom.2011.11.028.

(273) Etienne, M.; Schulte, A.; Mann, S.; Jordan, G.; Dietzel, I. D.; Schuhmann, W. Constant-Distance Mode Scanning Potentiometry. 1. Visualization of Calcium Carbonate Dissolution in Aqueous Solution. *Anal. Chem.* **2004**, *76* (13), 3682–3688. https://doi.org/10.1021/ac0349227.

(274) Kleijn, S. E. F.; Lai, S. C. S.; Koper, M. T. M.; Unwin, P. R. Electrochemistry of Nanoparticles. *Angew. Chemie - Int. Ed.* **2014**, *53* (14), 3558–3586. https://doi.org/10.1002/anie.201306828.

(275) Kang, M.; Perry, D.; Bentley, C. L.; West, G.; Page, A.; Unwin, P. R. Simultaneous Topography and Reaction Flux Mapping at and around Electrocatalytic Nanoparticles. *ACS Nano* **2017**, *11* (9), 9525–9535. https://doi.org/10.1021/acsnano.7b05435.

(276) Bentley, C. L.; Unwin, P. R. Nanoscale Electrochemical Movies and Synchronous Topographical Mapping of Electrocatalytic Materials. *Faraday Discuss.* **2018**, *210*, 365–379. https://doi.org/10.1039/c8fd00028j.

(277) Liang, Y.; Pfisterer, J. H. K.; McLaughlin, D.; Csoklich, C.; Seidl, L.; Bandarenka, A. S.; Schneider, O. Electrochemical Scanning Probe Microscopies in Electrocatalysis. *Small Methods* **2018**, 1–27. https://doi.org/10.1002/smtd.201800387.

(278) Momotenko, D.; McKelvey, K.; Kang, M.; Meloni, G. N.; Unwin, P. R. Simultaneous Interfacial Reactivity and Topography Mapping with Scanning Ion Conductance Microscopy. *Anal. Chem.* **2016**, *88* (5), 2838–2846. https://doi.org/10.1021/acs.analchem.5b04566.

(279) Şen, M.; Takahashi, Y.; Matsumae, Y.; Horiguchi, Y.; Kumatani, A.; Ino, K.; Shiku, H.; Matsue, T. Improving the Electrochemical Imaging Sensitivity of Scanning Electrochemical Microscopy-Scanning Ion Conductance Microscopy by Using Electrochemical Pt Deposition. *Anal. Chem.* **2015**, *87* (6), 3484–3489. https://doi.org/10.1021/acs.analchem.5b00027.

(280) Pfisterer, J. H. K.; Liang, Y.; Schneider, O.; Bandarenka, A. S. Direct Instrumental Identification of Catalytically Active Surface Sites. *Nature* **2017**, *549* (7670), 74–77. https://doi.org/10.1038/nature23661.

(281) Wang Joseph. Analytical Electrochemistry; John Wiley & Sons, Inc., 2006.

(282) https://www.britannica.com/technology/scanning-electron-microscope.

http://rcin.org.pl

(283) Kazmiruk, V. Scanning Electron Microscopy; InTech Open, 2012.

(284) Schatten, H. Scanning Electron Microscopy for the Life Sciences; Cambridge University Press, 2013.

(285) Nanakoudis, A. EDX Analysis with a Scanning Electron Microscope (SEM): How Does it Work? https://blog.phenom-world.com/edx-analysis-sem.

(286) http://blog.brukerafmprobes.com/category/guide-to-spm-and-afm-modes/.

(287) Eaton, P.; West, P. Atomic Force Microscopy; Oxford University Press, 2010.

(288) Kirchner, C. N.; Hallmeier, K. H.; Szargan, R.; Raschke, T.; Radehaus, C.; Wittstock, G. Evaluation of Thin Film Titanium Nitride Electrodes for Electroanalytical Applications. *Electroanalysis* **2007**, *19* (10), 1023–1031. https://doi.org/10.1002/elan.200703832.

(289) Wittstock, G.; Asmus, T.; Wilhelm, T. Investigation of Ion-Bombarded Conducting Polymer Films by Scanning Electrochemical Microscopy (SECM). *Fresenius. J. Anal. Chem.* **2000**, *367* (4), 346–351. https://doi.org/10.1007/s002160000389.

(290) Liu, L.; Yellinek, S.; Valdinger, I.; Donval, A.; Mandler, D. Important Implications of the Electrochemical Reduction of ITO. *Electrochim. Acta* **2015**, *176*, 1374–1381. https://doi.org/10.1016/j.electacta.2015.07.129.

(291) Nogala, W.; Kannan, P.; Gawinkowski, S.; Jönsson-Niedziolka, M.; Kominiak, M.; Waluk, J.; Opallo, M. Tailored Gold Nanostructure Arrays as Catalysts for Oxygen Reduction in Alkaline Media and a Single Molecule SERS Platform. *Nanoscale* **2015**, *7* (24), 10767–10774. https://doi.org/10.1039/C5NR02077H.

(292) Wang, M. S.; Zhang, Y.; Muhammed, M. Critical Evaluation of Thermodynamics of Complex Formation of Metal Ions in Aqueous Solutions .3. The System Cu(I,II)-Cl(-)e at 298.15 K. *Hydrometallurgy* **1997**, *45* (1–2), 53–72. https://doi.org/Doi 10.1016/S0304-386x(96)00074-6.

(293) Meng, Y.; Bard, A. J. Measurement of Temperature-Dependent Stability Constants of Cu(I) and Cu(II) Chloride Complexes by Voltammetry at a Pt Ultramicroelectrode. *Anal. Chem.* **2015**, *87* (6), 3498–3504. https://doi.org/10.1021/acs.analchem.5b00052.

(294) Herrero, E.; Buller, L. J.; Abruña, H. D. Underpotential Deposition at Single Crystal Surfaces of Au, Pt, Ag and Other Materials. *Chem. Rev.* **2001**, *101* (7), 1897–1930. https://doi.org/10.1021/cr9600363.

(295) Ikemiya, N.; Miyaoka, S.; Hara, S. Observations of the Cu (1 x 1) Adlayer on Au (111) in a Sulfuric Acid Solution Using Atomic Force Microscopy. *Surf. Sci.* **1994**, *311*, L641–L648.

(296) Nakamura, M.; Endo, O.; Ohta, T.; Ito, M.; Yoda, Y. Surface X-Ray Diffraction Study of Cu UPD on Au (111) Electrode in 0.5 M H2SO4 Solution: The Coadsorption Structure of UPD Copper, Hydration Water Molecule and Bisulfate Anion on Au (111). *Surf. Sci.* **2002**, *514*, 227–233. https://doi.org/10.1016/S0039-6028(02)01634-5.

(297) Chung, J.; Won, D. H.; Koh, J.; Kim, E. H.; Woo, S. I. Hierarchical Cu Pillar Electrodes for Electrochemical CO_2 Reduction to Formic Acid with Low Overpotential. *Phys. Chem. Chem. Phys.* **2016**, *18* (8), 6252–6258. https://doi.org/10.1039/c5cp07964k.

(298) Actis, P.; Tokar, S.; Clausmeyer, J.; Babakinejad, B.; Mikhaleva, S.; Cornut, R.; Takahashi, Y.; López Córdoba, A.; Novak, P.; Shevchuck, A. I.; et al. Electrochemical Nanoprobes for Single-Cell Analysis. *ACS Nano* **2014**, *8* (1), 875–884. https://doi.org/10.1021/nn405612q.

(299) Yu, Y.; Noel, J. M.; Mirkin, M. V.; Gao, Y.; Mashtalir, O.; Friedman, G.; Gogotsi, Y. Carbon Pipette-Based Electrochemical Nanosampler. *Anal. Chem.* **2014**, *86* (7), 3365–3372. https://doi.org/10.1021/ac403547b.

(300) O'Connell, M. A.; Lewis, J. R.; Wain, A. J. Electrochemical Imaging of Hydrogen Peroxide Generation at Individual Gold Nanoparticles. *Chem. Commun.* **2015**, *51* (51), 10314–10317. https://doi.org/10.1039/C5CC01640A.

(301) Nogala, W.; Velmurugan, J.; Mirkin, M. V. Atomic Force Microscopy of Electrochemical Nanoelectrodes. *Anal. Chem.* **2012**, *84* (12), 5192–5197. https://doi.org/10.1021/ac300744t.

http://rcin.org.pl

(302) Nogala, W.; Rozniecka, E.; Rogalski, J.; Opallo, M. PH-Sensitive Syringaldazine Modified Carbon Ceramic Electrode for Bioelectrocatalytic Dioxygen Reduction. *J. Electroanal. Chem.* **2007**, *608* (1), 31–36. https://doi.org/10.1016/j.jelechem.2007.05.001.

(303) Xi, S.; Shi, T.; Long, H.; Xu, L.; Tang, Z. Suspended Integration of Pyrolytic Carbon Membrane on C-MEMS. *Microsyst. Technol.* **2015**, *21* (9), 1835–1841. https://doi.org/10.1007/s00542-014-2263-z.

(304) Zukowska, G. Z.; Nogala, W.; Svartsov, Y.; Marcinek, M. L.; Rogalski, J.; Szot, K.; Opallo, M. In Situ Micro-Raman Studies of Syringaldazine-Entrapped Composite Electrodes Modified with Laccase. *ECS Trans.* **2010**, *25* (16), 29–44. https://doi.org/10.1149/1.3300060.

(305) Kiss, A.; Nagy, G. New SECM Scanning Algorithms for Improved Potentiometric Imaging of Circularly Symmetric Targets. *Electrochim. Acta* **2014**, *119*, 169–174. https://doi.org/10.1016/j.electacta.2013.12.041.

(306) Zhao, C.; Wittstock, G. Scanning Electrochemical Microscopy for Detection of Biosensor and Biochip Surfaces with Immobilized Pyrroloquinoline Quinone (PQQ)-Dependent Glucose Dehydrogenase as Enzyme Label. *Biosens. Bioelectron.* **2005**, *20* (7), 1277–1284. https://doi.org/10.1016/j.bios.2004.04.019.

Instytut Chemii Fizycznej PAN
BIBLIOTEKA
B. 519/20

http://rcin.org.pl

Biblioteka Instytutu Chemii Fizycznej PAN
F-B.519/20
10000000107072

http://rcin.org.pl